Universidade de Aveiro

2015

Departamento de Engenharia de Materiais e Cerâmica

Sebastian Czesław Złotnik

Estruturas 2D Funcionais de Tantalatos Alcalinos para Microelectrónica e Aplicações Relacionadas

Functional Alkali Tantalate 2D Structures for Microelectronics and Related Applications

Universidade de Aveiro

2015

Departamento de Engenharia de Materiais e Cerâmica

Sebastian Czesław Złotnik

Estruturas 2D Funcionais de Tantalatos Alcalinos para Microelectrónica e Aplicações Relacionadas

Functional Alkali Tantalate 2D Structures for Microelectronics and Related Applications

Tese apresentada à Universidade de Aveiro para cumprimento dos requisitos necessários à obtenção do grau de Doutor em Ciência e Engenharia de Materiais, realizada sob a orientação científica da Doutora Paula M. L. S. Vilarinho, Professora Associada do Departamento de Engenharia de Materiais e Cerâmica da Universidade de Aveiro.

Thesis presented to the University of Aveiro in fulfillment of the requirements for the awarding of the degree of Doctor in Materials Science and Engineering under the scientific guidance of Professor Paula M. L. S. Vilarinho, Associate Professor of the Department of Materials and Ceramic Engineering of the University of Aveiro.

Apoio financeiro da FCT e do FSE no âmbito do III Quadro Comunitário de Apoio.

“The important thing in science is not so much to obtain new facts as to discover new ways of thinking about them.”

Sir William Henry Bragg
Nobel Prize in Physics in 1915

“Any knowledge that doesn’t lead to new questions quickly dies out: it fails to maintain the temperature required for sustaining life.”
“It’s just not easy to explain to someone else what you don’t understand yourself.”

Wisława Szymborska
Nobel Prize in Literature in 1996

o júri / the jury

presidente

Prof. Doutor Artur Manuel Soares da Silva

professor catedrático da Universidade de Aveiro

vogais / examiners committee

Prof. Doutor Jorge Ribeiro Frade

professor catedrático da Universidade de Aveiro

Prof. Doutor Abílio de Jesus Monteiro Almeida

professor associado da Faculdade de Ciências da Universidade do Porto

Prof. Doutora Paula Maria Lousada Silveirinha Vilarinho

professora associada da Universidade de Aveiro (orientador)

Prof. Doutor Mário António Caixeiro Castro Pereira

professor auxiliar da Escola de Ciências da Universidade do Minho

Doutora María Lourdes Calzada Coco

investigadora da Instituto de Ciencia de Materiales de Madrid, Consejo Superior de Investigaciones Científicas (CSIC)

agradecimentos / acknowledgements

The majority of experimental work was performed at the Department of Materials and Ceramic Engineering, part of the associated laboratory: CICECO (Centre for Research in Ceramics and Composite Materials) – Aveiro Institute of Materials, and I am mostly grateful to my supervisor Prof. Paula M. Vilarinho for giving me the opportunity to do PhD under her supervision. Her constant encouragement, guidance and excellent mentorship over the past four years could help me to develop, organize, write and present good scientific communications, ending up with this thesis.

Thermochemical studies were carried out in collaboration with Prof. Alexandra Navrotsky and Dr. Sulata K. Sahu from the University of California, Davis (USA). I want to acknowledge them for an opportunity to conduct the experimental part in their laboratories, using a custom-made calorimetry setups.

Some part of the work was performed in The Instituto de Ciencia de Materiales de Madrid (ICMM), Consejo Superior de Investigaciones Cientificas (CSIC) in Madrid (Spain) in the group of Electroceramics for Information Technologies. I would like to thank Prof. M. Lourdes Calzada, Dr. Ricardo Jiménez and Dr. Iñigo Bretos for allowing me to learn how effectively oxide films can be prepared using chemical solution deposition method.

Special acknowledges go to Dr. David Tobaldi, a post-doc at DEMaC working on the topic of heterogeneous photocatalysis. He allowed me with his assistance to conduct studies on photocatalytic degradation. Since then I got very interested in a topic.

I also want to thank Prof. Maria Helena V. Fernandes and Dr. Marisa Maltez-da Costa for their scientific and moral support during the work on biological assays. The inspiring discussions helped me to understand the current needs in biomedical applications.

Then, plenty of others have had impact on the work over last years. I would like to express my sincere gratitude to my colleagues from the Electroceramics Group, the administrative and technical staff of the DEMaC and other departments at UA, and all the rest that I did not mention. The excellent atmosphere they created, their empathy, patience and moral support made my stay in Portugal enjoyable and profitable. Of course special thanks go to **Monika**, for her support at work and in everyday life.

I acknowledge FCT, the Portuguese Foundation for Science and Technology, for financial support, under the grant SFRH/BD/67023/2009.

palavras-chave

electricerâmicos, perovsquite, pirocloro, tantalatos alcalinos, $KTaO_3$, $LiTaO_3$, $NaTaO_3$, ferroeléctricos, incipientes ferroeléctricos, formação da fase, cinética, termoquímica, filmes finos, deposição for solução química, sol gel, síntese hidrotermal, estado sólido, fotocatálise, biomateriais

resumo

Tantalatos e niobatos alcalinos, como $K(Ta / Nb)O_3$, $Li(Ta / Nb)O_3$ and $Na(Ta / Nb)O_3$, são uma família atrativa de compostos ferroeléctricos livres de chumbo com estrutura perosvquítica. As suas propriedades versáteis fazem destes potencialmente interessantes para aplicações em microelectrónica, foto catálise, energia e biomédica. Entre os compostos acima citados, os compostos de tantalato de potássio, $KTaO_3$ (KTO), tem atraído bastante atenção como substitutos para o amplamente conhecido titanato de estrôncio, $SrTiO_3$ (STO). KTO é um óxido perovsquítico com comportamento paraelétrico quântico, quando eletricamente estimulado, e elevada polaribilidade tornando viável engenhar as suas propriedades através de estímulos internos e externos. No entanto os problemas na sua produção, quer em macroescala quer em nanoestruturas 2D, tornam estes compostos numa alternativa pouco viável para a substituir o STO. Consequentemente, e de forma a contribuir cientificamente para aumentar o conhecimento sobre as aplicações dos tantalatos, os principais objectivos desta tese são: i) produzir e caracterizar filmes finos de tantalatos alcalinos através de deposição de solução química em substratos rígidos, à base de silício, e a baixas temperaturas de forma a serem compatíveis com a tecnologia de silício; ii) complementar o conhecimento científico sobre estes materiais funcionais relativamente às suas características termodinâmicas; iii) explorar aplicações alternativas para os tantalatos alcalinos, como a foto catálise.

No que diz respeito à síntese, foi focalizada no entendimento da formação de fase no tantalato de potássio sintetizado por diferentes métodos, de modo a controlar a cristalização da estrutura perovsquítica desejada e evitar a formação da fase pirocloro a baixas temperaturas e fases deficientes em potássio.

Em tantalatos alcalinos o processo de formação da fase desejada está longe de estar plenamente analisado, como é o caso das perovsquites que contêm chumbo, consequentemente o trabalho foi inicialmente focado na compreensão da relação processo-fase para identificar as forças motrizes responsáveis por regular o processo de síntese.

Foi realizada um estudo comparativo da formação de fase via método convencional de reação do estado sólido e via método de sol-gel. A análise estrutural revelou que a estrutura piroclórica intermédia $K_2Ta_2O_6$ não foi formada em nenhuma etapa da reação via método do estado sólido. Por outro lado em processos baseados em solução, como os baseados em alcóxidos, a cristalização perovsquítica ocorre através da indesejada fase pirocloro intermédia; a baixas temperaturas a fase pirocloro é dominante e sofre a transformação para perovsquite a >800 °C. A análise cinética efectuada usando o modelo Johnson-Mehl-Avrami-Kolmogorow e a difração de raio-X quantitativa (DRX), demonstraram que nos pós obtidos pelo método sol-gel, a cristalização ocorre em duas etapas: i) no estágio inicial a reação é denominada por

nucleação primária, o mecanismo é controlado por fronteira de fase, e ii) no segundo estágio, o baixo valor do expoente de Avrami, $n \sim 0.3$, não segue nenhuma categoria reportada impossibilitando assim uma clara identificação do mecanismo. Posteriormente, e em colaboração com o grupo da Professora Alexandra Navrostky da Universidade da Califórnia, Davis, foram realizados estudos de termodinâmica, usando calorimetria de solução de óxidos fundidos a alta temperatura. Foram calculadas as entalpias de formação das três estruturas: pirocloro, perovsquite e tetragonal tungsténio bronze $K_6Ta_{10.8}O_{30}$ (TTB). As entalpias de formação relativas aos óxidos correspondentes, ΔH_f^{ox}, para $KTaO_3$, $KTa_{2.2}O_6$ e $K_6Ta_{10.8}O_{30}$, são -203.63 ± 2.84 kJ/mol, -358.02 ± 3.74 kJ/mol e -1252.34 ± 10.10 kJ/mol, respectivamente; enquanto que as relativas aos elementos, ΔH_f^{el}, para $KTaO_3$, $KTa_{2.2}O_6$ e $K_6Ta_{10.8}O_{30}$ são -1408.96 ± 3.73 kJ/mol, -2790.82 ± 6.06 kJ/mol e -13393.04 ± 31.15 kJ/mol, respectivamente. As possíveis reações de decomposição, de $KTa_{2.2}O_6$ para $KTaO_3$ e Ta_2O_5 (reação 1) ou para $K_6Ta_{10.8}O_{30}$ e Ta_2O_5 (reação 2), foram propostas e o cálculo das entalpias resultou em 308.79 ± 4.41 kJ/mol e 895.79 ± 8.64 kJ/mol, respectivamente. As reações são fortemente endotérmicas, indicando que estas decomposições são energeticamente desfavoráveis, uma vez que é improvável que qualquer termo de entropia possa sobrepor-se a uma entalpia tão positiva. Os estudos termodinâmicos provaram que o pirocloro é energeticamente mais estável que a perovsquite para temperaturas baixas. Assim, a organização local dos precipitados amorfos canaliza a cristalização para a estrutura mais favorável, que é a pirocloro com uma organização local similar; a distância entre os vizinhos mais próximos na fase amorfa, ou na fase ordenada a baixo alcance, é similar à do pirocloro.

Tendo em conta a derivação estequiométrica no sistema KTO, selecionar a técnica de fabricação / deposição de filmes finos mais apropriada é uma questão-chave, especialmente no que concerne aos óxidos ferroeléctricos complexos. A deposição por solução química tem sido o método de processamento mais reportado, para crescimento de filmes finos de KTO, mas o método clássico de alcóxidos permite cristalizar a fase perovsquite a temperaturas >800 °C enquanto que a temperatura máxima de estabilidade para os substratos de silício platinizado é ~700 °C. Portanto, foi usado um processo alternativo baseado em dióis, com precursores carboxilados de potássio, com o objectivo de estabilizar os precursores em solução, evitando assim o uso de solventes tóxicos e diminuindo a temperatura de cristalização da fase perovsquite. A análise dos pós revelou que no caso de KTO*ac* (solução baseada em acetato de potássio), uma mistura de fase perovsquite e pirocloro foi detectada a uma temperatura de apenas 450 °C, e a transformação gradual em estrutura perovsquítica monofásica ocorre quando as temperaturas sobem acima de 750 °C, no entanto a fase $KTaO_3$ monofásica não é obtida. No caso do KTO*acac* (solução com acetil-acetona de potássio, cadeia alquílica longa carboxilato de metal), um amplo pico é detectado a temperaturas <650 °C, característico de estruturas amorfas, enquanto que a elevadas temperaturas, os planos de difração das fases pirocloro e perovsquite são visíveis e a perovsquite $KTaO_3$ monofásica é conseguida a temperaturas >700 °C. A análise de infravermelhos mostrou que estas diferenças acontecem devido à deformação da estrutura base dos carbonatos sob aquecimento.

Uma série de filmes finos de tantalatos alcalinos foram depositados por spin-coating em substratos de silício, usando a metodologia baseada em dióis. Filmes monofásicos de perovsquite $KTaO_3$ depositados usando solução de KTO*acac* foram obtidos a uma temperatura de apenas 550 °C; os filmes foram recristralizados em fornos de aquecimento rápido em atmosfera de oxigénio durante 5 minutos com taxa de aquecimento de 30 °C/seg. Outras composições, $LiTaO_3$ (LTO) e $NaTaO_3$ (NTO), foram depositados com sucesso em substratos de silício a 650 °C. O carácter ferroeléctrico do LTO à temperatura ambiente foi provado. Infelizmente, não foi possível medir as propriedades eléctricas do KTO no condensador paralelo devido às interfaces filme-substrato ou filme-eléctrodo. Assim sendo, estudos futuros são necessários para compreender esta questão. Foram também conduzidos estudos com vista às possíveis aplicações; dois casos de estudo: i) estudo da atividade fotocatalítica de tantalatos e niobatos alcalinos para decomposição de poluentes, e ii) estudo de bioatividade de filmes ferroelétricos de tantalatos alcalinos como revestimento funcional para regeneração óssea.

Recentemente, tem sido dedicada muita atenção ao desenvolvimento de novos materiais fotocatalíticos, e as composições à base de óxido de tântalo e nióbio tem demonstrado capacidade de fotocatálise na reação de separação da água devido ao elevado potencial das bandas de condução. Assim, várias composições das famílias dos tantalatos e niobatos alcalinos foram testadas como catalisadores para degradação do azul de metileno. Os resultados mostram valores de atividade promissores para alguns dos compostos, sendo o $KNbO_3$ o mais ativo de entre os testados, alcançando valores acima de 50 % na degradação do pigmento após 7 h sob exposição a UVA. No entanto algumas modificações nas composições dos pós podem melhorar a sua performance.

No que concerne à regeneração óssea, é importante obter plataformas que através de estímulos apropriados consigam assegurar a adesão e direcionar o crescimento, a proliferação e a diferenciação celular. Neste contexto, foi aqui explorada uma estratégia alternativa para revestimento de implantes ósseos, baseada na regeneração óssea mediada por sinais elétricos. Esta estratégia implica revestir substratos metálicos de aço inoxidável tipo 316L (316L-SST), com camadas de $LiTaO_3$ ferroeléctrico, funcionalizadas através de polarização elétrica ou de irradiação com luz UV. Foi demonstrado que a formação de fosfato de cálcio na superfície e a adsorção de proteínas é consideravelmente melhorada quando o 316L-SST é revestido com filmes ferroelétricos funcionalizados. Esta estratégia pode ser encarada como um conjunto de orientações para o desenvolvimento de plataformas eletricamente funcionalizadas, capazes de estimular a regeneração de tecidos, promovendo a associação direta do implante com os tecidos hospedeiros, contribuindo assim para a redução de falhas na reabilitação com implantes ósseos.

keywords

electroceramics, perovskite, pyrochlore, alkali tantalates, $KTaO_3$, $LiTaO_3$, $NaTaO_3$, ferroelectrics, incipient ferroelectrics, phase formation, kinetics, thermochemistry, thin films, chemical solution deposition, sol gel, hydrothermal method, solid state, photocatalysis, biomaterials

abstract

Alkali tantalates and niobates, including $K(Ta / Nb)O_3$, $Li(Ta / Nb)O_3$ and $Na(Ta / Nb)O_3$, are a very promising ferroic family of lead-free compounds with perovskite-like structures. Their versatile properties make them potentially interesting for current and future application in microelectronics, photocatalysis, energy and biomedics. Among them potassium tantalate, $KTaO_3$ (KTO), has been raising interest as an alternative for the well-known strontium titanate, $SrTiO_3$ (STO). KTO is a perovskite oxide with a quantum paraelectric behaviour when electrically stimulated and a highly polarizable lattice, giving opportunity to tailor its properties via external or internal stimuli. However problems related with the fabrication of either bulk or 2D nanostructures makes KTO not yet a viable alternative to STO. Within this context and to contribute scientifically to the leverage tantalate based compounds applications, the main goals of this thesis are: i) to produce and characterise thin films of alkali tantalates by chemical solution deposition on rigid Si based substrates, at reduced temperatures to be compatible with Si technology, ii) to fulfil scientific knowledge gaps in these relevant functional materials related to their energetics and ii) to exploit alternative applications for alkali tantalates, as photocatalysis.

In what concerns the synthesis attention was given to the understanding of the phase formation in potassium tantalate synthesized via distinct routes, to control the crystallization of desired perovskite structure and to avoid low temperature pyrochlore or K-deficient phases.

The phase formation process in alkali tantalates is far from being deeply analysed, as in the case of Pb-containing perovskites, therefore the work was initially focused on the process-phase relationship to identify the driving forces responsible to regulate the synthesis. Comparison of phase formation paths in conventional solid-state reaction and sol-gel method was conducted. The structural analyses revealed that intermediate pyrochlore $K_2Ta_2O_6$ structure is not formed at any stage of the reaction using conventional solid-state reaction. On the other hand in the solution based processes, as alkoxide-based route, the crystallization of the perovskite occurs through the intermediate pyrochlore phase; at low temperatures pyrochlore is dominant and it is transformed to perovskite at >800 °C. The kinetic analysis carried out by using Johnson-Mehl-Avrami-Kolmogorow model and quantitative X-ray diffraction (XRD) demonstrated that in sol-gel derived powders the crystallization occurs in two stages: i) at early stage of the reaction dominated by primary nucleation, the mechanism is phase-boundary controlled, and ii) at the second stage the low value of Avrami exponent, $n \sim 0.3$, does not follow any reported category, thus not permitting an easy identification of the mechanism. Then, in collaboration with Prof. Alexandra Navrotsky group from the University of California at Davis (USA), thermodynamic studies were conducted, using high temperature oxide melt solution calorimetry. The enthalpies of formation of three structures: pyrochlore, perovskite and tetragonal tungsten bronze $K_6Ta_{10.8}O_{30}$ (TTB) were

calculated. The enthalpies of formation from corresponding oxides, ΔH_f^{ox}, for $KTaO_3$, $KTa_{2.2}O_6$ and $K_6Ta_{10.8}O_{30}$ are -203.63 ± 2.84 kJ/mol, - 358.02 ± 3.74 kJ/mol, and -1252.34 ± 10.10 kJ/mol, respectively, whereas from elements, ΔH_f^{el}, for $KTaO_3$, $KTa_{2.2}O_6$ and $K_6Ta_{10.8}O_{30}$ are -1408.96 ± 3.73 kJ/mol, -2790.82 ± 6.06 kJ/mol, and -13393.04 ± 31.15 kJ/mol, respectively. The possible decomposition reactions of K-deficient $KTa_{2.2}O_6$ pyrochlore to $KTaO_3$ perovskite and Ta_2O_5 (reaction 1) or to TTB $K_6Ta_{10.8}O_{30}$ and Ta_2O_5 (reaction 2) were proposed, and the enthalpies were calculated to be 308.79 ± 4.41 kJ/mol and 895.79 ± 8.64 kJ/mol for reaction 1 and reaction 2, respectively. The reactions are strongly endothermic, indicating that these decompositions are energetically unfavourable, since it is unlikely that any entropy term could override such a large positive enthalpy. The energetic studies prove that pyrochlore is energetically more stable phase than perovskite at low temperature. Thus, the local order of the amorphous precipitates drives the crystallization into the most favourable structure that is the pyrochlore one with similar local organization; the distance between nearest neighbours in the amorphous or short-range ordered phase is very close to that in pyrochlore.

Taking into account the stoichiometric deviation in KTO system, the selection of the most appropriate fabrication / deposition technique in thin films technology is a key issue, especially concerning complex ferroelectric oxides. Chemical solution deposition has been widely reported as a processing method to growth KTO thin films, but classical alkoxide route allows to crystallize perovskite phase at temperatures >800 °C, while the temperature endurance of platinized Si wafers is ~700 °C. Therefore, alternative diol-based routes, with distinct potassium carboxylate precursors, was developed aiming to stabilize the precursor solution, to avoid using toxic solvents and to decrease the crystallization temperature of the perovskite phase. Studies on powders revealed that in the case of KTO*ac* (solution based on potassium acetate), a mixture of perovskite and pyrochlore phases is detected at temperature as low as 450 °C, and gradual transformation into monophasic perovskite structure occurs as temperature increases up to 750 °C, however the desired monophasic $KTaO_3$ perovskite phase is not achieved. In the case of KTO*acac* (solution with potassium acetylacetonate), a broad peak is detected at temperatures <650 °C, characteristic of amorphous structures, while at higher temperatures diffraction lines from pyrochlore and perovskite phases are visible and a monophasic perovskite $KTaO_3$ is formed at >700 °C. Infrared analysis indicated that the differences are due to a strong deformation of the carbonate-based structures upon heating.

A series of thin films of alkali tantalates were spin-coated onto Si-based substrates using diol-based routes. Interestingly, monophasic perovskite $KTaO_3$ films deposited using KTO*acac* solution were obtained at temperature as low as 650 °C; films were annealed in rapid thermal furnace in oxygen atmosphere for 5 min with heating rate 30 °C/sec. Other compositions of the tantalum based system as $LiTaO_3$ (LTO) and $NaTaO_3$ (NTO), were successfully derived as well, onto Si substrates at 650 °C as well. The ferroelectric character of LTO at room temperature was proved. Some of dielectric properties of KTO could not be measured in parallel capacitor configuration due to either substrate-film or film-electrode interfaces. Thus, further studies have to be conducted to overcome this issue.

Application-oriented studies have also been conducted; two case studies: i) photocatalytic activity of alkali tantalates and niobates for decomposition of pollutant, and ii) bioactivity of alkali tantalate ferroelectric films as functional coatings for bone regeneration.

Much attention has been recently paid to develop new type of photocatalytic materials, and tantalum and niobium oxide based compositions have demonstrated to be active photocatalysts for water splitting due to high potential of the conduction bands. Thus, various powders of alkali tantalates and niobates families were tested as catalysts for methylene blue degradation. Results showed promising activities for some of the tested compounds, and $KNbO_3$ is the most active among them, reaching over 50 % degradation of the dye after 7 h under UVA exposure. However further modifications of powders can improve the performance.

In the context of bone regeneration, it is important to have platforms that with appropriate stimuli can support the attachment and direct the growth, proliferation and differentiation of the cells. In lieu of this here we exploited an alternative strategy for bone implants or repairs, based on charged mediating signals for bone regeneration. This strategy includes coating metallic 316L-type stainless steel (316L-SST) substrates with charged, functionalized via electrical charging or UV-light irradiation, ferroelectric $LiTaO_3$ layers. It was demonstrated that the formation of surface calcium phosphates and protein adsorption is considerably enhanced for 316L-SST functionalized ferroelectric coatings. Our approach can be viewed as a set of guidelines for the development of platforms electrically functionalized that can stimulate tissue regeneration promoting direct integration of the implant in the host tissue by bone ingrowth and, hence contributing ultimately to reduce implant failure.

Table of Contents

List of Figures

List of Tables

List of Symbols

$\langle D \rangle$	average crystallite diameter
ΔH_{ds} (ΔH_1, ΔH_2, ΔH_3)	enthalpy of drop solution
ΔH_f (ΔH_4)	enthalpy of formation
ΔH_f^{el} (ΔH_f^0)	enthalpy of formation from elements
ΔH_f^{ox}	enthalpy of formation from oxides
A	absorption
$\mathring{A}$	angstrom, unit of length
a, b, c	lattice parameters
A_1, E	transverse and longitudinal optical modes
C	capacitance
C_0, C_S	methylene blue concentration
C_C	spring constant of AFM cantilever
d_{33}, d_{31}	nonlinear optical coefficients
D_P	mean particle size
E	electric field
E_g	energy band gap
f_0	free resonance frequency of AFM cantilever
hv	photon energy; *h* stands for Planck constant and *v* for frequency
I	current
k	reaction rate constant
K	adsorption coefficient
k_{app}	apparent photocatalysis rate constant
l	optical path length
M	mode of the crystallite size distribution
n	refractive index
n (n_1, n_2)	Avrami exponent
r, k	photocatalytic reaction constants
r_{33}^T, r_{31}^T	electro-optic coefficients
R_{RMS}	roughness (root mean square)
R_{wp}, R_{exp}, χ^2	agreement factors
S	Seebeck coefficient
S	scattering coefficient
SA_{BET}	BET surface area
t	time
t_{2g}	symmetry of energy bands

$tan\delta$	dielectric loss
T_C	Curie temperature
V	voltage
x_p	volume fraction
α	thermal expansion coefficient
γ_{hyd}	hydrated surface energy (enthalpy)
γ^{SV}	surface tension (energy)
ε_r, ε'	dielectric permittivity
λ	wavelength
ξ	dye photodegradation efficiency

List of Abbreviations

2D	two-dimensional
316L-SST	type 316L stainless steel
3D	three-dimensional
A(Ta / Nb)O_3	alkali tantalate / niobate
$A_2B_2O_{7-\delta}$	pyrochlore structure
ABO_3	perovskite structure
AC	alternating current
AcOH	acetic acid, $C_2H_4O_2$
AFE	antiferroelectric
AFM	atomic force microscopy
AOPs	advanced oxidation processes
AP-I & AP-II	annealing procedure I and II
ATO	silver tantalate, $AgTaO_3$
ATR	attenuated total reflectance
BET	Brunauer–Emmett–Teller
BFO	bismuth ferrite, $BiFeO_3$
Bio-MEMS	biological/biomedical microelectromechanical systems
BSA	bovine serum albumin
BST	barium strontium titanate, (Ba, Sr)TiO_3
BTO	barium titanate, $BaTiO_3$
Cont'd	continued
CSD	Chemical Solution Deposition
DC	direct current
DFT	density functional theory
DRS	diffuse reflectance spectroscopy
DTA / TG	differential thermal analysis / thermogravimetry
e.g.	for example
EDS	energy-dispersive X-ray spectroscopy
EPMA	electron probe microanalysis
EQS	environmental quality standards
etc.	and so on (*et cetera* – Latin)
EtOH	ethanol, HOC_2H_5
FE	ferroelectric
FTIR	Fourier transform infrared spectroscopy
FWHM	full width at half maximum

GPS	Global Positioning System
GTB	Gatehouse tungsten bronze
H_1, H_2	tungsten-bronze-type compounds
HA	hydroxyapatite, $Ca_{10}(PO_4)_6(OH)_2$
Hacac	acetylacetone, $C_5H_8O_2$
HTB	hexagonal tungsten bronze
i.e.	that is (*id est* – Latin)
ICP	inductively coupled plasma
IR	infrared
JCPDS-PDF	Joint Committee on Powder Diffraction Standards-Powder Diffraction File (The International Centre for Diffraction Data – ICDD)
JMAK	Johnson-Mehl-Avrami-Kolmogorov method (equation)
Kacac	potassium acetylacetonate, $KO_2C_5H_7$
KLT	potassium lithium tantalate, (K, Li)TaO_3
KNN	potassium sodium niobate, (K, Na)NbO_3
KOAc	potassium acetate, $KO_2C_2H_3$
KOEt	potassium ethoxide, KOC_2H_5
KTN	potassium tantalum niobate, K(Ta, Nb)O_3
KTO	potassium tantalum oxide / potassium tantalate
KTOac	potassium tantalate solution using KOAc
KTOacac	potassium tantalate solution using Kacac
KTO*per*	potassium tantalate – perovskite $KTaO_3$
KTO*pyr*	potassium tantalate – pyrochlore $K_2Ta_2O_6$ / $KTa_{2.2}O_6$
KTO*ttb*	potassium tantalate – tetragonal tungsten bronze $K_6Ta_{10.8}O_{30}$
LED	light-emitting diode
LiOEt	lithium ethoxide, $LiOC_2H_5$
LNO	lithium niobate, $LiNbO_3$
LTO	lithium tantalate, $LiTaO_3$
MB	methylene blue, $C_{16}H_{18}N_3SCl$
MEA	monoethanolamine, C_2H_7NO
MIM	metal-insulator-metal
NaOAc	sodium acetate, $NaO_2C_2H_3$
NTO	sodium tantalate, $NaTaO_3$
PE	paraelectric
PFM	piezoresponse force microscopy
PMN	lead magnesium niobate, $Pb(Mg_{1/3}Nb_{2/3})O_3$
PMN-PT	lead magnesium niobate-lead titanate, $1\text{-}x Pb(Mg_{1/3}Nb_{2/3})O_3\text{-}x PbTiO_3$
PZT	lead zirconate titanate, Pb(Zr, Ti)O_3

RF	radio frequency
RT	room temperature
RTA / RTP	rapid thermal annealing / rapid thermal processing
SBF	simulated body fluid
SEM	scanning electron microscopy
SFM	scanning force microscopy
SPM	scanning probe microscopy
STO	strontium titanate, $SrTiO_3$
Ta(OEt)$_5$	tantalum(V) ethoxide, $Ta(OC_2H_5)_5$
TEC	thermal expansion coefficient
TTB	tetragonal tungsten bronze structure
TTB$_S$	orthorhombic distorted tetragonal tungsten bronze with superstructure
UHV	ultra high vacuum
UV	ultraviolet
WAXS	Wide-angle X-ray scattering
WPPM	Whole Powder Pattern Modelling
XAS	X-ray absorption fine structure
XPS	X-ray photoelectron spectroscopy
XRD	X-ray diffraction

Chapter 1. INTRODUCTION

1.1. Motivation

Tantalum, its binary oxide (Ta_2O_5), and ternary oxides (tantalates) have been repeatedly referred as being important players in a wide variety of applications [1-4]. Metallic tantalum possesses an excellent corrosion resistance (to majority of organic and inorganic acids), a refractory character (melting point ~3000 °C), and a high density (>15 g/cm^3), while and Ta_2O_5 has a dielectric strength (resistivity ~1015 Ω·m, dielectric constant ~25) and melting point ~1850 °C, among others [1, 4]. Tantalum is also used in medicine because of its lack of toxicity and very good compatibility with biological tissues; the favorable feature of tantalum is the formation of a thin, impenetrable oxide layer on the metal surface that is completely bioinert [5]. Main field of applications of Ta_2O_5 is in microelectronics, due to its thermodynamic stability with respect to copper, as well as in aerospace and military industry, due to high mechanical and chemical strength and temperature resistance [1, 5]. Among the tantalum compounds, tantalates possessing a perovskite-like (or disordered perovskite) structure are of potential interest, especially for the electronics industry, *e.g.* capacitor, electro-optical components. The best known compound is lithium tantalate, $LiTaO_3$ (LTO), with useful ferroelectric, pyroelectric and piezoelectric properties [6]. However, other tantalates, such as sodium tantalate, $NaTaO_3$ (NTO), and potassium tantalate, $KTaO_3$ (KTO), are frequently reported, being also used in solid solutions with other ferroelectrics, *e.g.* niobates, to obtain materials with modified electrical response [7-9].

There has been an extraordinary growth in telecommunication technologies for the consumer market, powered by fast and wireless communication systems. The need of high levels of circuitry integration and of devices operating at several different frequency bands leads to the production of electronically tunable matching networks and data storage accessories, simultaneously with size and costs reduction [10]. Therefore, functional materials, such as ferroelectric-related compositions, as well as hazardous-free compounds with respect to environmental issues, are of particular interest. Within these demands, alkali tantalates (and niobates) from a group of complex oxides are under intensive research investigations.

One of the most extensively studied systems, concerning functional oxide materials with perovskite-like structure and with useful electrical and electronic properties, either in bulk or thin films, are titanates, *e.g.* barium titanate, $BaTiO_3$, and strontium titanate, $SrTiO_3$. Their

solid solutions, (Ba, Sr)TiO_3, are very attractive for a wide spectrum of mainly electronic applications, such as memory components, pyroelectric detectors or tunable microwave devices. Tantalum based family of compounds, $A$$TaO_3$ (A = Li, Na, K), is considered as one of the alternatives for the titanates. Despite the similarities between the $A$$TaO_3$ and $A$$TiO_3$ systems, tantalates are more complex at the synthesis level, both for bulk ceramics and for thin films. In addition, there is a lack of information in the energetics of the tantalate perovskite-like structures that is also important from the industrial point of view, giving insight in the terms of their synthesis.

Besides that, tantalates are recognized as new promising semiconductors with a technological relevance in photocatalytic processes [4]. Tantalates have been considered as efficient photocatalysts for water dissociation under ultraviolet (UV) irradiation due to their wide band gaps. Their attractiveness lies on the position and high energy of conduction band, formed by Ta *5d* orbitals. However, the studies for other applications of photocatalysis, such as pollutant degradation, have not been sufficiently conducted. The UV-active tantalates might be applicable in organic oxidation both in water and in air. Therefore, a comparative study on the aqueous dye degradation with alkali tantalates and niobates assistance would be of interest.

The potential of tantalum in medical applications has been well highlighted, especially in regenerative medicine [5]. It is known that the foreign body reactions have plagued the attempts of clinical usage of metals for tissue and bone reconstructions, and tantalum, as bioinert and corrosion resistant metal, can have a relevant contribution in the field of orthopedics. On the other hand, tantalates with a piezoelectric nature can be considered as an effective alternative strategy to accelerate osseointegration of implanted parts, for example. It has been proven that a protein adhesion, a cell growth and proliferation are enhanced by electrically polarized materials surfaces [11, 12]. In lieu of this, piezoelectric tantalates, *e.g.* $LiTaO_3$, used as a coating of stainless steel, act as supports to stimulate biological responses, being a potential approach for successful osseointegration. Such a device may combine the mechanical benefits of metal with its surface-engineering by a ferroelectric. Because the biocompatibility of lithium tantalate and lithium niobate, $LiNbO_3$ (LNO), has been investigated only very recently by our group [13], and just a couple of works have been published on the response of cells on the surface of ferroelectric bulk crystals, while some contradictory results have been reported [11, 14, 15], it is clear that

there is the need for a much deeper and systematic approach. In addition most of these studies have been conducted on single crystals that are neither cost effective nor compatible with industrial manufacturing. Indeed, there is a need to develop an alternative strategy for bio-MEMS (biomedical microelectromechanical systems), functional implantable devices or tissue-engineered constructs, based on exploiting charge-mediating signals for tissue growth of thin transition oxide films.

1.2. Objectives of the thesis

The main aim of this PhD work is a study of series of thin films and nanostructures composed on alkali tantalates: $KTaO_3$, $LiTaO_3$ and $NaTaO_3$. Initially phase formation paths in potassium tantalate are examined, depending on processing routes using kinetic and thermodynamic approaches. For this purpose, samples (in form of powders) are prepared by various synthesis routes, *i.e.* conventional soli-state reaction, hydrothermal method and chemical solution deposition (sol-gel). The series of 2D nanostructures (thin films onto rigid substrates) composed of alkali tantalates are prepared via chemical solution deposition, with modified procedure (air-stable and low toxic). The deposited films by spin-coating are tested with respect to various processing parameters in order to control desired perovskite-like structures with minimum thermal budged. The as-produced samples are characterized by distinct advanced techniques in order to correlate different synthesis approaches with macroscopic properties, and in later stage engineer their features for specific applications. Additionally, alternative application-oriented case studies of alkali tantalates are performed: i) investigations of alkali tantalates and niobates as photocatalysts in aqueous dye degradation, and ii) bioactivity studies of LTO coated type 316L stainless steel (316L-SST) to improve the feasibility of bone-like apatite formation on the surface of LTO coatings. The effect of the functionalization of LTO coatings (electric charging and photofunctionalization) on protein adsorption is investigated since this is a crucial factor that may determine cell response.

Thus the following specific objectives are determined:

- Investigation of phase formation paths in the synthesis of potassium tantalate. It has been widely reported that intermediate defect pyrochlore and tetragonal tungsten bronze structures crystallize in KTO when selected particular preparation method and/or processing conditions. Kinetic and thermochemical approaches have been employed in the present work to understand decomposition reactions and further control the formation of the perovskite phase.
- Design of the precursors chemistry for processing of alkali tantalate sols for chemical solution deposition methods that allows the synthesis of tantalate compositions at relatively low synthesis temperature, that later permits to control the stoichiometry of the

compounds and at the same time to make them compatible with the silicon technology. Investigation of the effect of potassium precursor on the phase evolution is performed.

- Fabrication of 2D structures (thin films) based on dielectric and ferroelectric materials (alkali tantalates), towards processing from environmental-friendly protocols (diol route). Influence of heat-treatment regime, alkali excess, atmosphere, underlayer, is examined.
- Systematic and deep characterization of the fabricated thin films from the structural, microstructural and physical response point of view to establish the required relations between processing and properties.
- Characterization of powders and coatings for non-conventional (alternative) applications: i) demonstration of photocatalytic activity for toxic dye degradation of alkali tantalates and niobates powders with versatile crystal structures, and ii) application of ferroelectric LTO films as protective coatings of metallic implants for bone regeneration.

1.3. Organization of the thesis

The thesis is organized as follows:

Chapter 1 is an introduction to the thesis, presenting motivation part with specific objectives.

Chapter 2 provides a state of the art to the materials investigated in the thesis. The importance of functional materials, with the particular emphasis on complex oxides with perovskite-like structure, ABO_3, is presented. Knowledge on tantalum-based complex oxides and their significance in various applications is revised and systematically presented. The chapter includes a detailed review of structural, physical and chemical properties of alkali tantalates, *i.e.* $KTaO_3$, $LiTaO_3$ and $NaTaO_3$, and includes published works on solution processed 2D tantalum oxides based structures. Additionally, non-conventional applications of this group of materials is reviewed as well, *i.e.* photocatalytic activity for water splitting and pollutant degradation, and the very new concept of piezoelectricity applied for tissue engineering in particular for bone tissue engineering, where biocompatible piezoelectrics may be the basis of a new set of bio-MEMS.

Chapter 3 presents the experimental methods implemented in the thesis: processing procedures and characterization techniques.

Chapter 4 is fully devoted to present and discuss the obtained results. Within this chapter, five subsections are presented corresponding to the following topics: 4.1 – thermochemistry of alkali tantalate and niobate perovskites, 4.2 – phase formation process in potassium tantalate, 4.3 – distinct solution processing routes of alkali tantalates, with particular emphasis to potassium tantalate, and thin films deposition, 4.4 – photocatalytic degradation of alkali tantalates and niobates, and 4.5 – proof of concept of the exploitation of ferroelectric $LiTaO_3$ as a coating of biocompatible stainless steel supports to stimulate biological responses towards enhanced osseointegration.

And finally, chapter 5 summarizes the work, and draws main conclusions. Based on the present achievements, future work is proposed.

Chapter 2. STATE OF THE ART

2.1. Functional materials

Functional materials are materials that can perform certain functions when triggered by environmental changes, such as stress, electric and magnetic field, and temperature variations, or when stimulated by control signals. The difference between a device and a functional material arises from the fact that the functional material preserves its functional property even when its volume is split, while the device is normally a multicomponent instrument that fails when it is disintegrated [16].

Functional materials are generally characterised as those materials, which possess particular inherent properties and functions of their own, *e.g.* ferroelectricity, piezoelectricity, magnetism or energy storage functions, and they are found in all classes of materials: ceramics, metals, polymers and organic molecules. A good example is the offer of Hitachi Group of high functional materials in a wide range of fields, from social infrastructure, including electrical power and next-generation energies, industry, urban development, and telecommunications, to the electronic products that are an intimate part of our daily lives (Figure 2-1) [17].

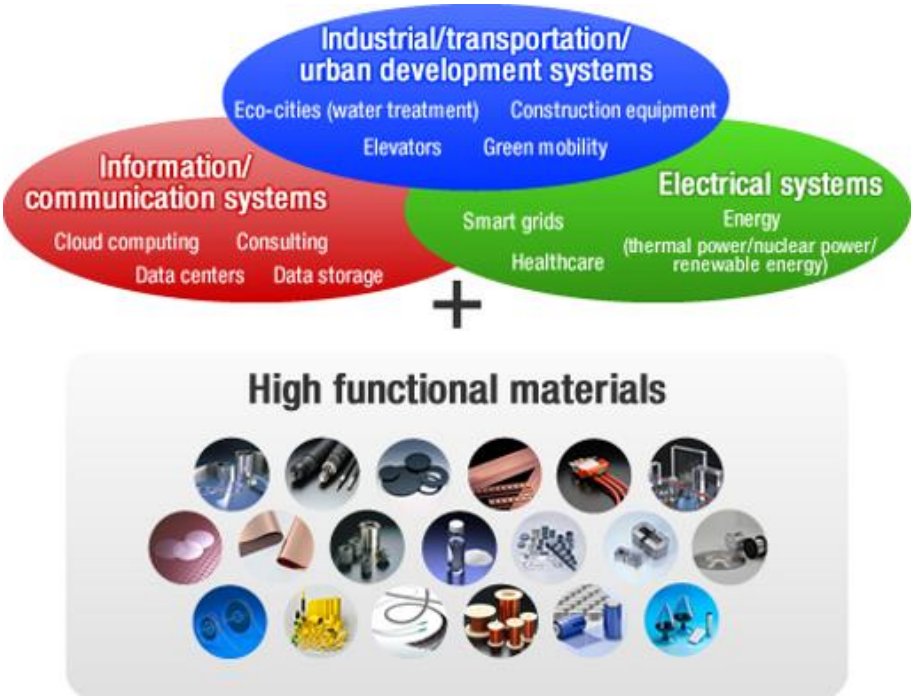

Figure 2-1. Spectrum of high functional materials offered by the Hitachi Group [17].

3. STATE OF THE ART

Functional ceramic materials consist of a huge group of inorganic compounds that by definition are non-metallic and non-water-soluble. This family in which the main characteristics, such as electricity, magnetism, heat, light or force are used to detect, transform, couple, transport, and store information, are characterized by their major properties [18]. It is extremely difficult to cover completely this topic, but for convenience these materials can be categorized due to the responsive nature and based on their potential applications, as following:

- *Electrical/magnetic* (electroceramics), to be used as insulators, semiconductors, conductors and magnets;
- *Optical*, to be used as components for various lenses, lasers, fibers;
- *Chemical*, to be used as catalysts, sensors;
- *Biological*, to be used as biomaterials, mostly for implants, and as nanomaterials in drug delivery systems.

Functional ceramics mainly include ferroelectrics, piezoelectrics, dielectrics, semiconductors, superconductors, magnetics, and currently very attractive group of multiferroics that show simultaneous ferroelectric with ferromagnetic (or antiferromagnetic) ordering and coupling between them that leads to many potential applications. The dominant compositions, among them, are oxides that offer a variety of chemical, physical, structural and microstructural features.

Considering functional oxides, ferroelectrics are essential components, being used in a wide spectrum of applications, mainly for microelectronics [19, 20]. The main characteristic of the ferroelectric material is that it exhibits an electric dipole moment without an external electric field, and their direction may be switched by the application of an alternating field – exhibiting the so-called phenomena of polarization reversal. This property is associated with the existence of domains (regions with common polarization direction), being useful in various electronic applications [19]. They are a relevant group of materials that in polar (non-centrosymmetric crystal symmetry, below Curie temperature, T_C) and paraelectric (PE; centrosymmetric crystal structure) states can be used in wide spectrum of applications, such as memory systems, sensors and actuators, and tunable high frequency devices, among others [21-25]. From this group, ceramic titanates, *i.e.* $Pb(Zr, Ti)O_3$ (PZT), $(Ba, Sr)TiO_3$

(BST), *etc.*, are currently about 50 % of total sales of electroceramics, being commercially used as capacitors, sensors, actuators, transducers, resonators and thermistors [26].

Ferroelectric material holds its main functionality in polar state (below T_C), but is also useful above T_C, in the PE state. In this non-polar phase the ferroelectric is normally characterized by a high dielectric permittivity which strongly depends on the temperature, applied external field and mechanical stress [21]. This parameter is important in defining capacitors with high capability to store electrical energy. Ferroelectrics in PE phase are useful in tunable microwave devices, *e.g.* phase shifters as components in electronically scanned phased-array antennas for communications and radar applications, because of their low dielectric losses and reasonable tunability (dependence of a dielectric permittivity on the applied bias electric field). In this respect, the incipient ferroelectrics (or quantum paraelectrics), such as $SrTiO_3$ and $KTaO_3$, are of great interest because they do not possess phase transition into polar phase at any temperature. Behaviour of the incipient ferroelectrics at low temperature is determined by the quantum oscillations of the crystal lattice [27].

The dominant compounds of inorganic ceramic materials are perovskite oxides, ones of the most studied class of functional materials for electronic, solar energy and other applications. They are identified based on the crystal structure, ABO_3, ideally being cubic one with some typical crystallographic criteria. Most compounds in the perovskite family have the BO_6 octahedra tilted in various ways, giving different types of coordination and deviations from ideal high-symmetry cubic structure [28]. Thus, the physical properties change due to the corresponding modification of crystal and electronic structures. The perovskite structure is capable of hosting above 90 % of the metallic elements from the periodic table, either on the *A* or *B* site, being highly tunable structure through substitution and mixed oxidation states [29]. It leads to a huge number of compounds with extraordinary properties, such as ferroelectricity ($BaTiO_3$, $KNbO_3$, PZT), piezoelectricity (PZT, $(K, Na)NbO_3$ - KNN), ferromagnetism ($SrRuO_3$), ionic-electronic conductivity ($(La, Sr)MnO_3$), high electron mobility ($SrTiO_3$), nonlinear optical ($LiNbO_3$, $LiTaO_3$), catalytic ($NaTaO_3$) properties, and so on [29, 30]. Being studied for a long time, the perovskite compounds are still not discovered completely, leading to astonishing explorations from time to time, especially at the interfaces between films and substrate, or between layers in heterostructures [28]. Figure 2-2 presents some of the discovered phenomena in the bulk and at the interfaces in heterostructures of perovskite oxides.

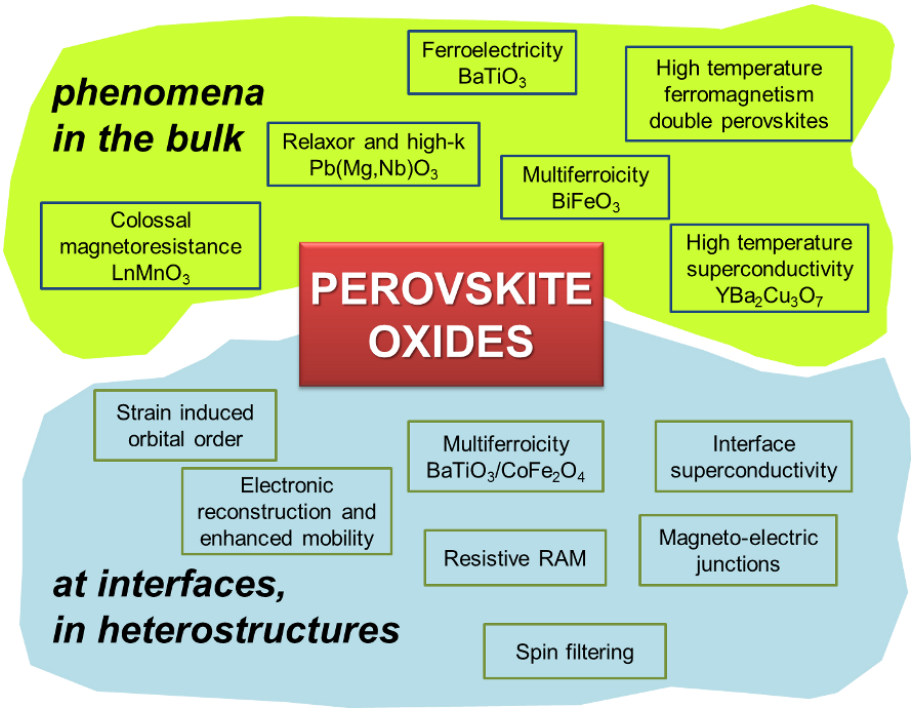

Figure 2-2. Functionalities of perovskite oxides, in the bulk and thin films forms. Some particular compositions and their special features are highlighted [28].

So far compositions from the solid solution between $PbZrO_3$ and $PbTiO_3$ (PZT) are the most successful perovskite structure materials on the market, being used in piezoelectric actuators, sensors and transducers [31]. However, the use of PZT that contains more than 60 wt% of lead will be soon severely restricted, due to lead toxicity [32]. Therefore, there is a need of sustainable materials and manufacturing routes to use lead-free alternatives compatible with the current most restrict environment directives.

2.2. Importance of tantalum and its oxides

Nowadays, among a number of perovskite systems, there is a demand to explore novel compounds, or engineer already existing compositions, in order to prevent the use of lead-based systems [33], and to produce materials at low cost using abundant elements [34]. Due to that reason, tantalum (and niobium) oxides have been considered as a group of the most promising compounds on the list of functional materials for future technologies [35].

Tantalum (Ta) is a transition metal with unique features. It is one of the most refractory metals with high melting temperature, >2000 °C, and low vapour pressure, thus the element is extremely stable. Moreover, Ta has an excellent resistance to corrosion (similar to some glasses like silicates) due to a natural protective oxide layer [1, 4, 5]. This oxide layer is normally tantalum pentaoxide, Ta_2O_5, one of the most important compound in optical, electronic and medical applications [4]. Over the last decades, Ta_2O_5 is well-recognized as a dielectric material used as a capacitor due to its high dielectric constant. Lately, a 3D nonvolatile memory structure composed of Ta_2O_5 with excellent switching behaviour was tested and proposed as an alternative for high density devices based on solid-state memory technology [36]. It can be found in microelectronic components of mobile phones, smartphones, laptop computers and portable music players, *etc.* [37]. Due to its extremely low failure rate, Ta_2O_5 is used in medical equipment, *e.g.* hearing aids, pace maker. Tantalum and its binary oxide are also widely implemented in orthopedic implants, because of relatively good biocompatibility in comparison to other metals [5]. It has been used in medical applications as suture wires, foils, slips and plates for reconstructive surgery. Apart from the mentioned applications, it is used in alloys (for aircraft construction) and industrial cutting tools (tantalum carbide) as well [1-3].

Recently, Ta_2O_5 has become an interesting material for photocatalytic reactions, as a semiconductor material with a band gap ~4 eV [4]. Although its large band gap makes Ta_2O_5 only responsive to UV-light, the electronic band structure has particular features interesting for H_2 evolution reaction during water splitting, *i.e.* the valence band maximum and the conduction band minimum overlap the redox potentials of H^+/H_2 and O_2/H_2O.

Some examples of industrial uses for tantalum are shown in Figure 2-3 and Table 2-1 [1].

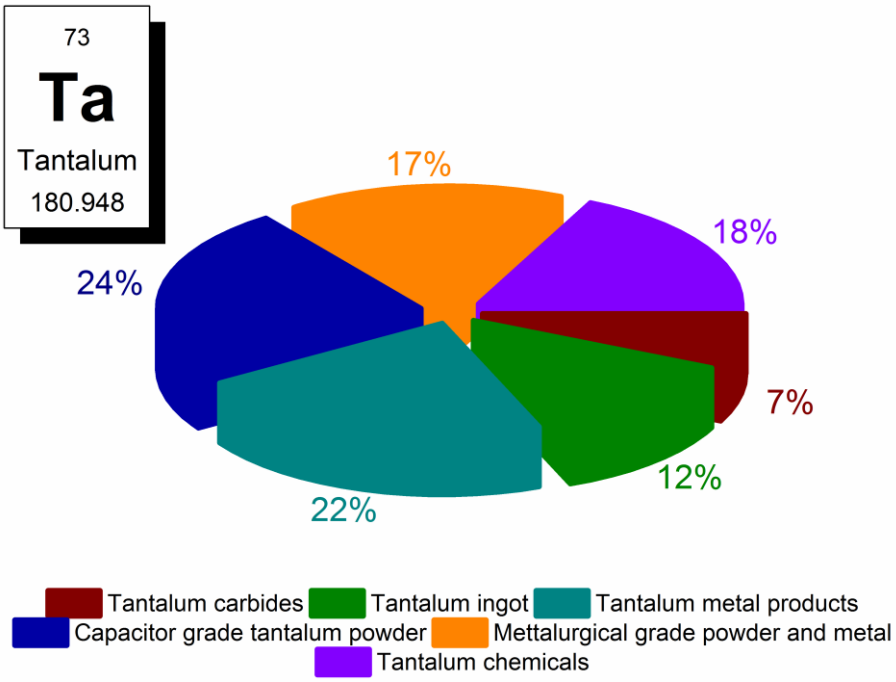

Figure 2-3. End-uses of tantalum (2010) [1].

In 2010, the largest Ta production (24 %) was dedicated for capacitor-grade powders (some sources suggest even 48 %), while 17 % in the manufacture of metallurgical grade powders. Almost 18 % of Ta production was used to manufacture tantalum chemicals, ~22 % for metal products, and considerably less for tantalum carbides (7 %) and ingot (12 %). Tantalum and niobium are transition metals with very similar physical and chemical properties, and thus very commonly grouped together. In case of Nb however, almost 90 % of global niobium production was used to manufacture ferro-niobium, used in high strength low alloy steels.

Tantalum production is comparatively widespread; African countries (Rwanda and the Democratic Republic of Congo) are responsible for over 60 % of the global production, and additional production comes from Brazil with minor amounts also produced in Malaysia and Canada [1, 3]. However, Ta was listed to emerge as “critical” global metals and is expected to become highly scarce from 2015 [38]. Tantalum is one of the largest groups of metals which still exhibit end-of-life recycling rates of <1 %, therefore more efficient recycling methods for this metal still have to be explored [2].

Table 2-1. Summary of the main industrial uses of Ta [39].

Industry	Usage	Tantalum product
Automotive	Anti-lock brake systems, airbag activation systems and engine management modules	Ta powder
Ceramics and surface coatings	Ceramic capacitors, glass coatings, camera lenses and X-ray film	Ta oxide and yttrium tantalate
Chemicals	Chemical processing equipment	Ta metal
Construction	Cathode protection systems for large steel structures, e.g. oil platforms and corrosion resistant fasteners (screws), and nuts and bolts	Ta metal (sheets, rods, plates and wire)
Engineering	Cutting tools	Ta carbide
Electronics	Capacitors, surface acoustic wave filters for sensor and touchscreen technologies, hard disc drives, LED lights	$LiTaO_3$, Ta powder, Ta ingots and Ta nitride
Medicine	Pace makers, hearing aids and prosthetic devices (hip joints)	Ta metal
Metallurgy	Furnace parts, superalloys for jet engines and rocket engine nozzles	Ta metal and Ta ingots
Military	Missile parts, ignition systems, night vision goggles and GPS	Ta ingots and Ta oxide

2.3. Alkali tantalates

Within the demands to search for lead-free alternatives, tantalum (and niobium) oxides based systems, such as alkali tantalates and niobates, have been considered as a group of the most promising compounds on the list of functional materials for future technologies [32, 35].

Alkali tantalate oxides, ATaO$_3$ (A – metal ion: Li, Na or K), are tantalum oxide based compounds that possess the perovskite type structure based on the TaO_3^- anions octahedral arrangement. Potassium tantalate, KTaO$_3$ (KTO), lithium tantalate, LiTaO$_3$ (LTO), and sodium tantalate, NaTaO$_3$ (NTO) are distinct members of this group. In terms of ferroic properties, the presented compounds are either incipient ferroelectrics, such as KTO and NTO, or ferroelectric, such as LTO.

KTO, LTO and NTO present diverse properties. Table 2-2 presents some of their structural, physical and chemical characteristics. KTaO$_3$ is an incipient ferroelectric in the paraelectric state in the whole temperature range, and in addition exhibits quite low dielectric losses (~10^{-4} – 10^{-5}) [40]. LiTaO$_3$ is a high temperature ferroelectric, up to >600 °C, with good electro-optical properties. Moreover, (K, Li)TaO$_3$ solid solution can be formed (with limited solubility of Li in KTO), showing attractive macroscopic dielectric response at low temperatures [41]; described in more details in the next section. NaTaO$_3$ is also an incipient ferroelectric [42]. Moreover, it is a compound with tunable crystal structure (monoclinic, orthorhombic or cubic) [43] that is useful for photocatalytic applications. In the later sections the crystal and electronic structures, thermochemistry and processing of the three alkali tantalate compounds are presented in details.

Table 2-2. Selected structural, physical and chemical characteristics of $ATaO_3$, where A = K, Li or Na [6, 44-47]. These alkali tantalates present versatile features in wide temperature range.

	$KTaO_3$	**$LiTaO_3$**		**$NaTaO_3$**			
Molecular weight, g/mol	268.04	235.89		251.94			
Crystallographic data							
State:	PE	FE	PE	PE	PE	PE	PE
Crystal system:	cubic	trigonal	trigonal	orthorhombic	orthorhombic	tetragonal	cubic
Space group:	Pm3m	R3c	$R\bar{3}c$	Pcmn	Bmmb	P4/mbm	
Lattice parameters:	a = 3.9885 Å	a_{hex} = 5.1543 Å, c_{hex} = 13.7835 Å, or a_{rh} = 5.474 Å, α_{rh} = 56 10.5' (at RT)		a = 5.4842 Å, b = 7.7952 Å, c = 5.5213 Å (at RT)	a = 7.8453 Å, b = 7.8541 Å, c = 7.8633 Å (at 803 K)	a = 5.5552 Å, c = 3.9338 Å (at 893 K)	
Transition temp., T_C (°C)	-	660		480	550	630	
Band gap energy, E_g (eV)	3.7	4.0		4.0			
Thermal expansion (linear TEC) α, ($\times 10^{-6}$ C^{-1})	6.8	$\alpha_a \sim 16.1$ $\alpha_c \sim 4.1$		-			
Refractive index n (in the visible region)	> 2.2	> 2.1		-			

2.3.1. Potassium tantalate

KTO system was referred for the first time in 1949 by Matthias that reported a ferroelectric type activity [48]. Later on, Wemple [49] proved that the ferroelectric transition actually does not occur down to ~2 K, but any traces of impurities in the lattice may induce a ferroelectric behaviour, while in $SrTiO_3$ this was already known in 1950s [50]. After that $KTaO_3$ has started to be classified as an incipient ferroelectric, in which the ferroelectric state is never reached as temperature goes down to 0 K. Additionally, KTO has a high permittivity (~240 at room temperature (RT; 4.3 GHz), and 4700 at 5.4 K; 965 GHz [40]) and low dielectric loss (0.00009 at 300 K and 0.00004 at 5.4 K; 3 GHz [40]). Figure 2-4 presents the timeline of the most relevant publications regarding $KTaO_3$ system, with the separation on single crystals, ceramics and thin films. The research on single crystals has been more active than in ceramics and thin films.

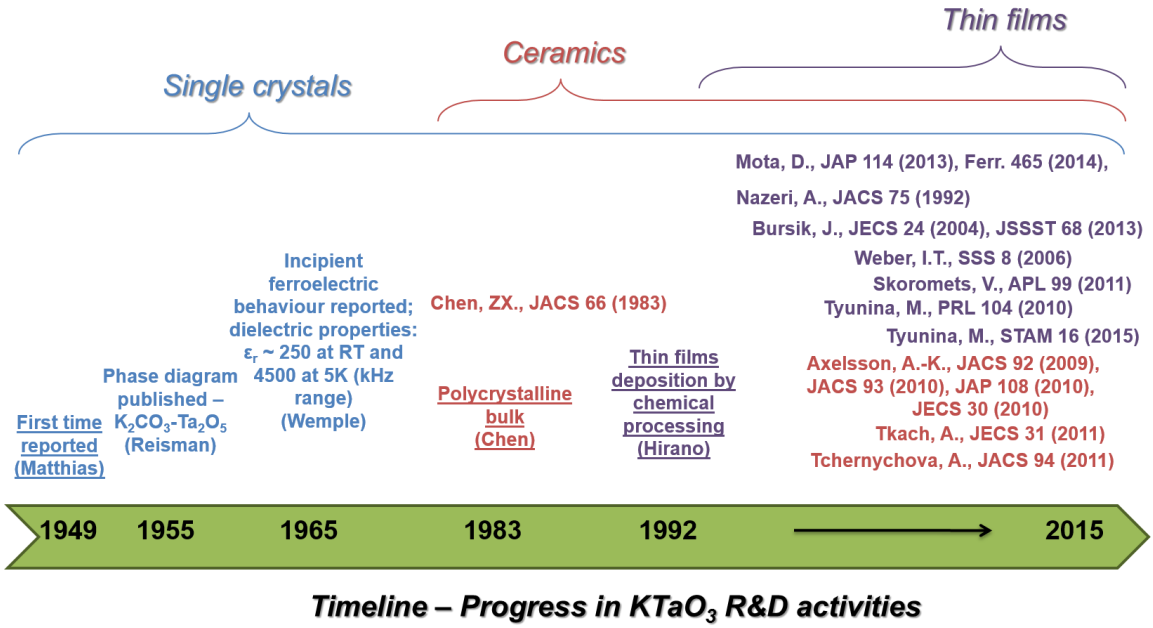

Figure 2-4. Timeline presenting the progress in $KTaO_3$ publications, with the most relevant reports on single crystals, ceramics and thin films. It shows the publications with significant contributions to the topic of potassium tantalate.

2.3.1.1. *Crystal and electronic structures of $KTaO_3$*

The crystal structure of potassium tantalate is a simple cubic perovskite structure with space group $Pm\bar{3}m$ presented in Figure 2-5 *(a)*. It can be viewed as TaO_6 octahedra with shared vertices forming a 3D-framework and K located in the cuboctahedral voids as shown in Figure 2-5 *(b)* [51, 52]. In other words, O atoms are positioned on the cube faces, Ta atoms at the center of the cube, and K atoms at the cube corners. The lattice parameter of KTO was calculated to be a = 3.9883 Å [53].

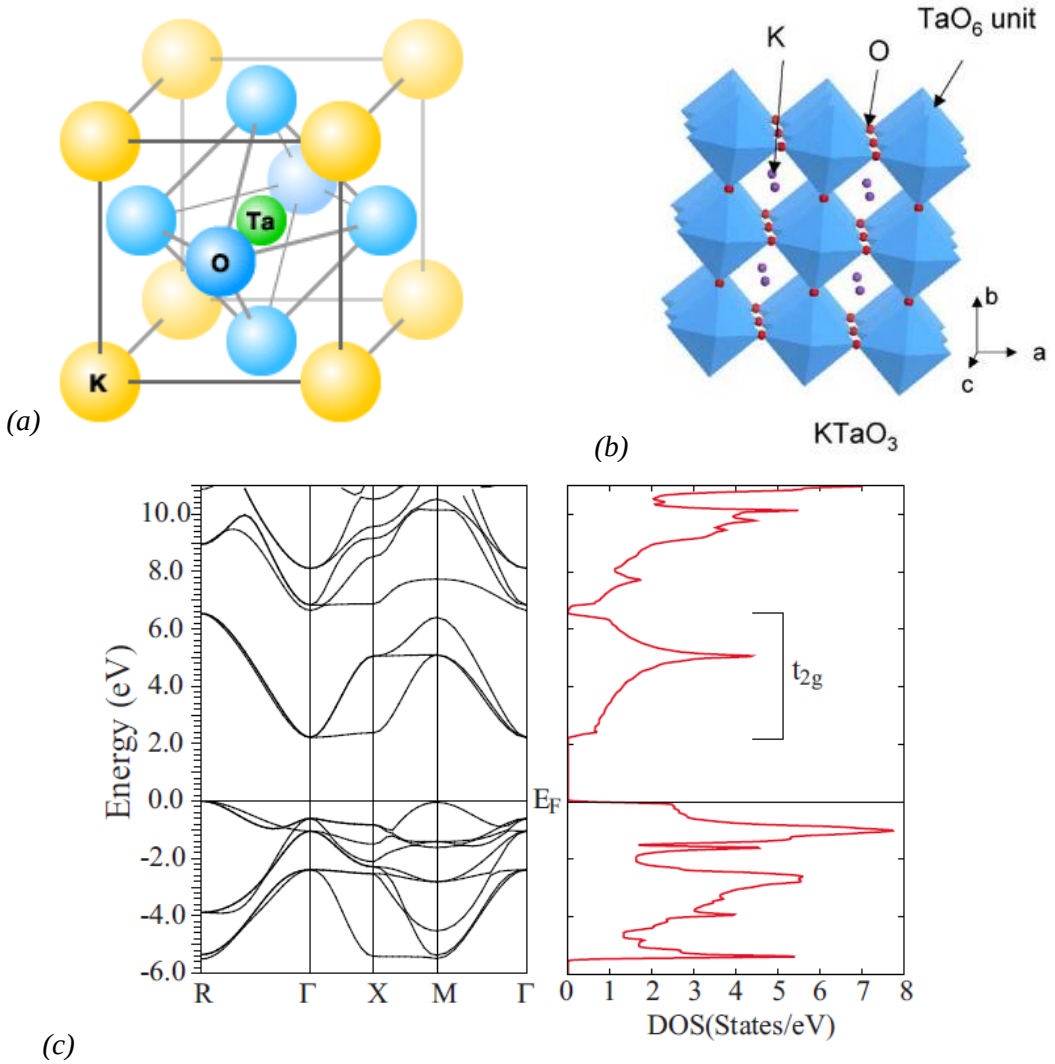

Figure 2-5. The crystal structure of $KTaO_3$ – (a) and (b) [52], and the calculated band structure and the density of states of $KTaO_3$ – (c) [54].

The electronic structure of pure KTO was calculated using the density functional theory (DFT), and Figure 2-5 *(c)* shows the band structure and the density of states of KTO [54]. The valence bands are of O *2p* character, while the low lying conduction bands are of Ta *5d*, t_{2g} character (three t_{2g} bands right above the Fermi level); higher lying conduction bands are of Ta e_g, K *d*, and Ta *sp* character. KTO has an indirect band gap, the valence band maxima lies at *R* point, while the conduction band minima is at the center Γ of the Brillouin zone, with experimentally determined value of ~3.6 eV [55, 56].

Incipient ferroelectric KTO remains in centrosymmetric cubic structure down to very low temperatures. KTO possesses also highly polarizable lattice that is very sensitive to small amounts of impurities, defects and other external stimuli, leading to relaxor, glass-like and ferroelectric behaviours [41]. Because of its low dielectric loss at high frequency it is a good candidate for microwave electronic applications [40]. Besides, KTO exhibit a relatively large Seebeck coefficient, *S*(300 K) = -160 μV/K, when electrons from dopants, *e.g.* Ba, are introduced to the system due to the multiplicity of the bands, making it an important compound for thermoelectric devices [54].

2.3.1.2. Ta_2O_5-K_2CO_3 phase diagram

The whole compositional phase diagram of Ta_2O_5 - K_2O (K_2CO_3) was firstly published by Reisman *et al.* [57]. Later study of Roth *et al.* [58] complemented part of the diagram between Ta_2O_5 and $KTaO_3$; both diagrams are shown in Figure 2-6. Four compounds with different metal ratios were determined: KTa_5O_{13} (I) and $K_2Ta_4O_{11}$ (II) (K-deficient), $KTaO_3$ (III) (stoichiometric), and K_3TaO_4 (IV) (K-excess). The perovskite $KTaO_3$ phase melts at 1370 °C, and the temperature of the eutectic point between $KTaO_3$ and K_3TaO_4 is 1090 °C. Roth *et al.* [58] found several more high temperature phases: $K_4Ta_{10}O_{27}$, two hexagonal phases (H_1 and H_2), as well as four high-temperature tungsten-bronze-type compounds (GTB – Gatehouse tungsten bronze, TTB_S – orthorhombic distorted tetragonal tungsten bronze with superstructure, HTB – hexagonal tungsten bronze, and TTB – tetragonal tungsten bronze), which compositions differ.

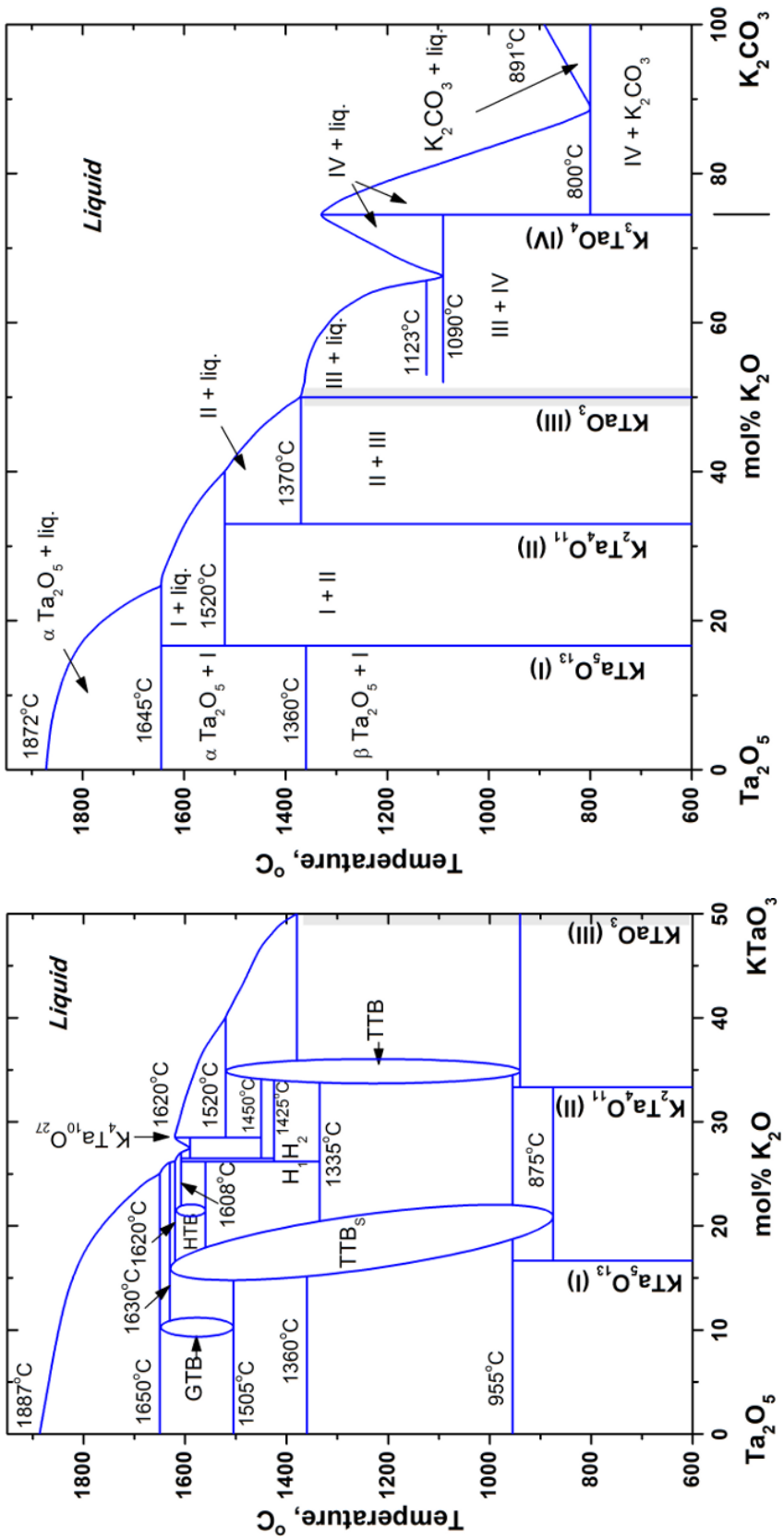

Figure 2-6. Phase diagrams of Ta_2O_5-$KTaO_3$ (after Roth et al. [58]) and Ta_2O_5-K_2O (K_2CO_3) (after Reisman et al. [57]). GTB – Gatehouse tungsten bronze at 88.5 % of Ta_2O_5; TTB_S – orthorhombic distorted tetragonal tungsten bronze with superstructure at 85-80 % of Ta_2O_5; HTB – hexagonal tungsten bronze at 78.25 % of Ta_2O_5; H_1, H_2 – hexagonal phases at 73.85 % and 73.5 % of Ta_2O_5, respectively; TTB – tetragonal tungsten bronze at ~66 % of Ta_2O_5 ($K_6Ta_{10.8}O_{30}$).

K_2O (K_2CO_3)–Ta_2O_5 system seems to be also interesting from the application point of view because many compounds (oxides) composed of K and Ta can be formed. A cubic perovskite $KTaO_3$ with stoichiometric K:Ta = 1 is the dominant phase between ~40 and ~60 mol% of K_2O. Besides $KTaO_3$, defect pyrochlore $K_2Ta_2O_6$ (KTO*pyr*) was found to be formed at relatively low temperatures [52, 59-61]. KTO*pyr* has the same chemical composition as the perovskite phase, but its crystal structure is arranged differently, since TaO_6 octahedra are greatly distorted (Figure 2-7 *(a)*). The ideal pyrochlore formula is $K_2Ta_2O_7$ and the structure consists of a network of TaO_6 octahedra with all their corners around hexagonal cavities, and a K–O tetrahedron is positioned inside the cavities [62]. However, the lack of some oxygen atoms in this pyrochlore structure gives rise to stable defect pyrochlores as $K_2Ta_2O_6$, and the refined lattice parameter of this cubic structure is 10.6058 Å [52]. In addition, the structure refinement of strongly K-deficient and hydrated pyrochlore $KTa_2O_5(OH) \cdot xH_2O$ synthesized via hydrothermal method [63-65] yielded a cubic unit cell and a = 10.6193 Å [63]. Finally, TTB $K_6Ta_{10.8}O_{30}$ (KTO*ttb*) is another interesting compound (with K:Ta ratio of 0.56) that has rather complex layered structure, which consists of TaO_6 octahedra joined by sharing corners, and the layers are perpendicular to the c axis (Figure 2-7 *(b)*) [66, 67]. The lattice parameters are a = 12.56 Å and c = 3.978 Å, while chemical composition differs from perovskite and pyrochlore structures. KTO*ttb* was recently found to be a good candidate for photocatalytic applications [68].

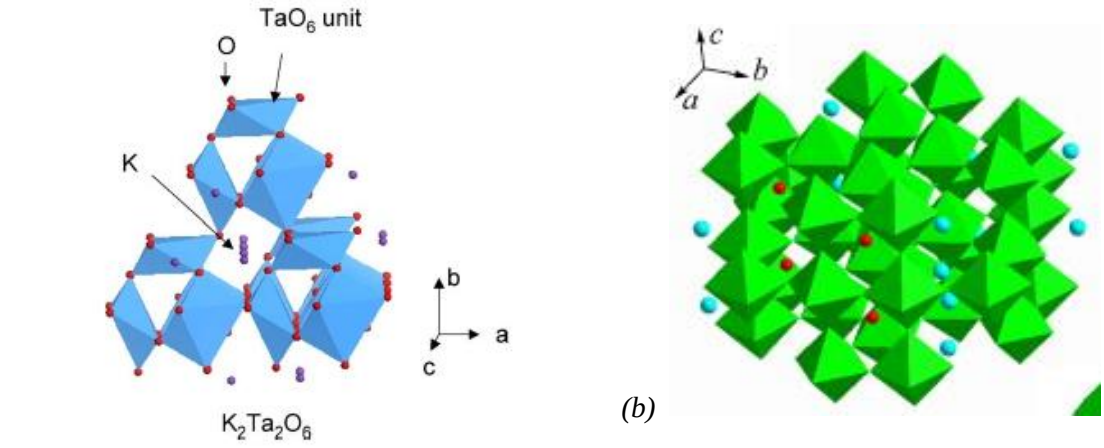

Figure 2-7.Crystal structures of (a) $K_2Ta_2O_3$ [52], and (b) $K_6Ta_{10.8}O_{30}$ [67]. TaO_6 octahedra are linked differently in these two compounds.

2.3.1.3. Stimuli effects on dielectric properties

KTO is an analogue of $SrTiO_3$, an ABO_3 prototype with cubic structure at RT. Their structure, however, becomes disordered by dilute impurities or defects, leading to more complex perovskite symmetries. Both compounds exhibit classic ferroelectric soft mode behaviour, a long wavelength transverse optic phonon mode whose frequency decreases (softens) with decreasing temperature. Although for both of them this frequency tends to zero as temperature goes down to 0 K, the soft mode condensation is prevented by quantum fluctuations, which stabilize the high temperature phase. Therefore, $KTaO_3$ remains cubic symmetry at low temperatures, and $SrTiO_3$ remains tetragonal structure formed below an antiferrodistortive (cubic to tetragonal) transition at ~105 K [41]. The influence of quantum fluctuations on the dielectric response of these materials is shown in Figure 2-8. No decrease but only levelling-off of the dielectric permittivity as temperature approached 0 K is seen both for $SrTiO_3$ and $KTaO_3$.

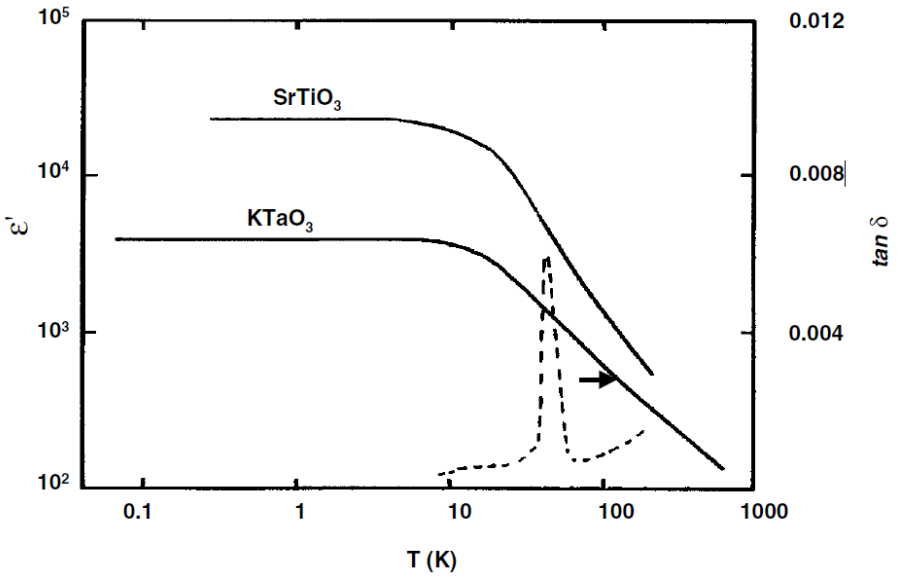

Figure 2-8.Temperature dependence of dielectric permittivity, ε', of $SrTiO_3$ and $KTaO_3$, showing the quantum paraelectric behaviour [41].

Figure 2-9 shows the temperature dependence of the dielectric loss of undoped $KTaO_3$ and $KTaO_3$ with small contents of impurities (Nb, Na and Fe) [69]. An irregularity in the dielectric loss is observed, at ~40 K. The amplitude of the peak is strongly sample dependent, being the smallest for "ultra-pure" samples. This peak originates from dipolar centres caused

by impurities or lattice defects (oxygen vacancies), causing some kind of off-stoichiometry in the crystal [41]. The same anomaly in the dielectric loss has been reported in the $KTaO_3$ samples intentionally doped with a number of cations [70, 71]. Additionally, the peak in the dielectric loss is not accompanied with any visible anomaly in the real part of the dielectric constant. Therefore, it is a kind of signature of sample purity level, and remains unsettled and unavoidable.

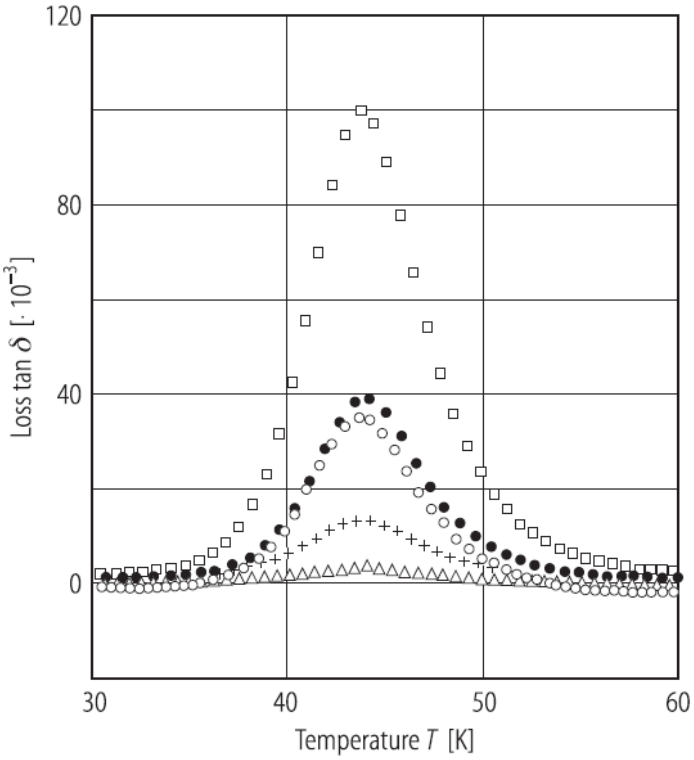

Figure 2-9. Temperature dependence of dielectric loss (tanδ), of undoped $KTaO_3$ (full circles ●), and with impurities (Nb – open triangles and crosses, Na – open circles and Fe – open squares; ≤1 %), measured at 1 kHz [69]. An anomaly ~40 K is observed due to the impurities.

Due to the highly polarizable host lattice, various factors can affect the dielectric properties of KTO, *e.g.* strain and substitutions can induce a ferroelectric phase transition in this compound [41, 72-75]. Impurities in $KTaO_3$, such as lithium ion occupying K site with formation of (K, Li)TaO_3 (KLT) system, and niobium ion substituting Ta in K(Ta, Nb)O_3 (KTN) compound, generate a ferroelectric state when a critical concentration (usually few percent) of the foreign ion is reached. In the KLT system, the transition to the long-range order is still unclear, but ferroelectric behaviour has been reported for compositions with >3 % of Li [41, 76-80]. The Li^+ ions, with a ionic radii of 1.25 Å – extrapolated for

coordination number =12 [81], easily occupy positions of K^+ (ionic radii of 1.64 Å [82]), and shift to an off-centre position in the [100] direction that originates a relatively large dipole moment. It is suggested that Li dipole (Li^+ ion has a relatively large dipole moment, which can interact with neighbouring) may polarize the unit cells, resulting in polar nanoregions, and then leads to the appearance of a dipolar glass- and relaxor-like behaviour at different Li concentrations. Figure 2-10 presents the influence of the Li doping in KTO on the dielectric constant (at 1 kHz) [83]. As Li content increases (raising the induced dipoles concentration), the peak in the dielectric constant shifts to higher temperatures. However, a structural phase transition does not occur in the presented KLT concentrations due to the relaxation caused by Li^+ ions hopping between crystallographically equivalent sites. In addition, strong frequency dispersion occurs in KLT [41].

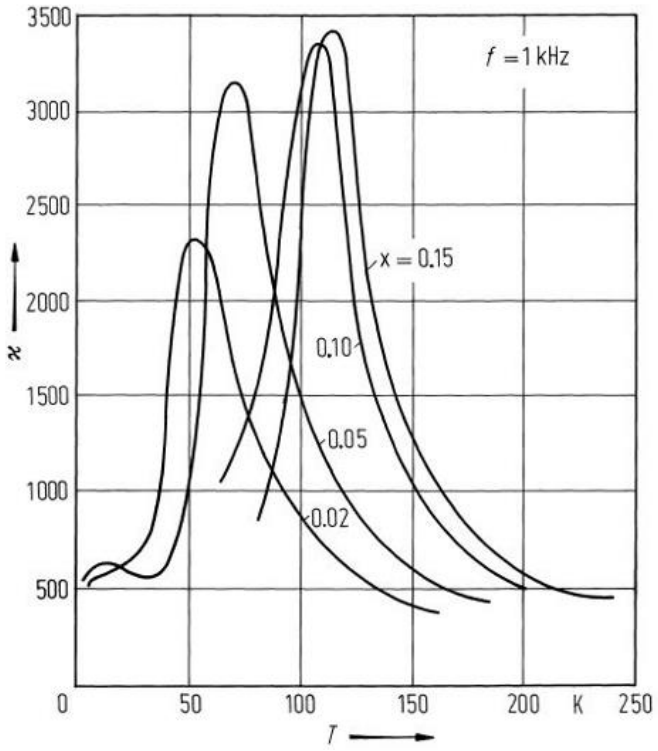

Figure 2-10. Temperature dependence of dielectric constant versus lithium content in KLT solid solution [83]. As Li content increases, transition shifts to higher temperatures.

In the case of Nb^{5+} doping on Ta site of $KTaO_3$ lattice (both ions have the same ionic radii – 0.64 Å [82]) and the situation is different than in KLT. The phase diagram of the $KTa_{1-x}Nb_xO_3$ system (KTN), in the entire composition range, was established long time ago [84], and a sequence of three structural phase transitions: cubic → tetragonal →

orthorhombic → rhombohedral (on cooling), was identified [85]. Thus, as Nb content increases, the phase transition shifts to higher temperatures, being well visible on the plot that represents the temperature dependence of the dielectric constant for various KTN compositions; see Figure 2-11 [86]. Generally, a magnitude of the peak increases with increasing $KTaO_3$ concentration [85, 86]. The T_C varies according to the formula $T_C = 676 \cdot x + 32$ (for $x > 0.047$). Below $x = 0.047$, KTN exhibits a dipolar glass behaviour, while above ~4.7 % of Nb it demonstrates a common ferroelectric phase transition. Additionally, it was reported that the DC voltage is able to tune the dielectric properties in KTN, making it promising for microwave tunable applications [74, 87, 88].

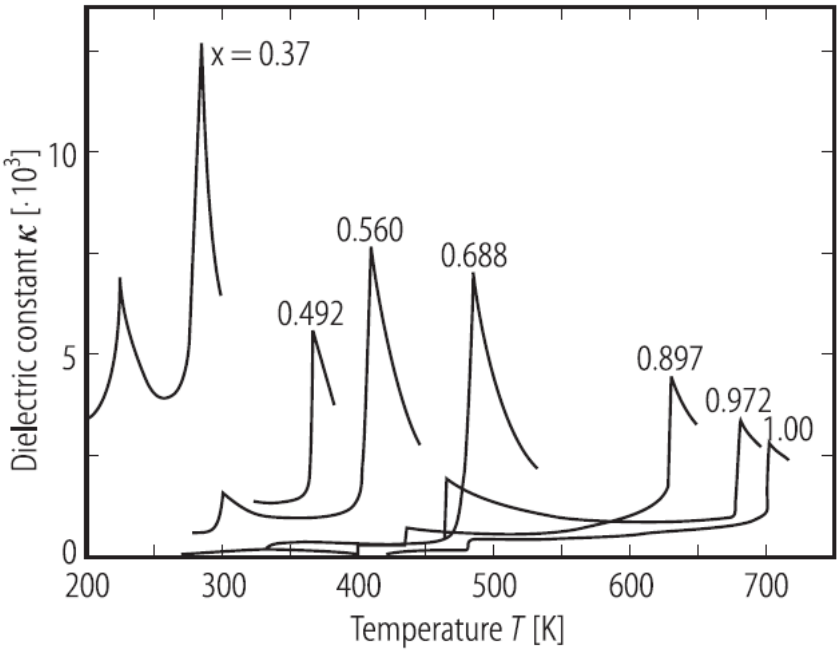

Figure 2-11. Dielectric constant versus temperature for some of the KTN compositions [86]. Sharp peaks present phase transitions dependent on composition.

Divalent and trivalent ions, such as Mn, Fe, Ni, and Co, can substitute Ta in KTO, and to preserve charge neutrality oxygen vacancies are formed [41]. The size considerations also lead to substitution on Ta site, because all the ions have an ionic radii ≤0.8 Å while K^+ has it >1.3 Å. This defect structure, caused by doping with aliovalent ions, influences also the dielectric response of KTO, creating an anomaly for lower dopant concentrations, mainly reflected in the temperature dependence of the dielectric loss [41, 70, 71, 89]. All the ions

make an impact on the dielectric relaxation (the relaxation response of a dielectric to an external AC electric field), but its nature is still not clear.

Microwave dielectric properties of single-crystal incipient quantum ferroelectrics were also measured at cryogenic temperatures [40]. The microwave dielectric loss of pure KTO is lower than in STO at temperatures below ~80 K (Figure 2-12), making KTO a competitive candidate for tunable microwave devices. It was claimed that both dominant multiphonon scattering losses and losses were estimated to be due to residual ferroelectric polarization. No ferroelectric phase transition was observed, and $KTaO_3$ remains paraelectric down to 5.4 K.

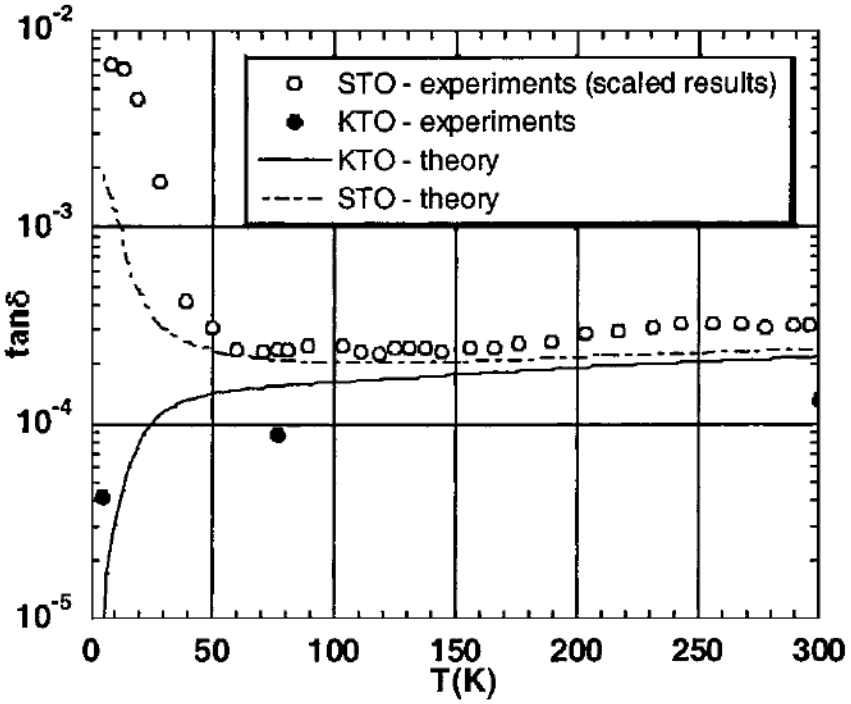

Figure 2-12. Temperature dependence of predicted and theoretical dielectric loss at 3 GHz and zero bias for $KTaO_3$ and $SrTiO_3$ [40].

The effects of temperature and pressure on the lattice parameter, *a*, and dielectric constant of KTO were studied [90]. Above room temperature the variation is linear and the linear expansion coefficient of $KTaO_3$ was calculated to be $\alpha = 6.8 \times 10^6\ C^{-1}$ (see value in Table 2-2). The pressure dependence of *a* parameter was investigated until 3 kbar at room temperature, showing also a linear decrease. Figure 2-13 illustrates the variation of the dielectric constant with pressure at different temperatures. KTO has a rather low compressibility and these changes are linear over the tested pressure range. It was also

reported that the application of a sufficient hydrostatic pressure supresses a relaxor phase in KTN and dielectric constant becomes frequency independent [41].

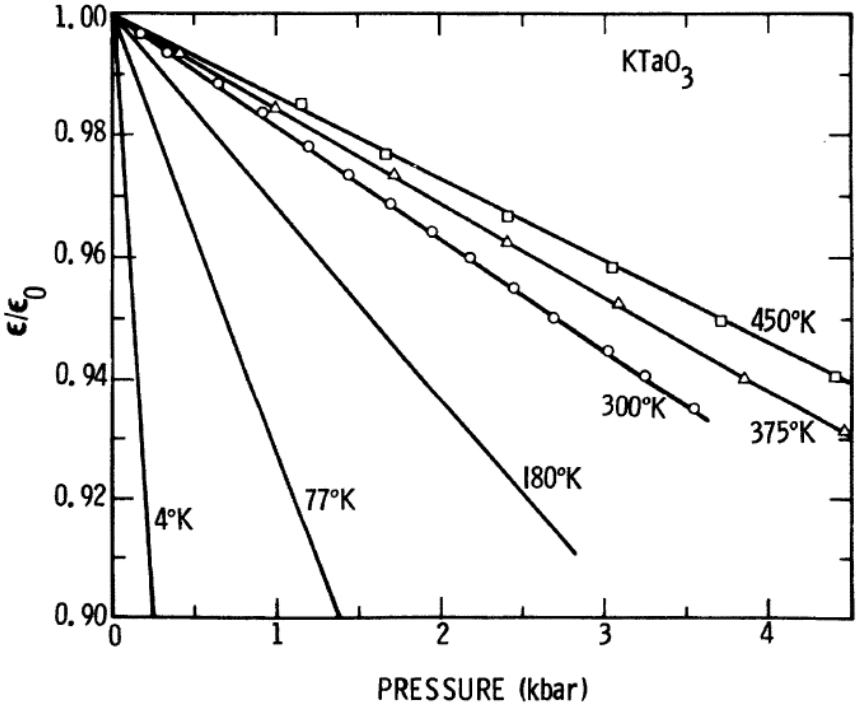

Figure 2-13.Temperature variation of dielectric constant of $KTaO_3$ at distinct pressures [90]. Pressure suppresses the magnitude of ε'.

There has been many studies reporting doping effect on dielectric properties in $SrTiO_3$. It was demonstrated that the isovalent *B*-site dopants, such as Zr^{4+}, Sn^{4+}, Ge^{4+}, have much smaller effect on dielectric properties comparing with isovalent *A*-site dopants (Ca^{2+}, Ba^{2+}, Pb^{2+}, Cd^{2+}) [91]. The dielectric anomalies with significant frequency dispersion were also observed in $SrTiO_3$ doped with *A*-site aliovalent dopants. The most known is solid solution of $SrTiO_3$ and $BaTiO_3$ (BST), forming a complete set of compositions with adjustable phase transitions [92]; decreasing $BaTiO_3$ content leads to a linear decrease of all the phase transition temperatures, but with different rates. BST can be considered as an analogue of KTN, both being suitable materials for tunable applications.

2.3.1.4. Synthesis of $KTaO_3$

Despite the interesting properties of KTO-based compounds, fabrication of polycrystalline bulk and thin films with perovskite structure is still a challenge. The perovskite phase development process in $KTaO_3$ ceramics and thin films has been narrowly investigated, in contrast to single crystals [59, 93-99], even though the nature of the perovskite phase formation and the origin of intermediate phase appearance is still not clear. Problems are mainly associated with: i) composition deviations that may occur because of the easy potassium volatility and strong covalent character of Ta–O bonds [98], and ii) formation of intermediate pyrochlore structures while using wet chemical methods (not reported in films grown by pulsed laser deposition) [61, 75, 96]. Several approaches have been proposed to overcome these difficulties and the most common of them is the use of K excess [61, 96, 100].

In general, the occurrence and stability of the formed phases are strongly dependent on the selected synthesis method and also on the chosen preparation conditions within the method, *e.g.* starting reagents, temperature, time, and atmosphere. The majority of the research studies on alkali tantalates has been conducted on single crystals with well-established processing parameters and methods, and processing of the bulk ceramics is rather rare even though they are cheaper to produce [101]. The bulk ceramics were mainly prepared by solid-state reactions but achieving monophasic and stoichiometric compounds with high relative density, >90 %, is still challenging [98, 101-103]. In case of KTO, initial excess of potassium, ≥2 %, is shown to be necessary to yield single phase ceramics with lattice parameters close to that of KTO single crystals. Moreover, it was found that initial potassium excess favours the grain growth [98, 101]. Furthermore, the starting reagents, potassium carbonate and tantalum pentaoxide, have to be carefully dried to ensure stoichiometry control. Worthwhile to note also that KTO sinters in very narrow temperature interval, >1300 °C, close to the melting point (1370 °C), leading to local melting and high degree of residual porosity. Some of the problems could be overcome when using pressure-assisted sintering from mechanochemically activated powders [103]. In this case the phase-pure and high quality KTO ceramics with relative density ≥95 % were obtained at temperatures <1300 °C, with properties comparable to single crystals.

2.3.1.5. Solution derived $KTaO_3$ thin films

$KTaO_3$-based thin films, derived from chemical solution deposition (CSD) techniques, have been mostly reported in the past two decades, starting in the beginning of 1990s [59, 93, 104, 105], and their structure and microstructure as a function of processing parameters were analysed. Table 4-17 presents the most important publications, in chronological order, reporting CSD-derived thin films with $KTaO_3$-based compositions, mainly solid solutions of $KTaO_3$ and $KNbO_3$ (KTN).

In the beginning of 1990s, Hirano *et al.* [93, 106, 107] reported the preparation of powders and thin films from metal alkoxide solutions, using ethoxide precursors dissolved under controlled atmosphere in ethanol, of a wide range of KTN compositions. Thermal X-ray diffraction (XRD) studies revealed that for increasing Ta-content higher crystallization temperature is needed for the perovskite phase formation; in the case of $KTaO_3$ a crystallization temperature of 850 °C was referred while for $KNbO_3$ only 650 °C is necessary. It was also demonstrated that water vapour with oxygen gas have prominent effect on the elimination of organic components during crystallization and consequently on the crystalline phase and preferred orientation of the films.

Further work was also conducted in 1990s by Nazeri and co-workers [59, 104, 105]. Sol-gel processing of solutions was varied in terms of potassium precursor, ethoxide or acetate, solvent, ethanol or methanol, and modifiers, acetylacetonate, triethylamine or vetiverol (chemical used in cosmetics). At the same time, tantalum and niobium ethoxide were used in all the routes. However, these studies were mostly focused on finding the most appropriate from the various substrates for the formation of perovskite KTN phase. It was found that such substrates as single crystals of $SrTiO_3$ and MgO matching most from the crystallographic point of view (2 and 5 % misfit between the *d*-spacings to KTN, respectively), facilitate the formation of desired $KTaO_3$, although no further explanations were provided.

Later, Kuang *et al.* [94, 95, 108, 109] reported preparation of KTN ($KTa_{0.65}Nb_{0.35}O_3$) thin films by a sol-gel process as well. The simple procedure with metal ethoxides as precursors dissolved in ethanol without additives was used. Firstly, the study on precursor powders revealed the existence of a complex reaction resulting in the formation of double metal

alkoxides: $KTa(OC_2H_5)_6$ and $KNb(OC_2H_5)_6$; see Figure 2-14. The dimeric structure of the tantalum compound was proposed to consist of an edge shared octahedral structure where each tantalum atom is bonded to two bridging and four terminal ethoxide groups. Then, the precursor solution was used to fabricate thin films, and the effects of processing parameters, *i.e.* substrate, heating rates, potassium excess, crystallization atmosphere, *etc.*, were assessed. Highly oriented perovskite KTN(100) thin films were prepared on sapphire substrates at 750 °C and on $SrTiO_3$(100) substrates at 650 °C.

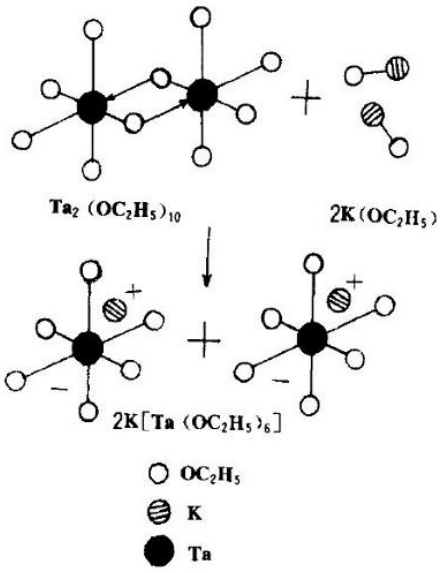

Figure 2-14. Proposed model for complex formation of double metal alkoxide: $KTa(OC_2H_5)_6$ [94]. The dimeric structure consists of an edge shared octahedral structure where each tantalum atom is bonded to two bridging and four terminal ethoxide groups.

In 21st century, Buršík *et al.* [60, 96, 97, 110] synthesized for the first time KTN thin films with high Ta content (≥95 %) via sol-gel. Precursor solutions were prepared using metal iso-butoxide precursors: $K(OCH_2CH(CH_3)_2)$ and $Ta(OCH_2CH(CH_3)_2)_5$, and absolute iso-butanol, $(CH_3)_2CHCH_2OH$, with an addition of diethanolamine as modifier. Distinct K:Ta sols stoichiometry, annealing regimes, various substrates and buffer interlayers were implemented in the work. Optimum parameters as reaction atmosphere, proper alkali excess in the starting solution, underlayers, *etc.*, were set for perovskite phase formation (Figure 2-15). Figure 2-15 *(a)* present a scheme of annealing procedures (slow and fast) used for KTN thin films crystallization [96]. Taking into account the volatility and reactivity of potassium a fast-heating strategy was selected to minimize potassium losses. Annealing of

the films on SiO_2 or Si(100) at the constant temperature (600 °C) by slow heating led to pyrochlore formation, while fast heating yielded perovskite crystallization.

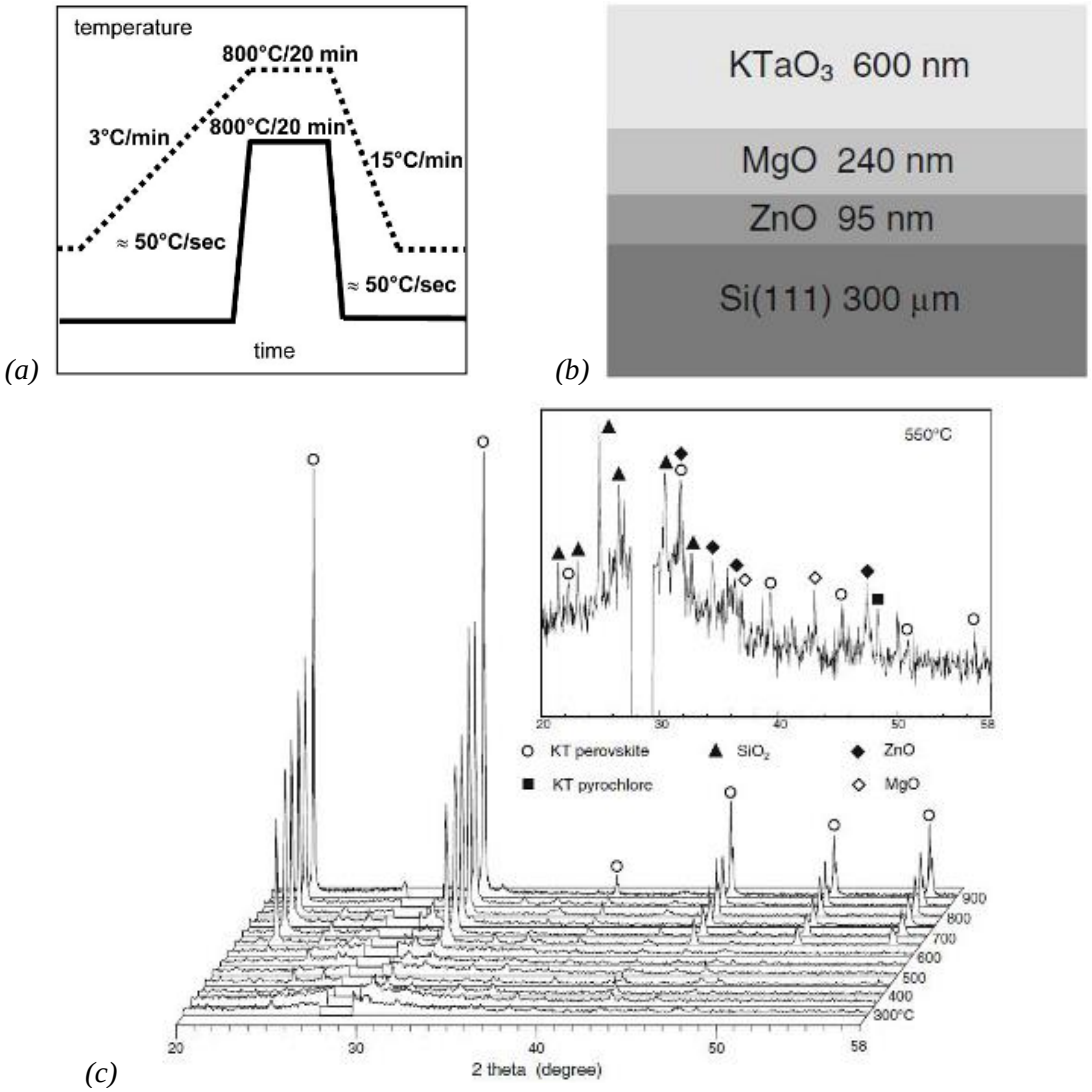

Figure 2-15. Factors affecting the phase formation in KTO thin films processed by chemical solution deposition: annealing regimes – (a) [96], underlayers, i.e. ZnO/MgO – (b) [60], and reaction atmosphere (at distinct temperatures, in O_2) – (c) [60]. Perovskite KTO is facilitated using rapid thermal processing, substrate (or buffer layers) with crystallographic matching, and oxygen atmosphere.

Figure 2-15 *(b)* shows a scheme of thin films sequence deposited on Si(111) substrate [60]. ZnO-MgO buffer layers were inserted between Si substrate and KTO film in order to prevent the reaction between basic potassium precursor and acidic silicon. Additionally, MgO holds cubic crystal structure, similar to $KTaO_3$ with reasonably low

lattice misfit, ~5 % at room temperature, promoting crystallization of perovskite KTO. Crystallized KTO thin films were successfully prepared at temperature >700 °C in air and O_2 atmosphere. And Figure 2-15 *(c)* illustrates the phase evolution of KTO thin films processed at distinct temperatures in oxygen atmosphere that facilitates pyrochlore decomposition and perovskite formation.

However, the topic on solution derived KTO thin films is not fully explored because, for instance, the changes in the structure and microstructure have not been fully studied in details, and their correlation to the microscopic properties still have to be investigated.

2.3.2. Lithium tantalate

Lithium tantalate, $LiTaO_3$ (LTO), like lithium niobate, $LiNbO_3$ (LNO), possesses a combination of unique electro-optical, acoustic, piezoelectric, pyroelectric and non-linear optical properties. LTO and LNO crystals are colourless, chemically stable, insoluble in water or organic solvents, and have high melting points. They both have low acoustic losses and rather high non-linear optical coefficients, d_{33} = 14 pm/V and d_{31} = 0.9 pm/V (for LTO), being very attractive materials for optical frequency conversion. The values of the nonzero electro-optic coefficients at 633 nm for static electric field for LTO are: r_{33}^T = 30 pm/V and r_{31}^T = 30 pm/V [6]. Consequently LTO is a suitable material for applications in acoustic, electro-optical and non-linear optical devices, high-temperature acoustic transducers, receivers-transmitters of acoustic vibrations, air force acceleration meters, acoustic wave delay lines, deflectors, generators of non-linear distorted waves, acoustic filters, electro-optical Q-modulators (Q-switch), encoders-decoders, filters in television receivers, video-recorders and decoders, converters, frequency doublers and resonators in laser systems, non-linear elements in parametric light generators, *etc.* [111-114]. Since for some of these applications a high degree of optical uniformity, usually obtained in the single crystals, is required, LTO and LNO are generally produced in the form of crystals.

2.3.2.1. Crystal and electronic structures of $LiTaO_3$

Lithium tantalate does not exhibit a typical perovskite structure, but it has an ABO_3 lattice with a sequence of distorted oxygen octahedra joined by their faces along a trigonal, polar

c-axis [44], as visualised in Figure 2-16 *(a)* [115]. The O atoms form distorted octahedra with shared faces and exhibit a quasi-hexagonal arrangement. The Li and Ta cations each occupy one-third of these oxygen octahedra, whereas another third is empty (intrinsic vacancy). Figure 2-16 *(b)* shows a LTO/LNO crystal with a hexagonal symmetry: $a = b \neq c$, $\alpha = \beta = 90°$ and $\gamma = 120°$ [116] and a unit cell consisting of 30 atoms.

LTO possesses a non-centrosymmetric *R3c* space group (3m point group) symmetry at room temperature. In contrast to normal perovskites, both Li and Ta cations lie within oxygen octahedra and both Li and Ta are displaced from the centres of their respective octahedra along the *c*-axis [111]. This structure is classified as a $LiNbO_3$-type, and can be described as a very distorted derivative of the perovskite one, to which a displacive transformation is related with [117].

The strong TaO_6 distortion causes that the internal O–Ta–O bond angle and the interoctahedron Ta–O–Ta angle are reduced to ~170° and to 144°, respectively [118]; the deviation from the linear configuration results in reduced interatomic orbital overlap, which explains the significantly reduced bandwidth.

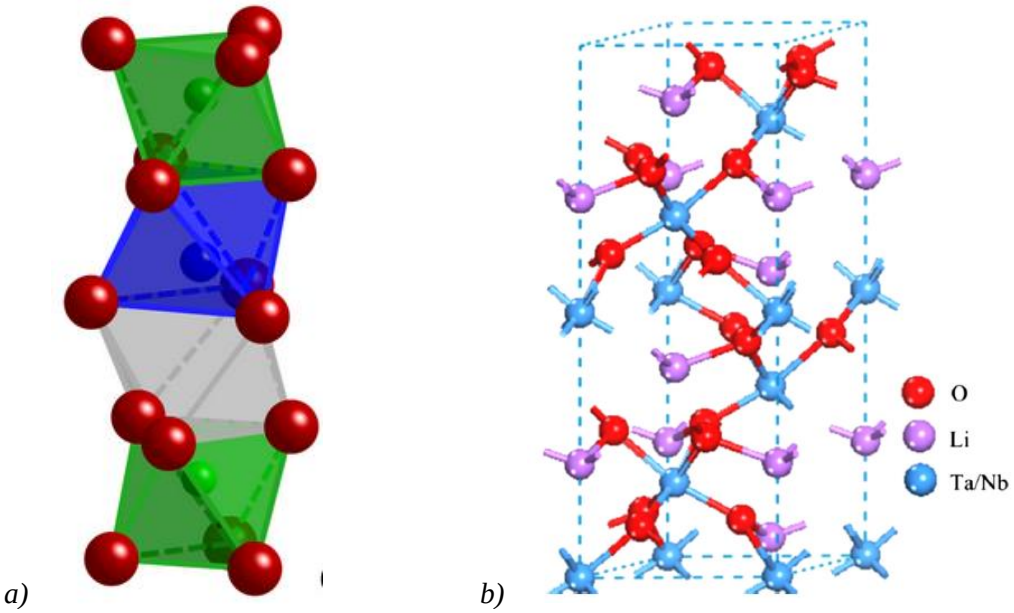

a) *b)*

Figure 2-16. (a) Crystal structure of $LiTaO_3$ visualized as a sequence of distorted octahedral along the (0001) axis (red balls represents O, blue Li and green Ta) [115], and (b) crystal structure of Li(Ta or Nb)O_3 with a hexagonal symmetry [116]; there are 30 atoms in the cell of the compounds.

The electronic band structure of LTO was recently computed using the first-principles plane-wave pseudopotential density functional theory [116]. The calculated band structure of LTO compound is depicted in Figure 2-17, where the energy unit is eV and the Fermi level is set to be at the valence band maximum. The density of states was determined revealing that the valence band is mainly composed of O *2p* and Ta *5d* states hybridized with small amount of Ta *s* states, and the conduction band is composed of Ta *5d*, O *s* and Li *s* states. However, the band gap of LTO determined from optical adsorption is reported to fall in a wide range of 3.9–5 eV [118]. The differences between the electronic density of states of LTO, both at the ferroelectric and paraelectric configurations, were also examined [44]. The results indicate that the electronic structures at these phases are very similar, the lithium is almost completely ionized and its electronic distribution does not change during the phase transition. The only difference was the band gap value: the band gap in the ferroelectric phase was about 4.0 eV, decreasing by about 15 % in the paraelectric phase. The origin of ferroelectricity in LTO was studied in the same work. It was disclosed that the driving mechanism behind the ferroelectric instability is the hybridization between the *d* state on Ta atom and the *2p* state on O leading to the displacement towards each other (an order-disorder model), and Li is rather passive. This is in contrast to the classical perovskite ferroelectrics with *A*-site atoms large enough to allow the oxygen to move towards the *A* atoms. The assessment of the Ta–O distances in KTO and LTO revealed that the oxygen octahedra are larger in KTO than in LTO. Even though Ta atoms never displace to the off-center position in KTO, while Ta exhibits a ferroelectric distortion in LTO.

Both $LiTaO_3$ and $LiNbO_3$ show a second order phase transition from a high temperature paraelectric phase with space group symmetry $R\bar{3}c$ (point group $\bar{3}m$) to a ferroelectric phase of *R3c* symmetry at Curie temperatures T_C of ~690 °C and ~1190 °C, respectively. This transition corresponds to a loss of the inversion symmetry at the transition point, which allows the development of the spontaneous polarization along the polar *c* axis [111, 116, 119-122]. The calculated lattice constants (via first-principles calculations based on the density functional theory) for $LiTaO_3$ are: a = 5.1296 Å and c = 13.9385 Å, and are very close to the experimental values reported by Abrahams *et al.* and determined by X-ray and neutron diffractions [121, 122]: a = 5.1543 Å and c = 13.7835 Å, within error <1.5 %.

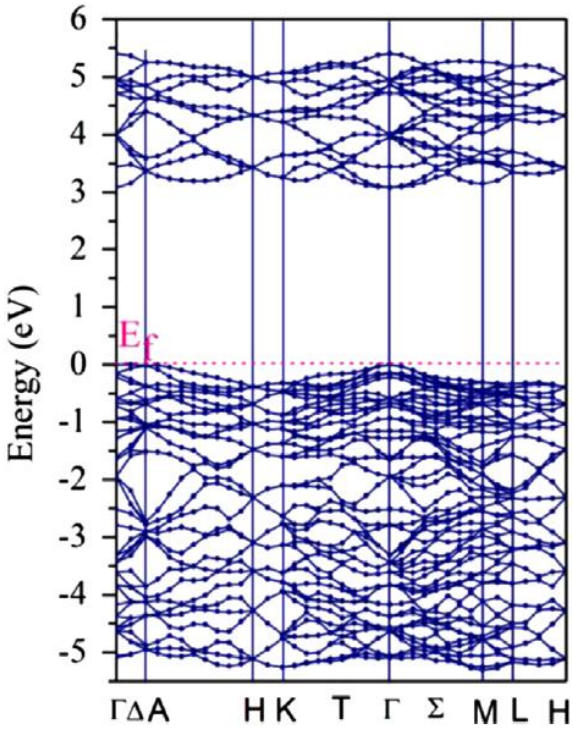

Figure 2-17. The calculated band structure of $LiTaO_3$, along the symmetry lines of the first Brillouin zone [116]; the unit of energy is in eV and the Fermi level is set to be at the valence band maximum. LTO has a direct band gap along the Γ point direction.

LTO undergoes only a single phase transition, from the low temperature FE phase to the high temperature PE phase, as proven by dielectric studies [123, 124]. Figure 2-18 shows the temperature dependence of dielectric constant at different frequencies selected as 100 Hz, 1, 10 and 50 kHz, indicating the following effects [123]: i) the magnitude of the dielectric constant maximum rapidly decreases with frequency until it is hardly detectable at 50 kHz, ii) the peak shifts to higher temperatures with increase of frequency, reaching ~720 °C at 50 kHz (a dispersion over wide temperature range), and iii) the dielectric constant increases rapidly at higher temperatures particularly at low frequencies (it can be associated with an additional polarization process).

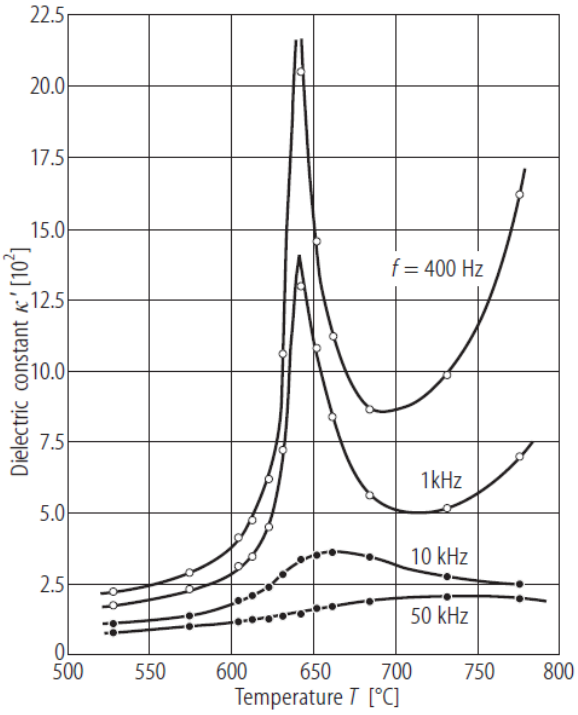

Figure 2-18. Temperature and frequency dependence of dielectric constant for stoichiometric LTO ceramic; temperature is limited to the range of 520-780 °C, and frequency in the range of 0.4-50 kHz. The phase transition can be observed ~650 °C [123].

A comparison with light-scattering measurements suggests that the phase transition in LTO has an intermediate character between the displacive and order-disorder categories [124].

2.3.2.2. Processing of $LiTaO_3$

Fabrication of such active elements like LTO single crystals is crucial, and some crystal growth methods, like Czochralski process, allow the growth of large size (~1–1.5 kg) and high-quality LTO crystals, which are non-hygroscopic, colourless, water-insoluble and have low transmission losses [125]. However, it is difficult to grow high quality stoichiometric LTO single crystals (with precise ratio Li:Ta = 1). LTO with Li:Ta ratio within 1 ± 0.3 % is referred as stoichiometric $LiTaO_3$, while most of the commercially available LTO crystals are congruent (with Li deficiency ~1.5 %), containing a large number of non-stoichiometric defects [126]. The main reason for the non-stoichiometry in LTO crystals is related to the complex phase diagram with a region of non-stoichiometric solid solubility of LTO at high

temperatures towards Ta excess. Thus, it leads to the existence of congruently melting compositions (solid and liquid phases in equilibrium). The main congruent composition of LTO is a composition with approximately 1.5 mol% Li deficiency from the stoichiometric one [126]. The non-stoichiometry in LTO has a tremendous effect on the Curie temperature, *i.e.* congruent LTO exhibits a T_C of ~600 °C, while that of stoichiometric LTO is nearly 700 °C. This behaviour can be related to point defects, *e.g.* Li vacancies, as well as Ta reduction to Ta^{4+} and its transfer to Li sites (so-called Ta antisites) [6]; even up to 5 % of Ta ions can occupy the Li sites in the lattice causing Ta site vacancies. Near-stoichiometric LTO crystals have a structure-sensitive nature due to its low defect density comparing to congruent LTO. As the composition changes from congruent to stoichiometric, the absorption edge shifts to shorter wavelengths, being favourable for many optoelectronic applications using ultraviolet (UV) light [126].

In the case of LTO bulk ceramics, the processing challenges are even more serious because the significant thermal stresses that occur upon cooling down to room temperature do not allow obtaining consolidated bodies, *i.e.* the obtained LTO bulk bodies will be cracked [127, 128]. Only recently, Chen *et al.* [127] succeeded to obtain dense (~95 %) and monophasic undoped LTO ceramics with rather large grains (~8 μm) using hot pressing at 1250 °C. Then, Yang *et al.* [128] could also obtain well-compacted ceramic but the preparation procedure is very poorly described, thus no information on detailed experimental protocol can be extracted.

It has been established that LTO single crystals grow congruently from a melt having Li deficient (~1.5 %) composition with enormous population of point defects. However, the processing of polycrystalline LTO is important in many applications, thus its processing needs to be further studied.

LTO thin films have been widely reported, synthesized via distinct methods, frequently by sputtering [129-134], but chemical solution deposition is more attractive because of its low cost, availability, *etc.* Besides, it is the method that is used in LTO processing in this thesis. Mostly a classical alkoxide route [135-140] has been implemented using metal ethoxides as precursors, although also diol-based method has been reported as well [141-147]. More on the CSD processing of LTO films is described in chapter 4.3.

2.3.3. Sodium tantalate

Sodium tantalate belongs also to the family of the perovskites and has the same crystal structure as $CaTiO_3$ [148]. Matthias [48] reported that $NaTaO_3$ (NTO) was ferroelectric at room temperature, but it has not been confirmed by later measurements [149, 150], because NTO holds a centrosymmetric structure at room temperature [151, 152]. Moreover, recently it was demonstrated by low temperature dielectric studies that in fact NTO is an incipient ferroelectric [42, 153]. It means that the structural phase transitions are not driven by polar soft phonons from the Brillouin zone centre, but by soft phonons from Brillouin zone edge in *M* and *R* points, in contrast to classical ferroelectrics [153].

As in incipient ferroelectrics, the dielectric permittivity of NTO increases monotonically down to 4 K, without any peak up to 923 K [149]. However, there are only few studies on the dielectric response of $NaTaO_3$ [42, 149, 150, 153, 154]. Iwasaki and Ikeda [149] have not presented neither temperature dependence of the dielectric permittivity nor values of the dielectric permittivity for $NaTaO_3$, and Aleksandrowicz and Wojcik reported the temperature dependence of the dielectric permittivity from 300 to 1000 K, but values of the dielectric permittivity were quite low, from 4 up to 11 [150]. Konig *et al.* have also reported that density of the single-phase NTO ceramics sintered at temperature as high as 1640 °C was not enough for dielectric characterization, whereas NTO ceramics with secondary phase (Na-deficient $Na_2Ta_4O_{11}$), formed due to sodium evaporation, revealed the room-temperature permittivity of 142 with a negative temperature coefficient of permittivity between 123 and 823 K [154]. On the other hand, considerable attention was paid to the photocatalytic performance of NTO [155]; high photocatalytic quantum yield for water splitting into H_2 and O_2 under UV irradiation, was reported exceeding 50 %, when doped with La [156].

2.3.3.1. Crystal and electronic structures of $NaTaO_3$

NTO has an orthorhombic structure with space group *Pbnm* (a = 5.4768 Å, b = 5.5212 Å, and c = 7.7890 Å) at room temperature [148]. Neutron powder diffraction studies were conducted and the structural phase transitions in NTO were confirmed to be in the following order: the room temperature orthorhombic structure transforms to orthorhombic *Cmcm* at

around 700 K (a = 7.8337 Å, b = 7.8485 Å and c = 7.8552 Å at 773 K), then to tetragonal *P4/mbm* at 835 K ($a = b$ = 5.5503 Å and c = 3.9335 Å), and finally to cubic $Pm\bar{3}m$ above 890 K ($a = b = c$ = 3.9313 Å). The low temperature *Pbnm* structure is created by the tilting of TaO_6 along the *a*- and *b*-axes with the same angle but in opposite direction, and simultaneously along the *c*-axis with a different angle. The orthorhombic structure *Cmcm* is characterized by the simultaneous tilting of the oxygen atom octahedron about two of its tetrad axes, the tilting of successive octahedra being out of phase along the *b*-axis, and in phase along the *c*-axis [148]. It was reported by Hu and co-workers that the synthesis method (sol-gel, hydrothermal and solid-state) determines the crystalline structure of as-prepared $NaTaO_3$ powders at room temperature [43, 157, 158]. The refinement results showed that the sol-gel derived specimen has a monoclinic phase with a Ta–O–Ta bond angle of 179° while the hydrothermal and solid-state specimens have an orthorhombic phase with bond angles of 163° and 157°, respectively. The representation of cubic, monoclinic and orthorhombic structures is shown in Figure 2-19 *(a-c)*. Therefore, the differences in the crystal structure affect optical properties, for example photoluminescence intensity increases in the following order: solid state > hydrothermal > sol-gel, which is opposite to that of the Ta–O–Ta bond angle. On the other hand, the increase in the photocatalytic activity of $NaTaO_3$ in water splitting showed the same order as that of the Ta–O–Ta bond angle [43].

The electronic band structure of NTO (orthorhombic *Pbnm*) was computed by DFT calculations [159]. It was determined that the lowest valence bands are due to O *2s* states, the states at the top of the valence band are mainly of O *2p* character, while the states at the bottom of the conduction band are of Ta *5d* character. The contribution of Na atoms to Ta *5d* and O *2p* is very minor, indicating the high ionicity between Na and TaO_3 [160]. NTO has a direct band gap at the *Γ*-*Γ* point with the gap value estimated to be ~4.1 eV [159, 160].

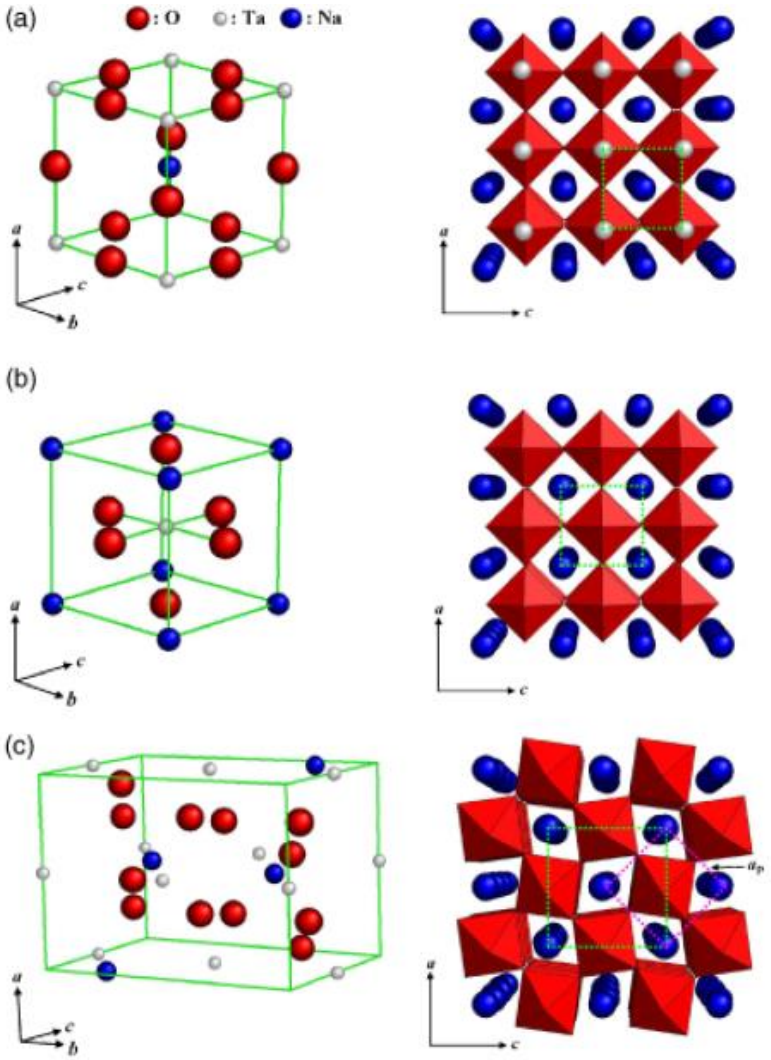

Figure 2-19. The unit-cell and the refined crystalline structures of $NaTaO_3$: (a) cubic phase, (b) monoclinic phase and (b) the orthorhombic phase [43].

2.3.3.2. Processing of $NaTaO_3$

Processing of NTO ceramics is also complicated. Firstly, the sintering temperature required to obtain dense and single phase bulk ceramics is higher than in KTO, >1500 °C [153, 161]. Secondary phases, such as $Na_2Ta_4O_{11}$ and $Na_2Ta_8O_{21}$, are frequently present in the sintered bulk ceramics at such high temperatures, affecting the electrical properties. If the sintering temperature is reduced to 1250 °C and Na excess used, the secondary phases are avoided and dense NTO ceramics reveal quite high dielectric permittivity which increases on cooling from 210 to 324 [42, 154].

Results on thin films of $NaTaO_3$ are barely reported in the literature. RF magnetron sputtered NTO film were grown on platinized Si substrate [42]. The dielectric properties were measured at low temperatures, and permittivity decreases with decreasing temperature revealing an anomaly at ~22 K (not associated with any irreversible polarization mechanism). Besides, a strong frequency dispersion was observed corresponding to a relaxation-like dispersion related with a polaronic-like character due to the charges induced by oxygen vacancies emerging from film processing [42].

2.3.4. A comparison between alkali tantalates and niobates

Perovskite alkali tantalates, $KTaO_3$, $LiTaO_3$ and $NaTaO_3$, and niobates, $KNbO_3$, $LiNbO_3$ and $NaNbO_3$, possess unique features for a number of applications. They are frequently compared together, mostly based on alkali metal, because of their similarities in certain features, *i.e.* structure, electrical, piezeoelectric and optical properties, applications. As alkali tantalates are quite deeply described in the previous sections, Table 2-3 presents some of the selected properties of alkali niobates; some of the analogous data sets are shown for alkali tantalates in Table 2-2.

For instance, both $NaTaO_3$ and $NaNbO_3$ (NNO) exhibit rich polymorphism over a wide range of temperatures, and possess attractive physical properties to be used as components in ferroelectric and piezoelectric applications, photocatalysts in water splitting and pollutant degradation, and thermoelectric materials [161-165]. While NTO is an incipient ferroelectric, NNO is an antiferroelectric (AFE) at room temperature, *i.e.* its dielectric permittivity increases as the electric field approaches the coercive field of AFE transition, which is the opposite trend with conventional ferroelectric systems where the permittivity decreases with increasing electric field [9]. The solid solution between NTO and NNO was discovered to be a new high-temperature and high-permittivity dielectric system that is suitable for base metal inner electrode capacitor applications [9].

Both $LiTaO_3$ and $LiNbO_3$ are ABO_3-type ferroelectrics with high Curie points, (T_C > 600 °C for LTO and >1100 °C for LNO) and are relevant materials with electro-optic applications due to high electro-optic coefficients, optical damage resistance and low loss [6, 123, 166]. $KNbO_3$ is a widely studied ferroelectric (analogous to $BaTiO_3$ in terms of

structural transitions) due to its large piezoelectric constant, electromechanical coupling coefficient, electro-optic coefficient and nonlinear optical coefficient [167-169], whereas $KTaO_3$ is an attractive dielectric material with very low microwave loss [40, 41].

Table 2-3. Summary of the selected properties of alkali niobates.

Variable	**$KNbO_3$**	**$LiNbO_3$**	**$NaNbO_3$**
Ferroelectric state (at RT)	FE	FE	AFE
Crystal structure (at RT)	Orthorhombic *(non-centrosymmetric)*	Trigonal *(non-centrosymmetric)*	Orthorhombic *(centrosymmetric)*
Band gap, E_g (eV)	3.3	4.1	3.5
Tolerance factor	1.03	0.78	0.94
Transition temperatures (°C)	I: 420 (cubic → tetragonal) II: 225 (tetragonal → orthorhombic) III: -10 (orthorhombic → rhombohedral)	1210 (trigonal → trigonal)	I: 640 (cubic → tetragonal) II: 570 (tetragonal → orthorhombic) III: 520 (orthorhombic → orthorhombic) IV: 480 (orthorhombic → orthorhombic) V: 360 (orthorhombic → orthorhombic) VI: -200 (orthorhombic → trigonal)

Moreover, solid solutions of $KNbO_3$ and $NaNbO_3$ (KNN) are currently being considered as potential substitutes for the present piezoelectric market leader, PZT [32]. KNN has a relatively high T_C ~ 420 °C, which is a considerable advantage over PZT [170] and good piezoelectric properties [171, 172]. Other type of solid solutions composed of $KNbO_3$ and $KTaO_3$, (KTN) are also recognized as systems with high potential for nonlinear electro-optical devices, *e.g.*, light beam modulators and deflectors due to relatively large electro-optic coefficients measured in single crystals: γ_{33} = 216.7 pm/V, γ_{13} = -21.2 pm/V, and γ_c = 242.9 pm/V (1 kHz) [173].

2.4. Alternative applications of tantalates

The use of advanced ceramics is growing as technologies, being developed in research laboratories and universities, then become adopted by industry. The new opportunities have raised in 21st century particularly in two emerging areas: i) photocatalysis for fuel production and environmental remediation, and ii) biomedical engineering. They are briefly introduced in the following sections.

2.4.1. Tantalates as photocatalysts

Energy (depletion of the fossil fuels) and environmental (gas emission and organics in wastewater) issues at the global level are important topics nowadays. It is indispensable to develop clean energy systems and methods for toxic organics disposals [155]. Energy production from renewable energy sources such as solar energy is highly recommended, whereas hydrogen as energy carrier can be considered a green energy alternative capable of powering almost everything, as illustrated in Figure 2-20 for the case of the automobiles power.

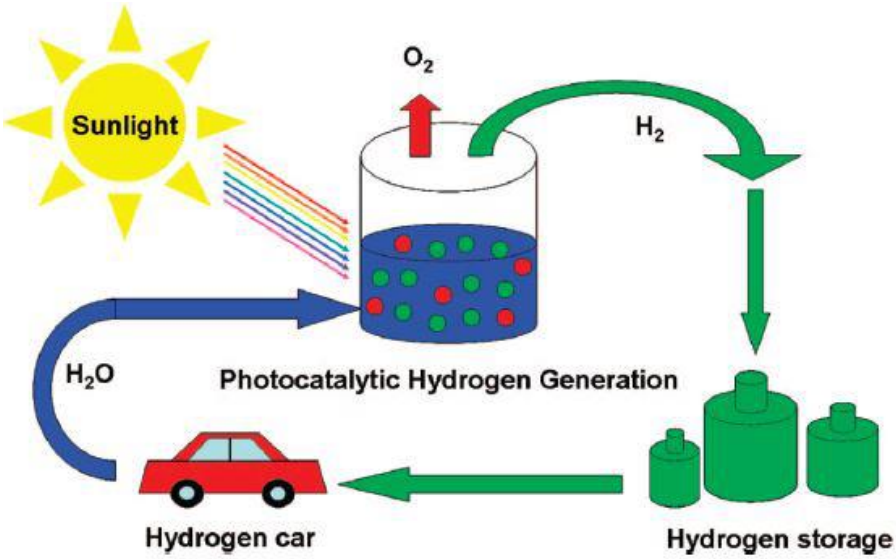

Figure 2-20. Diagram presenting the potential photocatalytic hydrogen generation for the hydrogen energy system [174].

On the other hand, one of the universal problems most affecting people throughout the world is inadequate access to clean water and sanitation. Problems with water are expected to grow in the coming decades, with growing population and water scarcity occurring globally, even in regions currently considered water-rich. Systematic and global research needs to be conducted to identify robust new methods of purifying water at lower cost and with less energy, minimizing the use of chemicals and impact on the environment at the same time [175]. In both developing and industrialized nations, a growing number of contaminants are entering water supplies from human activity: from traditional compounds such as heavy metals to emerging micropollutants, such as endocrine disrupters and nitrosoamines [176, 177]. More effective, lower-cost, robust methods to disinfect and decontaminate waters from source to point-of-use are needed, without further stressing the environment or endangering human health by the treatment itself [175]. Conventional methods of water disinfection and decontamination cannot address many of these problems.

Environmental pollution is a recognized issue of major concern since a wide range of contaminants has been found in aquatic environment at ng/L to μg/L levels. In Europe, in the beginning of 21st century, a strategy was defined to identify the priority substances concerning aquatic ecosystems, followed by the definition of environmental quality standards (EQS) in 2008. Recently it was launched the Directive 2013/39/EU (by the European Parliament) that updates the water framework policy highlighting the need to develop new water treatment technologies to deal with such problem [178].

Conventional physicochemical treatment methods, *e.g.* activated carbon adsorption, can only partially decompose some pollutants. And most importantly, these treatment methods are often chemically, energetically and operationally intensive, focused on large systems, and thus require considerable infusion of capital (injection of funds) and engineering expertise and infrastructure, thus, making them unattractive for global implementation. As an alternative, photocatalysis process has been considered a most promising way to remove non-biodegradable organic pollutants, because this process decomposes the organic pollutants to innocuous substances. Therefore, design and preparation of efficient photocatalytic materials are very important topics [68, 175].

Semiconductor catalysts are capable materials used in photocatalysis. For instance, the heterogeneous solar photocatalytic detoxification process is based on the use of near-

ultraviolet radiation to photo-excite a semiconductor catalyst in contact with water and in the presence of oxygen. Besides, some semiconductors can also be used to degrade particular contaminants due to their electronic structure [175]. The mechanism of the photocatalytic process generated by semiconductors is schematically represented in Figure 2-21. Absorption of a photon with an energy *hv* greater or equal to the band gap energy (E_g) generally leads to the formation of an electron/hole pair in the semiconductor. These charge carriers subsequently either recombine and dissipate the input energy as heat, get trapped in metastable surface states, or react with electron donors and acceptors adsorbed on the surface. Simultaneously, in the presence of a fluid (water) a spontaneous adsorption occurs (water and pollutant - P). Each ion formed subsequently reacts to form the intermediates and final products [175]. Furthermore, the oxidative species formed, *e.g.* hydroxyl radicals, react with the organic pollutants by their oxidation (photocatalytic oxidative degradation).

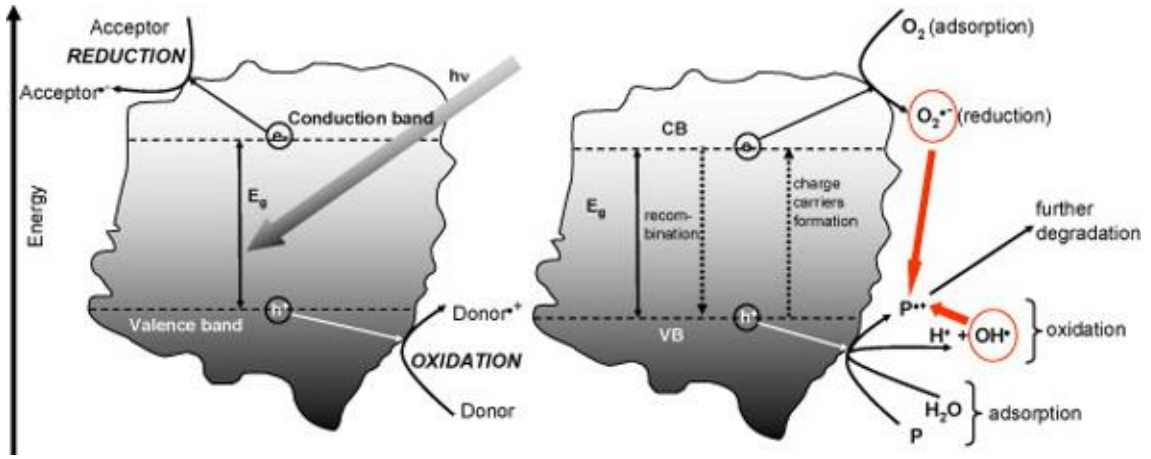

Figure 2-21. Scheme presenting the mechanism of photocatalysis in a semiconductor particle in the presence of water containing a pollutant [175].

Among different semiconductors, titanium dioxide (TiO_2) has been extensively investigated (since 1970s because of Fujishima and Honda findings [179]) for decomposing organic pollutants being the most effective [155, 174]. TiO_2 is chemically inert, photoactive, photostable and non-toxic, and the mechanism of its activity is well established [180]. However, even though it is one of the most efficient photocatalyst, its application is limited due to several reasons: i) inefficient utilization of visible light, ii) low adsorption of organic pollutant, iii) difficulty in distributing particles uniformly, iv) difficulty in recovery of

nanosized particles, and v) aggregation of nanosized particles [181]. All of these issues can result in slower photocatalytic degradation rate and reduced activity.

Today, perovskites are considered as serious alternatives in various catalytic applications, mainly due to their ease of synthesis, low cost and the extraordinary capability of their structure to accommodate a wide range of elements, and consequently tailoring their properties [182]. They are attractive because of their intrinsic redox properties. For instance, some of them can be reduced to an intermediate oxygen-deficient compounds, and this phenomena can be easily modified by substitution of *A*- or *B*-site cations, *e.g.* (La, Sr)$MnO_{3-\delta}$. It was also established that perovskites can adsorb a large amount of oxygen, both in the bulk and on the surface, and desorbs two types of oxygen: α-O_2 (weakly bonded to the surface) and β-O (coming primary from the bulk). Acid-base properties are also key parameters conditioning the activity of materials for catalytic reactions. Therefore, a major progress on the development of ABO_3-based photocatalysts has been achieved by means of different modification strategies based on the fundamental principle and process of photocatalysis, as well as on the crystal structure and chemical component characteristics. The studies have been carried out for targeting mostly water splitting, whereas compounds such as $SrTiO_3$ and $NaTaO_3$ have an important value as model photocatalysts to reveal the structure-activity relationship [183].

Recently, much attention has also been paid to develop new type of photocatalytic materials, such as niobium and tantalum oxide based photocatalysts, because of their attractive electronic and crystal structures. Ta-based oxides are known to be active photocatalysts for water splitting under UV irradiation. Under band gap irradiation (4.0 eV), Ta_2O_5 alone can only produce a very small amount of H_2 and no O_2 from pure water [184, 185]. However if Ta_2O_5 is modified with NiO and RuO_2, it displayed great activity for the overall water decomposition [186]. The addition of Na_2CO_3 is also effective for improving the photocatalytic activity of Ta_2O_5. Mesoporous Ta_2O_5 was found to be an active catalyst for photocatalytic water decomposition after NiO loading [187]. Although the walls of the mesoporous Ta_2O_5 were amorphous, the photocatalytic activity was higher than that of crystallized Ta_2O_5. The small wall thickness of the mesoporous Ta_2O_5 favoured the migration of excited electron to the surface. When mixed with TiO_2, the mesoporous Ta-Ti mixed oxides showed relatively high activities (~1.7 mmol/h of H_2) for photocatalytic hydrogen generation from methanol/water mixtures under the irradiation of $\lambda > 300$ nm.

However, a higher concentration of TiO_2 in the mixed oxides led to the destruction of the mesoporous structure [188]. A comprehensive revision focused on tantalum-based semiconductors for water splitting was recently reported by Zhang *et al.* [4]

Additionally, various tantalates (complex oxides) have been studied as photocatalysts. Since tantalates possess conduction bands consisting of Ta *5d* orbitals located at a more negative position than titanates (Ti *3d*) and niobates (Nb *4d*), they have the electronic structure more prone to redox processes [68, 186]. Therefore, tantalum based complex compounds have also been attracting great attention because of their high photocatalytic properties. It was reported that alkali tantalates showed relatively high activities for photocatalytic water splitting into H_2 and O_2 under UV irradiation [186], and the excess of alkali in the synthetic process of the solid-state reaction even improved the photocatalytic activities of them, following the order: $KTaO_3 < NaTaO_3 < LiTaO_3$ (H_2: 29 < 160 < 430 μmol/h; O_2: 13 < 86 < 220 μmol/h) [189]. Doping (loading) with NiO [190, 191] and nanosized Au particles [192] was reported to have an efficient function as co-catalysts for photocatalytic water splitting. Among them, $NiO/NaTaO_3$ was the most photocatalytically active (synthesized via solid state) and produced H_2 and O_2 from pure water with a quantum yield of 28 % at 270 nm (~2.2 mmol/h of H_2 and ~1.1 mmol/h of O_2) [191]. Contrary to the solid-state reaction method, both the hydrothermal [193, 194] and the sol-gel methods [158] produced $ATaO_3$ (*A* = K, Na) with good crystallinity as well as high surface areas. Thus, using nanocrystalline NTO photocatalytic activity in water splitting as high as >20 mmol/h of H_2 production was provided, being much higher than that in the solid-state produced material [194]. Studies on KTO revealed that small amount of acceptor dopants such as tri- or tetravalent cations was effective for improving the photolysis activity [195, 196]. For instance, $NiO/KTaO_3$ doped with 8 mol% of Zr^{4+} exhibits H_2 formation as high as 122.3 μmol/h, while photocatalytic activity on the well-known photocatalyst Pt/TiO_2 was 106.1 μmol/h [195]. The increased activity was brought by an increase in the lifetime of the photoexcited charge, which in turn was caused by a decrease in the charge density. Additionally, various structures of K-Ta oxides, *e.g.* pyrochlore $K_2Ta_2O_6$ and tetragonal tungsten bronze $K_6Ta_{10.8}O_{30}$ [68], exhibit attractive photocatalytic activity. Thus, H_2 formation is of one magnitude higher in pyrochlore than perovskite KTO [52].

Many more other works have been reported, showing enormous progress over the years. However, the recent developments are still far from large-scale applications, therefore there is a need to continue a study on tantalates. For instance, there is a lack of direct comparison of the selected pollutant degradation efficiency using alkali tantalates and niobates with perovskite-like structures. Therefore, it is worthwhile to conduct systematic investigations in solid-liquid phase.

2.4.2. Tantalates and niobates as biomaterials for bone regeneration

Bone and joint degenerative and inflammatory problems affect millions of people worldwide [197]. Many diseases often require surgery, including total replacement of the natural joint in case of its deterioration. Besides, numerous bone fractures, low back pain, osteoporosis, scoliosis and other musculoskeletal problems need to be solved by using permanent, temporary or biodegradable devices [197, 198]. Therefore, orthopedic biomaterials are meant to be implanted in the human body as constituents of devices that are designed to perform certain biological functions by substituting or repairing different tissues such as bone, cartilage or ligaments and tendons, and even by guiding bone repair when necessary [198].

The orthopedic implant sector forms a significant portion of the worldwide biomedical industry. Orthopedic implants are manufactured devices that have been designed and developed to fulfil particular functions when implanted into the living body, and usually for specific indications [199]. Implants may consist of a single type of biomaterial such as in surgical stainless steel plates, or comprise a number of different biomaterials working together in modular parts, such as in a total hip replacement system which may contain up to 4 or more different materials, *i.e.* titanium, cobalt-chrome alloy, polyethylene and polymethylmethacrylate [5, 199]. Since the human body consists of a highly corrosive environment, very stringent requirements are imposed on the particular properties of candidate materials. Consequently, the first generation of biomaterials consisted of easily available materials of industrial use that were required to be as inert as possible in order to reduce their corrosion and their release of ions and particles after implantation [198]. These materials do not possess any ability to interact with biological environment. Mechanical properties also play a leading role in the selection of the candidate material for the implant

manufacture. The concept of biocompatibility, associated with a set of *in vitro* and *in vivo* standardized tests, was introduced in order to assess the biological behaviour of synthetic materials [198].

Synthetic materials used for bone repair can be divided into: ceramics, polymers, metals and composites where at least two classes of materials are combined together [200]. Ceramics may have a structure that mimics the one of natural bone, and thus were considered attractive materials in this respect [201, 202]. This category of materials includes oxides, phosphates, carbonates, nitrides, carbides, carbons and glasses. Those designed to interact with living tissues are called bioceramics [203]. Research efforts at the end of the past century were devoted to biodegradable and bioactive ceramics, sometimes denoted as second generation bioceramics (bioactive or biodegradable). Biodegradable bioceramics are designed to fulfil specific functions for a given period of time, helping in the self-repair processes of the living organism, and are subsequently resorbed. The critical aspect in the design of these bioceramics is their relatively fast degradation rate, with the loss of their mechanical properties, compared to the slower new bone formation process [204]. The lifetime of the current hip prosthesis is usually 15-20 years before the need for a painful, dangerous, and expensive revision surgery. Therefore, longer lifetime (>20 years) is needed [204]. Bioactive ceramics can react with physiological fluids, but only at a surface level, giving rise to a sequence of surface reactions producing a strong bond between the material and the bone. Well-known bioactive ceramics are hydroxyapatite (HA) and certain compositions of glasses and glass-ceramics. Bioactive and biodegradable ceramics are clinically used as bone fillers, bone cements or for coating metallic implants [200, 203].

Previous biomaterial development has pursued mimicking bone chemical composition and structure [205]. However, since it is known that piezoelectricity, and in particular the piezoelectric nature of collagen, plays a vital role in the development and maintenance of natural bone, it can be considered essential in fracture healing [206-208]. Owing to the piezoelectric nature of bone, the development of piezoelectric material with good biocompatibility can be considered as a promising alternative for orthopedic prosthetic implants [12]. Though promising, not much is known at the moment. Interest is growing in a new generation of biomaterials which seek to influence healing by mimicking the electrical effects in bone, including the creation of a negative or a positive charge at the surface of the

biomaterial. Two methods can be employed to create a surface charge [209]: i) to polarize an ionic biomaterial by application of an electric field at elevated temperature to displace cations and anions in opposite directions (*e.g.* polarization by electric field of hydroxyapatite between two Pt electrodes leading to the ordering of lattice OH^- ions due to the reorientation of protons around O^{2-}), and ii) to develop a piezoelectric biomaterial so that a charge is generated under the application of a mechanical stress (*e.g.* composites containing $BaTiO_3$ in which piezoelectric behaviour originates from electrical dipole of ferroelectric material).

Therefore, such piezoelectric ceramics as $BaTiO_3$ have been studied *in vitro* and *in vivo* and demonstrated to be a potential biomaterial [210-213]. The addition of $BaTiO_3$ as a secondary phase to bioactive HA improves the electrical properties, such as dielectric constant, piezo- and pyroelectric coefficients [214, 215] as well as mechanical properties (such as fracture toughness) [216]. The cell proliferation and growth were also studies in these composites, demonstrating that the application of pulse electric field during the cell culture experiments were enhanced, but within a narrow window of voltage/frequency of electrical stimulation [217]. The cell-material interaction was not fully explored but it was speculated that the electrical signal is expected to activate extracellular signal molecules during field application and then bound to cell surface receptor proteins. The signals can be further transferred via molecular switch mechanisms to intracellular signalling proteins.

Moreover, $BaTiO_3$ has been demonstrated to improve the human osteoblast cell response in terms of increased cell density, viability, and mineralization on poly(vinylidene-trifluoroethylene)-$BaTiO_3$ composites as compared with that on parent polymeric matrix [218]. In view of the potentiality to achieve an improved electrical, mechanical, and biological response due to $BaTiO_3$ addition (Figure 2-22), HA - *x*$BaTiO_3$ composite with different concentrations of $BaTiO_3$ attracted foremost attention as an orthopedic implant in recent years [12]. The surface charges built by polarization have the role of promoting this competitive reaction, especially the Ca^{2+} ion behaviour. The possible reason for enhanced cellular response on negatively poled samples has been explained on the basis of the electrostatic interaction between the charged entities, such as Ca^{2+} (they also attract the proteins). Thus, the key point is to attract firstly Ca ions.

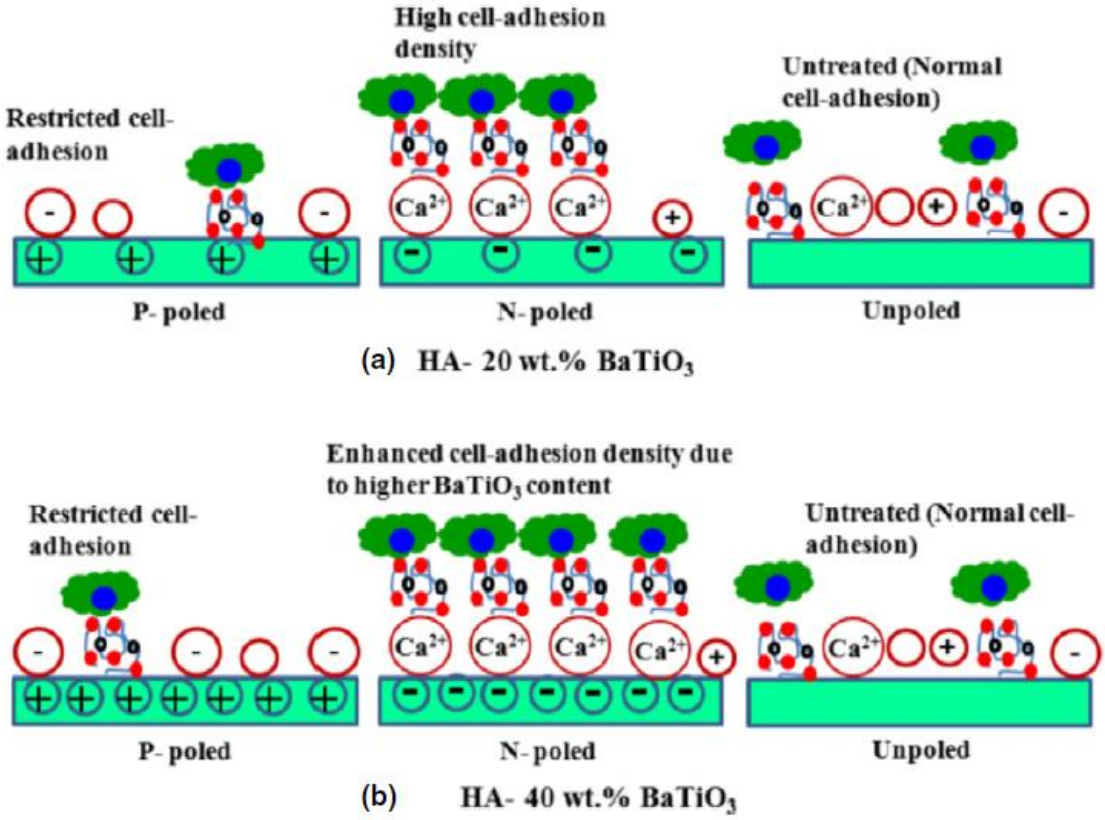

Figure 2-22. Schematic representing the response of poled (P- and N-) and unpoled surfaces toward the cell-material interaction during cell culture experiment [12] The cell-material interaction is improved in N-poled ones in contrast to P-poled and unpoled.

Besides the well-known BTO, alkali tantalate and niobate oxides have been reported to be bioactive and biocompatible as well [11, 13, 219-221]. Among them, (K, Na)NbO_3, $LiTaO_3$ and $LiNbO_3$ piezoelectrics are good candidates as biomaterials for bone repairing. KNN was even patented as material for implants, and toxicology tests showed no presence of any bacterial products [219].

Metallic materials, such as stainless steel, Co–Cr–Mo alloys, and titanium and tantalum alloys, have found extensive application as orthopedic devices, either permanent or temporary. When the orthopedic device has to remain permanently in the body, the bonding between the implant and the living tissue deserves attention, besides that alloys have excellent mechanical properties in load-bearing sites. These metallic alloys have in common a high corrosion resistance in physiological media mainly due to the formation of a passive oxide film that reduces the corrosion rate by blocking the transport of metallic ions and

electrons [222]. Surface characterization of these metallic alloys is quite important, and one of the ways of minimizing corrosion products, which might be released from the implant to the surrounding tissue, consists in applying a protective biocompatible coating that improve the material-tissue interaction [222, 223]. The quality of the newly formed layer can be assessed in terms of mechanical and structural integrity by nanoindentation and small-angle X-ray scattering experiments (X-ray photoelectron spectroscopy (XPS) and wide-angle X- ray scattering (WAXS)). Such study was reported in a hybrid organic–inorganic TEOS–MTES (tetraethylorthosilicate–methyltriethoxysilane) sol-gel-made coating on AISI 316L stainless steel [222].

It was also demonstrated that simple chemical, thermal and mechanical surface treatments of alloys for permanent implants improve their performance [222-226]. Kokubo *et al.* reported that titanium and tantalum metals and their alloys spontaneously bond to living bone if treated in NaOH solution and then heat treated [225]; Na^+ ions via exchange with the H_3O^- ions from the fluid form –OH containing groups on the surface. The formation of bone-like apatite on such material is induced by functional groups, such as Si–OH, Ti–OH, Zr–OH, Nb–OH, Ta–OH, –COOH, and PO_4H_2 because they possess negative charge that then induces apatite formation via formations of an amorphous calcium compound (calcium silicate, calcium titanate, and amorphous calcium phosphate).

An important issue with the synthetic implant materials is their slow osteogenic ability (interaction with tissue in bone growth or repair). To stimulate osseointegration, a number of solutions have been suggested, including surface coatings [227], growth factors [228], surface charges [229], electric field [230], physico-chemical treatments [231]. Owing to the electrical nature of cells and the presence of various ions in the cell culture media/body fluid, external electric field, and surface charge mediated cellular response appears to be appealing. However, the response of cells toward an externally applied electric field depends upon the electric field parameters, *i.e.* field strength, pulse duration, time and sequence of electrical stimulation, etc. [217, 230]. Therefore, a selection of particular conditions is crucial to take full advantage of these phenomena, and ultimately reduce the rejection rate and facilitate osseointegration.

Although most of these materials are biocompatible and/or biodegradable, there is a lack of stimulatory cues for guided bone tissue regeneration. However, if the implant itself is able

to deliver particular chemical and physical functions stimulating faster tissue regeneration and avoiding scarring, some of these limiting issues will be overcome. Consequently the use of electrically active compounds can assist bone remodeling. Among them, piezoelectrics may have a prominent role, thus their uniqueness is worthwhile to explore in the field of regenerative medicine. Within this group alkali-based perovskite oxides (so-called lead-free piezoelectrics) might be proposed as biomaterials with enhanced biological responses due to their superior electromechanical properties.

Chapter 3. EXPERIMENTAL METHODS

3.1. Experimental procedures

A description of the experimental aspects for the processing and characterization of powders and thin films used in this work is presented in this chapter. The basic principles of the used synthesis methods, namely chemical solution deposition, conventional solid state reaction and hydrothermal synthesis are presented. The main characterization techniques utilized in the course of the work are described, with precise conditions used for the samples preparation.

3.1.1. Chemical solution process

The chemical solution deposition (CSD) technique has been successfully applied for the fabrication of electronic oxide thin films, being an effective method in thin films technology. It has been recognized as a low cost methodology with good control of the material stoichiometry, permitting a good uniformity of the obtained film and the tailoring the solution chemistry for continuous coatings [232, 233]. The CSD technique was firstly reported for functional oxides in the end of 1970s in the preparation of perovskite titanate based thin films, $BaTiO_3$ [234]. Since then, it has been widely implemented in the processing of many different dielectric, piezoelectric and ferroelectric oxide compounds.

The CSD contains three major steps: i) preparation of the precursor solution (usually it involves organic chemistry), ii) deposition of the precursor solution onto a substrate (spin or dip-coatings, spraying, among others), and iii) crystallization of the desired phase (normally two-stage thermal treatment: drying and annealing) [233]. The first step that involves the precursor solution preparation, is crucial and can be grouped in three most implemented categories [232, 235, 236]:

- *Sol-gel process*, based on the use of alkoxides as starting reagents and alcohol (methanol, ethanol, 2-methoxyethanol, 1,3-propanediol, etc.) as solvent. The reactions in this process lead to formation of M–O–M bonds (M – metal), through hydrolysis and condensation (water and/or alcohol elimination).
- *Metallo-organic decomposition*, uses water-insensitive metal carboxylate compounds because their reactivity is low and the chemical interactions between the different

precursor compounds is minimal. They do not undergo significant condensation reactions during either solution preparation or film deposition. The basic approach consists of simply dissolving the metallo-organic compounds in a common solvent, and combining the solutions to yield the desired stoichiometry.

- *Chelate process* (sometimes is called also hybrid), characterized by the use of multiple metal-organic precursors (carboxylate and alkoxide) with acetic acid, acetylacetone or amine compounds as modifying ligands. Typically, the acetate, or in general, the carboxylic acid groups, coordinate the metal species in a bidentate fashion, and frequently act as bridging ligands, linking metal centers together to form oligomers or small polymers.

For technological applications, the film deposition onto substrates and its crystallization are particularly important for device designing.

The stock solution is coated on the substrate thus appropriate treatment of the surface of the substrate is critical. It is absolutely necessary to clean the substrate to eliminate the contaminants in order to ensure good adhesion and quality of the film.

The selection of the deposition method depends on many factors and desired applications. Spin-coating requires flat substrates and implies considerable solution loss but it provides good uniformity and excellent thickness control. Dip-coating can be used for coating complex and irregular substrate shapes but easily may origin thickness variations, voids and pin holes and is quite appropriate if one wants both sides of the substrate coated. Spray-coating is fast and highly efficient but rather expensive [235]. And final heat treatment, also referred as structural evolution or phase formation (film formation, densification and crystallization), defines the structure, microstructure, texture, and the most importantly the properties of the coatings [233, 236].

In this work sol-gel and hybrid types of CSD, in which precursor solutions have been tailored, were used for powders synthesis and thin films growth. Two distinct procedures were utilized: i) classical alkoxide route (sol-gel process) as typically reported in the literature for the case of $KTaO_3$ [59, 96, 104, 237], and ii) diol route (hybrid process), properly modified for the synthesis of alkali tantalate solutions ($KTaO_3$, $LiTaO_3$ and $NaTaO_3$). Considering environmental awareness in electroceramics research, hazardous substances have been avoided and the use of organic solvents such benzene, toluene or

2- methoxyethanol was eliminated. These hazardous substances, together with a long list of others, involve health and safety risks in addition to the environmental impact produced by the by-products [238]. Therefore, other compounds with identical functionality but lower toxicity level, *i.e.* carboxylic acids or glycols, were selected and employed. The stages of preparation of thin films via chemical solution deposition are shown in Figure 3-23. As we can see, four steps were involved: i) precursor solution preparation, ii) thin film deposition using spin-coating, iii) drying (pyrolysis; heat-treatment that is used to eliminate volatile species of the reactions in the precursor solution), and iv) annealing (crystallization of oxide layer).

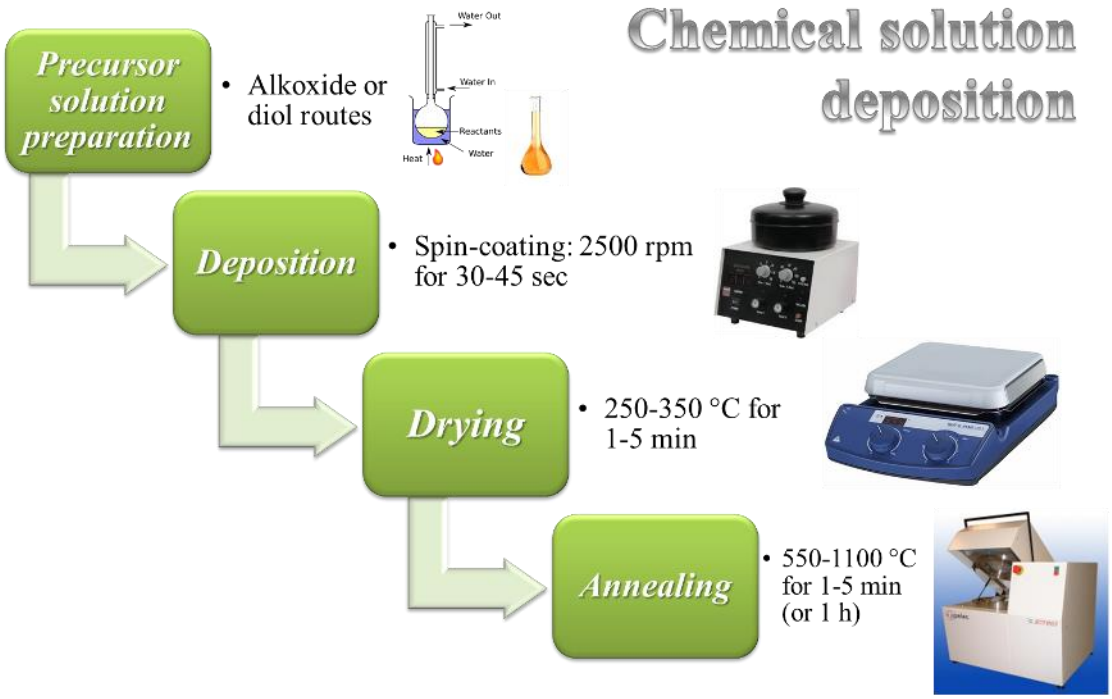

Figure 3-23. Schematic of preparation route of $KTaO_3$, $LiTaO_3$ and $NaTaO_3$ thin films via chemical solution deposition, with four major steps: precursor solution preparation, deposition, drying and annealing. Detailed conditions are included.

3.1.1.1. Precursor solutions preparation via alkoxide route

Purely alkoxide route was initially used. Thus, potassium ethoxide (KOC_2H_5, 95 %, Aldrich – KOEt) and tantalum ethoxide ($Ta(OC_2H_5)_5$, 99 %, ABCR – $Ta(OEt)_5$) were chosen

as starting organic precursors for the synthesis of $KTaO_3$ solution, together with absolute ethanol (HOC_2H_5, 99.9 %, Merck – EtOH) as a solvent. The handling of chemicals and preparation of KTO solution was conducted in a dry argon chamber (glove box), since the used metal alkoxides are very sensitive to moisture. Acetic acid ($C_2H_4O_2$, 99.8 %, Merck – AcOH) or acetylacetone ($C_5H_8O_2$, 99 %, Merck – Hacac) were added to stabilize the solutions towards hydrolysis, acting as chelating agents. In order to compensate the potassium loss due to evaporation during heat treatments, 25–30 % of excess of potassium in KTO solutions with respect to the stoichiometric concentration was used. The scheme of $KTaO_3$ sols preparation is illustrated in Figure 3-24.

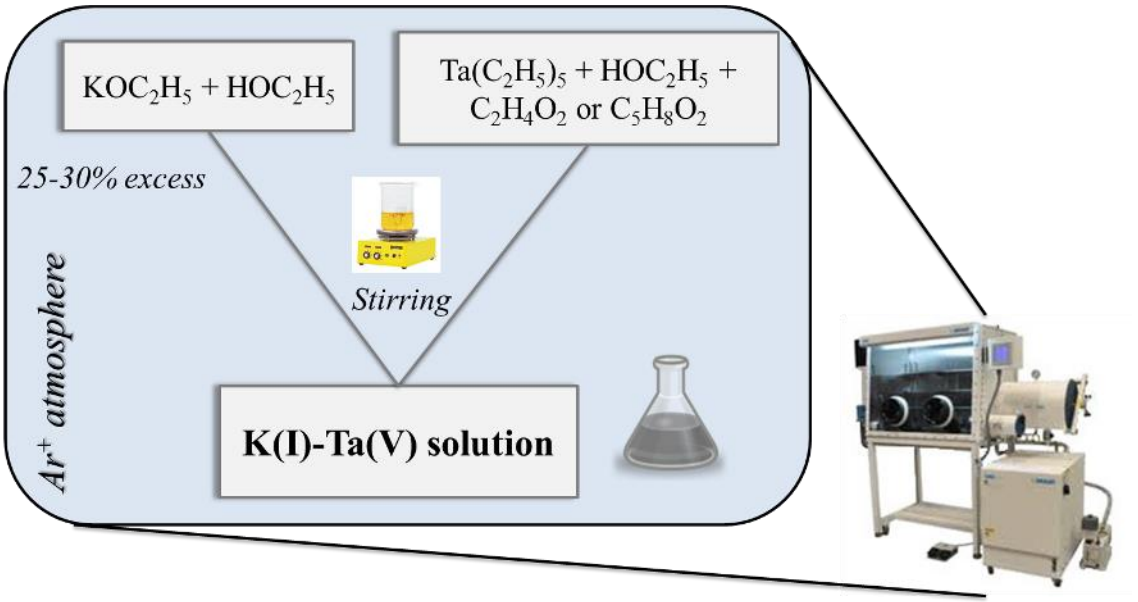

Figure 3-24. $KTaO_3$ precursor solutions preparation via alkoxide route, under controlled atmosphere in a glove box.

Firstly, potassium and tantalum ethoxides were dissolved in absolute ethanol separately by mixing at room temperature under controlled atmosphere; Ta(V) solution was already stabilized by adding chelating agent. Then, individual solutions were joined into one glassware, concentrated to get 0.05–0.2 M stock solutions, and kept mixing for several hours. The stable and partially condensated products were further stirred for 12 h in ambient to form fine solutions.

3.1.1.2. Precursor solutions preparation via diol route

Concerning the diol-based solution strategy for KTO, two different sols were prepared using potassium acetate ($KOOCCH_3$, > 99 %, ChemPur GmbH – KOAc,) and potassium acetylacetonate hemihydrate ($K(CH_3COCHCOCH_3) \cdot ½\ H_2O$, 99.5 %, Multivalent Ltd – K*acac*) as K precursors. Hereafter, the K-Ta solutions with those precursors are denoted as KTO*ac* and KTO*acac*. Figure 3-25 presents the synthesis scheme of the KTO*ac* and KTO*acac* precursor solutions preparation. Firstly, stable potassium precursor sols were synthesized via a diol route. Metal precursors were handled under controlled atmosphere and humidity in a glove box, in order to avoid undesired hydration. Potassium acetate and acetylacetonate were refluxed in the presence of the chelating agent, 1,3-propanediol ($HO(CH_2)_3OH$, 98 %, Aldrich Chemical – 1,3-diol) in a 1:5 molar ratio for 8 h under N_2 atmosphere. Solutions containing a 25 mol % of K(I) excess were prepared, in order to compensate its loss during heat treatment. Ta(V)-glycol sol was synthesized by refluxing tantalum pentaethoxide ($Ta(OEt)_5$, 99.98 %, Aldrich Chemical), and 1,3-diol in a 1:5 molar ratio. Reflux at 110 °C was maintained for 8 h under inert N_2 atmosphere, and then ethanol was removed by distillation. The procedure for preparing air-stable (low moisture sensitive) and non-toxic Ta(V)-glycol was followed by Calzada and Gonzalez procedure [239]. It was proven that other metal compounds, *i.e.* strontium and bismuth 2-ethyl-hexanoates, can be easily soluble with Ta(V)-glycol, resulting in precipitate-free solutions of complex oxide systems.

Potassium acetate (K(I)-sol_{ac}) or potassium acetylacetonate (K(I)-sol_{acac}) solutions were added to Ta(V)-glycol sol at room temperature (according to 1.25:1 molar ratio), to obtain stock and transparent KTO*ac* and KTO*acac*, respectively. Before deposition, solutions were diluted with dry ethanol (EtOH, 99.8 %, Panreac, max. 0.02 % water), to obtain solutions of KTO*ac* or KTO*acac* with suitable concentrations. The drying of KTO*ac* and KTO*acac* solutions at ~150 °C for 24 h led to dark yellow gels.

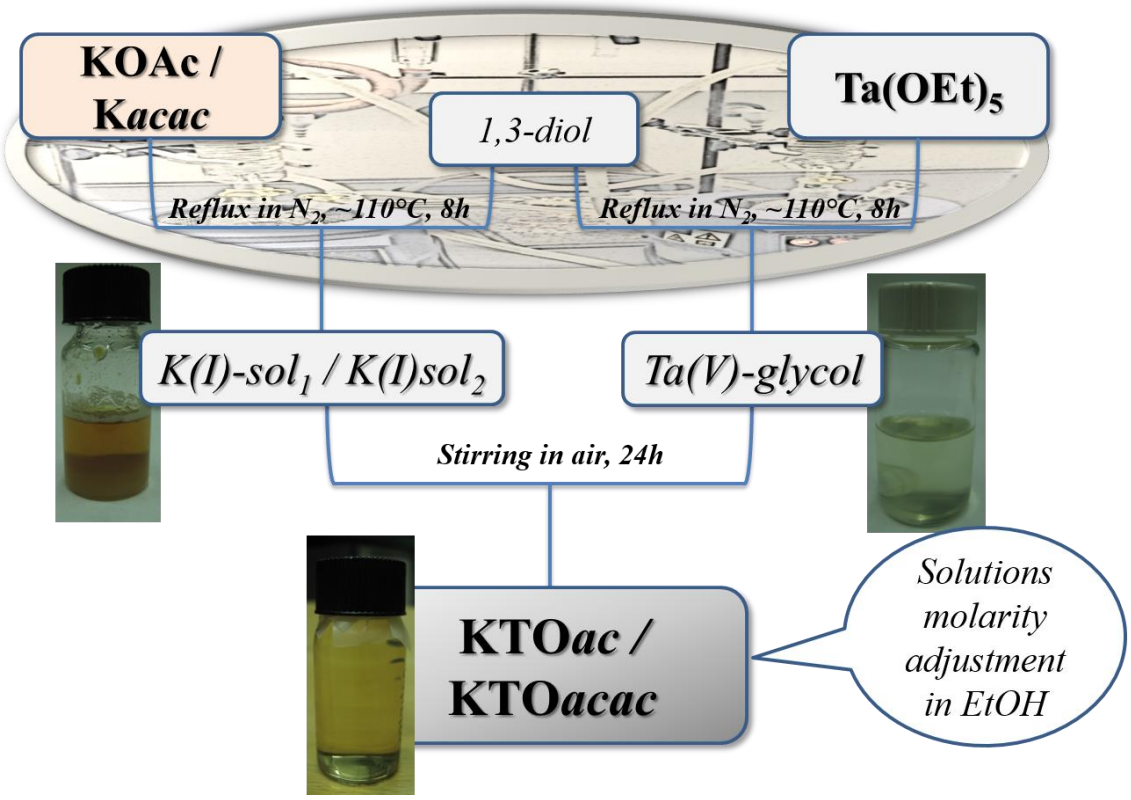

Figure 3-25. Synthesis scheme used for the preparation of the $KTaO_3$ precursor solutions – KTOac and KTOacac, using two distinct potassium precursors – KOAc and Kacac, respectively. Photographs of each solutions are included as well.

In the case of $LiTaO_3$ and $NaTaO_3$, the procedure was similar, and the used reagents for LTO and NTO were lithium ethoxide ($LiOC_2H_5$, 95 %, Aldrich – LiOEt) and sodium acetate anhydrous ($NaOOCCH_3$, 99.9 %, ChemPur GmbH – NaOAc), respectively. Then the further steps were as described in the previous paragraphs, and the only difference was related to the initial molar ratio of the precursor solutions: Li:Ta and Na:Ta were set as 1.

3.1.1.3. Thin films deposition – spin-coating

All films were deposited by spin-coating, according to the scheme presented in Figure 3-26. Two spin coaters were used, the commercial precision KW-4A Spin Coater (Chemat Technology, Inc.) located at DEMaC, University of Aveiro and the films were deposited at 2500-3500 rpm for 30-45 sec and TP 6000 gyrset system (SET-Micro-Controle group

model) located at ICMM-CSIC, Madrid and the films were deposited at 2500 rpm for 45 sec. Then, two different procedures for films drying and crystallization were utilized:

- *Annealing procedure I (AP-I)*: drying on a hot plate at 100 - 150 °C for 2 min, pre-annealing (pyrolysis) in a tubular furnace at 350-400 °C for 8 min, and a final crystallization after certain number of deposition-drying cycles (normally 3-5 cycles) in pre-heated horizontal tubular furnace; the films were directly introduced into the furnace that was set at desired temperature, and then quenched by removing them after 1 h.
- *Annealing procedure II (AP-II)*: drying (and pyrolysis) on a hot plate at 350 °C for 5 min, and crystallization using Rapid Thermal Processing (RTP) (Qualiflow JetFirst 100 and Jetstar 100T); the rapid processing was conducted with an heating rate of ~30 °C/sec, and with a short dwelling time: ~5 min under an oxygen atmosphere (pressure of 1 atm); RTP is regularly used to anneal functional oxides films, promoting films densification and crystallization with reduced thermal-budget and avoiding deleterious reactions with the substrate and between layers.

KTO thin films prepared via KTO*ac* and KTO*acac* procedures were fabricated in a clean room a 100 class clean-room with a laminar flux hood (CAM-1300-V) and a sterile air circulator unit (Telstar FFU), at ICMM-CSIC, Madrid, Spain.

Commercial electroded silicon-based wafers, $Si/SiO_2/TiO_2/Pt$ (Inostek Inc.), were used as substrates, where the preferentially oriented (111) platinum (Pt, ~150 nm) and titanium oxide (TiO_2, ~20 nm) layers were prepared by sputtering; TiO_2 acts as adhesion and barrier layer.

Prior to the film deposition, 10 ×10 mm to 30 × 30 mm substrates were carefully cleaned, using absolute ethanol and acetone (CH_3COCH_3, Panreac) or 2-propanol ($CH_3CHOHCH_3$, Panreac, for analysis), to effectively remove undesired particles and grease to improve the adhesion and to guarantee a high quality of the coatings. The cleaning was carried out in an ultrasonic bath for 5 min in each organic solvent. Additionally, the precursor solutions were filtered through a membrane filter (Millipore), with ~0.2 μm pore size, before being dispended on the substrate.

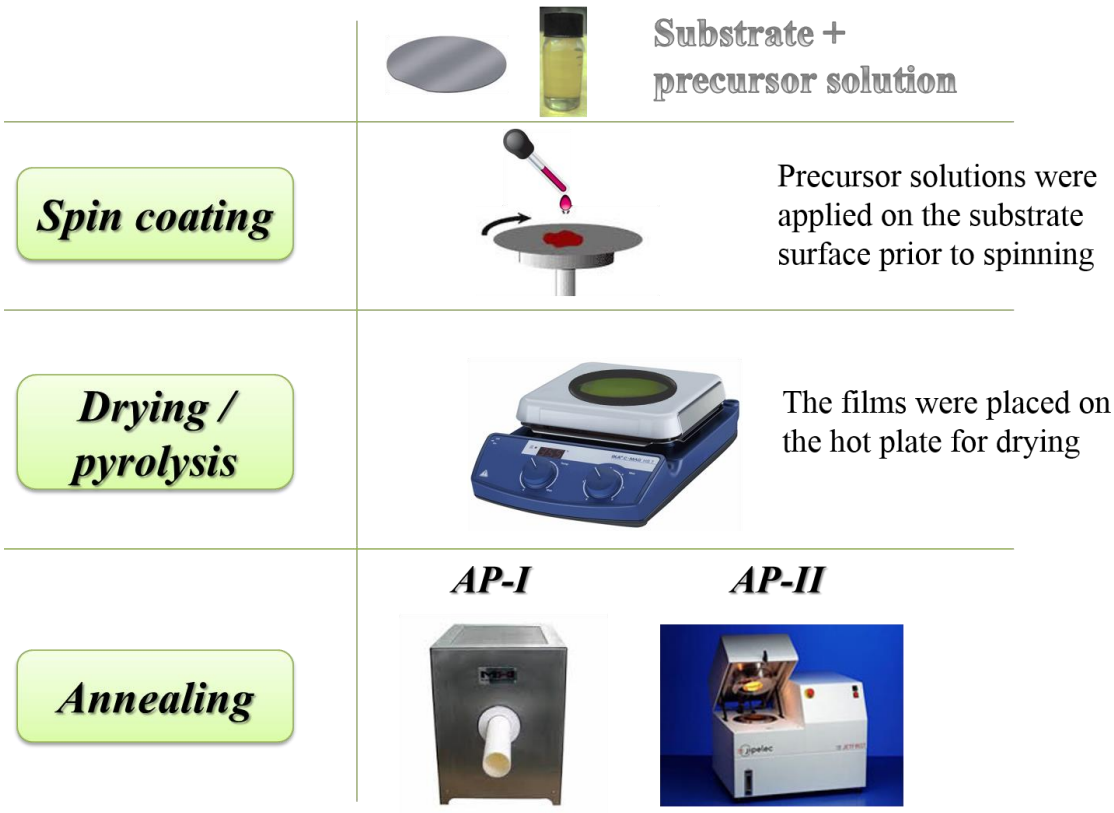

Figure 3-26. Thin films deposition and crystallization via AP-I and AP-II procedures.

3.1.2. Solid state reaction

Conventional solid-state method was employed to prepare potassium tantalum oxide compounds, as described in Figure 3-27. Potassium carbonate (K_2CO_3, Merck, 99 %) and tantalum pentoxide (Ta_2O_5, Sigma-Aldrich, 99 %) were chosen as reagents; K_2CO_3 was dried at ~100 °C for minimum 12 h prior to the use due to its hygroscopic character. The reagents were weighed according to the stoichiometric calculation of the desired composition; additional 3 wt. % of potassium precursor was used for perovskite $KTaO_3$, in order to compensate K losses in subsequent heat treatments. The precursors were then ball milled in ethanol at 180 rpm for 5 h, using Teflon jars with zirconia balls. The mixtures were dried in an oven at 80 °C for about 12 h. The obtained powders were closely packed in alumina crucibles and calcined at various temperatures: 650, 750 and 850 °C, for $KTaO_3$, and 1100 °C for $K_6Ta_{10.8}O_{30}$, for periods of time varying between 2 to 5 h. Distinct calcination atmospheres were selected, as well: air, N_2 and O_2.

Similar processing steps were implemented to synthesize alkali tantalates ($LiTaO_3$ and $NaTaO_3$) and niobates ($KNbO_3$, $LiNbO_3$ and $NaNbO_3$). The sources of the alkali metal were metal carbonates: K_2CO_3, Li_2CO_3 (Merck, 99 %), Na_2CO_3 (Chempur, ≥99.5 %), and the transition metal, oxides: Ta_2O_5 and Nb_2O_5 (Chempur, 99.9 %). Calcination was conducted at 800 °C for 5 h, with heating and cooling rates of 5 °C/min.

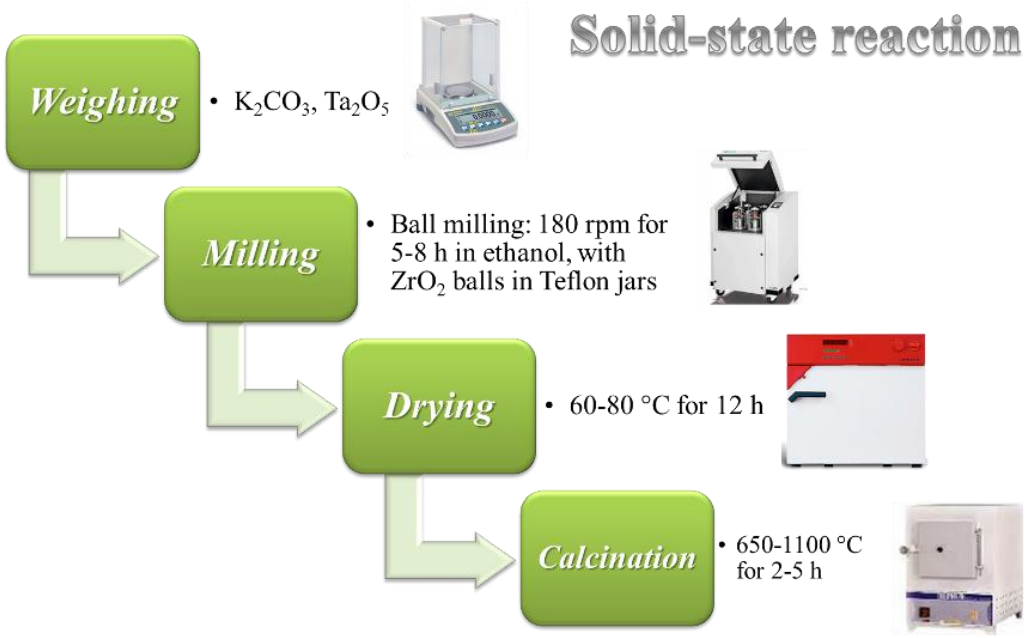

Figure 3-27. Scheme of potassium tantalum oxide powders processing by conventional solid-state reaction, including four major steps: weighing, milling, drying and calcination.

3.1.3. Hydrothermal method

The term hydrothermal usually refers to any heterogeneous reaction taking place in the aqueous solvents or mineralizers with high pressure and temperature assisted conditions. The reaction is normally carried out involving water as a catalyst at elevated temperatures (>100 °C) and pressure (>1 atm) in a closed system (autoclave) [240]. The advantages of the hydrothermal synthesis include the very low synthesis temperatures, the high purity of the products with good homogeneity, the control of the crystal symmetry and the particle size and particle size distribution, the simplicity and the low cost of the process [241].

K-deficient defective pyrochlore $KTa_{2.2}O_6$ was synthesized by hydrothermal method, as depicted in Figure 3-28, according to the report of Goh *et al.* [64]. The following reagents were used: Ta_2O_5 (Sigma-Aldrich, 99 %) and potassium hydroxide (KOH, Sigma-Aldrich, ≥85 %). The synthesis was conducted in a Teflon-lined autoclave in water media. The reagents/H_2O volume filled in ~75 % of the total volume, and KOH concentrations was adjusted as 1–6 M. The autoclave was sealed and kept in the oven at 160–185 °C for 6–24 h. The product of the reaction was filtered and washed with deionized water, and then dried in air at 100 °C.

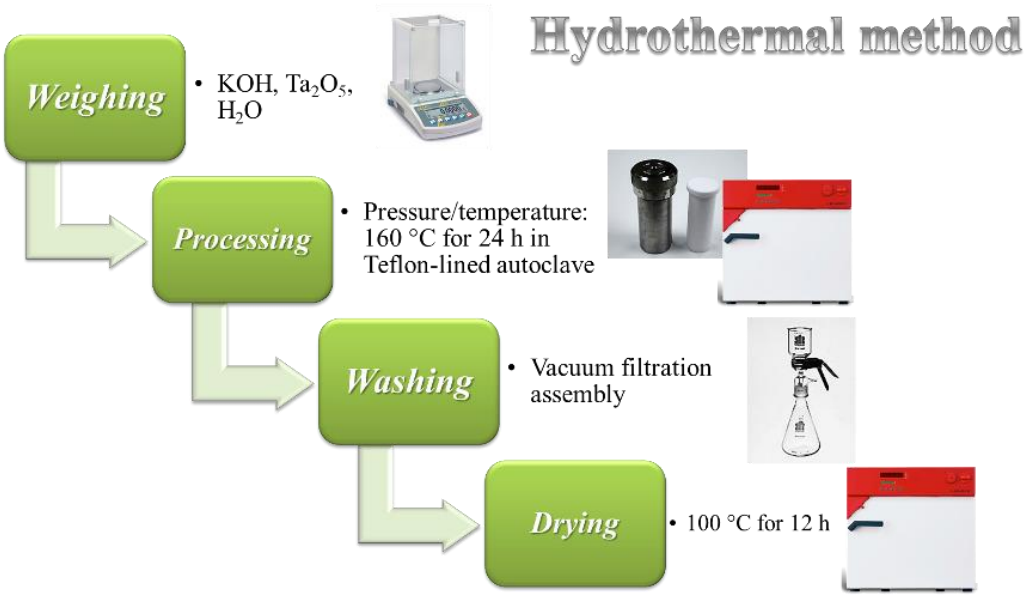

Figure 3-28. Scheme of powders processing by hydrothermal method.

3.2. Characterization techniques

A number of basic and advanced characterization techniques have been used in the thesis, to determine the structural, microstructural, thermal, electrical and surface properties, of the as-prepared structures.

3.2.1. Infrared Spectroscopy

Infrared, IR, spectroscopy is certainly one of the most important type of vibrational spectroscopy. This analytical technique is based on the vibrations of atoms in molecules, being excited by absorption of photons. An infrared spectrum is achieved by using infrared radiation (IR region correspond to the energies of the vibrations and rotations of molecules) that goes through a sample, and reflects a fraction of the incident radiation absorbed at particular energy. An infrared spectrum represents a fingerprint of a sample with a set of peaks that corresponds to the frequencies of vibrations between the bonds in material. Each compound produces different IR spectrum due to their unique combination of atoms [242].

A molecule can only absorb radiation when the incoming infrared radiation is of the same frequency as one of the fundamental modes of vibration of the molecule. Besides, the selection rules for infrared spectroscopy says that for a molecule to show IR absorptions, an electric dipole moment of the molecule has to change during the vibration. Vibrations can involve either a change in bond length (stretching) or bond angle (bending), and besides some bonds can stretch in-phase (symmetrical stretching) or out-of-phase (asymmetric stretching), and bend in-plane or out-of-plane [242, 243].

Reflectance spectroscopy is widely used in opaque powdered samples (mostly in oxides) from which light is reflected and not transmitted. Within this method, internal reflectance measurements can be conducted by using an attenuated total reflectance (ATR) cell in contact with a sample. The phenomena can be described as follows: a beam of radiation entering a crystal (with very high refractive index) undergoes total internal reflection when the angle of incidence at the interface, the sample and crystal, is greater than the critical angle. This technique allows to study both liquid and solid samples [243, 244].

IR spectroscopy provides specific information about chemical bonding and molecular structures of organic as well inorganic materials. Thus, it can assist in identifying unknown materials, determine the quality or consistency of samples or the amounts of components in a mixture [245]. The characteristic absorptions in the spectrum provide information about structural features of the molecules or functional groups, their conformation and local environment [246].

Figure 3-29. Instruments used in FTIR-ATR analysis: Specac's Golden Gate® ATR accessory and Brüker Tensor 27 (DQ, University of Aveiro).

In this thesis, Fourier Transform Infrared, FTIR, spectroscopy, with ATR cell, was used to study chemical bonding and molecular structures of the precursor sols, powders and coatings. It is a fast and a non-destructive technique that does not require external calibration.

FTIR spectrometer with a resolution of 1 cm^{-1}, and in the wavenumber range from 4000 to 300 cm^{-1} using Brüker Optics-Tensor 27 spectrometer operating in ATR mode with Specac's Golden Gate® ATR accessory (high performance single reflection monolithic diamond ATR product), was used (Figure 3-29). The OPUS 5.0 software (Brüker) was programmed to record spectra by adding 128 scans for each spectrum before Fourier transformation.

3.2.2. Thermal analysis

Thermal analysis refers to a variety of measuring methods, which involve a physical or chemical change of the sample on heating. In general, the sample to be analysed is contained

in a suitable crucible, then placed in a furnace and subjected to programmed temperature profile. During this procedure, one or more properties of the sample are monitored. Measurements are normally continuous and the heating rate is linear with time [247]. There are several methods commonly used, and two of them were simultaneously applied in the thesis: thermogravimetric analysis, TG, and differential thermal analysis, DTA.

Thermogravimetric analysis is a technique in which the change in the sample mass is traced as a function of sample temperature using a thermobalance. Mass changes occur when the sample losses or gains weight, producing variations in the TG curve. These changes can be caused by: evaporation of volatile constituents, loss of water, oxidation, thermal decomposition, structural transition, among other phenomena [248].

Differential thermal analysis is a technique in which the variation of the difference in temperature between the sample and a reference material is recorded on heating and/or cooling. Physical and chemical changes in the sample, either endothermic or exothermic, are detected relative to the inert reference. And the positive (endothermic) or negative (exothermic) peaks are reflected in the DTA curve. These changes provide information on transformations as phase transitions, crystallization, melting, sublimation, *etc.* [249].

Figure 3-30. Instrument utilized during DTA/TG analysis, Setaram Labsys DTA TG (DEMaC, University of Aveiro).

TG and DTA were used simultaneously (hereafter referred as DTA/TG) to study the thermal decomposition characteristics of the gel powders.

Setaram Labsys DTA/TG instrument (Figure 3-30) was utilized from room temperature to 1000 °C under distinct atmospheres: air, O_2 and N_2, with a heating rate of 10 or 40 °C/min.

3.2.3. X-ray Diffraction

X-ray diffraction (XRD) is extensively used in materials science, involving the assessment of X-rays scattered from electrons bound to atoms. When an X-ray beam hits an atom, the electrons around the atom start to oscillate with the same frequency as the incoming beam. The atoms in a crystal are arranged in a regular pattern, and in a very few directions there is constructive interference. The waves are in phase leading to well defined X-ray beams that leave the sample at various directions. Hence, a diffracted beam may be described as a beam composed of a large number of scattered rays mutually reinforcing one another [250].

X-rays are electromagnetic waves with much shorter wavelength than visible, ~1 Å, matching well to the interatomic distances in crystals and molecules. Therefore, diffraction effects are observed when x-ray radiation intrudes on periodic structures with geometrical variations on the length scale of the wavelength of the radiation. This technique is effective in determining the crystal structure of materials, identifying chemical compounds from their crystalline structure (but not from their chemical compositions) [251, 252].

X-rays are diffracted by the crystallographic planes of a crystalline solid, and the deflected waves of two crystal planes are in phase when the Bragg's Law relationship is satisfied:

$$n\lambda = 2d_{hkl} \sin \theta_{hkl} \quad (1)$$

where n stands for the number of planes, λ for the wavelength of incident monochromatic X-ray radiation, d_{hkl} for the spacing of parallel planes in the atomic lattice (*hkl* are so-called Miller indices) and θ_{hkl} for the particular Bragg (incident) angle.

The main function of a diffractometer is to detect X-ray diffraction from materials and to record the diffraction intensity as a function of the diffraction angle (2θ). Then, firstly a qualitative analysis is performed by comparing the experimental XRD data with reference patterns in the database provided by The International Centre for Diffraction Data®. This analysis is commonly performed, but other information can be retrieved from this experimental data: peak positions are associated to the lattice parameters and macro-strain, the intensity of the peaks is related to the crystal structure (atomic positions), preferred

orientation and texture, the profile of the peak (shape and full width at half maximum, FWHM) is related to domain size and micro-strain.

In the current work XRD technique was used to study the phase formation, lattice parameter evolution and crystallites size of the prepared materials.

Standard powder XRD analysis for the phase identification was mainly performed using a Rigaku D/Max-C diffractometer (Figure 3-31) with Cu-Kα radiation filtered by Ni. In general, the diffraction patterns were acquired from 10 to 70 ° (2θ) with a step length of 0.02 °. The X-ray patterns where processed afterwards using Jade 8.0 software.

In situ powder XRD, from room temperature to high temperatures (up to 1100 °C), were carried out by a PANalytical X'Pert Pro diffractometer (Figure 3-31), Cu-Kα radiation, 45 kV and 40 mA, with non-ambient XRD attachment (Anton Paar HTK-16N sample stage). The diffraction patterns were acquired from 20 ° to 50 ° (2θ) with a step length of 0.025 °. In the case of thin film analysis, other variant of the technique was implemented, so-called grazing incidence XRD.

Figure 3-31. X-ray diffraction equipments: Rigaku D/Max-C and PANalytical X'Pert Pro (DEMaC, University of Aveiro).

The grazing incidence geometry is surface selective, *i.e.* largely avoids scattering from the substrate. The total external reflection is only from a surface if the incident angle is small enough (typically 0.05–1.5°, depending on the substrate electron density and the X- ray energy). At these conditions the substrate is not entirely invisible to X-rays, but only an evanescent wave penetrates into and scatters from it. The X-ray intensity is therefore

highest at the surface, as desired, and it is possible to increase the surface selectivity further by reducing the incident angle and thus causing the passing wave to damp out faster [253].

The analysis of thin films was performed using PANalytical X'pert Pro instrument, and XRD patterns were recorded using small angle geometry configuration (GI-XRD, an incidence angle, $\omega = 2°$), in order to suppress the substrate contribution.

The presence of a strong texture can be described by the width of the orientation distribution function which can be approximately determined by a rocking curve of the sample with the XRD detector fixed at the corresponding diffraction angle 2θ. The smaller the FWHM of the rocking curve, the better the orientation of the textured sample [254]. The crystallographic texture of seeded KTO films was characterized by means of XRD rocking curves, obtained by tilting the thin film samples through the Bragg angle of the selected plane; in this case (001). The XRD patterns were analysed using HighScore Plus software.

Whole Powder Pattern Modelling, WPPM, is microstructural type of refinement of XRD pattern, analogous to structural refinement proposed by Rietveld [255]. The whole diffraction pattern is directly modelled considering the main microstructural features influencing peak profile: width, shape and position, and as well as taking into account instrumental effects and background. Main parameters are lattice parameters and defect content, expressed in terms of dislocation density, effective outer cut-off radius, dislocation character (edge/screw), contrast factor, twin and deformation fault probabilities, together with mean and variance of a grain size distribution [255]. This procedure allows to extract microstructural information from a diffraction pattern, by refining the model parameters via a non-linear least squares routine. The experimental peaks are fitted without any use of arbitrary analytical functions (*i.e.* Gaussian, Lorentzian, or Voigtian), as the diffraction peak profile is the result of a convolution of instrumental and sample-related physical effects. For that reason, WPPM method was utilized to extract some of the mentioned parameters, using PM2K software [256].

3.2.4. Electron Microscopy

Electron microscopy is a key characterization technique in many fields of materials science, generating images of material microstructures with very high magnification and resolution using accelerated electrons. The high resolution of electron microscopes is

achieved due to short wavelengths of the electrons, being ~10,000 times shorter than that of visible light. The resolution of electron microscopes reaches the order of 0.1 nm, making electron microscopes extremely useful for revealing ultrafine details of materials microstructure [257-259].

Scanning electron microscopy (SEM) is the most widely used type of electron microscope. SEM examines microscopic structures by scanning the surface of the materials, and an image is formed by a focused electron beam that scans over the surface area of a specimen. SEM is able to present the 3D appearance of the images because of its large depth of field [260, 261]. Besides diffraction and imaging, the high-energy electrons cause excitations of the atoms in the specimen giving chemical information. One of the analytical electron microscopy type of spectroscopy is energy-dispersive X-ray spectrometry (EDS). Characteristic X-rays from the chemical elements are used to determine the concentration of the different elements in the specimen, extracting quantitative data [258].

Figure 3-32. SEM microscopes: Hitachi S4100 and SU-70 (DEMaC, University of Aveiro).

Therefore, SEM equipped with an EDS detector is a powerful microscopic tool to study the microstructural features, surfaces and interfaces in multilayered structures, and giving insights on the chemical homogeneity of the specimens.

Hitachi S-4100 and Hitachi SU-70 SEM/EDS microscopes (Figure 3-32) were used to study the materials prepared in this thesis. The samples, either powders or bulk (top-view and cross-sections in case of thin films), were placed on the Al sample holder and then covered with a thin layer of carbon in order to make them conductive. This procedure was conducted using an Emitech K950 instrument.

3.2.5. Scanning Probe Microscopy

Scanning probe microscopy (SPM) is a technique to examine materials with a solid probe that scans the surfaces. SPM is a relatively new method for materials characterization, comparing with optical and electron microscopy, but currently considered as a powerful tool for surface structure studies. It examines surface features whose dimensions range from atomic spacing to a tenth of a millimetre. This technique is rather different from other microscopes because it does not create an image by focusing light or electrons, but it physically detects the surface of the samples with a sharp probe developing a map of the height of the specimen surface [261].

Atomic force microscope (AFM), also referred as the scanning force microscope (SFM), is a part of a larger family of instruments within the scanning probe microscopes. The main parts of the AFM control system are i) a high-precision positioning actuator, usually of piezoelectric construction; ii) sophisticated control electronics, and iii) a highly sensitive position detection scheme, typically optical (Figure 3-33 *(a)*) [262]. In AFM the probe is a tip mounted on a cantilever spring, which interacts directly with the surface, probing the repulsive and attractive forces, which exist between the probe and the sample surface (Figure 3-33 *(b)*) [263]. It allows to produce a high resolution 3D topographic image of the surface. The sample surface profiles are acquired in the vertical and lateral directions, and their resolution can be even better than 0.1 nm. The system is usually composed of a probe and its motion sensor, scanner, electric controller, computer, and it has to be installed in the vibration-free environment to avoid external interferences. Imaging in an AFM can be performed through various operational modes and the most common are: contact, tapping and non-contact [264].

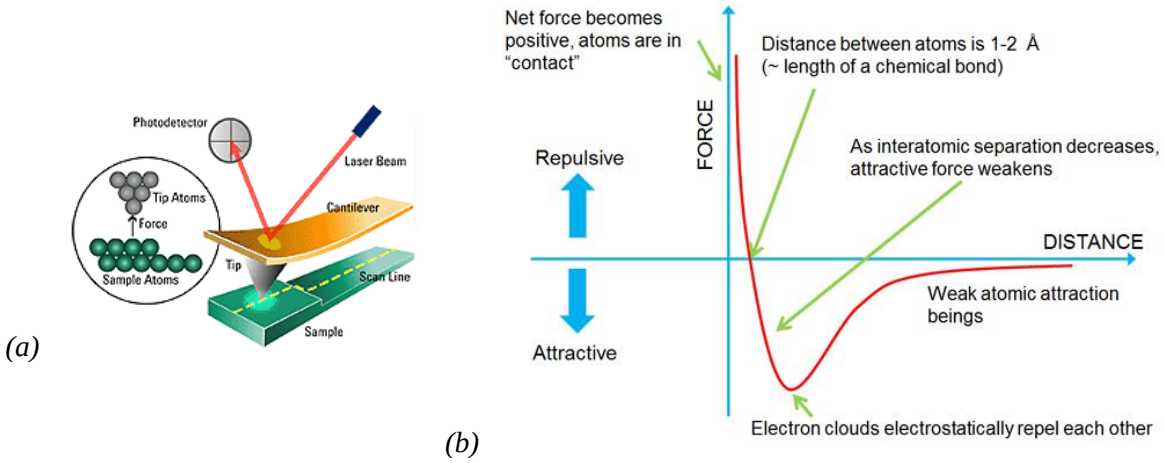

Figure 3-33. (a) Schematic presenting the AFM system [262], and (b) the interactions that occur between the probe and sample at the molecular level [263].

Piezoresponse force microscopy (PFM) is a SPM technique based on the detection of the mechanical response of a material to an applied electrical voltage through a conductive tip. For such electrical stimulus, the material locally expands or contracts. This technique has been developed to probe electromechanical coupling, important functionality of many materials, *e.g.* inorganic macro-molecular (piezoelectrics and ferroelectrics) and biological systems. PFM can be utilized to study domains, phase transitions, size effects, nucleation dynamics, *etc.* [265]. When the tip is in contact with the surface and the local piezoelectric response is detected as the first harmonic component of the tip deflection, the phase φ, of the electromechanical response of the surface yields information on the polarization direction below the tip. Detection of the lateral components of tip vibrations provides information on the in-plane surface displacement, known as lateral PFM. Provided that the vertical and lateral PFM signals are properly calibrated, the complete electromechanical response vector can be determined.

Atomic Force Microscopy with additional PFM mode was used to study the microstructure, topography and electrical response at a local scale of the films prepared in this thesis.

VEECO Multimode SPM Nanoscope IIIA was used (Figure 3-34), allowing morphology observations and piezoresponse characterization. Images were acquired using various probes: Al coated silicon tips (Nanosensors PPP-NCHR: C_C ~ 42 N/m, f_0 ~ 330 kHz), Ti/Pt coated Si tips (Micromash CSC37: C_C ~ 0.3 N/m, f_0 ~ 21 kHz) or Pt/Ir coated Si tips (Nanoworld EFM-20: C_C ~ 3 N/m, f_0 ~ 75 kHz).

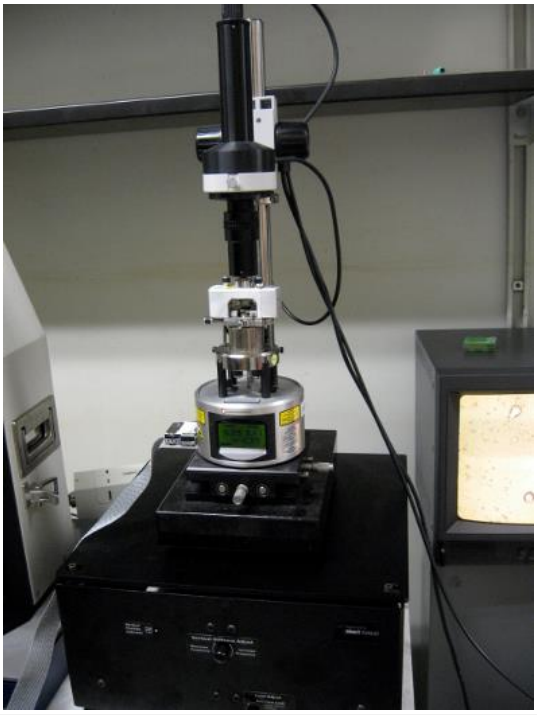

Figure 3-34. SPM setup, VEECO Multimode SPM Nanoscope IIAA (DEMaC, University of Aveiro).

It is important to remark that the PFM measurement procedure requires mechanical contact between the tip and the investigated material, thus the analysis was performed in contact mode. The vertical PFM was obtained when the mechanical oscillations were induced by AC voltage at 50 kHz to the tip. The lateral PFM measurements were conducted with the AC voltage at 5 kHz and 0 degree scan angle of the tip. In vertical PFM imaging, out-of-plane polarization is measured by recording the tip-deflection signal at the frequency of modulation. Lateral PFM is a technique where the in-plane component of polarization is detected as lateral motion of the cantilever due to bias-induced surface shearing [265].

The WSxM Scanning Probe Microscopy software was used to process the data from AFM and PFM analyses [266]. Using AFM, the roughness analysis of films surface was also carried out and the root mean square roughness, R_{RMS}, quantified by:

$$R_{RMS} = \sqrt{\frac{1}{N}\sum_{i=1}^{N} Z_i^2} \qquad (2)$$

where, N stands for the number of intervals (normally used was 100) and Z for height (in nm).

3.2.6. Electrical measurements

Every material has a distinctive set of electrical characteristics that are dependent on its structure, microstructure, defect structure, shape and processing, and accurate measurements of these properties provide valuable information for its application. Dielectrics are insulators and are characterized by a dielectric constant. It means that they have the ability to store energy when an external electric field is applied [267, 268].

Materials dielectric response measurements provide critical design parameter information for many electronics applications. For example, the dielectric losses of a cable insulator, the impedance of a substrate, or the frequency of a dielectric resonator can all be related to its dielectric properties [19].

The electrical response of dielectric materials are usually measured in a parallel plate capacitor configuration, where a dielectric is placed between two conductive plates that act as electrodes. Then, the capacitance is measured, being a parameter that reflects the ability of a material to store electrical charge. The capacitance of the dielectric material is related to dielectric constant. If an AC sinusoidal voltage source V is placed across the same capacitor, the resulting current I is a sum of a charging current I_C and a loss current I_R that is related to the dielectric constant [267].

$$I = I_C + I_R = \frac{i\omega\varepsilon^* V\varepsilon_0 S}{d_s} \tag{3}$$

where i is the imaginary operator, $\omega = 2\pi f$ is the angular frequency, ε_0 is the dielectric constant of the vacuum with the value 8.85×10^{-12} F/m, S is the area of the electrodes for a sample capacitor, d_s is the distance between electrodes (normally sample thickness), ε^* is the complex dielectric constant (permittivity).

The complex dielectric constant consists of a real part ε_r' which represents the storage and an imaginary part ε_r'' which represents the loss. The real part of the permittivity is a measure of how much energy from an external electric field is stored in a material, while the imaginary part is called the loss factor and is a measure of how dissipative a material is to an external electric field. The loss factor includes the effects of both dielectric loss and conductivity [267].

Capacitance-voltage (C–V) measurements are small signal measurements where a small AC field, *e.g.* 0.1 V, superimposed with a DC field is applied. The oscillating voltage is used to measure the capacitance and then plotted as a function of the DC bias. Generally, permittivity is calculated from capacitance, electric field *E* is calculated using thickness, and the permittivity data are plotted as a function of the applied DC field. Therefore, the type of dielectric material is recognized, either ferroelectric, paraelectric or antiferroelectric, as demonstrated in Figure 3-35. These measurements for ferroelectric materials are usually made with two sweeps, *i.e.* one from negative to positive bias and the other from positive to negative to show the hysteresis (butterfly-like loop). In the paraelectric state, the material does not exhibit any hysteresis, thus, the measurements can be made with a single sweep and the highest permittivity is observed at low fields. The C–V curve of the antiferroelectric displays a double peak butterfly type characteristics [269, 270]. The integration of C–V curve of FE leads to the reversible fraction of the FE polarization. While the amplitude of the capacitance shown by the C–V curve increases with decreasing (small signal) voltage excitation frequencies, the amplitude of the polarization shown by the P–V curve (not shown here) decreases for decreasing (large signal) voltage excitation frequencies. The peak of the C–V curve (correspond to the coercive voltage of the static hysteresis curve) occurs when the net polarization is zero and the maximum amount of domain walls is present. This increase of the capacitance is due to the reversible domain wall contribution to the permittivity. The C–V behaviour of PE (non-linear dielectric) is in contrast to FE materials, there are no irreversible contributions to the polarization [269]. The C–V curve of AFE displays in total four peaks: as the electric-field increasing from 0 to maximum values, dielectric constant of AFEs increases firstly, and reaches the first peak value and then decreases gradually (the phase switching from AFE to FE state is finished); similarly, as electric-field is decreased from maximum values to 0, dielectric constant also increases firstly and then declines and a second peak value is obtained in this course (which denotes the phase transformation from FE to AFE state) [270].

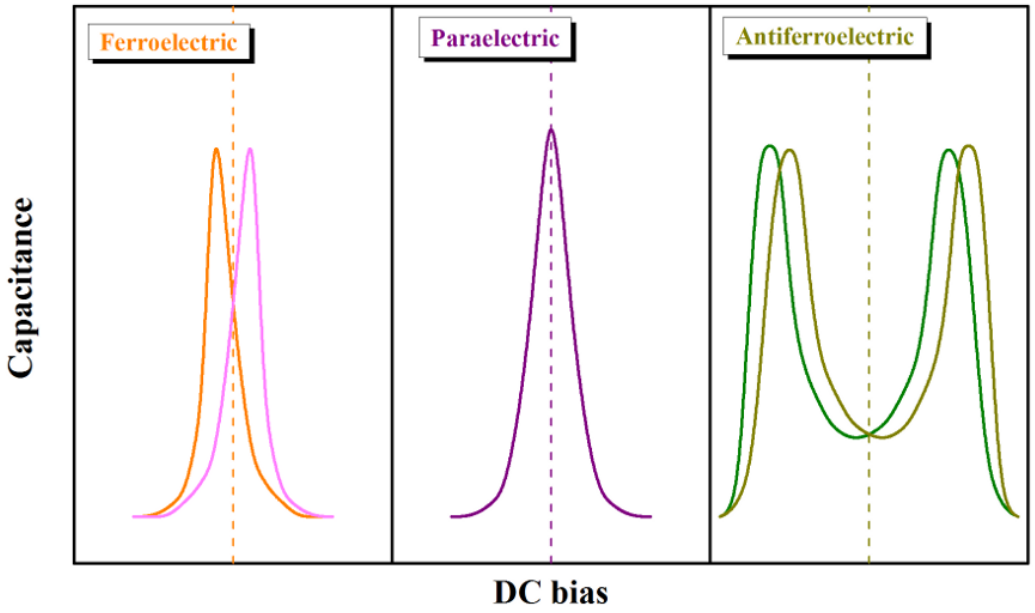

Figure 3-35. Capacitance versus DC bias for a ferroelectric, paraelectric and antiferroelectric material.

The dielectric and ferroelectric response in metal-insulator-metal (MIM) parallel capacitor configuration of thin films were conducted. The dual impedance parameter Z–θ was measured by Precision LCR Meter (Agilent E4980A) under an applied weak field of 0.1 V at 21 frequency points in the range from 100 Hz to 1 MHz with further recalculation to:

$$\varepsilon' = \frac{d_s \sin\theta}{\omega Z \varepsilon_0 S} \quad \text{and} \quad \tan\delta = \tan(90° - \theta) \tag{4}$$

Capacitance variations as function of DC voltage, referred as C–V measurements, were used to study the electrical behaviour of the $LiTaO_3$ and $NaTaO_3$ thin films under the DC applied voltages. C–V measurements of the thin films were performed using an AC signal at 10 kHz with a DC bias sweep from -20 V to +20 V using Precision LCR Meter (Agilent E4980A) controlled by a home-made software. The instrument's internal bias voltage was used to generate a DC field in the samples, while the capacitance was measured with the oscillator level set at 100 mV.

Circular Au top electrodes were sputtered using a SEM coating unit (E5000, Polaron Equipment Limit) with an argon partial pressure of 2 mTorr, an acceleration voltage of 12 kV and an emission current of 12 mA. To improve the quality of interface between the

metal electrodes and the samples, the samples with the sputtered electrodes were annealed at 200 °C for 30 min.

3.2.7. Other methods

Other characterization techniques were utilized in the thesis as well, however in a less extend. Therefore, only experimental conditions used for this work are presented.

3.2.7.1. Particle size analysis

The particle sizes and their distribution were determined by a laser particle size device (LS230 Beckman Coulter, Inc.). The measurements were collected in the range from 0.04 to 2000 μm. The surface area of the particles, SA_{BET} ($m^2 \cdot g^{-1}$) was evaluated by the Brunauer-Emmett-Teller (BET) method in which N_2 acted as adsorbate gas (Micromeritics Gemini 2375 equipment). Prior to the measurements, the samples were degassed at ~200 °C for 12 h.

More details about these methods can be found elsewhere [271, 272].

3.2.7.2. UV-vis measurements

UV-vis spectra of solid and liquid samples were acquired using a Shimadzu UV 3100 spectrometer, covering a wavelength range between 220 and 850 nm (0.2 nm step size). In the case of solid samples, $BaSO_4$ was used as reference. Then, the value of the band-gap was calculated from the spectra using the differential reflectance method: the first derivative of the reflectance $dR/d\lambda$ was plotted as a function of the wavelength λ, and this curve was fitted with a Gaussian function. The maximum of the plot determined from the fitting corresponds to the band-gap value. For liquids the sample was held in an optically flat, transparent container (cuvette). The reference cuvette contained the solvent in which the sample was dissolved and this is commonly referred to as the blank. Principles of UV-vis spectroscopy can be found in the textbook of Perkampus [273].

3.2.7.3. Optical profilometry

It is a non-contact interferometric-based method for characterization of surface topography. In this thesis, the 3D Optical Profiler (Sensofar PLu Neox, Sensofar Tech, Spain) was used to evaluate the surface roughness of LTO coatings. The confocal technique with 460 nm light was used, and with a 100X-N EPI objective. The output is a high resolution 3D profile of the surface, with an area of 175 × 132 μm and an image size of 1360 × 576 pixels. The RMS surface roughness, R_{RMS}, was calculated, as a root mean square average of the profile height deviations from the mean line. A comprehensive information about optical measurements of surface topography can be found in the book edited by Leach [274].

3.2.7.4. Contact angle measurements

The static contact angles, θ, of sessile drops of liquid (water) on LTO coatings were measured using a face contact angle set-up equipped with a camera (Contact angle meter SL200B, Kino Industry Co., USA). The procedure includes dosing and transferring a drop of the selected liquid (water in this case) to the surface of the solid, capturing the drop image, and fitting the drop profile by selecting curve equation. More details can be found in Kino User Manual [275]. A 2 μL droplet of distilled water was suspended from the tip of the microliter syringe, and then the sample stage was advanced toward the syringe tip until the droplets made contact with the coating surface. A contact angle was calculated based on the drop shape method (with the CAST®3.0 software) by drawing the drop profile of the captured drop image and fitting a Young-Laplace equation of capillarity. The surface wettability and surface energy were investigated.

3.2.7.5. X-ray Photoelectron Spectroscopy

X-ray Photoelectron Spectroscopic (XPS) analyses were performed on LTO films after functionalization, in order to study the surface functional groups. The experiments were carried out in an Ultra High Vacuum (UHV) chamber with a base pressure of 2×10^{-10} mbar. The system was equipped with a monochromatic AlKα (1486.74 eV) X-ray source, a hemispherical electron energy analyzer (SPECS Phoibos 150) and a delay-line detector.

High resolution spectra were recorded at normal emission take-off angle with a pass-energy of 20 eV, which provides an overall instrumental peak broadening of 0.5 eV. The resulting XPS spectra were calibrated in binding energy by referencing to the C *1s* peak from C–C at 285.0 eV. The XPS spectra were deconvoluted in Lorentzian-Gaussian curve components after removing a Shirley background. An introduction to principles of XPS is well-described elsewhere [276].

3.2.7.6. Electron Probe Microanalysis

The compositions of the synthesized samples (defect pyrochlore of potassium tantalum oxide, and alkali tantalate and niobate perovskites) were measured using wavelength dispersive electron probe microanalysis (EPMA) with a Cameca SX100 (Gennevilliers, France) instrument operated at an accelerating voltage of 15 kV, a beam current of 20 nA, and a beam size of 1 μm. Prior to the analysis, the samples were pelletized, annealed at distinct temperatures and duration (depending on composition) and carbon coated. Appropriate standards were used for elemental content measurements, and compositions were calculated from ~10 data points per sample. The analysis was carried out at the University of California, Davis (The Electron Microprobe Laboratory). More information can be found in the textbook by Mittemeijer [277].

3.2.7.7. Raman Spectroscopy

The Raman analysis was performed, in LTO films to determine their structural characteristics after incubation in SBF, using a HORIBA Jobin-Yvon Lab Raman spectrometer. Spectra were obtained with a 632.8 nm emission line of He-Ne laser (20 mW), giving a monochromatic red light. The Raman studies were carried out in the 150–1500 cm^{-1} frequency range, with the samples placed in a micro-Raman set-up. A basic theory of Raman spectroscopy is introduced by Ferraro *et al.* [278].

3.2.7.8. Inductively Coupled Plasma Spectroscopy

Inductively coupled plasma spectroscopy (ICP) was used to determine the ions concentration in Simulated Body Fluid (SBF) solutions, namely Ca, P and Li. The residual

SBF liquid from each immersed sample (preserved at ~5 °C) was characterized by ICP-MS using a Jobin-Yvon JY70 Plus (France), at the Central Analysis Laboratory (LCA) of the University of Aveiro. The ICP analysis was also conducted in LTO and LNO powders. 1.5 to 2.0 mg of each sample was dissolved in 40 mL of a mixture of 3 % HNO_3 (prepared from concentrated nitric acid, 70 %, EMD Chemicals by dilution using 18.2 mohm water) + 10 ml of 2 % HF (prepared from concentrated hydrofluoric acid, EM Science 48 % by dilution using 18.2 mohm water. The analyses were performed using an Agilent 7500CE ICP-MS, at the University of California, Davis.

Fundamental principles of ICP are presented elsewhere [279].

Chapter 4. RESULTS AND DISCUSSION

4.1. Thermodynamic stability of alkali tantalate and niobate perovskites

Abstract

Lead-free alkali niobates and tantalates currently form one of the most promising groups of ferroelectrics, piezoelectrics and related materials. In view of their importance, the enthalpies of formation for a set of alkali tantalates and niobates with perovskite-like structures, including $LiTaO_3$, $LiNbO_3$, $NaTaO_3$, $NaNbO_3$ and $KNbO_3$, from binary oxide components are measured by high temperature oxide melt solution calorimetry. The surface energies of nanocrystalline perovskites of these alkali tantalates and niobates were also experimentally determined for the first time by calorimetry. The stability of the lead-free perovskites of I–V type is discussed in terms of their tolerance factor and acid-base chemistry. The formation enthalpy becomes more exothermic (implying higher thermodynamic stability) and the surface energy increases (indicating greater destabilization for a given particle size) with the increase in the ionic radius of the A-site cations (Li, Na and K) and with increase in the tolerance factor. These correlations provide key insights into how lead-free niobates and tantalates behave during processing.

Due to recent demands for environmental friendly components and continuous developments of functional materials for current and future technologies, perovskite oxides are highly attractive compounds because of their remarkable properties important for various technological applications, as mentioned before. Ecologically driven needs for less toxic materials lead to the search for alternatives to lead-based systems, the family of alkali based perovskite tantalates and niobates being potentially strategic candidates (see Chapter 2 – State of the Art).

The group of perovskite materials with general formula *A*(Ta or Nb)O_3 (where *A* stands for alkali metal), *i.e.* tantalates, $NaTaO_3$, $LiTaO_3$ and $KTaO_3$, and niobates, $NaNbO_3$, $LiNbO_3$ and $KNbO_3$, is considered in a number of applications.

As described already in the state of the art, it is well known that processing single crystal and polycrystalline alkali tantalates and niobates is not a trivial task and some difficulties accompany the syntheses. The two most relevant problems are the moisture sensitivity of alkali precursors [171, 172, 280] and the considerable losses in alkali element content during synthesis at high temperature (due to their high vapour pressures) [172, 281, 282], which lead to compositional fluctuations. In addition, material stability (mechanical, thermal or chemical) is always a key aspect to ensure the durability of the device in which it is used [283].

Considering that the chemical and thermal stabilities of materials are strongly related to the formation energy of the compound [284-287], it is then crucial to know their thermodynamic properties to better control the processing parameters and, ultimately, the functional properties. However, there are only few data on enthalpy of formation on selected compounds ($LiNbO_3$ and $NaNbO_3$) within the group of alkali tantalates and niobates [288-291]. Moreover, there is a recent scientific interest in nanoparticles with perovskite-type structure due to the appearance of novel phenomena at the nanoscale. An example is absence of ferroelectricity in nanocrystalline $BaTiO_3$ [292]. Therefore, there is a need of investigation of surfaces and interfaces. Progress in calorimetry technique and developments in metrology over the past two decades have provided opportunity to collect extensive thermodynamic data on various systems [293-295]. High-temperature oxide melt solution calorimetry has been successfully demonstrated to measure the surface energies of an array of binary and ternary oxides directly [296-298] but not yet for alkali tantalate and niobate perovskites.

In this work we conducted a systematic study of the formation and surface enthalpies of $LiNbO_3$, $LiTaO_3$, $NaNbO_3$, $NaTaO_3$ and $KNbO_3$, while in the case of $KTaO_3$ only the enthalpy of formation was determined. These studies were carried out in collaboration with the group of Professor Alexandra Navrotsky from the University of California at Davis. The results are discussed in terms of the effect of different alkali metals on the A-site of the perovskites. The powders were synthesized by the mixed oxide method, and calcined at

relatively low temperature to ensure the synthesis of nanocrystalline powders. Enthalpies of the hydrated surfaces were determined using calorimetric measurements. These experimentally obtained data support discussion of surface processing phenomena, giving insights on nucleation, phase stability, sintering behaviour and mass transport.

4.1.1. Phase composition, structural and microstructural characterization

The as-synthesized set of alkali tantalate and niobate powders were analysed by XRD in the 2θ range of 20–70° (Figure 4-36), and in all cases monophasic patterns were detected within a detection limit of an equipment; XRD pattern of $KTaO_3$ (KTO*per-1*) is depicted later in the thesis when discussing phase formation in potassium tantalate. XRD patterns match the following JCPDS-PDF files: rhombohedral $LiTaO_3$ to 01-087-2461 (SG (space group): *R3c*), rhombohedral $LiNbO_3$ to 04-009-3436 (SG: *R3c*), orthorhombic $NaTaO_3$ to 04-010-2738 (SG: *Pnma*), orthorhombic $NaNbO_3$ to 04-014-2322 (SG: *Pbcm*) and orthorhombic $KNbO_3$ to 04-007-9572 (SG: *Bmm2*). The refined average crystallite size (diameter), $\langle D \rangle$, is 100.7, 103.1, 47.4, 63.9 and 72.5 nm for $LiTaO_3$, $LiNbO_3$, $NaTaO_3$, $NaNbO_3$ and $KNbO_3$, respectively (Table 4-4).

The chemical analyses were carried out to examine the compositions. The elemental composition of the Li-containing samples was analysed by ICP. According to ICP-MS $LiTaO_3$ and $LiNbO_3$ have compositions $Li_{1.002\pm0.004}Ta_{0.998\pm0.004}O_3$ and $Li_{1.003\pm0.006}Nb_{0.997\pm0.004}O_3$, whereas $NaTaO_3$, $NaNbO_3$ and $KNbO_3$ as determined by microprobe (EPMA), are $Na_{0.999\pm0.006}Ta_{1.001\pm0.007}O_{3\pm0.002}$, $Na_{0.998\pm0.009}Nb_{1.002\pm0.009}O_{3\pm0.008}$ and $K_{0.998\pm0.003}Nb_{1.002\pm0.003}O_{3\pm0.009}$, respectively. Within the experimental errors the prepared compounds are stoichiometric, thus they are used later in the thermodynamic calculations.

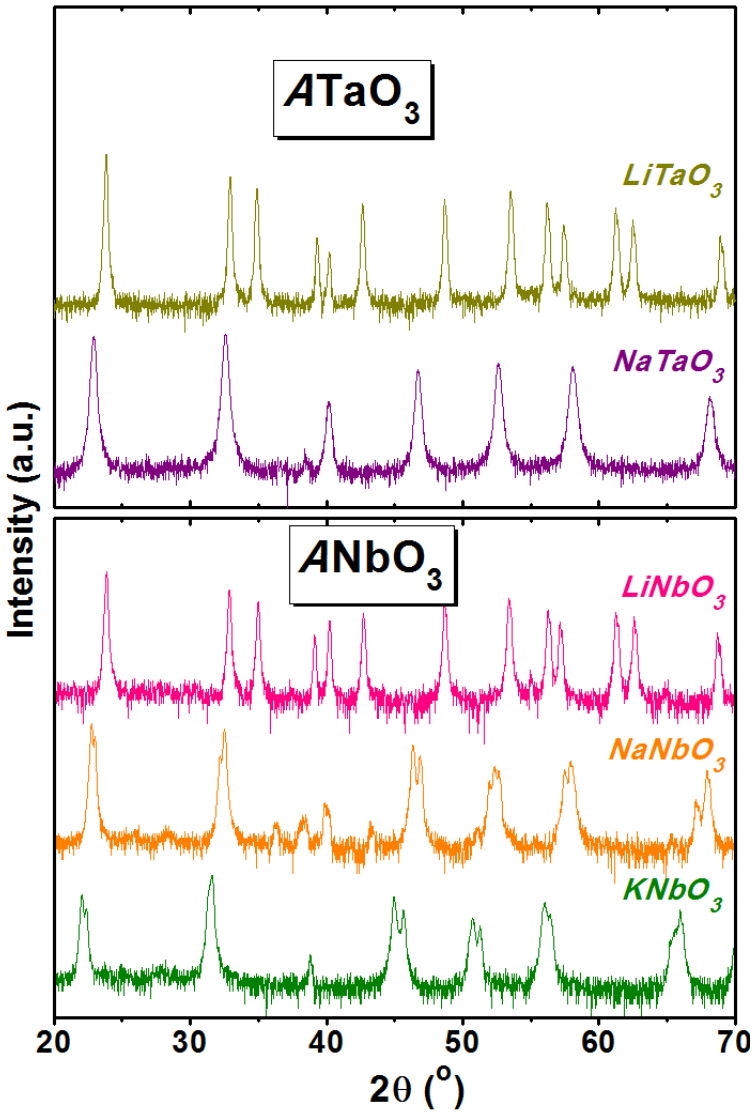

Figure 4-36. The XRD patterns of the alkali tantalates: $LiTaO_3$ and $NaTaO_3$, and niobates: $LiNbO_3$, $NaNbO_3$ and $KNbO_3$, with perovskite-like structures synthesized via conventional solid-state reaction. In all cases the samples were detected to be monophasic, matching to the following JCPDS-PDF files: rhombohedral $LiTaO_3$ to 01-087-2461 (SG: R3c), rhombohedral $LiNbO_3$ to 04-009-3436 (SG: R3c), orthorhombic $NaTaO_3$ to 04-010-2738 (SG: Pnma), orthorhombic $NaNbO_3$ to 04-014-2322 (SG: Pbcm) and orthorhombic $KNbO_3$ to 04-007-9572 (SG: Bmm2).

Table 4-4. Characterization and thermochemical data for alkali tantalates: $LiTaO_3$, $NaTaO_3$, and niobates: $LiNbO_3$, $NaNbO_3$ and $KNbO_3$.

	Surface area, SA_{BET} (m^2/g)	Crystallite size, $<D>$ (nm)		Water content, n, in $ABO_3 \cdot nH_2O$ (moles)	ΔH_{ds} (kJ/mol)		Surface energy, γ_{hyd} (J/m^2)
		From XRD	*From BET* [a]		*Bulk*	*Nano*	
$LiTaO_3$	7.62 ± 0.38	100.7 ± 5.8	106.2	0.040	93.79 ± 0.43	91.91 ± 0.42	1.04 ± 0.34
$LiNbO_3$	4.17 ± 0.35	103.1 ± 2.5	311.6	0.021	95.27 ± 0.21	94.52 ± 0.36	1.21 ± 0.68
$NaTaO_3$	8.97 ± 0.54	47.4 ± 3.1	94.4	0.082	88.77 ± 0.44	85.19 ± 0.65	1.58 ± 0.29
$NaNbO_3$	6.42 ± 0.55	63.9 ± 2.1	204.7	0.025	84.83 ± 0.38	82.56 ± 0.42	2.16 ± 0.57
$KNbO_3$	5.97 ± 0.37	72.5 ± 3.6	217.6	0.037	95.10 ± 0.41	91.93 ± 0.44	2.95 ± 0.59

[a] Calculated from SA_{BET}: $<D> = 6000 / (SA_{BET} \cdot \rho)$, using theoretical densities, ρ, of 7.415 g/cm^3 ($LiTaO_3$, JCPDS-PDF 01-087-2461), 4.618 g/cm^3 ($LiNbO_3$, JCPDS-PDF 04-009-3436), 7.089g/cm^3 ($NaTaO_3$, JCPDS-PDF 04-010-2738), 4.565 g/cm^3 ($NaNbO_3$, JCPDS-PDF 04-014-2322), and 4.619 g/cm^3 ($KNbO_3$, JCPDS-PDF 04-007-9572). Uncertainties are calculated as two standard deviations of the mean.

BET surface areas, SA_{BET}, of the nanocrystalline alkali tantalates and niobates are shown in Table 4-4. The SA_{BET} ranges from 4.17 to 8.97 m^2/g. Additionally the crystallite size <*D*> was calculated from BET surface area, assuming spherical crystallites (which is reasonable because of the relatively isotropic nanoparticles). The obtained <*D*> values range from 94.4 to 311.6 nm. Thus, the crystallite diameters calculated from BET surface area are rather different from those deduced from XRD, indicating that there is significant agglomeration in the nanocrystalline samples.

4.1.2. Solution calorimetry

High temperature oxide melt drop solution calorimetry was performed in a custom-made isoperibol Tian-Calvet twin microcalorimeter (University of California, Davis, CA), as seen in Figure 4-37. The solid samples are dropped in the high temperature solvent through the dropping tube. The heat released by the dissolving process contains heat content and heat of solution. The heat flow is measured by thermopiles, which are surrounded by inconel blocks and heaters are kept in the insulation. The integral of the heat flow within every minute along the reaction time gives the sum of the enthalpy of the solution and heat content. In some situations, a bubbling tube is used to help sample dissolving when necessary. Additionally, flushing the tube is used when gas evolution occurs during the process to keep the pressure constant [299].

The standard enthalpy of formation is a measure of the energy released or consumed when one mole of a substance is created under standard conditions from its pure elements [299, 300]. It is an enthalpy associated with the reaction that forms a compound from its elements in their most thermodynamically stable states. The formation enthalpy (ΔH_f) can be calculated by a designed thermocycle using the data of drop solution enthalpy (ΔH_{ds}). For example, assuming that *A* and *B* are two metal elements, oxygen has molar number of *x*, and the material has a formula ABO_x, the thermocycles can be written as:

$$ABO_x(25℃, solid) \rightarrow ABO_x(702℃, soln) \quad \Delta H_1 \tag{5}$$

$$AO(25℃, solid) \rightarrow AO(702℃, soln) \quad \Delta H_2 \tag{6}$$

$$BO(25℃, solid) \rightarrow BO(702℃, soln) \quad \Delta H_3 \tag{7}$$

$$AO(25℃, solid) + BO(25℃, solid) \rightarrow ABO_x(25℃, soln) \quad \Delta H_4 \tag{8}$$

where ΔH_1, ΔH_2, ΔH_3 are drop solution enthalpies measured by calorimetry, ΔH_4 is the formation enthalpy of ABO_x from oxides. The standard enthalpy change of formation is equal to the sum of the standard enthalpies of formation of the products subtracted by the sum of the standard enthalpies of formation of the reactants. Thus:

$$\Delta H_4 = \Delta H_2 + \Delta H_3 - \Delta H_1 \quad (9)$$

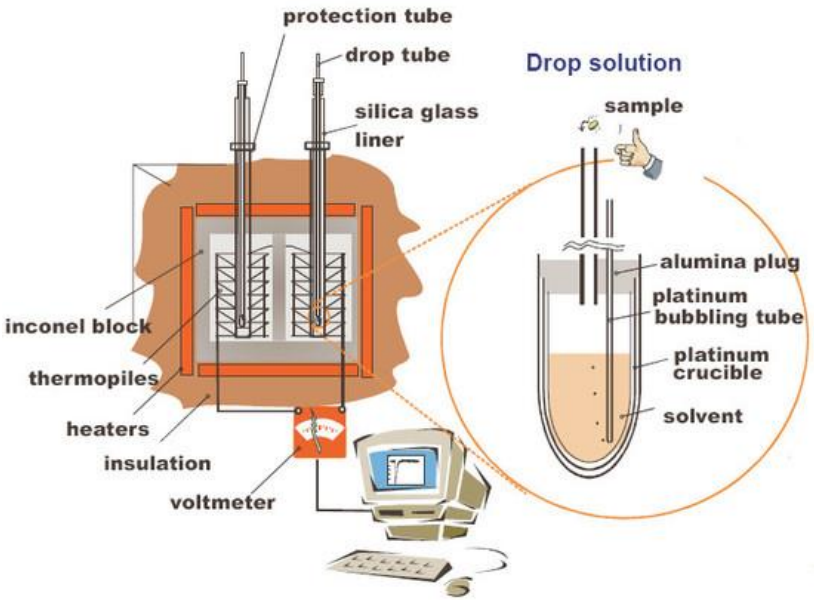

Figure 4-37. Scheme presenting the high temperature drop solution calorimeter developed by the group of Professor Alexandra Navrotsky at the University of California, Davis, CA (US) [301].

The calorimeter was calibrated against the heat content of 5 mg pellets of high purity α-Al_2O_3 (99.997 %, Alfa Aesar). The calorimetric assembly was flushed with oxygen at 43 ml/min and oxygen was bubbled through the solvent at 4.5 ml/min to aid dissolution. A number of ~5 mg pellets was loosely pressed, weighed and dropped from room temperature into 3 $Na_2O \cdot 4\ MoO_3$ solvent at 702 °C in the calorimeter. This methodology has been previously described [299, 302].

4.1.3. Calculation of surface and formation enthalpies

The measured average drop solution enthalpies (ΔH_{ds}) of bulk and nano $LiTaO_3$, $LiNbO_3$, $NaTaO_3$, $NaNbO_3$ and $KNbO_3$ are given in Table 4-4. The difference between the enthalpy of drop solutions, ΔH_{ds}, of the bulk and nano samples, corrected for water content, *n*, arises from the surface enthalpy term ($\gamma_{hyd} \cdot SA$, where *SA* is the surface area and γ_{hyd} is the surface enthalpy of the hydrated surface), essentially equivalent to the surface energy and as argued previously, very similar to the surface free energy [297]. The total water content, *n*, in $ABO_3 \cdot n\,H_2O$ was obtained from thermogravimetric analysis, by weighing the samples before and after heat treatment. The *n* normally corresponds to two terms: i) chemisorbed water, represented by adsorption enthalpies more negative than the enthalpy of water vapour condensation (-44 kJ/mol), and ii) physisorbed water, being characterized by adsorption enthalpies equal to the enthalpy of water vapour condensation [298, 303].

The γ_{hyd} is calculated as the difference between the drop solution enthalpies of macroscopic (bulk) and nanosized (nano) materials, divided by the difference in surface area:

$$\gamma_{hyd} = \frac{\Delta H_{ds}\ (bulk) - \Delta H_{ds}\ (nano)}{SA_{BET}} \qquad (10)$$

where γ_{hyd} represents the surface enthalpy of the hydrated surface, ΔH_{ds} stands for the drop solution enthalpy and SA_{BET} is the surface area. Since all nanocrystalline samples contain adsorbed water on their surfaces, the ΔH_{ds} values were corrected for water content following procedures described previously [298, 303]. The thermochemical cycle used for water correction for nanosized samples is given in Table 4-5. The energy of the hydrated surface is 1.04 ± 0.34, 1.21 ± 0.78, 1.58 ± 0.29, 2.16 ± 0.57 and 2.95 ± 0.59 J/m^2 for $LiTaO_3$, $LiNbO_3$, $NaTaO_3$, $NaNbO_3$ and $KNbO_3$, respectively. The measured surface energies refer to the real samples having a range of surface planes and defect structures. The nanoparticle surfaces are usually hydrated under ambient conditions, and the hydrated surface energy represents the thermodynamics of the surfaces. Only when nanoparticles are synthesized under special conditions, in a gaseous environment or in a vacuum, the anhydrous surface energy controls the thermodynamics of the growth process [304].

Table 4-5. Thermochemical cycle used for water correction for as-synthesized $LiTaO_3$, $LiNbO_3$, $NaTaO_3$, $NaNbO_3$ and $KNbO_3$.

ABO_3-$n$$H_2O$ (solid, 25˚C) → ABO_3 (soln., 702˚C) + $n$$H_2O$ (gas, 702˚C)	$\Delta H_1 = \Delta H_{ds}$
$n$$H_2O$ (gas, 702˚C) → $n$$H_2O$ (gas, 25˚C)	$\Delta H_2 = n$ (-25.1 ± 0.1) kJ/mol [305]
$n$$H_2O$ (gas, 25˚C) → $n$$H_2O$ (liq., 25˚C)	$\Delta H_3 = n$ (-44.0 ± 0.1) kJ/mol [305]
ABO_3 (solid, 25˚C) → ABO_3 (soln., 702˚C)	$\Delta H_4 = \Delta H_{ds} = \Delta H_1 + \Delta H_2 + \Delta H_3$

Soln. means dissolved in $3Na_2O \cdot 4MoO_3$

Table 4-6 and Table 4-7 present the thermochemical cycles used to determine the formation enthalpies of $KTaO_3$ and other perovskite-like materials, including $LiTaO_3$, $LiNbO_3$, $NaTaO_3$, $NaNbO_3$ and $KNbO_3$, respectively, both from oxides and elements. The formation enthalpies of $KTaO_3$, $LiTaO_3$, $LiNbO_3$, $NaTaO_3$, $NaNbO_3$ and $KNbO_3$ from constituent oxides ΔH_f^{ox} at 25 °C are -203.63 ± 2.92, -93.74 ± 1.82, -93.44 ± 1.55, - 147.35 ± 2.50, -141.63 ± 2.40 and -207.12 ± 1.85 kJ/mol, respectively. The formation enthalpies of $KTaO_3$, $LiTaO_3$, $LiNbO_3$, $NaTaO_3$, $NaNbO_3$ and $KNbO_3$ from elements, ΔH_f^0 at 25 °C are -1408.23 ± 3.75, -1415.94 ± 2.29, -1342.16 ± 1.72, -1378.00 ± 3.27, - 1298.80 ± 2.52, -1335.90 ± 2.73 kJ/mol, respectively.

Table 4-6. Thermodynamic cycle for obtaining the enthalpies of formation from oxides and elements for perovskite $KTaO_3$.

	Reaction	**Enthalpies**
From oxides	(1) $K_2O_{(xl,\ 25^\circ C)} \rightarrow K_2O_{(soln,\ 702^\circ C}$	ΔH_1 = -319.6 ± 4.6 kJ/mol [306]
	(2) $Ta_2O_{5\ (xl,\ 25^\circ C)} \rightarrow Ta_2O_{5\ (soln,\ 702^\circ C)}$	ΔH_2 = 90.41 ± 2.54 kJ/mo
	(3) $KTaO_{3\ (xl,\ 25^\circ C)} \rightarrow$ ½ $K_2O_{(soln,\ 702^\circ C)}$ + ½ $Ta_2O_{5\ (soln,\ 702^\circ C)}$	ΔH_3 = 89.03± 1.29 kJ/mol (ΔH_{ds})
	(4) ½ $K_2O_{(xl,\ 25^\circ C)}$ + ½ $Ta_2O_{5\ (xl,\ 25^\circ C)} \rightarrow KTaO_{3\ (xl,\ 25^\circ C)}$	ΔH_4 = ½ ΔH_1 + ½ ΔH_2 - ΔH_3 = **-203.63 ± 2.92 kJ/mol**
From elements	(5) 2 K + ½ $O_2 \rightarrow K_2O$	$\Delta H_f^{el}{}_{<K2O>}$ = -363.2 ± 2.1 kJ/mol [305]
	(6) 2 Ta + 5/2 $O_2 \rightarrow Ta_2O_5$	$\Delta H_f^{el}{}_{<Ta2O5>}$ = -2046.0 ± 4.2 kJ/mol [305]
	(7) $K_{(xl,\ 25^\circ C)}$ + $Ta_{(xl,\ 25^\circ C)}$ + 1.5 $O_2 \rightarrow KTaO_{3\ (xl,\ 25^\circ C)}$	$\Delta H_f^{el}{}_{<KTaO3>} = \Delta H_f^{ox}{}_{<(KTaO3>} + ½\ \Delta H_f^{el}{}_{<K2O>} + ½\ \Delta H_f^{el}{}_{<Ta2O5>}$ = **-1408.23 ± 3.75 kJ/mol**

Table 4-7. Thermochemical cycle used to calculate the formation enthalpies $LiTaO_3$, $LiNbO_3$, $NaTaO_3$, $NaNbO_3$ and $KNbO_3$.

	Reaction	**Enthalpies**
From oxides	(1) $Li_2O_{(xl,\ 25^\circ C)} \rightarrow Li_2O_{(soln,\ 702^\circ C}$	$\Delta H_1 = -90.3 \pm 2.5$ kJ/mol
	(2) $Nai_2O_{(xl,\ 25^\circ C)} \rightarrow Na_2O_{(soln,\ 702^\circ C}$	$\Delta H_2 = -207.56 \pm 4.25$ kJ/mo
	(3) $K_2O_{(xl,\ 25^\circ C)} \rightarrow K_2O_{(soln,\ 702^\circ C}$	$\Delta H_3 = -318.0 \pm 3.1$ kJ/mol
	(4) $Ta_2O_{5\ (xl,\ 25^\circ C)} \rightarrow Ta_2O_{5\ (soln,\ 702^\circ C}$	$\Delta H_4 = 90.41 \pm 2.5$ kJ/mol
	(5) $Nb_2O_{5\ (xl,\ 25^\circ C)} \rightarrow Nb_2O_{5\ (soln,\ 702^\circ C}$	$\Delta H_5 = 93.97 \pm 1.6$ kJ/mol
	(6) $LiTaO_{3\ (xl,\ 25^\circ C)} \rightarrow$ ½ $Li_2O_{(soln,\ 702^\circ C)}$+ ½ $Ta_2O_{5\ (soln,\ 702^\circ C)}$	$\Delta H_6 = 93.79 \pm 0.43$ kJ/mol
	(7) $LiNbO_{3\ (xl,\ 25^\circ C)} \rightarrow$ ½ $Li_2O_{(soln,\ 702^\circ C)}$+ ½ $Nb_2O_{5\ (soln,\ 702^\circ C)}$	$\Delta H_7 = 95.27 \pm 0.31$ kJ/mol
	(8) $NaTaO_{3\ (xl,\ 25^\circ C)} \rightarrow$ ½ $Na_2O_{(soln,\ 702^\circ C)}$+ ½ $Ta_2O_{5\ (soln,\ 702^\circ C)}$	$\Delta H_8 = 88.77 \pm 0.44$ kJ/mol
	(9) $NaNbO_{3\ (xl,\ 25^\circ C)} \rightarrow$ ½ $Na_2O_{(soln,\ 702^\circ C)}$+ ½ $Nb_2O_{5\ (soln,\ 702^\circ C)}$	$\Delta H_9 = 84.83 \pm 0.38$ kJ/mol
	(10) $KNbO_{3\ (xl,\ 25^\circ C)} \rightarrow$ ½ $K_2O_{(soln,\ 702^\circ C)}$+ ½ $Nb_2O_{5\ (soln,\ 702^\circ C)}$	$\Delta H_{10} = 95.10 \pm 0.41$ kJ/mol
	(11) ½ $Li_2O_{(soln,\ 702^\circ C)}$+ ½ $Ta_2O_{5\ (soln,\ 702^\circ C)} \rightarrow$ $LiTaO_{3\ (xl,\ 25^\circ C)}$	$\Delta H_{11} = ½\ \Delta H_1 + ½\ \Delta H_4 - \Delta H_6 = -93.74 \pm 1.77$ kJ/mol
	(12) ½ $Li_2O_{(soln,\ 702^\circ C)}$+ ½ $Nb_2O_{5\ (soln,\ 702^\circ C)} \rightarrow$ $LiNbO_{3\ (xl,\ 25^\circ C)}$	$\Delta H_{12} = ½\ \Delta H_1 + ½\ \Delta H_5 - \Delta H_7 = -93.44 \pm 1.48$ kJ/mol
	(13) ½ $Na_2O_{(soln,\ 702^\circ C)}$+ ½ $Ta_2O_{5\ (soln,\ 702^\circ C)} \rightarrow$ $NaTaO_{3\ (xl,\ 25^\circ C)}$	$\Delta H_{13} = ½\ \Delta H_2 + ½\ \Delta H_4 - \Delta H_8 = -147.35 \pm 2.46$ kJ/mol
	(14) ½ $Na_2O_{(soln,\ 702^\circ C)}$+ ½ $Nb_2O_{5\ (soln,\ 702^\circ C)} \rightarrow$ $NaNbO_{3\ (xl,\ 25^\circ C)}$	$\Delta H_{14} = ½\ \Delta H_2 + ½\ \Delta H_5 - \Delta H_9 = -141.63 \pm 2.27$ kJ/mol
	(15) ½ $K_2O_{(soln,\ 702^\circ C)}$+ ½ $Nb_2O_{5\ (soln,\ 702^\circ C)} \rightarrow$ $KNbO_{3\ (xl,\ 25^\circ C)}$	$\Delta H_{15} = ½\ \Delta H_3 + ½\ \Delta H_5 - \Delta H_{10} = -207.12 \pm 1.74$ kJ/mol

Table 4-7. Thermochemical cycle used to calculate the formation enthalpies $LiTaO_3$, $LiNbO_3$, $NaTaO_3$, $NaNbO_3$ and $KNbO_3$. (Cont'd.)

	Reaction	Enthalpies
From elements	(16) $2\ Li_{(xl,\ 25^{\circ}C)} + ½\ O_2 \rightarrow\ Li_2O_{(xl,\ 25^{\circ}C)}$	ΔH_{16} = -597.9 kJ/mol
	(17) $2\ Na_{(xl,\ 25^{\circ}C)} + ½\ O_2 \rightarrow\ Na_2O_{(xl,\ 25^{\circ}C)}$	ΔH_{17} = -414.9 kJ/mo
	(18) $2\ K_{(xl,\ 25^{\circ}C)} + ½\ O_2 \rightarrow\ K_2O_{(xl,\ 25^{\circ}C)}$	ΔH_{18} = -358.02 ± 3.74 kJ/mol
	(19) $2\ Ta_{(xl,\ 25^{\circ}C)} + ½\ O_2 \rightarrow\ Ta_2O_{5(xl,\ 25^{\circ}C)}$	ΔH_{19} = -2046.5 ± 4.2 kJ/mol
	(20) $2\ Nb_{(xl,\ 25^{\circ}C)} + ½\ O_2 \rightarrow\ Nb_2O_{5(xl,\ 25^{\circ}C)}$	ΔH_{20} = -1899.54 ± 1.5 kJ/mol
	(21) $Li_{(xl,\ 25^{\circ}C)} + Ta_{(xl,\ 25^{\circ}C)} + 3/2\ O_2 \rightarrow\ LiTaO_{3(xl,\ 25^{\circ}C)}$	$\Delta H_{21} = ½\ \Delta H_{16} + ½\ \Delta H_{19} + \Delta H_{11}$ = -1415.94 ± 2.29 kJ/mol
	(22) $Li_{(xl,\ 25^{\circ}C)} + Nb_{(xl,\ 25^{\circ}C)} + 3/2\ O_2 \rightarrow\ LiNbO_{3(xl,\ 25^{\circ}C)}$	$\Delta H_{22} = ½\ \Delta H_{16} + ½\ \Delta H_{20} + \Delta H_{12}$ = -1342.16 ± 1.72 kJ/mol
	(23) $Na_{(xl,\ 25^{\circ}C)} + Ta_{(xl,\ 25^{\circ}C)} + 3/2\ O_2 \rightarrow\ NaTaO_{3(xl,\ 25^{\circ}C)}$	$\Delta H_{23} = ½\ \Delta H_{17} + ½\ \Delta H_{19} + \Delta H_{13}$ = -1378.00 ± 3.27 kJ/mol
	(24) $Na_{(xl,\ 25^{\circ}C)} + Nb_{(xl,\ 25^{\circ}C)} + 3/2\ O_2 \rightarrow\ NaNbO_{3(xl,\ 25^{\circ}C)}$	$\Delta H_{24} = ½\ \Delta H_{17} + ½\ \Delta H_{20} + \Delta H_{14}$ = -1298.80 ± 2.52 kJ/mol
	(25) $K_{(xl,\ 25^{\circ}C)} + Nb_{(xl,\ 25^{\circ}C)} + 3/2\ O_2 \rightarrow\ KNbO_{3(xl,\ 25^{\circ}C)}$	$\Delta H_{25} = ½\ \Delta H_{18} + ½\ \Delta H_{20} + \Delta H_{15}$ = -1335.90 ± 2.73 kJ/mol

The formation enthalpies of alkali tantalate and niobate perovskites become more exothermic with increase in the size of the alkali cations. However for a given alkali cation, the niobate and tantalate perovskite have comparable energetics. $LiNbO_3$ has the reported enthalpy of formation from constituent oxides of -98.33 ± 1.70 kJ/mol [288], while for $NaNbO_3$ the enthalpy of formation values of -153.46 ± 2.33 kJ/mol [288] and - 157.40 ± 2.2 kJ/mol [289] were reported, being in good agreement with our present values. Formation enthalpy of $NaNbO_3$, ΔH_f^0 ($NaNbO_3$) determined by Popovič *et al.* [290] and Kobertz *et al.* [291] using Knudsen effusion mass spectrometry were found to be - 1220 kJ/mol and -1250.8 ± 7 kJ/mol, respectively. The enthalpy of formation was experimentally determined using three different approaches: i) from the partial sublimation enthalpies of Na (determined from vaporization of sodium niobate), ii) from the activity of sodium oxide in sodium niobate and derived from partial pressure data, and iii) from the heat capacity data from condensed phase studies [291]. These values of ΔH_f^0 match well with our results. The ΔH_f^0 of $LiNbO_3$, $NaNbO_3$ and $KNbO_3$ at 25 °C was calculated by Shigemi *et al.* [307-309] using a plane-wave pseudopotential method within a density functional formalism, and were found to be -1327.70 (rhombohedral *R3c*), -1291.04 (orthorhombic *Pbma*) and -1306.04 kJ/mol (orthorhombic *Bmm2*). Moreover, Körbel *et al.* [310] calculated the ΔH_f^0 to be -1336.51 and -1378.97 kJ/mol for $NaNbO_3$ and $KNbO_3$, respectively. These values agree well with our formation enthalpies derived using calorimetric techniques. Reznitskii [311] calculated the heat of reaction using the enthalpies of changes, $\Sigma\delta H$, in the cation coordination number, $\Delta H_f^{ox} = -31.3 + 0.84 \cdot \Sigma\delta H$ (kJ/mol), or from the function $\Delta H_f^{ox} = 2[-60 + 500 \cdot (1 - t)]$ (kJ/mol); the calculated values were -150.00 ± 60, -150.00 ± 60, -206.00 ± 26 and -206.00 ± 22 kJ/mol for $NaNbO_3$, $NaTaO_3$, $KNbO_3$ and $KTaO_3$, respectively, being in good agreement with our experimental data. Table 4-8 collects the experimental energetics of $LiTaO_3$, $LiNbO_3$, $NaTaO_3$, $NaNbO_3$, $KNbO_3$ and $KTaO_3$.

Table 4-8. Tolerance factor and energetics of $LiTaO_3$, $LiNbO_3$, $NaTaO_3$, $NaNbO_3$, $KNbO_3$ and $KTaO_3$.

	$LiTaO_3$	**$LiNbO_3$**	**$NaTaO_3$**	**$NaNbO_3$**	**$KNbO_3$**	**$KTaO_3$**
Tolerance factor, *t*	0.78	0.78	0.94	0.94	1.03	1.03
Formation enthalpy from oxides, ΔH_f^{ox}	-93.74 ± 1.77	-93.44 ± 1.48	-147.35 ± 2.46	-141.63 ± 2.27	-207.12 ± 1.74	-203.63 ± 2.92
Formation enthalpy from elements, ΔH_f^{0}	-1415.94 ± 2.29	-1342.16 ± 1.72	-1378.00 ± 3.27	-1298.80 ± 2.52	-1335.90 ± 2.73	-1408.23 ± 3.75
Hydrated surface energy, γ_{hyd} (J/m^2)	1.04 ± 0.34	1.21 ± 0.68	1.58 ± 0.29	2.16 ± 0.57	2.95 ± 0.59	-

4.1.4. Thermochemical stability of alkali tantalates and niobates

Figure 4-38 depicts the variation of formation enthalpies of $LiTaO_3$, $LiNbO_3$, $NaTaO_3$, $NaNbO_3$, $KNbO_3$ and $KTaO_3$ with respect to their tolerance factors. The tolerance factor, *t*, defines the structural stability, and is frequently referred in discussions related to the stability of perovskites. The tolerance factor of a perovskite compound is calculated by the following expression [312]:

$$t = \frac{r_A + r_O}{\sqrt{2}(r_B + r_O)} \tag{11}$$

Here, r_A, r_B, and r_O refer to the ionic radii of A^{1+}, B^{5+} and O^{2-}, respectively. The ionic radii were taken from Shannon's effective ionic radii table [82], and the coordination of 6 is assumed for Li^+, 8 for Na^+, 12 for K^+ and 6 for Ta^{5+} and Nb^{5+}. In the ideal cubic perovskite structure, the ratio of the A–O bond length ($r_A + r_O$) to the B–O length ($r_B + r_O$) equals $\sqrt{2}$, and thus $t = 1$. When this condition deviates, the structure distorts largely via tilting of its BO_6 octahedra or via displacement of the ion within the O octahedron, and thereby departs from the cubic symmetry [313]. With the increase in the tolerance factor of alkali tantalate and niobate perovskites formation enthalpies becomes more negative (Figure 4-38). It is an obvious indication of the stability of the structure, and for those perovskites with *t* close to 1, the enthalpies of formation are the most exothermic. Then it can be concluded that the higher the tolerance factor, the more stable the perovskite compound relative to their binary constituent oxides. Among alkali tantalates and niobates, K-containing perovskites are the most structurally stable because their tolerance factor is only +0.03 away from the ideal one.

The energetics of perovskite oxides and their phase stability can be discussed based on acid-base concepts [314, 315]. The enthalpy of formation of a ternary oxide such as ABO_3 (where A-site is occupied by ions: A^+, A^{2+} and A^{3+}, while B-site: B^{5+}, B^{4+}, B^{3+}, respectively) from the binary constituent oxides (reaction in the next equation) reflects the strength of the chemical bonds in the ternary oxide relative to those in the binary oxides.

$$\frac{1}{2}A_2O\left(or\ AO\ or\frac{1}{2}A_2O_3\right) + \frac{1}{2}B_2O_5(or\ BO_2\ or\ \frac{1}{2}B_2O_3) = ABO_3 \tag{12}$$

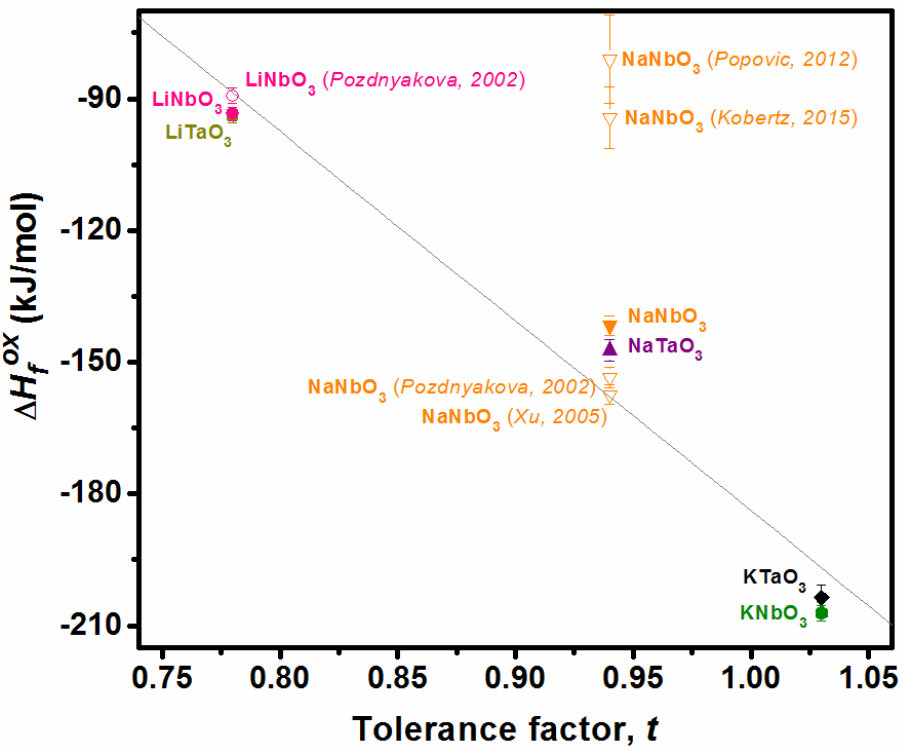

Figure 4-38. Experimental data of formation enthalpies, ΔH_f^{ox}, of alkali niobates and tantalates vs tolerance factor, t. Solid symbols correspond to data of the present study and open symbols to the literature data. The formation enthalpy is more exothermic for the perovskites with tolerance factor close to the ideal cubic, t = 1.

In the case of a ternary ABO_3 oxides, the most stable compounds form when the most basic binary A oxides combine with the most acidic B oxides (oxygen ions transferred from the base to the acid oxides). The oxide acidity/basicity can be measured in terms of ionic potential of the metal cation, z/r, where z is the formal charge and r the ionic radius. The larger the z/r of the cation, the less basic or the more acidic its oxide; the following grouping can be made: $z/r < 2$ – strongly basic, $2 < z/r < 4$ – basic, $4 < z/r < 7$ – amphoteric, $z/r < 7$ – acidic [313]. The concept was originally proposed by Lux [316], and then developed by Flood *et al.* [317, 318]. Then, the stability of ABO_3 perovskites can be defined by a parameter so-called stability index (ratio of ionic potential), s, which is defined as a z/r ratio between B and A cations:

$$s = \frac{(z/r)_B}{(z/r)_A} \tag{13}$$

Figure 4-39 depicts the relation of the experimental enthalpies of formation, ΔH_f^{ox}, of a number of perovskites to the ionic potential in the present study, together with other perovskites from the groups III-III, II-IV and I-V (and additionally mixed II-IV and I-V), as a function of *s*. The III-III group is represented by the lanthanides [319, 320]: $LaAlO_3$, $GdAlO_3$, $YAlO_3$, $DyAlO_3$, $EuAlO_3$, $LaGaO_3$, $NdGaO_3$, $LaFeO_3$, $EuFeO_3$, $GdFeO_3$, $DyFeO_3$ and $LuFeO_3$, the II-IV group by the titanates and zirconates [321]: $SrTiO_3$, $CaTiO_3$, $BaTiO_3$, $PbTiO_3$, $SrZrO_3$, $CaZrO_3$, $BaZrO_3$ and $PbZrO_3$, and the mixed II-IV and I-V group by $(Na_{1-x}Sr_x)(Nb_{1-x}Ti_x)O_3$ [289]. Since an A oxide acts as a base and a B oxide as an acid, thus, the larger the *s* the more stable the perovskite, *i.e.* more exothermic is the enthalpy of formation of the ternary oxide from its binary constituents. The basicity of the alkali oxides increases down the group, *i.e.* $Li_2O < Na_2O < K_2O$ (1.00 < 1.15 < 1.40, as it is based on an optical basicity scale [313]). Thus, when combining these binary alkali oxides with a transition metal oxide, *i.e.* Ta_2O_5 or Nb_2O_5, the ΔH_f^{ox} of $K(Ta/Nb)O_3$ is expected to be more negative than $Na(Ta/Nb)O_3$ and $Li(Ta/Nb)O_3$. It is clearly demonstrated in Figure 4-39 that with an increasing of *s*, ΔH_f^{ox} becomes more exothermic. The data for the III-III and mixed II-IV and I-V perovskites fall well on the trend, but some compositions from the II-IV and I-V type somewhat deviate from the polynomial fitted line.

Surfaces (and interfaces) play a crucial role in many relevant processes considering solids, *i.e.* chemical reactivity, catalysis, coarsening, sintering, polymorphic stability, and their energies are directly related to the driving forces of these phenomena [322, 323]. Many theoretical calculations of energies of variously oriented surfaces, interfaces, and grain boundaries have been reported, but there are only few experimental determinations due to the difficulties in such measurements. However, hydrous and anhydrous surface energies of nanomaterials have been successfully determined by using a calorimetric approach [298, 304, 324-326]. Therefore within this context the surface enthalpies of hydrated alkali tantalate and niobate nanoparticles were measured for the first time in this work. It has to be also pointed out that the performed experiments consider as well a range of surface planes and defect structures, thus the measured energies are an average of many planes, edges, kinks, steps, pits, corners, *etc.* [297].

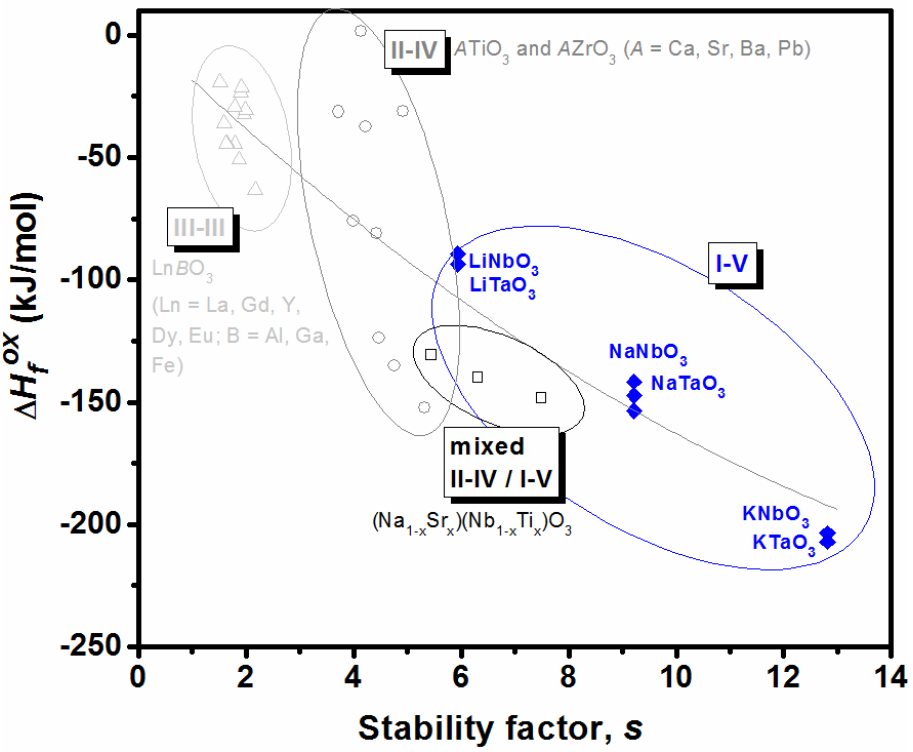

Figure 4-39. Formation enthalpies, ΔH_f^{ox}, of alkali tantalates and niobates (solid diamond symbols): $LiTaO_3$, $LiNbO_3$, $NaTaO_3$, $NaNbO_3$, $KNbO_3$ and $KTaO_3$, together with other perovskites (open triangles for III-III, open circles for II-IV and open squares for mixed II-IV and I-V type perovskites, taken from literature) as a function of stability index (ratio of ionic potential), s. The curve represents a polynomial fit to all the data.

Figure 4-40 *(a)* shows variation of formation enthalpies of alkali tantalates and niobates with their surface energies, along with the reported formation enthalpies and surface energetics of selected perovskite type titanates: $CaTiO_3$, $SrTiO_3$, $BaTiO_3$ and $PbTiO_3$ [298, 327]. The perovskites having more exothermic enthalpies of formation, ΔH_f^{ox}, appear to have higher surface energies. $PbTiO_3$ has a less exothermic integral enthalpy of water vapour adsorption, indicating a lower affinity of water and less hydrophilic character [298, 327]. It has been observed that the more ionic the perovskite, more exothermic the ΔH_f^0, the higher its surface energy, and more tightly it binds H_2O [327]. The surface energy increases with increase of the tolerance factor (Figure 4-40 *(b)*). The different surface energies of alkali tantalates and niobates are potentially important in the liquid phase synthesis of the nanoparticles, in particular influencing processes such as nucleation, growth, Ostwald

ripening, and nanoparticle stabilization. The higher surface energy may accelerate nucleation and growth [327].

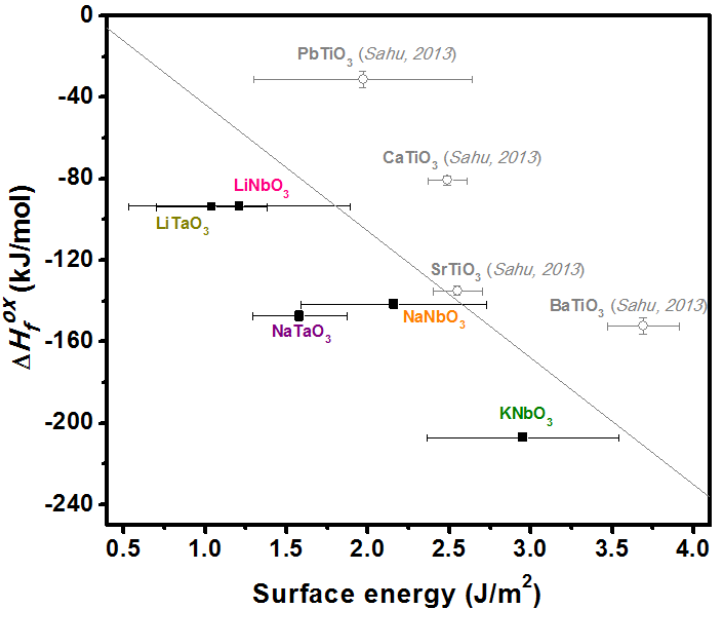

(a)

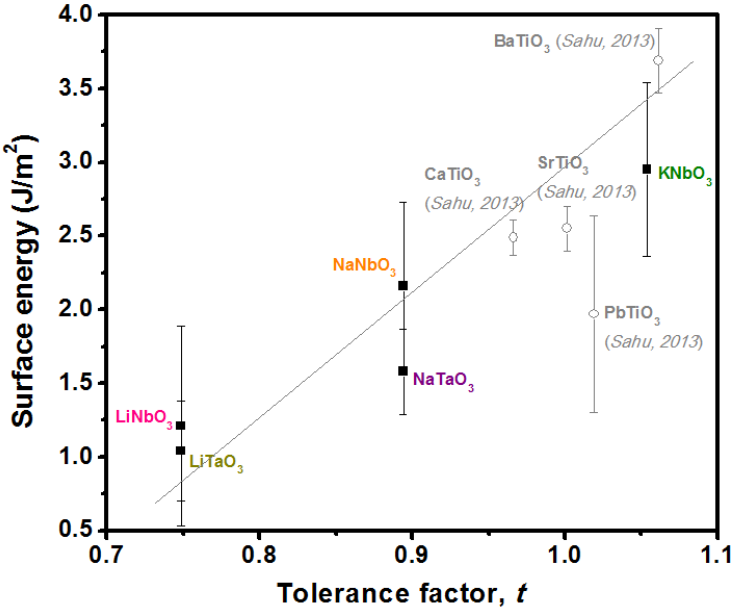

(b)

Figure 4-40. (a) Formation enthalpies of alkali niobate and tantalate together with $CaTiO_3$, $SrTiO_3$, $BaTiO_3$ and $PbTiO_3$ perovskites versus surface energies. The surface energy increases as the formation enthalpy becomes more exothermic. (b) Surface energies of alkali niobate and tantalate perovskites together with $CaTiO_3$, $SrTiO_3$, $BaTiO_3$ and $PbTiO_3$ versus tolerance factors. The γ_{hyd} increases with an increase of the t. Solid squares represents data from the present work and open circles to the literature data [298, 327].

Summary

Alkali tantalates and niobates with perovskite-like structures, including $LiTaO_3$, $LiNbO_3$, $NaTaO_3$, $NaNbO_3$, $KNbO_3$ and $KTaO_3$, were synthesized using the mixed oxide method and their formation enthalpies and surface energetics were determined by high temperature oxide melt solution calorimetry. The formation enthalpy becomes more exothermic (higher thermodynamic stability) and the surface energy increases with an increase in the ionic radius of the A-site cations (Li, Na and K) and the tolerance factor.

4.2. Phase formation in potassium tantalate

Abstract

Due to the complexity of the K_2O–Ta_2O_5 phase diagram, and hence the difficulty to obtain monophasic potassium tantalate compositions, a systematic study on the phase formation in potassium tantalate is carried out using *in situ* characterization techniques, solid-state kinetics and thermodynamic strategies. The sequence of the phase formation process in potassium tantalate, and its dependence on processing and experimental conditions is established. Our results show that only for wet chemical processes, *e.g.* sol-gel, hydrothermal, the formation of intermediate defect pyrochlore phase is detected. Its stoichiometry deviates depending on the experimental conditions within the same method. A kinetic study reveals that in stoichiometric pyrochlore the transformation into perovskite phase occurs in two stages, being also energetically more stable than that in the non-stoichiometric ones. The stoichiometry of a pyrochlore governs also the transformation path either to perovskite $KTaO_3$ or tetragonal tungsten bronze $K_6Ta_{10.8}O_{30}$. This work provides a comprehensive study on the process-phase relationship in K_2O–Ta_2O_5.

In general the phase formation process is rather complex, and it is essential to fully understand the mechanisms driving the changes when external forces as heat or pressure, among others, are applied to crystallize the desired phase. Regarding the ternary-based oxides with ABO_3 perovskite-like structures, only for Pb-containing compositions the phase formation and its dependence on the processing route is quite well established and have been studied over decades [328-331].

Generally, it has been observed in the perovskite lead based compounds that during relatively high synthesis temperature due to the loss of Pb compositional deviations occur

and a stable pyrochlore secondary phase is normally formed that deteriorates drastically the properties of the materials [328, 330]. The change in the composition may also be associated to an insufficient ions diffusion through the structure network due to the low temperature and short processing time. To avoid formation of second phases in lead based perovskite systems, typified by relaxor system *1-x* $Pb(Mg_{1/3}Nb_{2/3})O_3$-*x* $PbTiO_3$ (PMN-PT), the synthesis conditions and precursors chemistry have been changed.

In 1980s, Swartz and Shrout [328], and later Lejeune and Boilot [329] have thoroughly investigated the synthesis of relaxor ferroelectric lead magnesium niobate, $PbMg_{1/3}Nb_{2/3}O_3$ (PMN), due to the difficulty to prepare PMN ceramics with a monophasic perovskite structure. The phase diagram for PbO–MgO–Nb_2O_5 has a boundary between pyrochlore and perovskite solid solutions. So a small change in composition during the synthesis process can lead to the formation of a pyrochlore phase. Thus studying the kinetics of the phase formation in PMN from mixed oxides, a novel fabrication process was developed, the so-called columbite route, in which firstly magnesium and niobium oxides react to form $MgNb_2O_6$ prior to the reaction with PbO to form the perovskite phase [328]. The pyrochlore formation was avoided, since columbite structure of $MgNb_2O_6$ is an oxygen octahedra structure, similar to the perovskite one.

Apart from this knowledge, just recently Cardoso da Costa *et al.* [330] investigated the energetics of PMN-PT, quantifying and explaining the thermochemistry of the reactions involved in the synthesis and decomposition of this relaxor ferroelectric material. Using high temperature oxide melt solution calorimetry, the enthalpies of distinct synthesis procedures were examined. It was concluded that the columbite route and decomposition of PMN perovskite to pyrochlore and simple oxides: MgO and PbO, are energetically favourable. The enthalpy change for the reaction $MgNb_2O_6 + 3\ PbO \rightarrow 3\ Pb(Mg_{1/3}Nb_{2/3})O_3$ is - 25.74 ± 3.09 kJ, and the one of the decomposition to the simple oxide is -11.52 ± 3.48 kJ. Both reactions are exothermic, thus they are prone to occur.

In the case of Pb(Zr, Ti)O_3 (PZT) compositions, processed via solution based routes, the phase evolution is similar to all the other lead based perovskites, being as follows. Firstly, amorphous PZT is transformed into metastable and non-ferroelectric pyrochlore ($A_2B_2O_{7-\delta}$) at low temperatures. Then the perovskite structure nucleates and grows from the pyrochlore one. In this case, the nucleation energy, being much higher than the growth energy, is the

primary barrier for the perovskite crystallization [332, 333]. Therefore, a relatively high temperature (≥600 °C) is required to achieve the desired perovskite phase, raising difficulties for thin films preparation in terms of compatibility with the silicon technology due to enhanced interface diffusion and oxidation/degradation. The crystallization path of chemically derived PZT was recently studied by Kameda *et al.* [331]. The intermediate pyrochlore formation was avoided via solution processing, using monoethanolamine (MEA) as a modifier in the precursor solution with the 1:1 ratio between metal ions and MEA. Thus, the crystallization of perovskite PZT was promoted at low temperatures 400–500 °C. According to the authors during heat treatment Pb^{2+} is reduced to Pb^0, and isolated at the nanoscale level due to the strong MEA coordination to the metal atoms, together with local reducing environment causing lead deficiency. Therefore, the pyrochlore composition $Pb_2(Zr, Ti)_2O_{7-\delta}$ cannot be formed, and the perovskite $Pb(Zr, Ti)O_3$ becomes more stable and immediately crystallizes due to the later Pb oxidation and diffusion into Zr/Ti–O matrix. It is believed that final perovskite crystallization occurs through solid-state reaction between α-PbO and the amorphous Zr/Ti–O.

Regarding the alkali-based ternary oxides, such as $KTaO_3$ system, the phase formation process is far from being as deeply analysed as in Pb-containing perovskites. Such investigations were relatively well conducted on potassium sodium niobate [334, 335]. Malič *et al* [334] established the sequence of reactions during the synthesis of ternary oxides, $NaNbO_3$ and $KNbO_3$, as well as their solid solutions, KNN, from the carbonates and oxides. It was found that the first phase to form at the interface Na_2CO_3/Nb_2O_5 is $Na_2Nb_4O_{11}$ and only after the perovskite $NaNbO_3$. In the K_2CO_3/Nb_2O_5 the sequence of phases is $Nb_2O_5/K_6Nb_{10.88}O_{30}/K_4Nb_6O_{17}/KNbO_3$. In the $(K_2CO_3 + Na_2CO_3)/Nb_2O_5$ diffusion couple, the $(K, Na)NbO_3$ solid solution forms via the intermediate phase $(K, Na)_2Nb_4O_{11}$ at 600 °C. The reaction rate in the ternary system is determined by the diffusion of the slower species, *i.e.*, the potassium ions. The growth of the perovskite phase in the ternary system is favoured as compared with the binaries. Those findings imply that the solid-state synthesis of sodium potassium niobate requires extreme care.

The perovskite phase formation of $KTaO_3$, prepared by chemical solution processes, was reported to be rather complicated, especially in the fabrication of thin films onto rigid substrates [52, 59, 61, 96, 336]. The reasons are listed in chapter 2 (State of the Art). These issues still have not been entirely explored and explained in $KTaO_3$ system, leaving a gap in

understanding of relation between perovskite, $KTaO_3$, and intermediate pyrochlore, $K_2Ta_2O_6$, phases.

Within this context, this sub-chapter is focused on understanding the sequence of phase formation process in potassium tantalate, and its dependence on processing and experimental conditions. This issue is worthwhile to study, in order to prevent, control or overcome formation of stoichiometric perovskite structure and undesired intermediate phase. The work provides a comprehensive study on the process-phase relationship, including the identification of driving forces and interpretation of the mechanism. Comparison of phase formation pathways in conventional solid state reaction and attractive solution methods is presented and discussed.

4.2.1. Selected processing routes

In this study the following processing routes were selected: i) conventional solid-state reaction, ii) sol-gel method (alkoxide route), and iii) hydrothermal process. The list of the K–Ta oxides intentionally prepared and used in this part of the thesis is summarized in Table 4-9.

Table 4-9. Summary of the powders, K–Ta oxides, used in this work.

Sample	***Method***	***Composition***
K_2CO_3–Ta_2O_5	Conventional solid state (ball milled powders)	-
K-Ta	Sol-gel (amorphous powders)	-
KTOper-1	Conventional solid state (calcined at 850 °C)	$K_{1.005\pm0.001}Ta_{0.995\pm0.0004}O_{2.990\pm0.001}$ (by EPMA)
KTOper-2	Sol-gel (calcined at 900 °C)	$K_{0.998\pm0.001}Ta_{1.002\pm0.0003}O_{3.005\pm0.001}$ (by EPMA)
KTOpyr-0	Sol-gel (calcined at 550 °C)	$K_2Ta_2O_6$
KTOpyr-1	Hydrothermal (KOH: 3.2 M, 175 °C)	$K_{0.873\pm0.004}Ta_{2.226\pm0.003}O_{6\pm0.003}$ (by EPMA)
KTOpyr-2	Hydrothermal (KOH: 5 M, 175 °C)	$K_{1.128\pm0.006}Ta_{2.175\pm0.002}O_{6\pm0.006}$ (by EPMA)
KTOpyr-3	Hydrothermal (KOH: 6 M, 175 °C)	$K_{1.291\pm0.004}Ta_{2.142\pm0.002}O_{6\pm0.003}$ (by EPMA)
KTOttb	Conventional solid state (calcined at 1100 °C)	$K_6Ta_{10.8}O_{30}$

4.2.2. Structural phase evolutions from distinct routes

In this part of the work the phase formation in $KTaO_3$ is studied using *ex situ* and *in situ* XRD and DTA/TG. Firstly, the structural evolution of K_2CO_3–Ta_2O_5 prepared by conventional solid-state reaction, as a function of temperature and time is investigated. Figure 4-41 shows a set of *in situ* XRD diffractograms of K_2CO_3–Ta_2O_5 recorded in the 2θ range of 20–40° at distinct temperatures and times (in air). On the bottom of each graph, XRD patterns reflect the used reagents: orthorhombic Ta_2O_5, and monoclinic K_2CO_3. Eight patterns located in the middle of the graphs were recorded at elevated temperatures: 650 °C (Figure 4-41 *(a)*), 750 °C (Figure 4-41 *(b)*) and 850 °C (Figure 4-41 *(c)*), and collected for dwell times varying from 1 to 300 min. After cooling down to ambient temperature, a last XRD was recorded, representing the structure of the product of the reaction, and these patterns are shown at the top of every graph. When the mixture of reactants (K_2CO_3 and Ta_2O_5) reaches the temperature of 650 °C (Figure 4-41 *(a)*), the characteristic lines from starting oxides are still present, and then desired $KTaO_3$ phase forms. At the highest tested temperature, 850 °C (Figure 4-41 *(c)*), the perovskite phase is already developed after 1 min, and in the later stage the rest of reactants complete the reaction. For all the experiments only the X-ray diffraction lines from starting reagents as well as from the three characteristic planes of perovskite $KTaO_3$, *i.e.* (100) at ~22°, (110) at ~31°, and (111) at ~39°, consistent with JCPDS-PDF #38-1470, were detected. These patterns do not reveal any evidence of additional/intermediate phase(s).

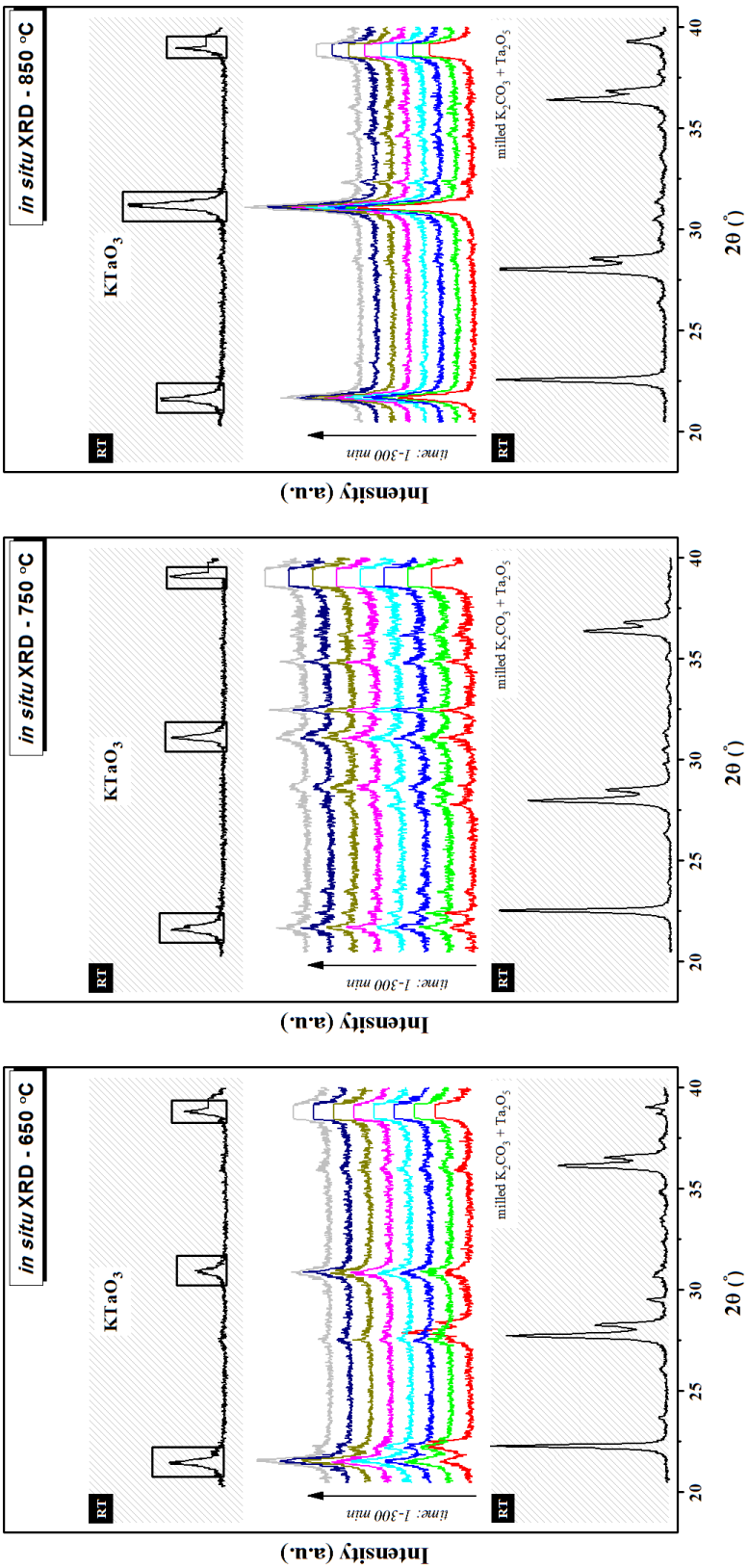

Figure 4-41. In situ XRD patterns of KTO powders obtained by conventional mixed oxides method, analysed at 650 °C (a), 750 °C (b) and 850 °C (c), at distinct times: 1–300 min. For all the experiments only the X-ray diffraction lines from the three characteristic planes of perovskite $KTaO_3$ in the products of the reactions, and there is no evidence of intermediate phases.

Additional experiments were planned and conducted, using oxidizing and reducing atmospheres. Figure 4-42 shows a series of XRD patterns, acquired in *ex situ* measurements, representing the phase evolution of double metal K–Ta oxide at various temperatures and calcination atmospheres. The graph presents the results of K_2CO_3–Ta_2O_5 calcined at three distinct temperatures: 650, 750 and 850 °C, and in N_2 and O_2 atmospheres; the bottom frame depicts the diffraction lines of $KTaO_3$ taken from JCPDS-PDF #38-1470. Most importantly, the results indicate that there is no evidence of intermediate phases for processing in the controlled atmospheres. Therefore, the processing atmosphere does not affect the $KTaO_3$ phase formation from mixed-oxide method. The calcination of K_2CO_3–Ta_2O_5 powders in a reducing and oxidizing atmosphere leads only to a negligible displacement of the diffraction peaks, that usually indicates a change in the lattice parameter *a* and is indicative of a lattice expansion or contraction. The calculated *a* values for $KTaO_3$ powders annealed at distinct atmospheres are following: at 850 °C – 3.9909 ± 0.0004 Å (in air, +0.05 %), 3.9878 ± 0.0001 Å (in N_2, -0.03 %), 3.9901 ± 0.0003 Å (in O_2, +0.03 %), at 750 °C – 3.9923 ± 0.0005 Å (in air, +0.08 %), 3.9903 ± 0.0002 Å (in N_2, +0.03 %), 3.9863 ± 0.0003 Å (in O_2, -0.07 %), at 650 °C – 3.9908 ± 0.0006 Å (in air, +0.04 %), 3.9888 ± 0.0003 Å (in N_2, -0.01 %), 3.9938 ± 0.0011 Å (in O_2, +0.12 %). The differences with respect to a lattice parameter from JCPDS-PDF #38-1470 are included in the brackets. In the present case this lattice variation might be due to the change of the vacancy concentration in the oxygen sublattice and/or to the change in the valence state of some cations [337].

In analogy to previously presented results on solid-state prepared powders, the phase evolution studies were also conducted on the sol-gel derived powders. XRD patterns of the powders measured *in situ*, up to 950 °C, with temperature interval of 50–100 °C, are depicted in Figure 4-43. Initially the amorphous dried powders were heated up to 600 °C, and then to higher temperatures: 700, 750, 800, 850, 900 and 950 °C. XRD patterns were collected at these selected temperatures, to follow the changes in terms of the formed phases and crystalline structures. At the lowest among the recorded temperatures, 600 °C, only the pyrochlore $K_2Ta_2O_6$ phase was detected. When the temperature increases a gradual increase of the crystallinity of the pyrochlore structure is observed, with further transformation into the perovskite phase at temperatures above 800 °C. As can be seen, at temperatures as high as ≥900 °C, the major structure is perovskite $KTaO_3$, although traces of pyrochlore $K_2Ta_2O_6$

are still present. Those residues might be related to the K-deficient pyrochlore due to K loss at such high temperatures. More results associated with defect pyrochlores are discussed in the next paragraphs.

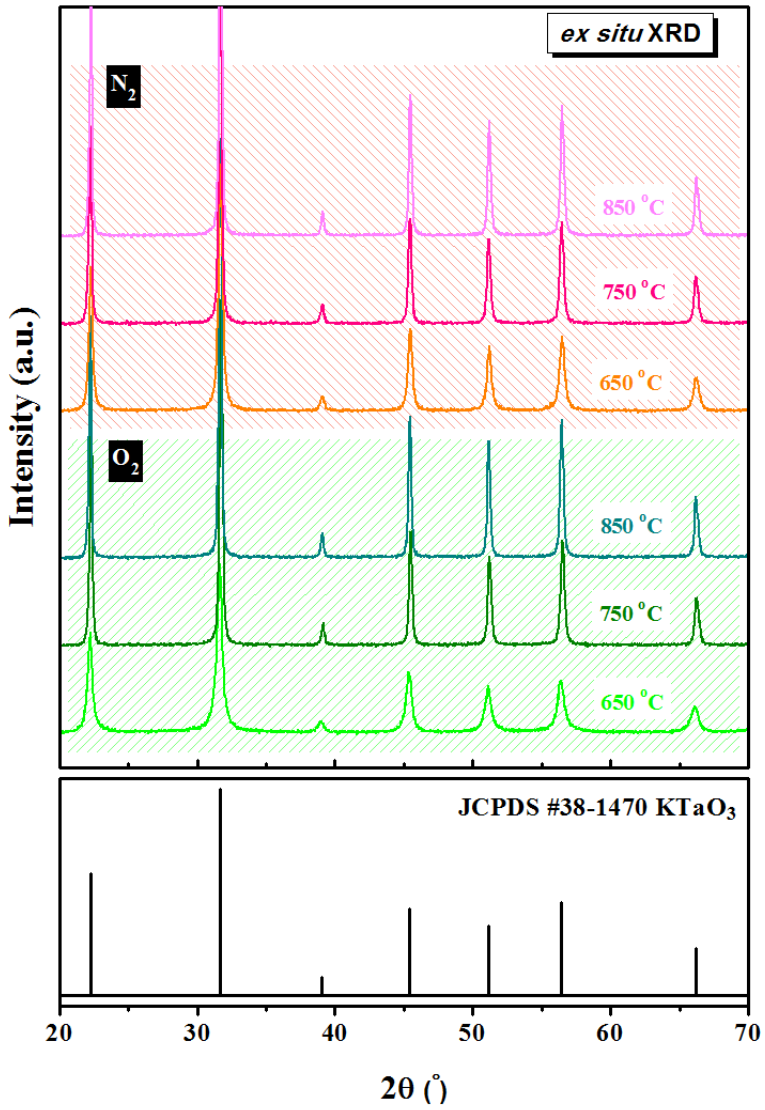

Figure 4-42. Ex situ XRD patterns of the samples annealed at three different temperatures: 650, 750 and 850 °C, and at two distinct atmospheres: O_2 or N_2. The results indicate that there is no evidence of intermediate phases while using processing in the controlled atmospheres, but only a negligible displacement of the diffraction peaks.

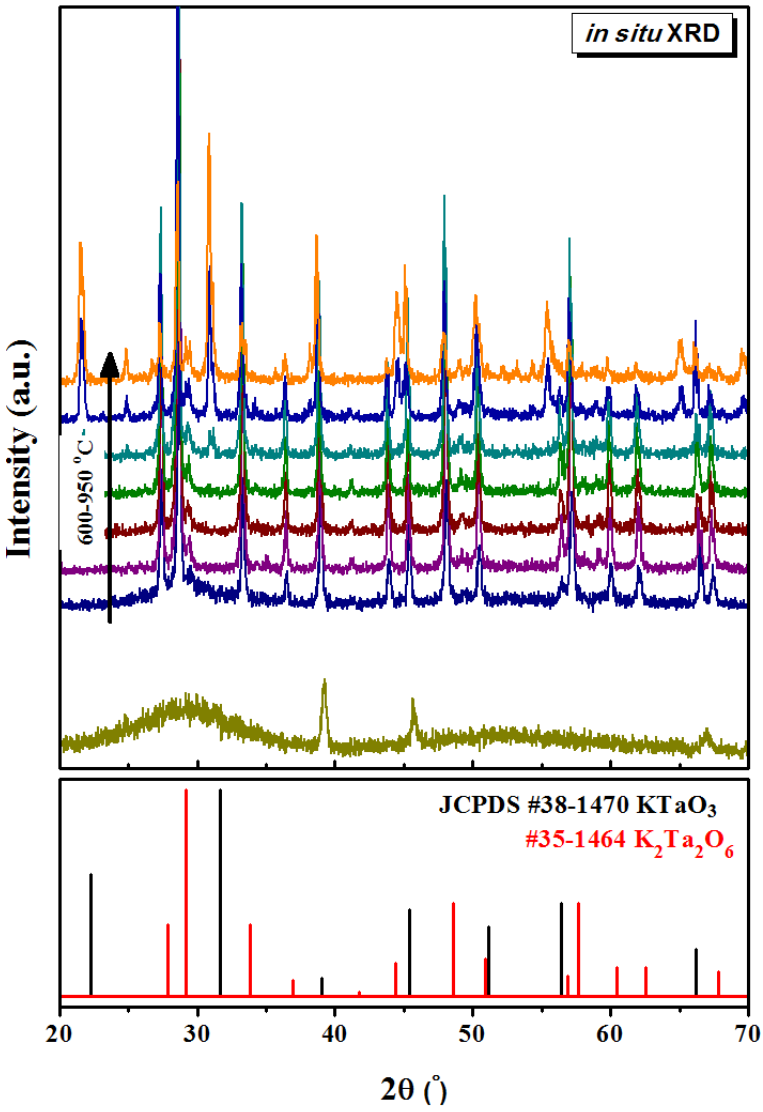

Figure 4-43. X-ray diffraction patterns of solution derived K-Ta powders (via sol-gel), recorded in situ at various temperatures: 600–950 °C (with intervals 50–100 °C). Pyrochlore $K_2Ta_2O_6$ is the main structure in the temperature range of 600–850 °C, while at ≥900 °C the perovskite $KTaO_3$.

Two distinct powders with pyrochlore structures, namely a sol-gel derived $K_2Ta_2O_6$ (KTO*pyr-0*) and a hydrothermally derived $KTa_{2.2}O_6$ (KTO*pyr-1*) one, were used for *in situ* XRD studies, in order to trace the decomposition of phases at higher temperatures and to clarify the presence/appearance of the pyrochlore phase at elevated temperatures. Figure 4-44 shows a set of XRD diffraction patterns recorded at distinct temperatures between 400–1100 °C, presenting the phase evolution for the sol-gel derived $K_2Ta_2O_6$ in Figure 4-44 *(a)*,

and for the hydrothermally prepared $KTa_{2.2}O_6$ in Figure 4-44 *(b)*. Bottom frames include the reference patterns of perovskite $KTaO_3$ (JCPDS-PDF #38-1470), pyrochlore $K_2Ta_2O_6$ (JCPDS-PDF #35-1464) and TTB $K_6Ta_{10.8}O_{30}$ (JCPDS-PDF #70-1088).

For both samples, the patterns recorded at low temperatures of 400–600 °C are very similar, matching well with the diffraction lines of $K_2Ta_2O_6$ JCPDS card. Then, at temperatures >600 °C, the decomposition paths start to be different: in the case of sol-gel derived KTO*pyr-0*, the lines of the perovskite phase appear at >600 °C, while in the case of hydrothermally prepared KTO*pyr-1*, the diffraction lines of the pyrochlore phase are still the only ones up to 900 °C and the TTB phase is evident at >900 °C with the absence of the perovskite phase at any stage. Therefore, the phase formation and decomposition paths in these two pyrochlore structures are different, and this difference is related to the initial stoichiometry, *i.e.* metal K:Ta ratio. It can be assumed that in the case of KTO*pyr-0* synthesized as stoichiometric, with an initial cationic ratio K:Ta ≈ 1 the decomposition product is the stoichiometric perovskite $KTaO_3$, while in the case of KTO*pyr-1* synthesized as non-stoichiometric, the decomposition product has a K:Ta ratio close to the TTB one (0.56). This proves that synthesis route and their conditions determine the stoichiometry of the pyrochlore phase.

Our results somehow contradict the previously reported results of Zhang *et al.* [68]. In Zhang *et al.* [68] report $K_2Ta_2O_6$ decomposes into TTB $K_6Ta_{10.8}O_{30}$ with volatilization of K_2O at 900 °C, and such huge loss of K is possible if long heat treatment at temperatures >900 °C is used. Defect pyrochlores have also been reported in lead-based systems, *e.g.* $Pb_2Ti_2O_6$ [338, 339], when being synthesized at low processing temperatures by solution methods.

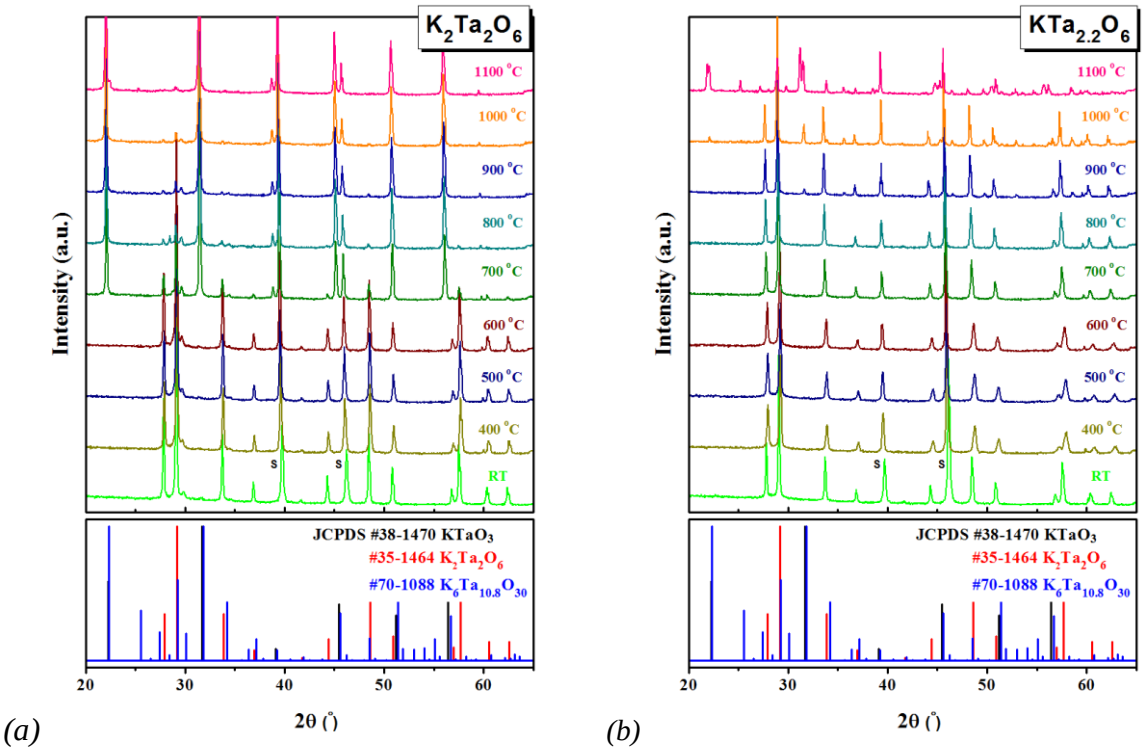

Figure 4-44. In situ XRD patterns of crystalline pyrochlore powders: (a) $K_2Ta_2O_6$ (KTOpyr-0; via sol-gel) and (b) $KTa_{2.2}O_6$ (KTOpyr-1; via hydrothermal method), recorded at various temperatures – 400–1100 °C. The bottom frames depict reference patterns of perovskite $KTaO_3$ (JCPDS-PDF #38-1470), pyrochlore $K_2Ta_2O_6$ (JCPDS-PDF #35-1464) and TTB $K_6Ta_{10.8}O_{30}$ (JCPDS-PDF #70-1088). Two different crystallization paths are detected.

Thermal analyses were also performed to record any physical and chemical changes undergoing during the thermal cycle. Figure 4-45 shows DTA/TG thermographs of amorphous K–Ta powders (which were used to process KTO*pyr-0* by sol-gel), recorded in air, O_2 and N_2, at a heating rate of 40 °C/min. Thermogravimetric changes are illustrated on the Figure 4-45 *(a)* in which the left *y* axis corresponds to the weight losses variation as the temperature increases. The overall losses (at 1000 °C) are: 20.6 % in O_2, 20.1 % in N_2, and 23.1 % in air, yielding no substantial difference. Half of the weight loss (~10 %) takes place upon heating to 200–300 °C. In the temperature range 500–900 °C, two more slight changes are detectable. No significant weight losses were observed above >900 °C. The main content of the weight losses is associated to the release of the organic species accommodated in the amorphous solid network that occur up to 500 °C. Simultaneously, coupled with TG, differential thermal analyses were conducted, and the results are depicted in Figure 4-45 *(a)*,

right *y* axis. The DTA thermographs are mostly composed of exothermic peaks which can be categorized into three groups, independent on the atmosphere. The first one is in the temperature range of 380–480 °C, second one is between 500–650 °C, and third one is between 700–850 °C. The only endothermic reaction occurs at <300 °C (maximum ~160 °C) and is characterised by a broad peak, that corresponds to ~10 % weight loss. This endothermic reaction is primary due to the elimination of residual solvents, as ethanol, and dehydroxylation (physically absorbed water, and possibly chemically bound water) [340].

Figure 4-45 *(b)* presents also the DTA results but the graph is plotted in the temperature range of 300–850 °C and the deduced phases formed on heating are marked. This representative sketch was executed based on the DTA/TG analysis and XRD data. The region of 380–480 °C is related to the organic oxidation effect. The reactions are more obvious in oxidizing atmosphere (revealing sharp peak) and in air atmosphere (revealing a broad peak), than in reducing one. Second range of 500–650 °C is attributed to the crystallization of pyrochlore $K_2Ta_2O_6$ structure. And the last one of 700–850 °C is definitely associated to the crystallization of perovskite $KTaO_3$ phase. The two temperature regimes of the crystalline phases, pyrochlore and perovskite, are overlapped in a certain temperature range.

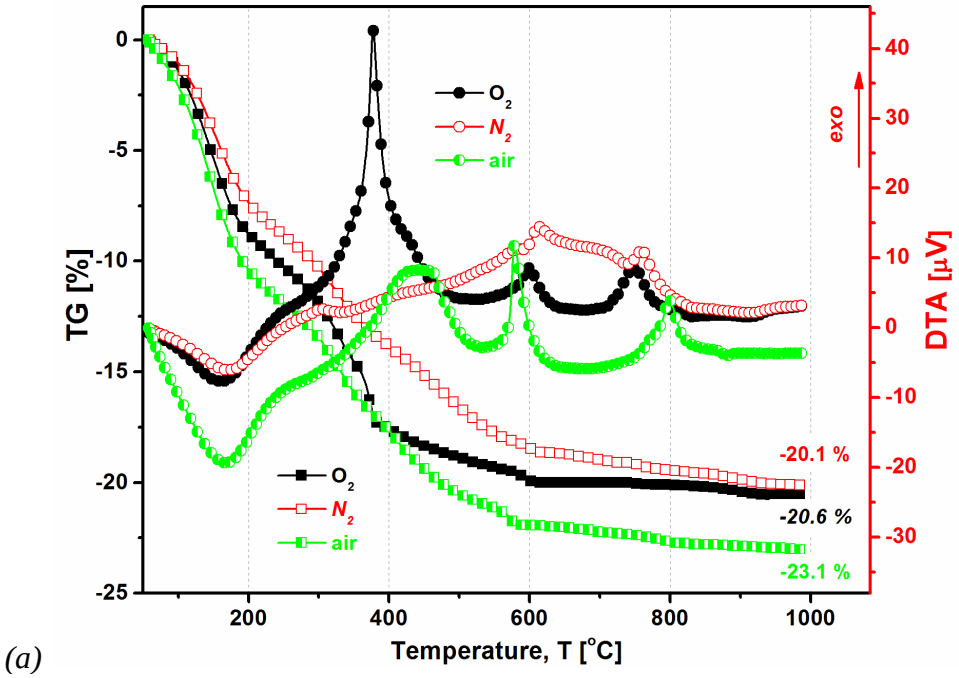

(a)

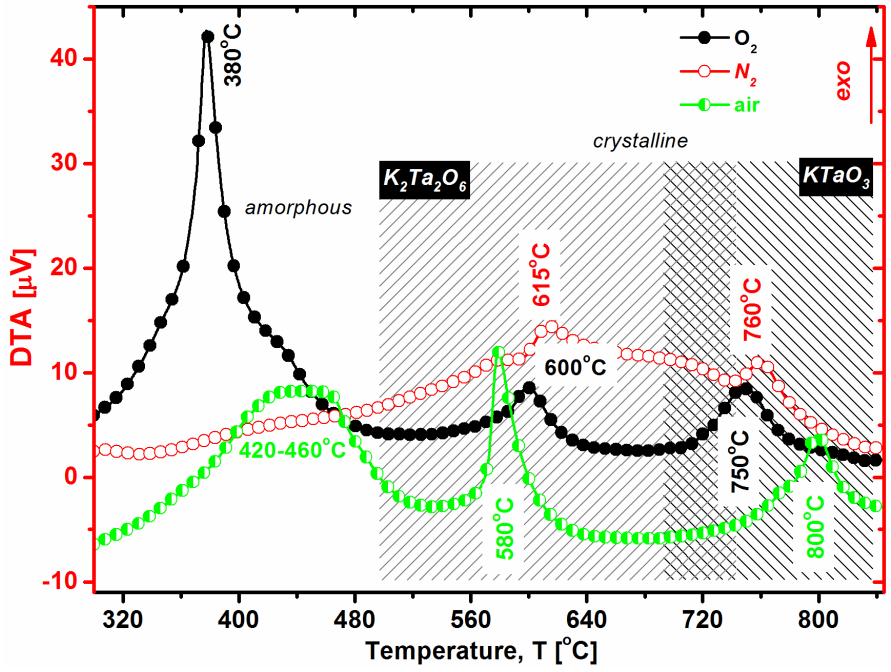

(b)

Figure 4-45. (a) DTA/TG thermographs show the temperature dependence (from room temperature up to 1000 °C) of weight changes (TG), and either exothermic or endothermic changes (DTA), performed in a controlled atmosphere (ambient, O_2 and N_2), at the heating rate of 40 °C/min. (b) DTA thermograph that depicts a temperature range: 300–850 °C, with the indications of particular phase existence: amorphous, pyrochlore and perovskite, deduced from thermographs and XRD results.

4.2.3. Kinetics of the phase formation

For a further understanding of the phase formation process a solid-state kinetic study of the phase formation of potassium tantalate was carried out and high temperature *in situ* XRD was used and processed. The K–Ta powders under investigation were synthesised by a sol-gel process (alkoxide route). The amorphous gels were prepared by exposing the solution to the ambient to promote the hydrolysis, and then dried at 60 °C for 12 h.

The amorphous powders were heated up to the temperatures in the range from 850 to 950 °C, and XRD patterns were collected after different time periods, from 1 to 150 min. Figure 4-46 depicts the *in situ* XRD in the short range of 2θ: 20–23° and 26–29°, that corresponds to the characteristic reflections of (100) $KTaO_3$ phase (left graph) and (311) $K_2Ta_2O_6$ phase (right graph), respectively. The presented XRD patterns were recorded at 850 (Figure 4-46 *(a)*) and 900 °C (Figure 4-46 *(b)*). The intensity of the perovskite (100) reflection is rather constant recorded at both temperatures (and time independent), but the peaks become slightly sharper. On the other hand, the pyrochlore (311) reflection declines with time (well visible in Figure 4-46 *(a)*). Thus, as the dwelling time increases, the gradual conversion of pyrochlore to perovskite phase transformation occurs. A similar behaviour was observed at 875, 925 and 950 °C. The rate of the phase transformation depends on the temperature and heating rate, being faster for the higher thermal conditions.

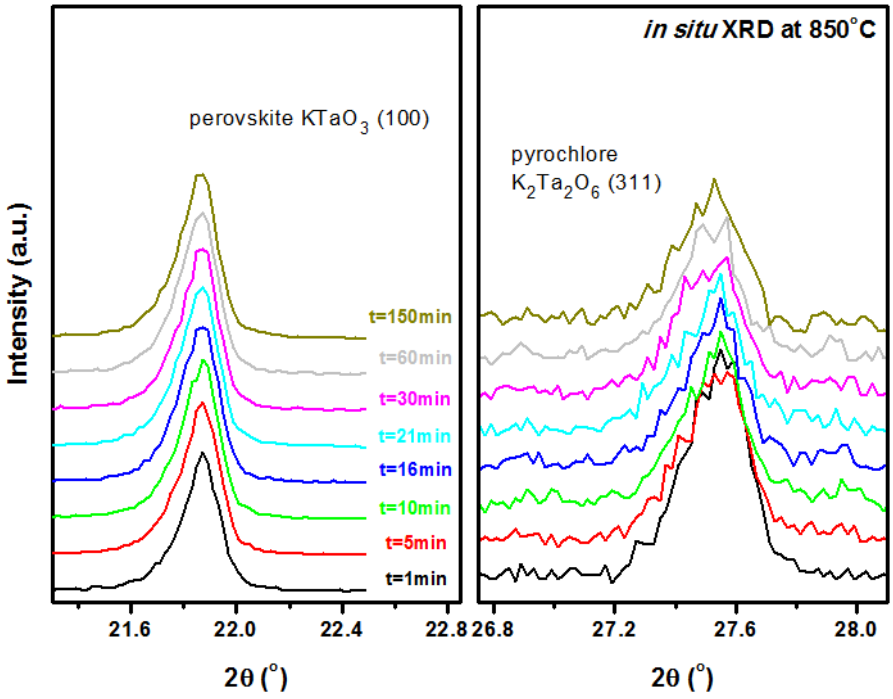

(a)

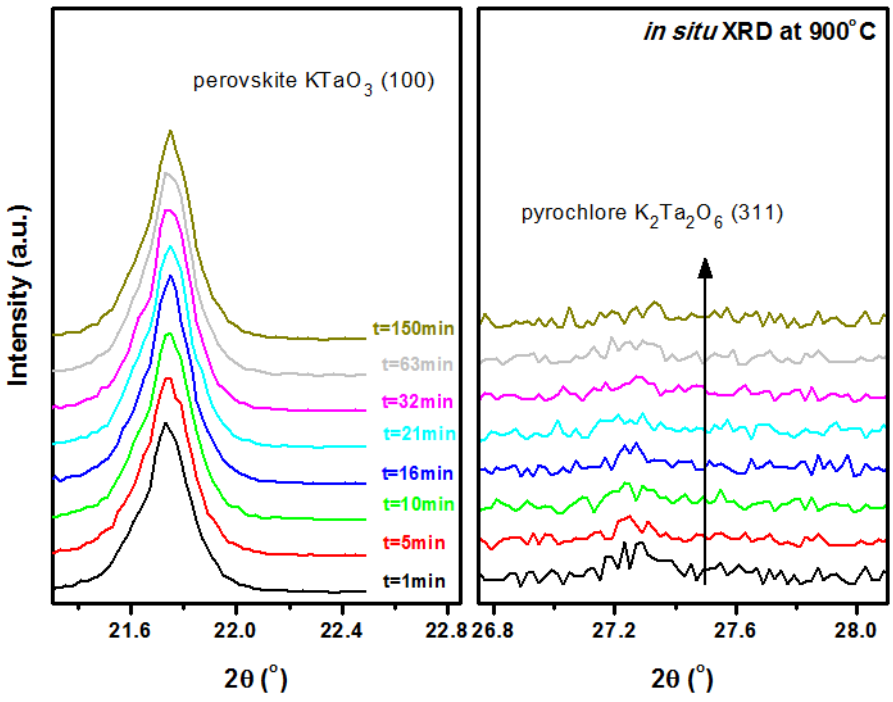

(b)

Figure 4-46. In situ XRD patterns of (100) $KTaO_3$ phase (left; 2θ = 21–22.5°), and (311) $K_2Ta_2O_6$ phase (right; 2θ = 26.7–28.2°), obtained at temperatures: (a) 850, and (b) 900 °C. The results indicate that the perovskite phase is developed with time while the pyrochlore one is reduced.

The kinetic analysis was carried out by using the Johnson-Mehl-Avrami-Kolmogorow (JMAK) model for isothermal crystallization processes, and combined with quantitative XRD data. The (100) reflection of $KTaO_3$, and (311) reflection of $K_2Ta_2O_6$ were selected as representatives of those phases. The used methodology is composed of the two following steps:

A. The volume fraction of crystallized potassium tantalate powders, x_P, as a function of reaction time was extracted from the XRD patterns, using the following equations [341, 342]:

$$x_P = \frac{Pw_A}{1 + (P-1)w_A} \tag{14}$$

where

$$w_A = \frac{I_P(100)}{I_R(311) + I_P(100)} \tag{15}$$

Here, I_P (100) and I_R (311) represent the integrated intensities of the (100) reflection of the perovskite phase, and the (311) reflection of pyrochlore phase, respectively. In present study, the P coefficient, which symbolizes the integrated intensity ratio of pyrochlore (311) reflection to perovskite (100) peak, was determined as 0.347, using the integrated intensities of standard powders. For pyrochlore (311) reflection it was the powder obtained from sol-gel process and annealed at 600 °C for 30 min, and for perovskite (100) reflection it was the powder fabricated by solid-state reaction at 850 °C for 5 h.

B. The volume fraction values, x_P, at time t are expressed by reaction constant k according to the isothermal JMAK kinetic equation [343-345]:

$$x_P = 1 - \exp[-(k \cdot t)^n] \tag{16}$$

Taking natural logarithms and rearranging equation (16), gives:

$$\ln[-\ln(1 - x_P)]_T = n \ln k + n \ln t \tag{17}$$

where, T stands for the temperature, t for the time, k for the reaction rate constant, and n for the Avrami exponent. From the plotted curves of ln [–ln(1–x_P)] versus ln$t$ the Avrami exponent and reaction constant can be extracted from the slope and its intercept with the y axis at each temperature.

Figure 4-47 shows Avrami plots of a $\ln[-\ln(1 - x_P)]$ as a function of $\ln t$ for the powders annealed at 900 and 950 °C. The crystalline fraction of perovskite $KTaO_3$ (x_P) increases with the reaction time.

The Avrami exponent values were also obtained from JMAK plots to determine the nucleation and growth processes. Interestingly, fitted results show that n values depend on the temperature, while the graphical representation clearly demonstrates that crystallization occurs in two stages. The early stage of the reaction at all temperatures, where $n_1 \sim 1.0$ ($R^2 = 0.99$ of the fitted regression line) is characteristic for phase-boundary controlled mechanism, is dominated by primary nucleation. At a later stage, where $n_2 \sim 0.3$ ($R^2 > 0.9$), most likely the slow formation of polycrystalline particles takes place by agglomeration of the already existing KTO crystals. However, the Avrami exponent does not follow any categories described in the JMAK model. Earlier studies on reaction kinetics in strontium bismuth tantalate also showed that the pyrochlore-to-perovskite phase transformation is a nucleation-controlled process and the nucleation of the perovskite phase is the rate-controlling step of the reaction [346]. It is notable that the reaction rate k of perovskite phase formation decreases about 12 times from early to later stage.

Thus, the kinetic study revealed that at the early stage of phase transformation from pyrochlore to perovskite the phase-boundary controlled mechanism takes place. It is reasonable results since the reaction occurs at the solid-solid interface. Nevertheless, those data are not conclusive, requiring further examination, such as thermochemical study, which is essential to understand the stability and reactivity of potassium tantalum oxides.

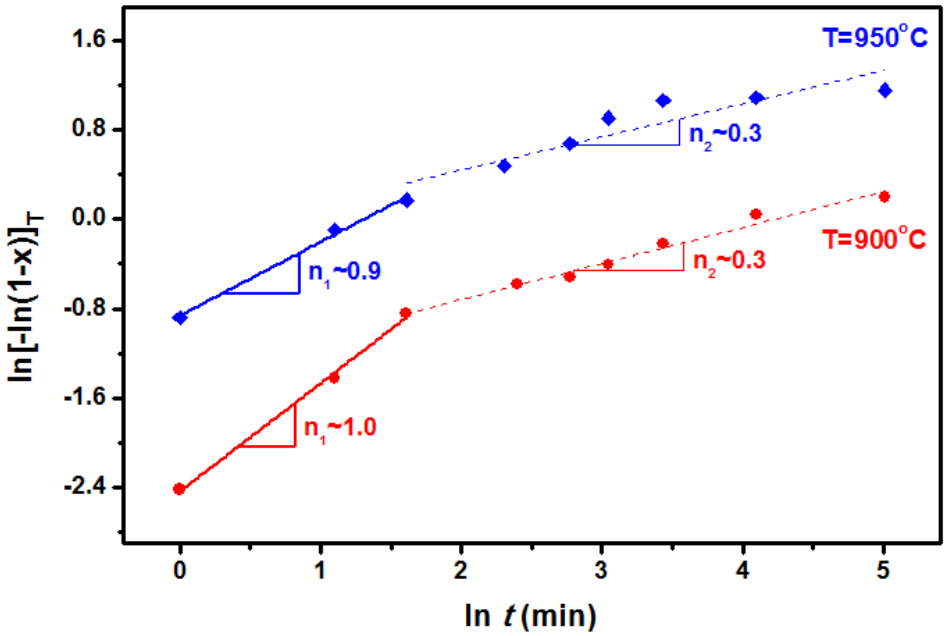

Figure 4-47. Avrami plot of ln [–ln(1–x_P)] as a function of ln t, for powders heat treated at two distinct temperatures: 900 and 950 °C. Two stage reaction is revealed, and at the early stage, n_1 ~ 1, the phase-boundary controlled mechanism is dominant.

4.2.4. Thermochemistry of potassium tantalate oxides

It was demonstrated that the energetics offer insight into phase transitions [330]. The following section reports for the first time thermodynamic data on a set of compounds of potassium tantalum oxide using oxide melt solution calorimetry. Heat capacities, standard entropies and enthalpies of formation, phase transformation and fusion can be obtained with calorimetric methods [301]. Recent developments in high-temperature oxide melt solution calorimetry make it possible to measure the energetics of refractory materials such as tantalates [300, 302]. Using this methodology, the formation and decomposition enthalpies of K–Ta oxides prepared by conventional solid state route and wet chemical based syntheses are obtained. Possible thermodynamic reasons for the perovskite formation and decomposition are discussed. Moreover, the stoichiometry of defect pyrochlore structure is addressed, as being poorly reported and discussed in the literature.

Figure 4-48 depicts the XRD patterns at 20–50° 2θ of the perovskite $KTaO_3$: KTO*per-1* and KTO*per-2*, and pyrochlores: KTO*pyr-0*, KTO*pyr-1*, KTO*pyr-2*, KTO*pyr-3*. At the bottom frame the reference patterns of perovskite $KTaO_3$ (JCPDS-PDF #38-1470) and defect pyrochlore $K_2Ta_2O_6$ (JCPDS-PDF #35-1464), are shown for comparative indexing. All the samples are monophasic within the detection limit of the equipment, *i.e.* for all the samples there are no additional Bragg reflections coming from secondary phases, except KTO*pyr-0*. Refined lattice parameter, *a*, is 3.9812 ± 0.0005 Å (-0.25 %) for KTO*per-1*, 3.9752 ± 0.0013 Å (-0.35 %) for KTO*per-2*, and 10.6141 ± 0.0003 Å (+0.17 %) for KTO*pyr-1*, 10.6214 ± 0.0010 Å (+0.24 %) for KTO*pyr-2* and 10.6227 ± 0.0011 Å (+0.25 %) for KTO*pyr-3*; the values in brackets reflect the differences of a parameter in respect to the references in JCPDS cards, particularly to 3.9891 Å (JCPDS-PDF #38-1470) and 10.5961 Å (JCPDS-PDF #35-1464) for $KTaO_3$ and $K_2Ta_2O_6$, respectively. In the case of KTO*pyr-0*, the lattice parameter was not refined, since the XRD pattern indicates the presence of secondary phases, making synthesized KTO*pyr-0* also not suitable for thermochemical measurements. Looking to the unit cell parameter of non-stoichiometric pyrochlores, it is detected that the lattice parameter increases with increasing KOH concentration in the hydrothermal processing. Such dependence should be related to the composition variation, presented in Table 4-9, particularly to the K:Ta ratio.

Compositional EPMA analyses were performed. For microprobe analysis, KTO*per* and KTO*pyr* powders were pelletized and annealed at 800 °C and 300 °C for 3 h in air, respectively. Annealing did not change the phase composition of the samples. XRD confirmed no change in diffraction patterns after heating, whereas the weight loss of each pellet after sintering was <0.1 %; the results are presented in Table 4-9. The $KTaO_3$ perovskites are confirmed to be stoichiometric, while all obtained pyrochlores are potassium deficient with K:Ta ratio of ranging from 0.39 to 0.60. Because K atoms are relatively big, their higher content in the crystal structure leads to an expansion of the lattice volume, and hence increase in the lattice parameter *a*. High metal non-stoichiometry was already reported in hydrothermally produced pyrochlore KTO [63, 64]. It was observed that a K:Ta ratio was ~0.5 and proposed that one of the oxygen atoms in the Ta_2O_6 unit is substituted by a hydroxyl ion making the compound hydrated. Additionally, Goh and co-workers [64] reported that at higher OH^- concentration the nearly stoichiometric perovskite is formed while at a lower OH^- concentration the non-stoichiometric pyrochlore is the one to be formed, whereas the

transformation takes place via a dissolution of pyrochlore and reprecipitation of perovskite with K:Ta ratio ~1. The structure of non-stoichiometric defect pyrochlore was described as Ta_2O_6 framework composed exclusively of vertex-shared octahedra, *i.e.* porous octahedral molecular sieve with three-dimensional tunnels [63].

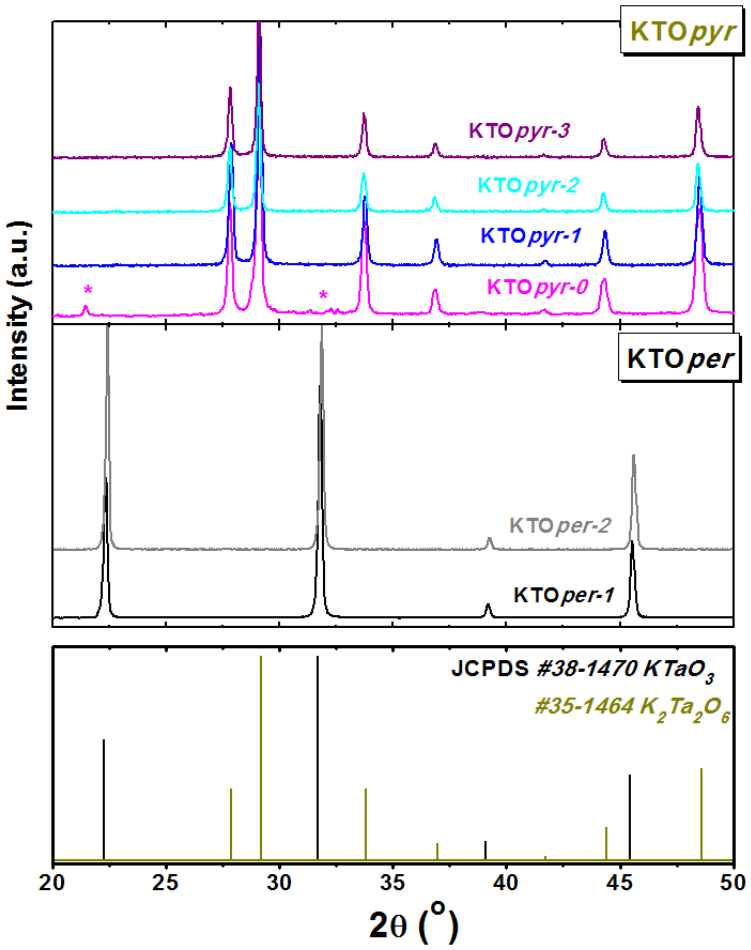

*Figure 4-48. X-ray diffraction patterns of as-prepared KTO powders with perovskite structure: KTOper-1 and KTOper-2, and with pyrochlore structure: KTOpyr-0, KTOpyr-1, KTOpyr-2 and KTOpyr-3. Bottom frame presents reference patterns of perovskite $KTaO_3$ (JCPDS-PDF #38-1470) and pyrochlore $K_2Ta_2O_6$ (JCPDS-PDF #35-1464). All patterns, except KTOpyr-0, show only characteristic peaks of either perovskite or pyrochlore phase. * – second phase.*

Calorimetric measurements were repeated several times to achieved statistically reliable data. The raw data of KTO*per-1* and KTO*per-2* are shown in Table 4-10.

Table 4-10. Statistical calorimetric data for perovskites. Enthalpy of drop solution, ΔH_{ds}, in sodium molybdate at 702 °C. The average value and associated error (two standard deviations from the mean) are calculated from nine values.

$KTaO_3$ (KTOper-1)		***$KTaO_3$ (KTOper-2)***	
Mass, mg	*ΔH_{ds} kJ/mol*	*Mass, mg*	*ΔH_{ds} kJ/mol*
5.215	90.7471	5.335	89.2084
5.166	90.4769	4.646	89.2368
5.002	88.9262	4.430	87.8421
4.700	86.8147	4.529	86.8354
5.538	87.2222	4.502	88.8905
5.283	91.6004	5.134	89.0048
5.242	90.6078	5.214	87.3470
4.910	90.0860	5.138	87.9821
5.301	88.8615	5.102	91.0690
	89.46 ± 0.98		**88.60 ± 0.84**

The enthalpies of drop solution, ΔH_{ds}, of KTO*per-1*, KTO*per-2*, KTO*pyr-1*, KTO*pyr-2* and KTO*pyr-3* are 89.46 ± 0.98, 88.60 ± 0.84, 300.50 ± 3.67, 287.82 ± 3.05, and 255.15 ± 1.41 kJ/mol, respectively, as summarized in Table 4-11. Thus there is no significant difference between the drop solution enthalpies of the two synthesized perovskites. The average ΔH_{ds} of $KTaO_3$, calculated using both KTO*per-1* and KTO*per-2* data is 89.03 ± 1.29 kJ/mol. It was used for the formation enthalpy calculations (presented in the previous section of the thesis (see Table 4-6).

Table 4-11. The drop solution enthalpies of perovskites, pyrochlores and Ta_2O_5. The average value and associated error (two standard deviations of the mean) are calculated from a number of values (8-9).

Compounds	***ΔH_{ds} (kJ/mol) in 2 $Na_2O \cdot 4\ MoO_3$***
$KTaO_3$ (KTOper-1)	89.46 ± 0.98 (9)
$KTaO_3$ (KTOper-2)	88.60 ± 0.84 (9)
$KTaO_3$	(89.03 ± 1.29) [#]
$K_{0.873}Ta_{2.226}O_6$ (KTOpyr-1)	300.50 ± 3.67 (8)
$K_{1.128}Ta_{2.175}O_6$ (KTOpyr-2)	287.82 ± 3.05 (8)
$K_{1.291}Ta_{2.142}O_6$ (KTOpyr-3)	255.15 ± 1.41 (9)
$K_2Ta_2O_6$	(180.68 ± 4.48) [§]
Ta_2O_5	(90.41 ± 2.5) [*]

[#]: Calculated from average of $KTaO_3$ (KTO*per-1*) and $KTaO_3$ (KTO*per-2*), and used for further calculations.
[§]: Extrapolated drop solution enthalpy of $K_{0.873}Ta_{2.226}O_6$ (KTO*pyr-1*), $K_{1.128}Ta_{2.175}O_6$ (KTO*pyr-2*) and $K_{1.291}Ta_{2.142}O_6$ (KTO*pyr-3*) to $K_2Ta_2O_6$ composition.
[*]: ΔH_{ds}<Ta_2O_5> 702 °C = ΔH_{ds} <Ta_2O_5> at 802 °C - ($H_{702\text{-}802^\circ C}$) = (112.88 ± 1.37) kJ/mol - [(131.36 ± 1.52) - (108.89 ± 1.50)] kJ/mol = (90.41 ± 2.5) kJ/mol.
where, ΔH_{ds}<Ta_2O_5> at 802 °C = (112.88 ± 1.37) kJ/mol, ($H_{702\text{-}802^\circ C}$) = ($H_{25\text{-}802^\circ C}$) - ($H_{25\text{-}702^\circ C}$), ($H_{25\text{-}702^\circ C}$) = (108.89 ± 1.50) kJ/mol and ($H_{25\text{-}802^\circ C}$) = (131.36 ± 1.52) kJ/mol.

Drop solution enthalpy of the stoichiometric pyrochlore phase, $K_2Ta_2O_6$ was determined from the extrapolated ΔH_{ds} of $K_{0.873}Ta_{2.226}O_6$ (KTO*pyr-1*), $K_{1.128}Ta_{2.175}O_6$ (KTO*pyr-2*) and $K_{1.291}Ta_{2.142}O_6$ (KTO*pyr-3*) as shown in Figure 4-49 to be 180.68 kJ/mol with an estimated uncertainty of 4.48 kJ/mol.

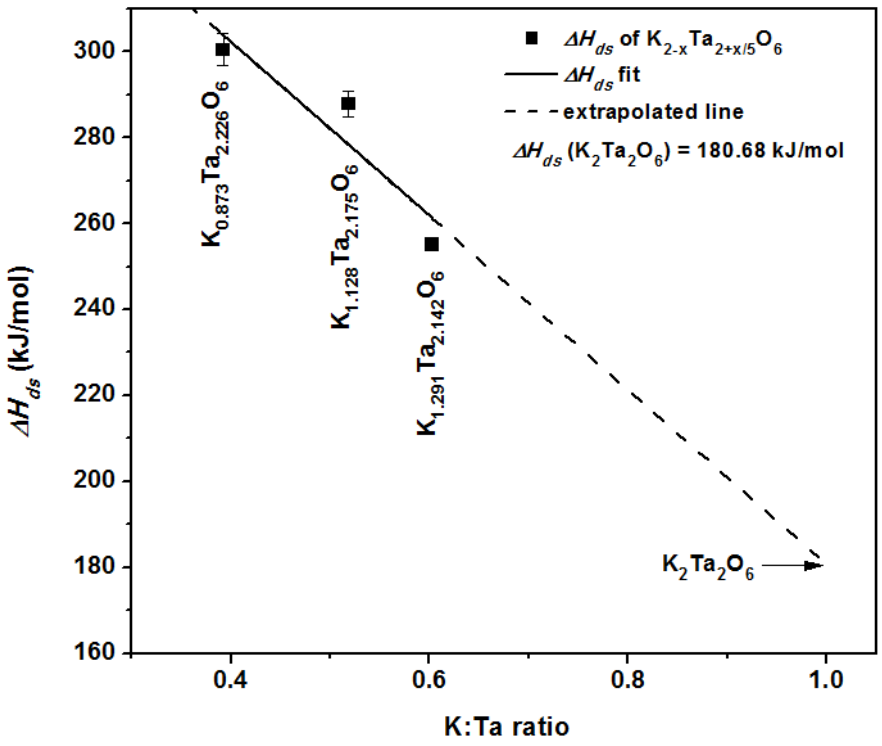

Figure 4-49. Plot of drop solution enthalpies of $K_{0.873}Ta_{2.226}O_6$ (KTOpyr-1), $K_{1.128}Ta_{2.175}O_6$ (KTOpyr-2) and $K_{1.291}Ta_{2.142}O_6$ (KTOpyr-3) vs K:Ta ratio.

The enthalpy of drop solution of K_2O in 3 Na_2O · 4 MoO_3 at 702 °C was taken from the literature [306]. Because of the slow dissolution of Ta_2O_5 in 3 Na_2O · 4 MoO_3 at 702 °C, the ΔH_{ds} of Ta_2O_5 was calculated at this temperature using the ΔH_{ds} of Ta_2O_5 in 3 Na_2O · 4 MoO_3 at 802 °C and the enthalpy increment from 702 °C to 802 °C, as shown in Table 4-12. The calculated drop solution enthalpy of Ta_2O_5 in 3 Na_2O · 4 MoO_3 at 702 °C is 90.41 ± 2.54 kJ/mol. For calculation of the enthalpies of formation from the elements, the enthalpies of formation of binary oxides from Robie *et al.* [305] were used.

Table 4-12. Calorimetric data for Ta_2O_5 - enthalpy of drop solution. The average value and associated error (two standard deviations from the mean).

Drop solution enthalpy at 802 °C		***Enthalpy increment ($H_{25\text{-}700°C}$)***		***Enthalpy increment ($H_{25\text{-}800°C}$)***	
Mass, mg	*ΔH_{ds} kJ/mol*	*Mass, mg*	*($H_{25\text{-}700°C}$) kJ/mol*	*Mass, mg*	*($H_{25\text{-}800°C}$) kJ/mol*
5.257	113.0996	7.087	110.2753	7.185	129.9732
5.617	114.8945	6.017	107.0827	5.182	130.4131
4.976	110.3256	6.738	107.4700	5.365	134.3246
7.808	115.3957	5.404	112.8443	6.615	130.8244
5.257	110.8581	4.431	112.0074	5.404	127.9982
5.207	111.4876	5.336	108.0637	5.963	130.6536
5.751	116.4064	5.026	108.0615	5.208	129.9568
5.415	113.0161	6.201	107.4491	5.142	131.6881
5.415	113.0161	5.533	106.7221	6.406	136.3741
6.251	110.3266				
	112.88 ± 1.37		**108.89 ± 1.50**		**131.36 ± 1.52**

The enthalpies of formation from component oxides and elements were obtained using suitable thermodynamic cycle presented in Table 4-6 and Table 4-13 for $KTaO_3$ and KTO*pyr* (pyrochlores with different stoichiometry), respectively. The calculated enthalpies of formation from corresponding oxides, ΔH_f^{ox}, for $KTaO_3$, $K_{0.873}Ta_{2.226}O_6$, $K_{1.128}Ta_{2.175}O_6$, $K_{1.291}Ta_{2.142}O_6$ and $K_2Ta_2O_6$ are -203.63 ± 2.92, -339.54 ± 5.03, -369.71 ± 4.84, - 364.78 ± 4.24 and -409.87 ± 6.89 kJ/mol, respectively, whereas those from elements, ΔH_f^{el}, for $KTaO_3$, $K_{0.873}Ta_{2.226}O_6$, $K_{1.128}Ta_{2.175}O_6$, $K_{1.291}Ta_{2.142}O_6$ and $K_2Ta_2O_6$ are - 1408.23 ± 3.75, -2775.46 ± 6.92, -2800.60 ± 6.76, -2790.68 ± 6.33 and - 2819.07 ± 8.42 kJ/mol, respectively.

Table 4-13. Thermodynamic cycle for obtaining the enthalpies of formation from oxides and elements for pyrochlores.

	Reaction	Enthalpies
From oxides	(8) $K_2O_{(xl,\ 25^\circ C)} \rightarrow K_2O_{(soln,\ 702^\circ C}$	ΔH_8 = -319.6 ± 4.6 kJ/mol [306]
	(9) $Ta_2O_{5\ (xl,\ 25^\circ C)} \rightarrow Ta_2O_{5\ (soln,\ 702^\circ C)}$	ΔH_9 = 90.41 ± 2.5 kJ/mo
	(10) $K_{0.873}Ta_{2.226}O_{6\ (xl,\ 25^\circ C)}$ → 0.437 $K_2O_{(soln,\ 702^\circ C)}$ + 1.113 $Ta_2O_{5\ (soln,\ 702^\circ C)}$	ΔH_{10} = 300.50 ± 4.76 kJ/mol
	(11) $K_{1.128}Ta_{2.175}O_{6\ (xl,\ 25^\circ C)}$ → 0.564 $K_2O_{(soln,\ 702^\circ C)}$ + 1.088 $Ta_2O_{5\ (soln,\ 702^\circ C)}$	ΔH_{11}= 287.82 ± 3.25 kJ/mol
	(12) $K_{1.291}Ta_{2.142}O_{6\ (xl,\ 25^\circ C)}$ → 0.646 $K_2O_{(soln,\ 702^\circ C)}$ + 1.071 $Ta_2O_{5\ (soln,\ 702^\circ C)}$	ΔH_{12} = 255.15 ± 1.41 kJ/mol
	(13) $K_2Ta_2O_{6\ (xl,\ 25^\circ C)} \rightarrow K_2O_{(soln,\ 702^\circ C)}$ + $Ta_2O_{5\ (soln,\ 702^\circ C)}$	ΔH_{13} = 180.68 ± 4.48 kJ/mol
	(14) 0.437 $K_2O_{(xl,\ 25^\circ C)}$ + 1.113 $Ta_2O_{5\ (xl,\ 25^\circ C)}$ → $K_{0.873}Ta_{2.226}O_{6\ (xl,\ 25^\circ C)}$	ΔH_{14} = 0.437 ΔH_8 + 1.113 ΔH_9 - ΔH_{10} = -339.54 ± 5.03 kJ/mol
	(15) 0.564 $K_2O_{(xl,\ 25^\circ C)}$ + 1.088 $Ta_2O_{5\ (xl,\ 25^\circ C)}$ → $K_{1.128}Ta_{2.175}O_{6\ (xl,\ 25^\circ C)}$	ΔH_{15} = 0.564 ΔH_8 + 1.088 ΔH_9 - ΔH_{11} = -369.71 ± 4.84 kJ/mol
	(16) 0.646 $K_2O_{(xl,\ 25^\circ C)}$ + 1.071 $Ta_2O_{5\ (xl,\ 25^\circ C)} \rightarrow K_{1.291}Ta_{2.142}O_{6\ (xl,\ 25^\circ C)}$	ΔH_{16} = 0.646 ΔH_8 + 1.071 ΔH_9 - ΔH_{12} = -364.78 ± 4.24 kJ/mol
	(17) $K_2O_{(xl,\ 25^\circ C)}$ + $Ta_2O_{5\ (xl,\ 25^\circ C)} \rightarrow K_2Ta_2O_{6\ (xl,\ 25^\circ C)}$	ΔH_{17} = ΔH_8 + ΔH_9 - ΔH_{13} = -409.87 ± 6.89 kJ/mol
From elements	(18) 2 K + ½ $O_2 \rightarrow K_2O$	ΔH_{18} = $\Delta H_f^{el}{}_{<K2O>}$ = -363.2 ± 2.4 kJ/mol [305]
	(19) 2 Ta + 5/2 $O_2 \rightarrow Ta_2O_5$	ΔH_{19} = $\Delta H_f^{el}{}_{<Ta2O5>}$ = -2046.5 ± 4.2 kJ/mol [305]
	(20) 0.873 $K_{(xl,\ 25^\circ C)}$ + 2.226 $Ta_{(xl,\ 25^\circ C)}$ + 3 $O_2 \rightarrow K_{0.873}Ta_{2.226}O_{6\ (xl,\ 25^\circ C)}$	ΔH_{20} = $\Delta H_f^{el}{}_{<K0.873Ta2.226O6>}$ = 0.437 ΔH_{18} + 1.113 ΔH_{19}+ ΔH_{14} = -2775.46 ± 6.92 kJ/mol
	(21) 1.128 $K_{(xl,\ 25^\circ C)}$ + 2.175 $Ta_{(xl,\ 25^\circ C)}$ + 3 $O_2 \rightarrow K_{1.128}Ta_{2.175}O_{6\ (xl,\ 25^\circ C)}$	ΔH_{21} = $\Delta H_f^{el}{}_{<K1.128Ta2.175O6>}$ = 0.564 ΔH_{18} + 1.088 ΔH_{19} + ΔH_{15} = -2800.60 ± 6.76 kJ/mol
	(22) 1.291 $K_{(xl,\ 25^\circ C)}$ + 2.142 $Ta_{(xl,\ 25^\circ C)}$ + 3 $O_2 \rightarrow K_{1.291}Ta_{2.142}O_{6\ (xl,\ 25^\circ C)}$	ΔH_{22} = $\Delta H_f^{el}{}_{<K1.291Ta2.142O6>}$ = 0.646 ΔH_{18} + 1.071 ΔH_{19} + ΔH_{16} = -2790.68 ± 6.33 kJ/mol
	(23) $2K_{(xl,\ 25^\circ C)}$+2 $Ta_{(xl,\ 25^\circ C)}$+3 $O_2 \rightarrow K_2Ta_2O_{6\ (xl,\ 25^\circ C)}$	ΔH_{23} = $\Delta H_f^{el}{}_{<K2Ta2O6>}$ = ΔH_{18} + ΔH_{19} + ΔH_{17} = -2819.07 ± 8.42 kJ/mol

Figure 4-50 represents the formation enthalpies of pyrochlores with different stoichiometries. The stability of pyrochlores increases with increase in the K:Ta ratio thereby confirming that the stoichiometric pyrochlore is energetically more stable than to the non-stoichiometric ones. Moreover, the formation enthalpy of 2 $KTaO_3$ (perovskites) (2 ΔH_f^{ox} = 2 (-203.63 ± 2.92) kJ/mol = -407.26 ± 5.84 kJ/mol is just by 2.62 ± 9.03 kJ/mol higher than that of $K_2Ta_2O_6$ (pyrochlore). Futhermore, plotting these values in Figure 4-50, one can find that the stability of $K_2Ta_2O_6$ (pyrochlore) and 2 $KTaO_3$ (perovskites) is almost the same within the experimental error.

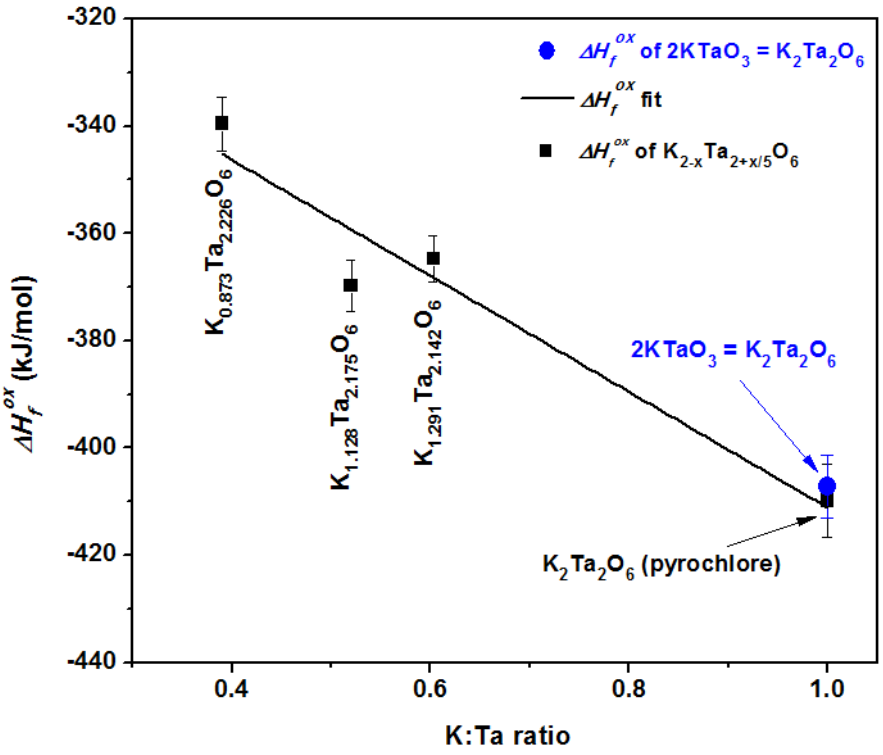

Figure 4-50. Plot of formation enthalpies of $K_{0.873}Ta_{2.226}O_6$ (KTOpyr-1), $K_{1.128}Ta_{2.175}O_6$ (KTOpyr-2) and $K_{1.291}Ta_{2.142}O_6$ (KTOpyr-3) vs K:Ta ratio.

Additionally, the TTB $K_6Ta_{10.8}O_{30}$ sample was synthesized and then analysed. The drop solution enthalpy is 781.75 ± 8.85 kJ/mol. The enthalpies of formation were obtained using the thermodynamic cycle presented in Table 4-14. The calculated enthalpy of formation from corresponding oxides, ΔH_f^{ox}, is -1252.34 ± 10.10 kJ/mol, and from elements, ΔH_f^{el}, is - 13393.04 ± 31.15 kJ/mol. Therefore, the possible decomposition reactions of K-deficient

KTO*pyr-1* pyrochlore to $KTaO_3$ perovskite and Ta_2O_5 (reaction 1) or to $K_6Ta_{10.8}O_{30}$ and Ta_2O_5 (reaction 2) were proposed, and the enthalpies were calculated to be 308.79 ± 4.41 kJ/mol and 895.79 ± 8.64 kJ/mol for reaction 1 and reaction 2, respectively. The reactions are strongly endothermic, indicating that these decompositions are energetically unfavourable, since it is unlikely that any entropy term could override such a large positive enthalpy. Hence, repeated compositional analysis of KTO*ttb* revealed compositional inhomogeneities, with possible secondary phases (not detected by XRD). Thus, the calculated enthalpies of formation of KTO*ttb* had to be excluded for further considerations in the phase decomposition paths.

Further discussion was conducted only on non-stoichiometric and stoichiometric KTO*pyr* and KTO*per* samples. The decomposition enthalpy of the stoichiometric pyrochlore ($K_2Ta_2O_6$) to the perovskite ($KTaO_3$), corresponding to the reaction: $K_2Ta_2O_6$ *pyr* → $KTaO_3$ *per*, is 2.62 ± 5.17 kJ/mol, determined from the drop solution enthalpy differences (Table 4-15) and indicates that the pyrochlore is energetically slightly more stable than perovskite, and is consistent with pyrochlore being the low temperature phase. This result agrees with the previous observations [60, 61].

Table 4-14. Thermodynamic cycle for obtaining the enthalpies of formation from oxides and elements for TTB $K_6Ta_{10.8}O_{30}$.

	Reaction	**Enthalpy of drop solution**
From oxides	(24) $K_2O_{(xl,\ 25^\circ C)} \rightarrow K_2O_{(soln,\ 702^\circ C}$	ΔH_{24} = -319.6 ± 4.6 kJ/mol [306]
	(25) $Ta_2O_{5\ (xl,\ 25^\circ C)} \rightarrow Ta_2O_{5\ (soln,\ 702^\circ C)}$	ΔH_{25} = 90.41 ± 2.5 kJ/mo
	(26) $K_6Ta_{10.8}O_{30\ (xl,\ 25^\circ C)} \rightarrow 3\ K_2O_{(soln,\ 702^\circ C)} + 5.4\ Ta_2O_{5\ (soln,\ 702^\circ C)}$	ΔH_{26} = 781.75 ± 5.85kJ/mol
	(27) $3\ K_2O_{(xl,\ 25^\circ C)} + 5.4\ Ta_2O_{5\ (xl,\ 25^\circ C)} \rightarrow K_6Ta_{10.8}O_{30\ (xl,\ 25^\circ C)}$	$\Delta H_{27} = 3\ \Delta H_{24} + 5.4\ \Delta H_{25} - \Delta H_{26}$ = **-1252.34 ± 20.10 kJ/mol**
From elements	(28) $3\ K_2O_{(xl,\ 25^\circ C)} + 5.4\ Ta_2O_{5\ (xl,\ 25^\circ C)} \rightarrow K_6Ta_{10.8}O_{30\ (xl,\ 25^\circ C)}$	$\Delta H_f^{ox}{}_{<K6Ta10.8O30>}$ = -1252.34 ±20.10 kJ/mol (ΔH_4)
	(29) $2\ K + ½\ O_2 \rightarrow K_2O$	$\Delta H_f^{el}{}_{<K2O>}$ = -363.2 ± 2.1 kJ/mol [305]
	(30) $2\ Ta + 5/2\ O_2 \rightarrow Ta_2O_5$	$\Delta H_f^{el}{}_{<Ta2O5>}$ = -2046.0 ± 4.2 kJ/mol [305]
	(31) $6\ K_{(xl,\ 25^\circ C)} + 10.8\ Ta_{(xl,\ 25^\circ C)} + 15\ O_2 \rightarrow K_6Ta_{10.8}O_{30\ (xl,\ 25^\circ C)}$	$\Delta H_f^{el}{}_{<K6Ta10.8O30>} = \Delta H_f^{ox}{}_{<K6Ta10.8O30>} + 3\ \Delta H_f^{el}{}_{<K2O>} + 5.4\ \Delta H_f^{el}{}_{<Ta2O5>}$ = **-13393.04 ± 31.15 kJ/mol**

Table 4-15. The drop solution enthalpy difference for the decomposition of pyrochlore ($K_2Ta_2O_6$) to perovskite ($KTaO_3$).

Reaction	Enthalpy difference of drop solution
$KTaO_3$ *per* (s, 25 °C) = $KTaO_3$ *per* (sol, 702 °C)	ΔH_{ds} = (89.03 ± 1.29) kJ/mol
$K_2Ta_2O_6$ *pyr* (s, 25 °C) = $K_2Ta_2O_6$ *pyr* (sol, 702 °C)	ΔH_{ds} = (180.68 ± 4.48) kJ/mol
$K_2Ta_2O_6$ *pyr* (s, 25 °C) = 2 $KTaO_3$ *per* (s, 25 °C)	$\Delta H_{decomp.}$ = (180.68 ± 4.48) - 2 (89.03 ± 1.29) = (2.62 ± 5.17) kJ/mol

It was experimentally proven (see Figure 4-44) as well as reported by Buršík *et al.* [60] that the stoichiometric pyrochlore ($K_2Ta_2O_6$) transforms into perovskite phase ($KTaO_3$) on heating to or above ~600 °C. Based on this transition temperature of pyrochlore to perovskite and assuming that the transition temperature is a reversible one, the entropy change corresponding to $K_2Ta_2O_6$ *pyr* → $KTaO_3$ *per* is (2620 J/mol) / (873 K) = 3.00 J/(mol·K). This calculated change in entropy for one formula unit of $K_2Ta_2O_6$ can be attributed to vibrational entropy, as any source of configurational entropy is minor since perovskite is unlikely to be disordered.

Table 4-16 presents the comparative experimental thermochemical data from this work and theoretical ones reported by Shigemi *et al.* [347]; there is a lack of data for K-deficient (non-stoichiometric) pyrochlores in the literature. Additionally, enthalpies of formation of constituent oxides, K_2O and Ta_2O_5 published by Robie *et al.* [305], are also included. The theoretical enthalpies of formation were evaluated using a plane-wave pseudopotential method within a density functional formalism, for the following crystal structures: K_2O (cubic, $Fm\bar{3}m$), Ta_2O_5 (monoclinic, *A2/m*) and $KTaO_3$ (cubic, $Fm\bar{3}m$). The values for potassium oxide are in relatively good agreement, within 10 % error. However for Ta_2O_5 and perovskite $KTaO_3$ the error is >10 %. For the later cases the simulations represent values being relatively far from the experimental ones that can be associated to the crystal structure selected for modelling. These energetic values provide experimentally determined data of thermodynamic stability of various potassium tantalum oxides, and may support discussion in further studies.

Table 4-16. Theoretical and experimental enthalpies of formation for K_2O, Ta_2O_5, $KTaO_3$, $K_{0.873}Ta_{2.226}O_6$, $K_{1.128}Ta_{2.175}O_6$, $K_{1.291}Ta_{2.142}O_6$, and $K_2Ta_2O_6$.

Compound	Enthalpies of formation, kJ/mol	
	Theoretical	*Experimental*
K_2O	-328.5 [347]	-358.0 [305] (+8.2 %)
Ta_2O_5	-1725.2 [347]	-2046.5 [305] (+15.7 %)
$KTaO_3$	-1221.5 [347]	-1408.23 ± 3.75 ^{el} (+13.3 %) (-203.63 ± 2.92) ^{ox}
$K_{0.873}Ta_{2.226}O_6$	-	(-2775.46 ± 6.92) ^{el} (-339.54 ± 5.03) ^{ox}
$K_{1.128}Ta_{2.176}O_6$	-	(-2800.60 ± 6.76) ^{el} (-369.71 ± 4.84) ^{ox}
$K_{1.291}Ta_{2.142}O_6$	-	(-2790.68 ± 6.33) ^{el} (-364.78 ± 4.24) ^{ox}
$K_2Ta_2O_6$	-	(-2819.07 ± 8.42) ^{el} (-409.87 ± 6.89) ^{ox}

The enthalpies of formation for perovskites ($KTaO_3$) and pyrochlores with different stoichiometry ($K_{0.873}Ta_{2.226}O_6$, $K_{1.128}Ta_{2.175}O_6$, $K_{1.291}Ta_{2.142}O_6$ and $K_2Ta_2O_6$) from corresponding oxides and elements were determined. These are the first energetics experimentally determined for the K_2O–Ta_2O_5 system. The enthalpy of formation of perovskite from oxides becomes less exothermic than from the pyrochlore phases, indicating a less stable structure with respect to the constituent oxides. The decomposition enthalpy of $K_2Ta_2O_6$ to $KTaO_3$ indicates that pyrochlore is energetically more stable than perovskite, and also confirms that pyrochlore is the low temperature phase. The decomposition paths of non-stoichiometric and stoichiometric pyrochlores were presented and discussed. The implications of the reported results are significant to explore the transition paths between various structures in K-Ta system. This work provides understanding of the thermodynamic stability of each phase, supplying knowledge to the phase formation process, phase stability and kinetics within K_2O–Ta_2O_5 system.

4.2.5. Proposed crystallization paths

The crystallization pathway of conventional solid state and solution-based KTO clearly shows such differences: i) pyrochlore is not formed at any stage of standard solid state reaction, even changing the reaction atmosphere, ii) intermediate KTO*pyr* phase is formed during solution processes at low temperatures, while KTO*per* and KTO*ttb* phases can be obtained at high temperatures.

Energetic studies proved that pyrochlore is energetically a more stable phase than the perovskite at low temperature. This is in agreement with Ostwald's step rule for polymorphic materials, stating that it is not the most stable phase with the lowest amount of free energy that is initially formed, but the least stable form lying nearest to the original state in free energy [348]. In another words, stoichiometric pyrochlore phase crystallizes first, and then at higher temperatures it is transformed into perovskite structure, its equivalent in terms of chemical composition. Similar behaviour was observed by Guy-Lussac [349] stating that during crystallization, unstable forms are frequently obtained first, and then they transform into a stable form. Our study clearly demonstrate that the perovskite is stable above 700 °C when using solution based synthesis process. Based on those results, a qualitative free energy-temperature diagram can be drawn (as presented in Figure 4-51), showing the relation between the different states. It is based on the similar scheme that was proposed by Roy [350] and later by Schwartz [351]. The diagram provides useful demonstration of energies of each state for understanding the sequence of transformation pathway. Conversion of a metastable gel with an amorphous matrix to a crystalline forms needs driving forces. Although the crystalline state has lower Gibbs free energy than the amorphous gel slow reaction kinetics delay the transformation. Additional thermal energy must be provided to surmount the barrier for nucleation of the pyrochlore phase firstly, and then to grow into perovskite one. In the other scenario, the K-deficient pyrochlore can transform into the TTB structure.

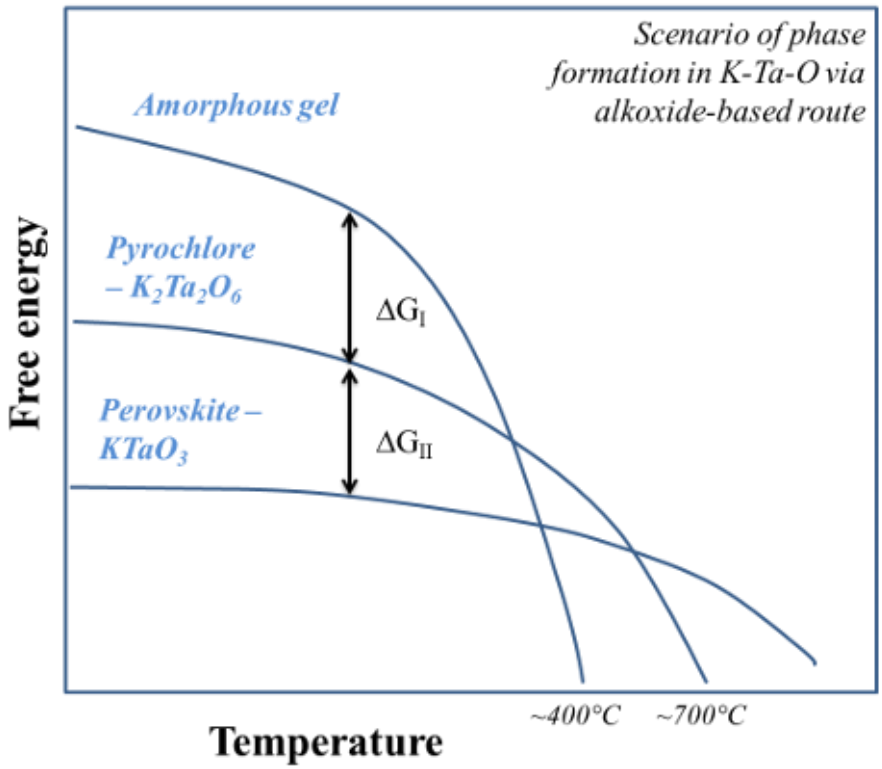

Figure 4-51. Qualitative energy-temperature diagram for the two polymorphic modifications of potassium tantalate (K:Ta = 1:1).

Another important aspect that has to be taken into account is related to the local structure of those phases, mostly the amorphous and the pyrochlore one. The study of local structures in lead titanate synthesized by wet chemical route was reported by Camargo *et al.* [339]. Detailed structural investigations of amorphous phase and cubic pyrochlore $Pb_2Ti_2O_6$ by X- ray absorption fine structure (XAS) spectroscopy revealed that the local structure around titanium is essentially the same in both cases. Thus, the local order of the amorphous precipitates drives the crystallization into the most favourable structure that is the pyrochlore one with similar local organization. Additionally, Reaney *et al.* [338] proved on lead zirconium titanate (PZT) that the distance between the nearest neighbours in the amorphous or short-range ordered phase is very close to that in pyrochlore. Therefore, transition from amorphous to pyrochlore is believed to be kinetically favoured over a direct transition to the perovskite.

Using the presented results, the phase diagram of Ta_2O_5–$KTaO_3$ reported by Roth *et al.* [58] has to be modified, as presented in Figure 4-52.

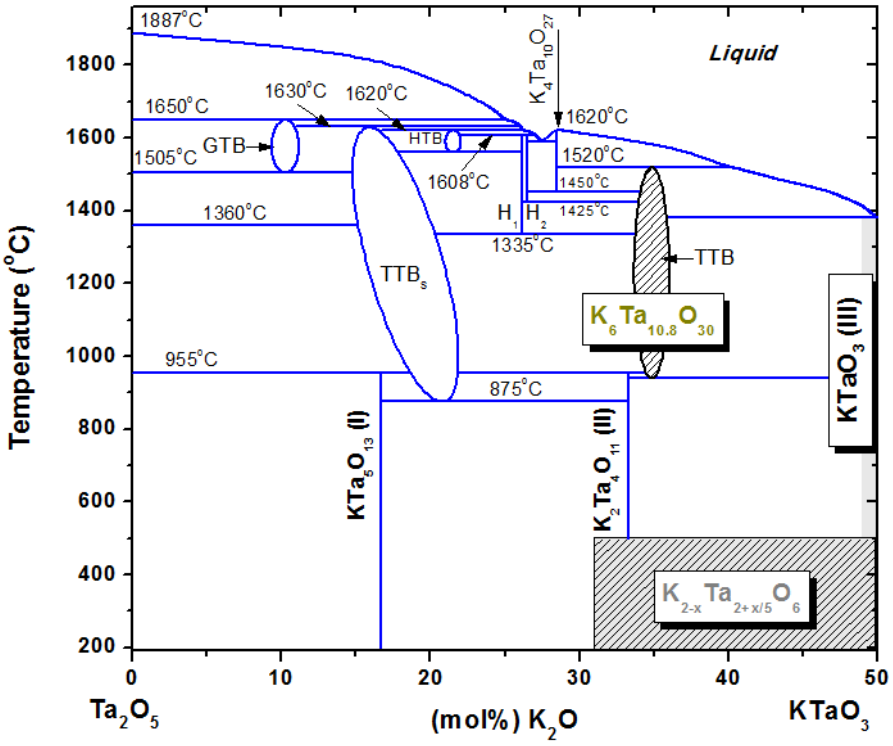

Figure 4-52. Phase diagram of Ta_2O_5–$KTaO_3$ according to Roth et al. [58], with emphasis on the phases: perovskite $KTaO_3$ (III), pyrochlores $K_{2-x}Ta_{2+x/5}O_{6-\delta}$ and tetragonal tungsten bronze $K_6Ta_{10.8}O_{30}$ (TTB). Assignations on the diagram correspond to: GTB – Gatehouse tungsten bronze (89 % of Ta_2O_5), TTBs – tetragonal tungsten bronze with superstructure (83.3 %–80 % of Ta_2O_5), HTB – hexagonal tungsten bronze (77.3 % of Ta_2O_5), H_1 and H_2 – hexagonal phases (73.85 % and 73.5 % of Ta_2O_5, respectively).

The phases of potential interest: perovskite $KTaO_3$ (III), pyrochlores $K_{2-x}Ta_{2+x/5}O_6$ (not present in the original source) and TTB $K_6Ta_{10.8}O_{30}$, are marked on the diagram in order to help understanding their relations. Designations on the diagram are the same like presented in Figure 2-6. As can be deduced from Ta_2O_5–$KTaO_3$ phase diagram, low temperature pyrochlores can be transformed into either perovskite or TTB while appropriate stoichiometry is controlled. The differences between these compositions arise from structural (crystallographic symmetry and bond lengths), and chemical (K:Ta stoichiometry) factors. As reported by Ishihara *et al.* [52], the calculated free volume of the unit cell is 16.81×10^{-3} and 28.00×10^{-3} nm^3 for $KTaO_3$ and $K_2Ta_2O_6$, respectively, meaning that packing of atoms in pyrochlore structure is looser. The difference in potassium deficient pyrochlore is further increased, due to bigger lattice parameter +0.17 %, causing the Ta–O

distance longer than in perovskite $KTaO_3$ and pyrochlore $K_2Ta_2O_6$. These differences influence the electronic band structure, as band gaps of 5.2 eV and 3.9 eV for stoichiometric $K_2Ta_2O_6$ and $KTaO_3$, respectively, have been determined [52]. TTB $K_6Ta_{10.8}O_{30}$ has rather complex layered structure, which consists of TaO_6 octahedra joined by sharing corners, and the layers are perpendicular to the *c* axis [66, 67]. Besides that, its chemical composition (K:Ta ratio of 0.56) differs from perovskite and pyrochlore structures, thus when processed it has to be compensated by appropriate Ta_2O_5 content that can be due to high processing temperature K volatilization.

Therefore, chemical and physical differences between these three compounds are obvious, although their phase transition relations are not so clear. The following phase transition sequences, based on the literature and on our data, are suggested: i) the low temperature stoichiometric pyrochlore $K_2Ta_2O_6$ transforms into perovskite $KTaO_3$ at temperatures >550 °C, depending on conditions [60, 61], ii) potassium deficient defect pyrochlore $KTa_{2.2}O_6$ transforms into TTB $K_6Ta_{10.8}O_{30}$ at ≥900 °C but not into perovskite, and iii) TTB is possible to be obtained from perovskite $KTaO_3$ eliminating sufficient amount of K by long heat treatment at temperatures >900 °C.

Summary

The pyrochlore-to-perovskite phase transformation in potassium tantalate is a complex process, most likely associated with the precursor types used in synthesis method. Understanding the nature of this phenomena is crucial namely for the fabrication of thin films at lower temperatures to be compatible with silicon technology.

It was demonstrated that the synthesis by chemical solution methods leads to the formation of low temperature intermediate pyrochlore structures. The stoichiometry of this phase determines the decomposition path and product, originating either a perovskite $KTaO_3$ or a tetragonal tungsten bronze $K_6Ta_{10.8}O_{30}$. The solid-state kinetic study showed that the crystallization of the perovskite phase from sol-gel route occurs in two stages.

Therefore, the enthalpies of formation for perovskite and pyrochlores were determined for the first time. The results are significant to explore the transitions between K-Ta structures, providing an insight on the thermodynamic stability within the K_2O–Ta_2O_5 system.

4.3. Chemical solution deposition of alkali tantalate thin films

Abstract

Chemical solution deposition is a versatile and attractive method used for the deposition of the complex oxides thin films. In the present work the alkoxide-based K-Ta solutions are initially used to prepare $KTaO_3$ thin films on platinized Si substrates. However, the stability of those precursor solutions and their thermal decomposition lead to the crystallization of the perovskite $KTaO_3$ phase only at high temperatures, ≥900 °C. Even a seeding of KTO films by using various oxides does not promote the perovskite phase formation at lower temperatures. Therefore, an alternative processing route, namely diol-based sol-gel process, is implemented in order to increase the chemical stability of the precursor solutions and to reduce the crystallization temperature of $KTaO_3$. In fact, the three-folded strategy is used: i) 1,3-diol as a solvent, ii) potassium precursors with different molecular structures to change K-Ta solution chemistry, and iii) annealing in oxygen atmosphere by rapid thermal processing. Successfully, the perovskite $KTaO_3$ phase is obtained in the films annealed at temperatures <700 °C, using the precursor solution with potassium acetylacetonate. Thus, the crystallization temperature of the perovskite structure is reduced by ~200 °C, comparing to KTO films derived from the alkoxide-based route, being compatible with Si technology. A proof of concept is also used for the other alkali tantalate films deposition, namely LTO and NTO.

Film fabrication techniques can be divided into two general classes: physical vapour deposition (PVD) techniques and chemical deposition techniques, which include chemical vapour deposition (CVD) and chemical solution deposition (CSD). Taking into account the possible stoichiometric deviations in the KTO system, the selection of the most appropriate

fabrication/deposition technique for thin films is a key issue [24, 352, 353]. Various fabrication techniques that include physical and chemical methods have been exploited, and it has been proven that wet chemical routes are ones of the most important approaches for the synthesis of complex oxide thin films and powders. The main advantages of the chemical solution methods include the ability to synthesize compounds at relatively low temperatures and simultaneously with a very good stoichiometric control [232, 354, 355].

In general, solution synthesis involves the intimate mixture of the liquid precursors (inorganic, organic and alcoholic solutions) at a molecular level in order to obtain a homogeneous solution at the atomic level which by precipitation will originate a solid precursor. Solution techniques include among others the precipitation and co-precipitation, hydrothermal synthesis, sol-gel, emulsion process, molten salt synthesis and spray pyrolysis. In each of these techniques the nucleation and growth of the solid phase occur through a reaction in the liquid phase. Due to the high level of atomic and/or molecular homogeneity attained in solution these techniques give rise to high chemical homogeneous solid products [19].

$KTaO_3$-based thin films derived from CSD are listed in Table 4-17. The most important publications are included, in chronological order. Investigations have started in 1990s, by groups of Hirano, Nazeri and Kuang, and mostly metal ethoxides were used as precursors, *e.g.* K, Ta and Nb ethoxides. The studies of Hirano *et al.* [93, 106, 107] revealed that relatively high crystallization temperature is needed, 850 °C, to obtain monophasic perovskite phase in $KTaO_3$. Nazeri *et al.* [59, 104, 105] focused their work on modifying the precursor solutions and finding the proper substrate for the perovskite phase formation. Then, Kuang *et al.* [94, 95, 108, 109] reported the study on precursor powders and the formation of a double metal complex. However, the studies on KTO-based thin films described above were carried out in KTN compositions, with a maximum Ta content <90 %. Only in 2000s, Buršík *et al.* [60, 96, 97, 110] processed KTO without Nb doping, using metal iso-butoxide as precursors, K excess and seed layers to promote perovskite phase formation. Crystallized KTO thin films were successfully prepared at temperature >700 °C in air and O_2 atmosphere. More details are presented in Chapter 2 – State of the Art.

Table 4-17. Review of the selected reports on chemical solution deposition of $KTaO_3$-based thin films. A wide spectrum of different synthesis routes was reported.

Group/ references	Compositions	Cryst. temp.	Experimental details	Remarks
Hirano *et al.* [93, 106, 107]	$K(Ta_{1-x}Nb_x)O_3$, x = 0.35, 0.5 and 0.65	≥675 °C	Precursors and solvents: K-, Nb- and Ta-ethoxide, ethanol Precursor solution procedure: mixing in a dry nitrogen chamber, reflux for 24 h or 48 h Heat-treatment: pyrolysis at 300 °C for 1 h (5 °C/min), crystallization by slow heating (5 °C/min) or rapid thermal processing (pre-heated furnace) for 1 h in O_2 and H_2O/O_2 flow Substrates: (100)Pt/(100)MgO, sapphire (α-Al_2O_3), SiO_2 glass, (100)Si	
Nazeri *et al.* [59, 104, 105]	$K(Ta_{1-x}Nb_x)O_3$, x = 0.2, 0.35, 0.5 and 0.65	550-900 °C ≥750 °C – KTN*per* onto MgO and $SrTiO_3$	Precursors and solvents: K-acetate or -ethoxide, Nb- and Ta-ethoxide, ethanol or methanol, acetylacetonate or triethylamine or vetiverol Precursor solution procedure: mixing in a dry nitrogen chamber, reflux for 24 h Heat-treatment: drying at > 100 °C, crystallization by conventional heating (5-8 °C/min) for 0.5-2 h in O_2, H_2O flow, or by rapid thermal processing (pre-heated furnace) from 10 s to 5 min in N_2 Substrates: (100)MgO, (110) and (100)$SrTiO_3$, (0001)sapphire, SiO_2 glass, (111)Si	K:Ta = 1.05, 1.10 and 1.15;
Kuang *et al.* [94, 95, 108, 109]	$K(Ta_{1-x}Nb_x)O_3$, x = 0.35	500-900 °C >700 °C – oriented KTN*per* onto MgO and $SrTiO_3$	Precursors and solvents: K-acetate or -ethoxide, Nb- and Ta-ethoxide, ethanol, acetic acid Precursor solution procedure: mixing in a dry N_2 chamber, reflux for 24 h Heat-treatment: drying at 400 °C for 30 min (200 °C/h), crystallization by conventional heating, in air or O_2 Substrates: quartz glass, (100)Si, (100) and (110)$SrTiO_3$, sapphire, yttria-stabilized ZrO_2, (012)$LaAlO_3$, Pt-coated (111)Si, (100)MgO	K:Ta = 1 and 1.10

Table 4-17. Review of the selected reports on chemical solution deposition of $KTaO_3$-based thin films. A wide spectrum of different synthesis routes was reported. (Cont'd.)

Group/ references	Compositions	Cryst. temp.	Experimental details	Remarks
Buršík *et al.* [60, 96, 97, 110]	$K(Ta_{1-x}Nb_x)O_3$, x = 0, 0.05, 0.21, 0.36, 0.53, 0.74, 0.82, 0.86 and 1	400-900 °C >850 °C: KTO*ttb* ≥600 °C: KTO*per* (using particular conditions) <600 °C: KTO*pyr* + KTO*per*	Precursors and solvents: K-, Nb- and Ta-iso-butoxide, iso-butanol, dietanolamine Precursor solution procedure: mixing in a dry nitrogen chamber, reflux for 30 min Heat-treatment: drying at 110-200 °C for 5-60 min, pyrolysis at 550-600 °C for 5-10 min (in pre-heated furnace), crystallization by slow heating and rapid thermal processing (~ 50 °C/s; pre-heated furnace) for 5-30 min in air, effect of oxygen flow (20 cm^3/min) during annealing: 400-900 °C Substrates: (100)MgO, (0001)Al_2O_3, SiO_2 glass, (100)Si and (111)Si	K:Ta = 1.05-1.07 and 1.25; Buffer layers: Al_2O_3, Y-stabilized ZrO_2, $PbTiO_3$, $PbTiO_3$-Al_2O_3, $KNbO_3$, MgO, ZnO
Guilloux-Viry *et al.* [61]	$K(Ta_{1-x}Nb_x)O_3$, x = 0	500-800 °C 750 °C – KTO*per*	Polymeric precursor method (Pechini process) Precursor and solvents: K carbonate and Ta-ethoxide, citric acid, ethylene glycol, ethylenediamine Heat-treatment: pyrolysis at 300 °C for 4 h in air, crystallization by slow heating (5 °C/min) for 1 h at 500-800 °C Substrates: Al_2O_3, (100)$SrTiO_3$, (100)$LaAlO_3$	K:Ta = 1.25
Malič *et al.* [237, 356, 357]	$K(Ta_{1-x}Nb_x)O_3$, x = 0, 0.4	700-900 °C 900 °C – KTO*per*	Precursors and solvents: K-acetate, Nb- and Ta-ethoxide, 2-methoxyethanol Precursor solution procedure: mixing in a dry atmosphere, reflux for 1-48 h, distillation Heat-treatment: pyrolysis at 350 °C for 2 min, crystallization by rapid thermal processing (15 K/s) for 5-15 min in constant flow of nitrogen and oxygen (4:1) during annealing: 700-900 °C Substrates: (0001)Al_2O_3	K:Ta = 1.10

The stability of the alkoxide solutions, and the effects of hydrolysis and post-deposition heat treatment on the crystallization were presented. The following factors affect the perovskite KTO phase formation in solution processed thin films: i) a proper stoichiometry of metals in starting precursor solution (K:Ta > 1) in order to compensate alkali losses during multiple heat treatments; ii) a relative stability of precursor solution to be able to deposit on the substrate; iii) a suitable substrate, preferably with matching crystal structure and lattice parameter to KTO, in order to avoid or minimize strain; and iv) an oxygen atmosphere during annealing to facilitate organic degradation during pyrolysis, and shift perovskite phase formation to lower temperatures.

Metal alkoxides represent the most important class of compounds used in the synthesis of precursor solutions for CSD processing of thin film materials [358]. They offer a number of advantages, such as high purity, good solubility in organic solvents and chemical reactivity and options for chemical modifications. Metal alkoxides are typically regarded as Lewis acids, which means that they can interact with molecules having lone pairs of electrons, *i.e.* Lewis bases. The most obvious consequence of non-stabilized metal alkoxides is that they are very sensitive towards the nucleophilic attack of water molecules. Hence in the presence of water, hydrolysis is induced quickly and this leads to the formation of metal hydroxides with the concurrent release of alcohol molecules [358]. Therefore, they need to be carefully handled under controlled atmosphere, normally in a glove box. Their chemistry is very well presented in the textbook published by Turova *et al.* [359].

High reactivity of the chemically unmodified metal alkoxides towards water results most often in massive uncontrolled phase separation, precipitation, on hydrolysis of their solutions by pure water or its solutions in organic solvents [360]. In order to synthesize stable and reproducible precursor solutions with a maximum degree of homogeneity and long term stability, the control of the hydrolysis behaviour and the nuclearity of the metal alkoxide is the key to achieve this goal. Chelating agents, such as acetylacetone and acetic acid, are often the reagents of choice to adjust the reactivity of the metal alkoxides in the precursor solutions. They are both low molecular weight and low boiling point chelating ligands. Other chelating agents are available but less used for CSD processing [358]. It was established that introduction of modifying ligands decreased the reactivity of precursors in the hydrolysis and condensation reactions, and the proposed explanation of the introduction of chelating ligands is: i) not changing significantly the charge distribution in the molecules, ii) blocking

the coordination sites of the metal atoms, and iii) shielding the metal atoms from condensation by non-hydrolysable and thus not removable ligands [361].

Besides the alkoxides, metal carboxylates are the second most frequently used reagents for the synthesis of precursor solutions. The length and chemical nature (single or double bonds, linear or branched shape, number and type of hetero atoms, *etc.*) of this organic residue determines the polarity and the decomposition behaviour of the acid and the corresponding carboxylate, respectively [362]. Short chain carboxylic acids (1-4 carbons) are soluble in water, whereas longer carboxylic acids are less soluble in polar solvents due to the increasing hydrophobic nature of the longer alkyl chain. These longer chain acids tend to be rather soluble in less-polar solvents such as ethers, alcohols, toluene, *etc.* [362]. The choice of the carboxylate for CSD should fulfil the following criteria: i) available as highly pure materials, ii) stable in air, iii) soluble in an adequate solvent, among other. Metal acetates are the most investigated carboxylates. In the case of the alkali precursor, potassium acetate was also used in the synthesis of KTO precursor solutions.

As mentioned above, potassium and tantalum ethoxides are very reactive, hydrolysis and condensation is fast when water is added. The control of those two reactions is important in a multicomponent system, such as $KTaO_3$. Thus, due to poor stability and high sensitivity to external conditions of KTO-based solutions, and their adequate precursors, the molecular structures of the precursor solutions derived from alkoxides and stabilized by acetic acid and acetylacetonate were briefly investigated.

Besides, it was reported in other systems that in order to promote the formation of the required phase and to optimize the microstructure of the films, template oxide layers (seed layers) between the substrate and the film should be used [363]. It was reported in $P(Zr, Ti)O_3$ (PZT) and $SrBi_2Ta_2O_9$ systems [364], that the deposition of thin layers of constituent composition prior to ultimate one can reduce the processing temperature, increase the homogeneity of composition, and dielectric and ferroelectric response of the as-produced films. Kwok and Desu presented a PZT deposition method in which a very thin (45 nm) seeding layer of $PbTiO_3$, which has a low activation energy for the perovskite formation, was used to provide the nucleation sites needed for the low temperature perovskite formation. The perovskite formation temperature of PZT was lowered from 900 °C to 750 °C using this method [365]. The use of $SrTiO_3$ (STO) as a seed layer was also

studied; PZT films with STO buffer layers are dense and exhibit a columnar structure. STO buffer layers have significant influence on the crystallization of PZT thin films. PZT thin films with STO buffer layers are fully crystallized at the annealing temperatures of 550 °C, resulting in excellent electrical properties [366]. Perovskite $LaNiO_3$ (LNO) seed layer was also employed to grow $Pb_{0.97}La_{0.02}(Zr_{0.88}Sn_{0.10}Ti_{0.02})O_3$ (PLZST 2/88/10/2) antiferroelectric thin films at lower temperature using the sol-gel method. PLZST 2/88/10/2 thin films were fully crystallized after being annealed at a lower temperature of 450 °C [367]. Therefore, perovskite oxides: $KTaO_3$ (KTOs), $SrTiO_3$ (STOs) and $LaNiO_3$ (LNOs) were chosen as a seed layers in this approach. STO may act as a diffusion barrier, and enhance the densification of lead-based films [364, 368]. Moreover, due to similar crystallographic features of STO to potassium tantalate, it is possible to reduce the strain at the interfaces, caused by lattice mismatch (in-plane lattice misfit between STO and KTO is -2.1 %) [366, 369]. And, $LaNiO_3$, which is a pseudocubic perovskite with a lattice parameter of 0.384 nm, is known as a good conductive oxide; it can increase the electrical performance of KTO thin films, acting as a bottom electrode as well as Pt layer but also forms a template to enable the growth of high quality KTO films [370, 371].

Another strategy was then pursued, using diol-based CSD route. A diol-based sol-gel process uses 1,3-propanediol as a solvent due to its considerably lower toxicity comparing to 2-methoxyethanol [238]. 1,3-propanediol is considered a non-bridging bidentate ligand which polar groups (alcohols) can bond to different metal precursors, like alkoxides and acetates, giving rise to a cross-linked network of molecules. These molecules are often treated with oligomeric nature [238]. Additionally, the strategy includes the design of the chemistry of the precursors through the change of the alkaline carboxylate precursor with different alkyl chain length. It was reported by Hoffmann *et al.* [372, 373] and Bretos *et al.* [374] that the careful choice of alkaline earth reagents changes the thermal decomposition of the precursor solution improving the formation of the desired perovskite phase, either in (Ba, Sr)TiO_3 or (Pb, Ca)TiO_3 compositions. For alkaline earth carboxylates the length of the alkyl chain significantly affects the chemical and physical properties of the compound such as the polarity or solubility and the thermal decomposition behaviour [375]. The nucleation, density and subsequently the grain size of the films are affected by the decomposition temperature of the alkaline earth carboxylate compound: i) while using carboxylates with long alkyl chain result in a high density of perovskite type nuclei formed

at low temperatures, ii) the use of short alkyl chain precursors results in nucleation of oxo-carbonate seeds at higher temperatures and in a lower density of nanograins [372, 375]. These intermediate phase nuclei may then act as seeds for the crystallization of the perovskite phase.

Therefore, in this part of the thesis the multiple strategies are presented to effectively fabricate the films composed of alkali tantalates, on platinized Si substrates. The diol-based route is firstly tested on KTO and then implemented for LTO and NTO.

4.3.1. Experimental methods

In this thesis, different synthesis routes within chemical solution deposition method are used, *i.e.* alkoxide route and the combination of diol-based sol-gel method with precursor chemistry adjustment. The experimental details are described in Chapter 3 – Experimental Methods. Table 4-18 presents some information about processing of alkali tantalates, KTO, LTO and NTO, by CSD.

Table 4-18. Experimental details of alkali tantalates synthesized by CSD.

CSD route	*A:Ta ratio*	*Metal precursors*	*Solvent / modifiers*	*Remarks*
KTO				
Alkoxide	1.25	KOEt & $Ta(OEt)_5$	EtOH / AcOH & Hacac	K-excess *AP-I*
Diol	1.1–1.25	KOAc / Kacac & $Ta(OEt)_5$	1,3-diol & EtOH	K-excess KTO*ac* (from KOAc), KTO*acac* (from Kacac) *AP-II*
LTO				
Diol	1	LiOEt & $Ta(OEt)_5$	1,3-diol & EtOH	Stoichiometric *AP-II*
NTO				
Diol	1	NaOAc & $Ta(OEt)_5$	1,3-diol & EtOH	Stoichiometric *AP-II*

In the study of seeding of KTO thin films, the selected compositions were prepared by chemical solution deposition. The precursor solutions of STO and LNO with metal precursors concentrations of 0.05 M. The used synthesis protocols are:

- The STOs sol was synthesized by using strontium acetate ($Sr(CH_3COO)_2$ – $Sr(OAc)_2$, ABCR, 98 %), dissolved in heated acetic acid (T ≈ 60 °C) and then diluted with 1,2-propanediol ($C_3H_8O_2$, Merck, 99 %), and tetra-n-butyl orthotitanate ($Ti(OC_4H_9)_4$, Merck, 98 %). Detailed procedure is described elsewhere [376].
- The LNOs sol was prepared by dissolving lanthanum nitrate hexahydrate ($La(NO_3)_3 \cdot 6\ H_2O$, Merck, 99 %) and nickel nitrate hexahydrate ($Ni(NO_3)_2 \cdot 6\ H_2O$, Sigma-Aldrich, 99.999 %) in acetic acid and distilled water. As an additive, derivative of formamide – n,n-dimethylformamide ($HCON(CH_3)_2$ – DMF, Sigma-Aldrich, 99.8 %) was used in the final sol in order to stabilize it and enhance wetting to the substrates and in consequence avoid cracking during heating [370, 371].

Thin layers of each chosen compositions were firstly coated on platinized Si substrates. Then, the seed layers were pre-annealed for 20 min, at 500 (KTOs) or 600 °C (STOs and LNOs), prior to KTO films deposition on them.

4.3.2. Modification of K-Ta precursor solutions

The present section describes two distinct routes of precursor solution preparation, in order to obtain stable and stock solutions of KTO composition. The stability of the precursor solutions has a major impact on the quality and properties of the final films.

4.3.2.1. Alkoxide route

When potassium and tantalum ethoxides are added into a solution to form a sol or a gel, precipitates often form. Acetylacetone is an effective complex in stabilizing alkoxides because the enolic form of β-diketones contains a reactive hydroxyl group that reacts readily with metal alkoxides [377]. In addition, the gelation behaviour of alkoxides can be modified by carboxylic acid, such as acetic acid. The molecular structure of the precursor sols, with the addition of the AcOH and Hacac, was examined, and the FTIR spectra of the modified KTO sols are presented in Figure 4-53. The intense and broad band in the 3500–3100 cm^{-1}

region is attributed to the stretching vibrations of OH from alcohols. The C–H stretching and bending bands are detected at 2950 and 900 cm^{-1}, respectively. The region with the absorption bands at ~1400 cm^{-1} are characteristic for the symmetrical vibrations and bending vibrations (in plane) of COO^- groups arising from two types of ligands, Hacac and AcOH. In the range of 1200–1000 cm^{-1}, C–O stretching bands are observed. The region <800 cm^{-1} represents the characteristic infrared absorptions of the Ta–O vibrations. Most importantly, for both of the precursor solutions the IR spectra from 4000 to 350 cm^{-1} are almost identical. This means that both modifiers act as a chelating agents, giving required stability of KTO sols.

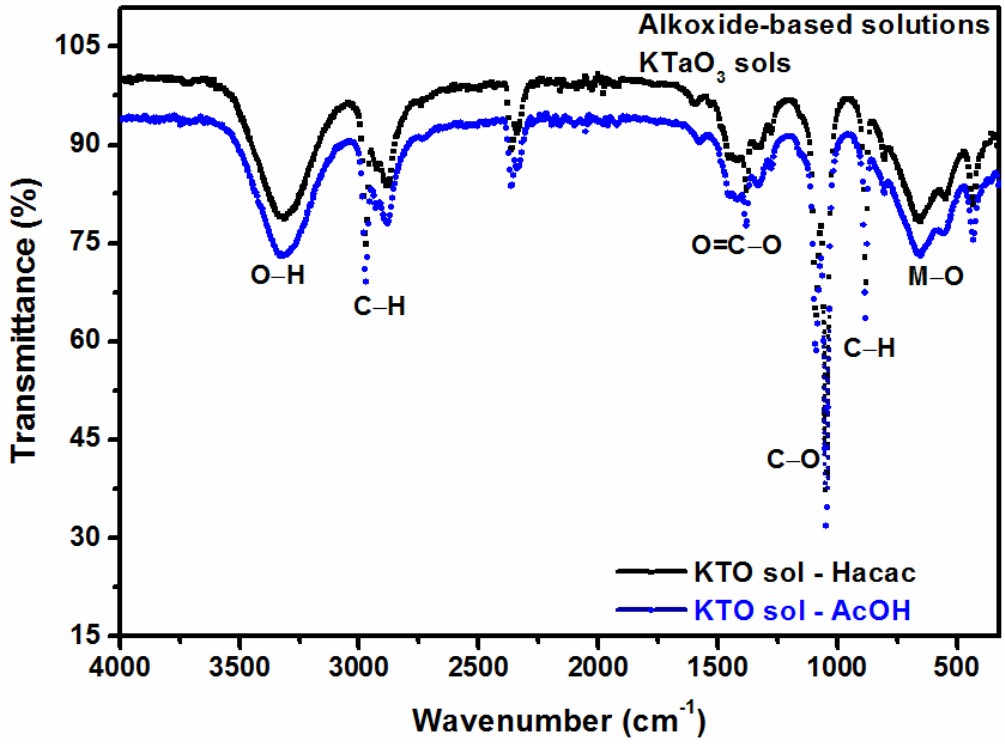

Figure 4-53. FTIR spectra of (K-Ta)OEt$_x$ solutions, modified by two distinct additives, AcOH and Hacac.

Therefore, the crystallization behaviour of the gels was followed by thermal analysis, namely DTA and TG, and supported by *in situ* XRD data presented in the previous sub-chapter (Figure 4-45 and Figure 4-44 *(a)*). The DTA and TG results for the dried gels, together with the XRD results, indicated the critical temperature ranges for the removal of the organic species and for the crystallization of the desired perovskite phase. By combining

the DTA, TG, and XRD results, the temperatures of the pyrochlore and perovskite phase formation were determined. Complete transformation, from pyrochlore to perovskite, is achieved at temperatures >850 °C after 1 h of heat treatment. It is worthwhile to mention that the phase transformation is strongly related to the rate of heating.

4.3.2.2. Diol route

In this work we investigated the influence of K precursors on the formation conditions of pyrochlore and perovskite KTO compounds. Based on the understanding of the mechanism an alternative processing route is presented.

Double metal K(I)-Ta(V) solutions were prepared through chemical solution method, using so-called diol-based route named due to the use of 1,3-diol that acts as complex-formation organic compound. As described in the experimental section (and partially presented in Table 4-18), both metal-based solutions were separately prepared by reflux, forming air-stable sols, and then mixed together according to the molar ratio of K:Ta = 1.25:1, in case of both precursor solutions (KTO*ac* and KTO*acac*). The studies were performed on gel powders and thin films. Initially, thermal decomposition analyses of the powders, and then further structural characteristics of the powder samples were conducted.

Thermal decomposition studies of dried KTO*ac* and KTO*acac* gels were firstly investigated. Figure 4-54 shows DTA/TG profiles of both gels, recorded from room temperature up to nearly 1000 °C with heating rate of 10 °C/min in air atmosphere. These thermographs might be divided into three temperature regimes: I. <550 °C, II. 550–750 °C, and III. >750 °C, as marked in the figure.

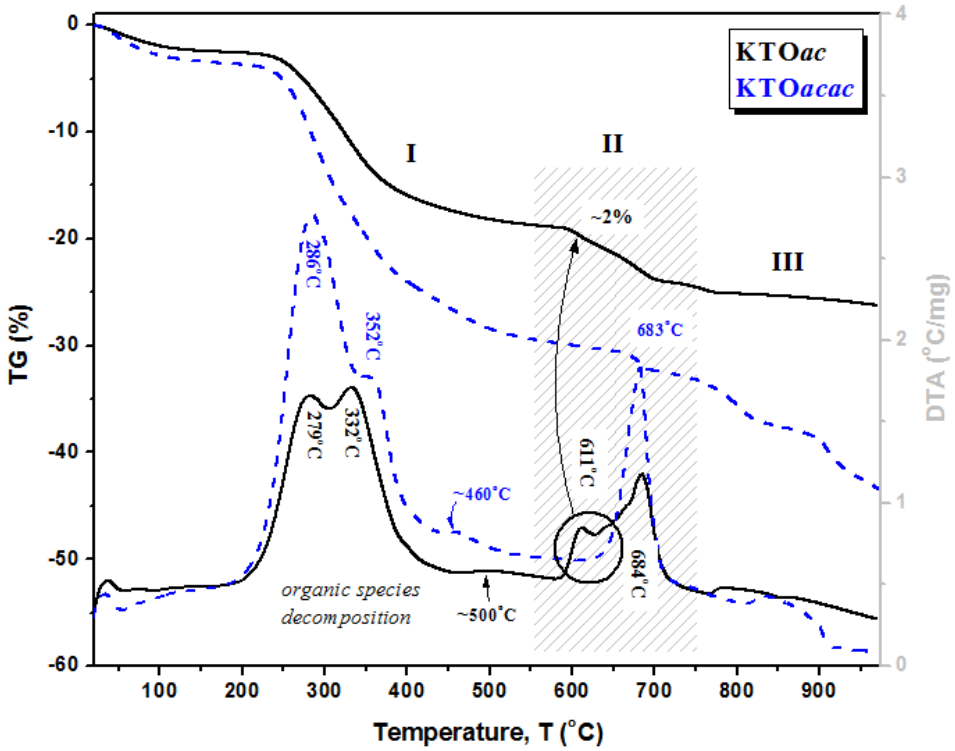

Figure 4-54. Thermal decomposition profiles (DTA – right scale, and TG – left scale) of two distinct K-Ta diol-based gels, KTOac and KTOacac.

In the temperature regime I and at the lowest temperature the organic species are decomposed and associated with a weight loss of 18.7 % in the case of KTO*ac* and 29.4 % in the case of KTO*acac*; this mass variation that progresses as the temperature increases is driven by the combustion and volatilization of precursors and solvents with possible water (H_2O), carbon dioxide (CO_2) and acetone (CH_3COCH_3) release. This mass variation is also related with the bimodal-like shape of the exothermic reactions <400 °C (at 279 and 332 °C in KTO*ac*, at 286 and 352 °C in KTO*acac*), and singular broad but weak exothermic signals centred at ~500 °C in KTO*ac* and ~460 °C in KTO*acac*.

In the temperature regime II (550–750 °C) additional mass loss occurs (~5.9 % for KTO*ac* and ~2.8 % for KTO*acac*, with respect to the state at 550 °C) accompanied by exothermic events. At these temperatures it is probable that nucleation and crystallization of intermediate phases occur, *i.e.* carbonates and pyrochlore. The thermal profiles of both precursors slightly differ due to additional exothermic peak at 611 °C (with corresponding weight loss ~2 %) visible for KTO*ac*. However, the other exothermic peak in this regime (relatively strong and sharp in shape), centred at ~680 °C in both powders, may correspond

to further CO_2 degradation masking a possible endothermic features related to phase transformation from low temperature intermediate structures to desired perovskite one, as proven by XRD studies (Figure 4-55). In the regime III, continuous weight loss takes place, 2.6 % for KTO*ac* and 14.1 % for KTO*acac*, probably accompanied by incomplete decomposition of potassium carbonates due to K-excess. The high temperature regimes (II and III), >550 °C, are not easy for interpretation. Certainly, the formation regimes of those polymorphs (perovskite and stoichiometric pyrochlore) depends on the potassium precursor used in double metal precursor solution preparation.

The thermal study of both potassium precursors separately (not presented here) revealed major differences in the products elimination profiles with the following characteristics:

(i) KOAc goes through 5 various processes on heating (either endothermic or exothermic) in a temperature range up to ~500 °C, with the complete K_2CO_3 decomposition at ~890 °C;

(ii) Kacac changes via 8 detected reactions up to ~455 °C, with decarboxylation at ~890 °C, as in the KOAc.

This evidences that potassium acetylacetonate decomposes into simple oxide, K_2O, much faster on heating than potassium acetate, to be then available to form double metal complex with Ta. Possibly a rupture of the potassium acetylacetonate bonds during the synthesis reactions of the KTO*acac* sol occurs as well. For the alkaline acetates (potassium and sodium), the intermediate is the corresponding oxalate, which decomposes and yields the metal carbonate [362]. Although, it is known that both, metal acetate and metal acetylacetonate, decompose into acetone and metal carbonate of initial reagent [378-380], K*acac* precursor somehow facilitates the formation of complex K(I)-Ta(V) and hinders the crystallization of undesired pyrochlore $K_2Ta_2O_6$. Presumably, the thermal decompositions of K*acac* and Ta(V)-glycol are comparable thus leading to the homogeneous nucleation of perovskite phase throughout the amorphous matrix, like it was demonstrated in BST [375].

The effect of potassium precursor in KTO*ac* and KTO*acac* precursor solutions on structural evolution, amorphous/intermediate (carbonate or pyrochlore)/perovskite phases, was then evaluated on the powders. Figure 4-55 presents a set of XRD patterns of *(a)* KTO*ac* and *(b)* KTO*acac* powders, recorded with *in situ* XRD analysis (2θ = 12–60°) at distinct temperatures: 450, 550, 600, 615, 650, 680, 700 and 750 °C; the reference patterns of

perovskite $KTaO_3$ (JCPDS-PDF card #38-1470) and pyrochlore $K_2Ta_2O_6$ (JCPDS-PDF card #35-1464) are plotted on the bottom of the graphs, for facile comparative observations. Both compositions are amorphous at the initial stage, as confirmed by the existence of broad bands in the patterns centred at ~30° of 2θ. In the case of KTO*ac* a relatively low annealing temperature, 450 °C, is enough to crystallize both polymorphs, as it is displayed on the mixed pattern with characteristic diffraction lines of perovskite $KTaO_3$ and pyrochlore $K_2Ta_2O_6$. For temperatures >600 °C, the perovskite phase becomes the dominant one, but only at >700 °C comes to be monophasic $KTaO_3$. The phase evolution for KTO*acac* differs from KTO*ac* ones. KTO*acac* heated up to ~600 °C is still amorphous, and the fingerprints of crystallized polymorphs show up just for ≥650 °C; at ≥700 °C monophasic $KTaO_3$ patterns are observed (within the experimental detection limits). Thus, lower temperatures are required for the synthesis of monophasic KTO from KTO*acac* precursor solution when compared with KTO*ac*.

For comparative structural analysis at the low temperatures recorded range, XRD patterns of KTO*ac* and KTO*acac*, registered at 450, 500, 550 and 600 °C, are plotted once again in Figure 4-56, but the *y*-axes (intensity) are adjusted (logarithmic scale) to trace the low-intensity diffraction lines of intermediate potassium (bi)carbonate structures. The 2θ range of interest is 20–40°. The detected phases are: Δ K_2CO_3 (JCPDS-PDF #10-2694), ♦ $K_4H_2(CO_3)_3 \cdot ½\ H_2O$ (JCPDS-PDF #20-0886), • $K_2CO_3 \cdot ½\ H_2O$ (JCPDS-PDF #01-1014) and * $KHCO_3$ (JCPDS-PDF #14-4690).

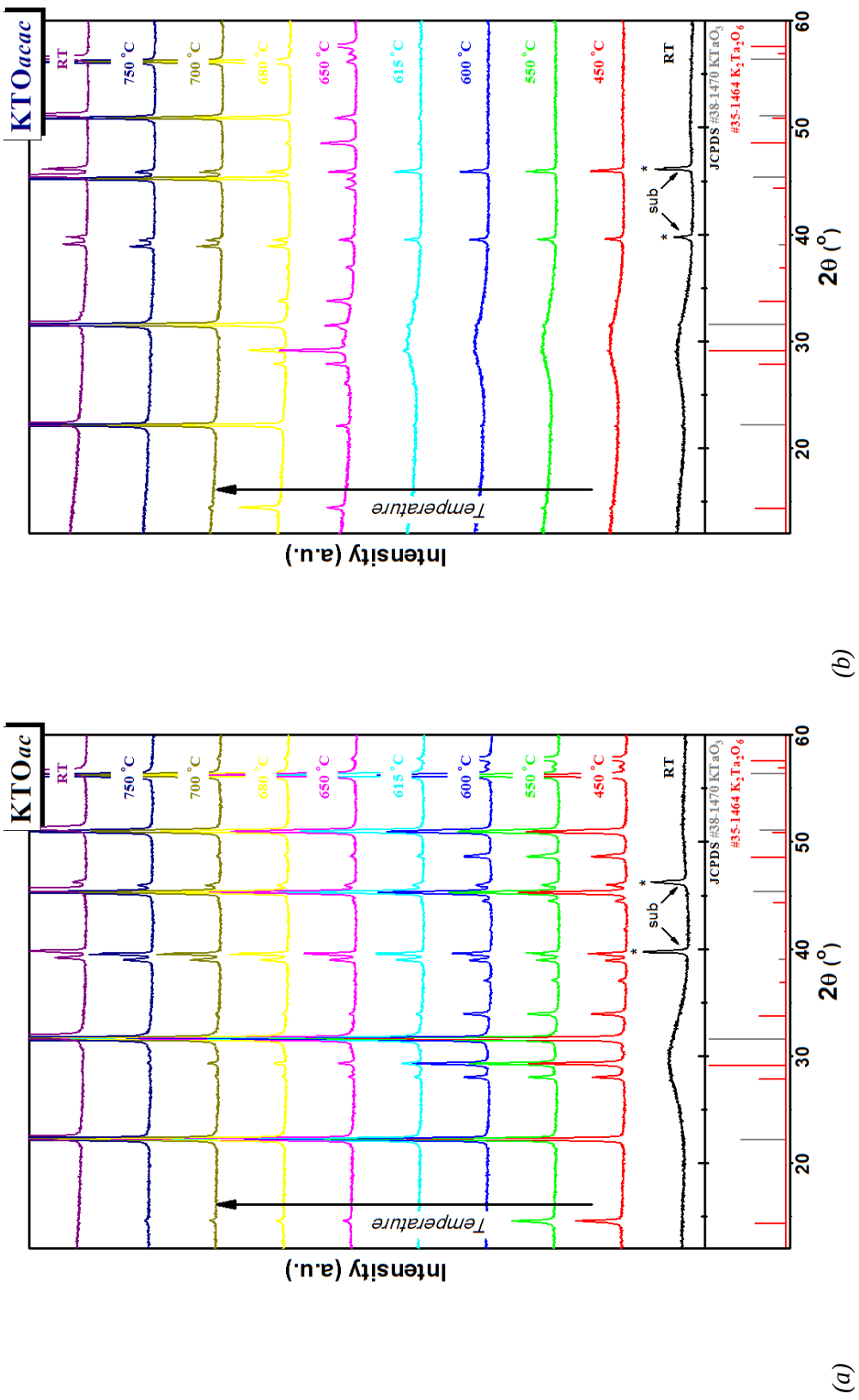

Figure 4-55. In situ X-ray diffraction (XRD) analyses of KTOac (a) and KTOacac (b) powders, with patterns recorded at elevated temperatures in the range 450–1000 °C and within 2θ of 12–60°. Bottom frames present XRD database patterns of pyrochlore $K_2Ta_2O_6$ (JCPDS-PDF card #35-1464) and perovskite $KTaO_3$ (JCPDS-PDF card #38-1470) structures.

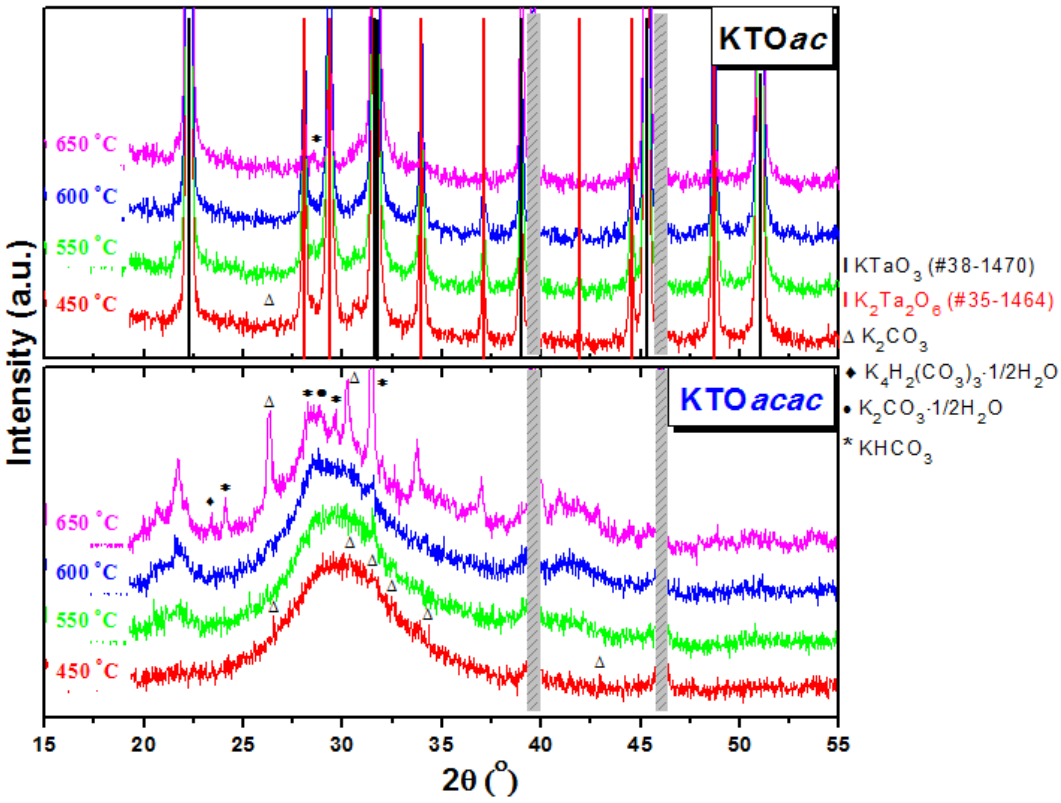

(c)

*Figure 4-56. In situ XRD patterns of KTOac and KTOacac powders, hold at 450, 500, 550 and 600 °C (2θ of 20–55°), with adjusted intensity scale. Diffraction lines of potassium (bi)carbonate structures are marked: Δ K_2CO_3 (JCPDS-PDF #10-2694), ♦ $K_4H_2(CO_3)_3 \cdot 1/2\ H_2O$ (JCPDS-PDF #20-0886), • $K_2CO_3 \cdot 1/2\ H_2O$ (JCPDS-PDF #01-1014) and * $KHCO_3$ (JCPDS-PDF #14-4690).*

KTO*ac* structural evolution is rather straightforward, with an instant crystallization of pyrochlore $K_2Ta_2O_6$ and perovskite $KTaO_3$ already at 450 °C (strong and sharp diffraction peaks). In case of KTO*acac*, the phase evolution starts from amorphous to crystalline perovskite, but the series of potassium (bi)carbonate structures are detected. It was reported that alkali ions, such as K, in the presence of CO_2 and water vapour undergo the two-stage reaction: carboxylation and hydration, with formation of intermediate products of $K_2CO_3 \cdot ½\ H_2O$ and $K_4H_2(CO_3)_3 \cdot ½\ H_2O$, and then rapidly convert to $KHCO_3$ [381]. Analogous situation occurs in phase development of KTO*acac*. Thus, the study conducted on powders revealed that the use of distinct potassium precursor, metal carboxylate with short carboxylate chain or metal β-diketonate, changes completely the phase evolution path resulting in the formation of intermediate structures at different temperature regimes.

In order to complement the previous structural studies and investigate a type of chemical constituents formed during the thermal treatment of gels, a series of infrared (IR) analyses were performed on KTO*ac* and KTO*acac*. IR data bring valuable information for systems with functionalized ligands, such as carbon-based ones, and can be used as an auxiliary technique for the identification of the functional groups present in the compounds. Figure 4-57 depicts a set of FTIR spectra of KTO*ac* and KTO*acac* powdered gels dried at 150 °C for 24 h and then crystallized at distinct temperatures, 550–1000 °C for 60 min in air, with heating and cooling ramps of 10 °C/min. The top curve in each graph represents the spectra of as-dried gels, either KTO*ac* or KTO*acac*, and the other curves at the bottom frame (in colours) represent powders calcined at distinct temperatures.

A number of bands are detected in the IR spectra of as-dried gels. For both precursor solutions the intense and wide band at ~3350 cm^{-1} is attributed to the hydrogen bonds in water molecules and/or alcoholic hydroxyl, ν(OH). The minor bands at 2975–2835 cm^{-1} are characteristics of alkoxy ligands C–H stretches [382]; these C–H vibrations correspond to the asymmetric and symmetric stretching of the CH_3 and CH_2 groups. These bands were reported in Ta(V)-glycol sol [239], while Ta cation is bonded to five diol groups. The other bands, *i.e.* the bending vibrations: δ(C–O–H) ~ 1415 cm^{-1} and δ(O–H) ~ 640 cm^{-1}, are overlapped by other bands. Besides, the characteristic bands of the transition metal alkoxides, in this case is $Ta(OEt)_5$, are also detected in KTO*ac* and KTO*acac*, with the positions of ν(C–O)Ta and ν(Ta–O) at ~1070 and ~555 cm^{-1}, respectively [383]; this can be an indication that not all ethoxy groups were exchanged with glycols.

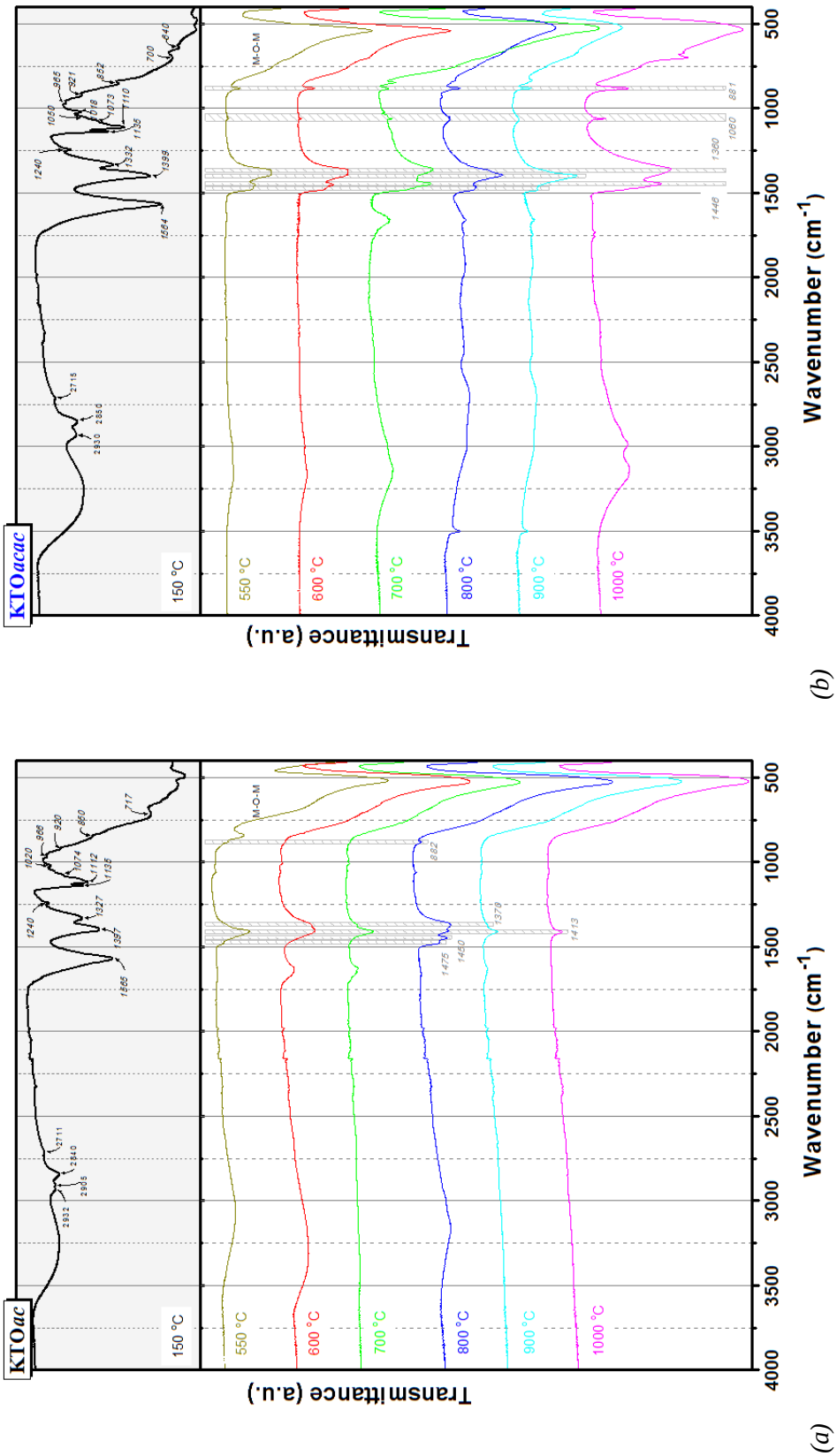

Figure 4-57. FTIR spectra of KTOac (a) and KTOacac (b) gels heat-treated at selected temperature 150-1000 °C for 60 min, with heating rate of 10 °C/min.

The carboxylic acid salts, as KOAc in KTO*ac* solution, have very strong characteristic absorption bands in the region 1670–1540 cm^{-1} due to the asymmetric stretching vibration of CO_2^-, $v_{as}(COO^-)$, and the symmetric stretching vibration of carboxylate anion, $v_s(COO^-)$, gives rise to a band of lower intensity in the range of 1440–1330 cm^{-1} with two or three peaks in the IR spectra; two weaker bands at 860–610 cm^{-1} and 700–450 cm^{-1} are associated to CO_2^- scissor and wagging vibrations, respectively [243, 382]. The coordination mode of carboxylate to metal can be predicted by determining the parameter $\Delta v = [v_{as}(COO^-) - v_s(COO^-)]$ by IR spectroscopy; while Δv is <200 cm^{-1}, the carboxylate is bonded as a bridging ligand [384]. Metal acetylacetonates, as K*acac* in KTO*acac* solution, have the combined absorbance bands of the acetylacetonate groups in the positions: $v(C{=}C) + v(C{=}O)$ at ~1560 and ~1400 cm^{-1}, and $v(CH_3)$ at ~1330 cm^{-1} [382, 385, 386]. During reactions that occur within solutions, ester and ethers elimination processes take place, involving metal precursors and solvent, confirmed by these various bands in the wavenumber 1150–1000 cm^{-1}. Then, these series of absorption bands, described above, completely disappear in the samples calcined >500 °C, when the combustion and volatilization of organic species is completed. Only the low frequency absorption in the range <800 cm^{-1} indicates the presence of various contributions related to multiple M–O (metal-oxygen) bonds, and various bands of (bi)carbonate compounds play key role.

Hence, the interpretation of carboxylate, CO_2^-, and (bi)carbonates bands comes on the first plan; the carboxylate groups originate from alkali precursors and chains of the glycol, while carbonate free and coordinated ions are associated with highly probable alkali metal carbonate formation. It is crucial to trace their bands in order to understand the differences in thermal decompositions while using various K precursors: K*acac* or KOAc in the KTO*acac* or KTO*ac*, respectively. As reported by Miller and Wilkins [387], characteristic bands of potassium carbonate, K_2CO_3, are clearly detectable in the samples heat-treated at high temperatures, >500 °C, with frequencies ~880, 1060, 1360 and 1450 cm^{-1}. However, their assignment to particular structures of distinct (bi)carbonate and hydroxyl species is necessary to understand differences in KTO*ac* and KTO*acac*.

In the recorded range of wavenumber, 400–4000 cm^{-1}, there are four absorption bands characteristic of the free (non-coordinated) carbonate ions, CO_3^{2-} (with D_{3h} point group symmetry). The carboxylate ions may bond to a metal atom through oxygen as a unidentate or bidentate ligand or may act as a bridge between two metal atoms. Therefore, its bands

assignment is significant to verify the type of coordination, and the following modes are characteristic for carboxylate-carbonate compounds: i) the C–O asymmetrical stretching vibrations, $v_{3(as)}$(E'), centered at ~1400 cm^{-1} (with two shoulders at ~1480 and ~1360 cm^{-1}), ii) in-plane CO_3^{2-} bending the C–O symmetrical stretching, $v_{1(s)}$(A1'), at ~1060 cm^{-1}, iii) out-of-plane CO_3^{2-} bending, v_2(A2"), at ~880 cm^{-1}, and iv), v_4(E'), at ~680 cm^{-1}. Additionally, a band at ~1640 cm^{-1} corresponds to a combination of the v_1 and v_4 modes: $v_1 + v_4$ [246, 382, 388-391]. The symmetrical C–O stretching vibration, $v_{1(s)}$, is IR-inactive, while v_2, $v_{3(as)}$ and v_4 are IR-active. However, the $v_{1(s)}$ vibration is activated in the hydrated form of K_2CO_3 because of the slight distortion from the original D_{3h} structure of CO_3^{2-} due to K^+ ions and water molecules [388, 392]. Besides, while the shape, intensity, position and splitting of $v_{1(s)}$ and $v_{3(as)}$ upon heating vary, this indicates strong deformation of CO_3^{2-} ions because of the (bi)carbonato complex formation.

The IR spectra of the KTO*ac* calcined at 550 °C displays characteristic vibrations of $v_{3(as)}$ at 1407 cm^{-1} (with two weak shoulders at 1480 and 1365 cm^{-1}), $v_{1(s)}$ at 1057 cm^{-1} and v_2 at 880 cm^{-1} modes, indexed with vibrational bands of the non-coordinated CO_3^{2-} ions (Figure 4-58 *(a)*). The samples calcined at 600 and 700 °C revealed additional bands at ~1630 cm^{-1}, being evidence of hydrogen bicarbonate ions, HCO_3^-, which gradually decrease in intensity and vanish when the powders were heat-treated at 900 and 1000 °C; the same scenario occurs for vibration bands at 1410, 1060 and 880 cm^{-1}. In contrary, IR spectra of KTO*acac* calcined at 550 °C depicts additional bands, comparing to KTO*ac*, in the range of 1480–1360 cm^{-1}, as being assigned to polydentate coordination of carbonate ions most probably resulting from the existence of K_2CO_3 (Figure 4-58 *(b)*). In powders calcined at 700–900 °C, bands at ~1660 cm^{-1} are present, indexed to bicarbonate coordination resulting from $K_4H_2(CO_3)_3 \cdot ½\ H_2O$ and $KHCO_3$ compounds. This type of structures are usually formed by the precipitation of surface hydroxyl groups. Characteristic bands of (bi)carbonate compounds at 1444, 1360, 1060 and 880 cm^{-1} remain in the samples treated at the highest temperature, 1000 °C. Besides, the intensity of the bicarbonate bands in the KTO*acac* is higher than in KTO*ac*. The observation is consistent with the mass loss of TG curves of both precursor solutions, meaning that the organic content of KTO*acac* is higher than that of KTO*ac*, and (bi)carbonate compounds are favoured in KTO*acac*.

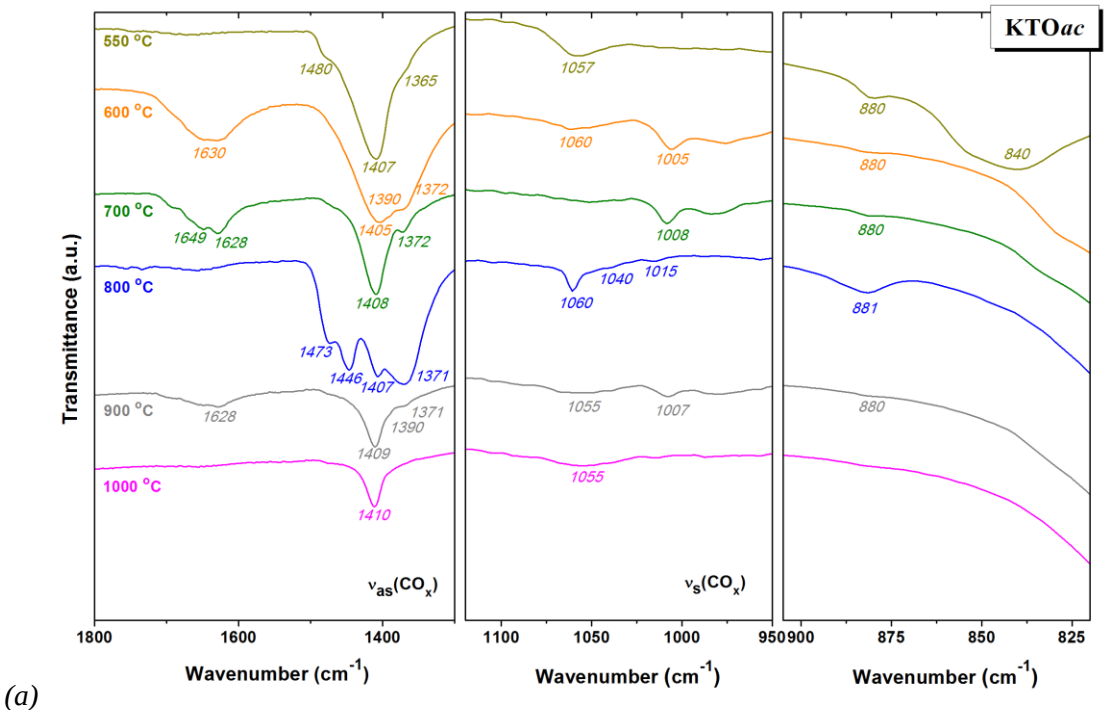

(a)

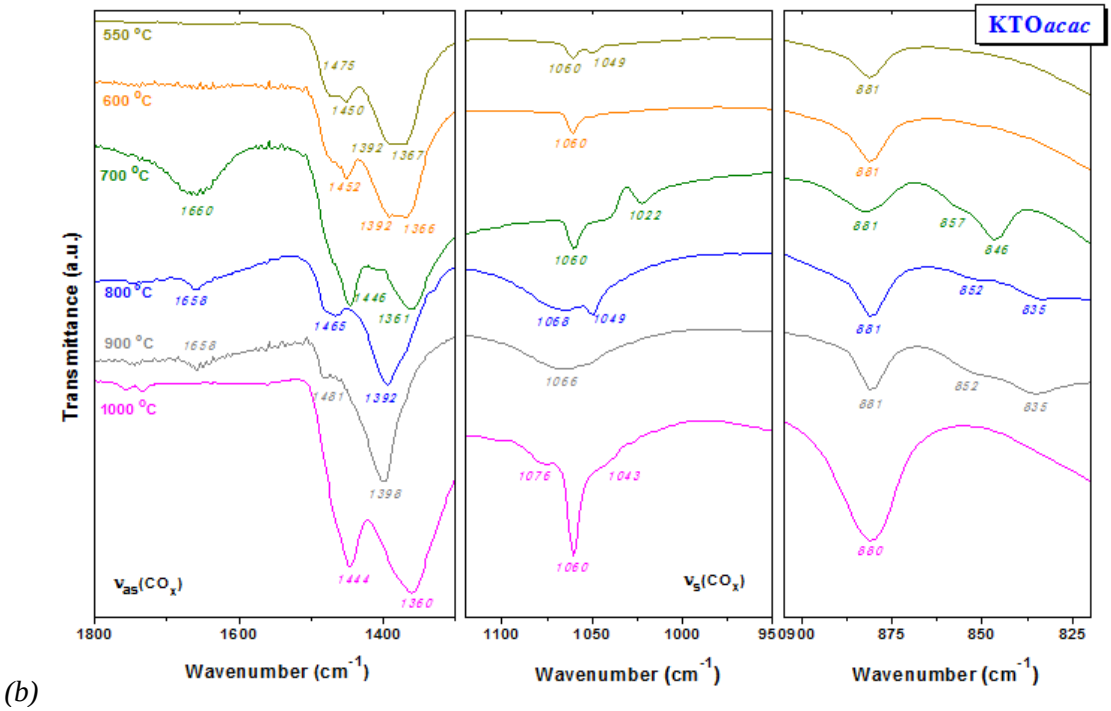

(b)

Figure 4-58. FTIR spectra of KTOac (a) and KTOacac (b) gels heat-treated at selected temperature 550-1000 °C for 60 min, separated into three characteristic ranges of CO_3^{2-}.

To note that even though crystalline structures of pyrochlore and perovskite are formed at lower temperatures, <800 °C, the remaining potassium ions due to their initial excess is available for the formation of various (bi)carbonate structures. The by-products of organic

decomposition, CO and CO_2, may easily interact with surface oxygen and K^+, and in consequence the carbonate compounds can be produced. Other reason was proposed by Buršík *et al.* [60], stating that due to relatively high stability of K_2CO_3 its re-formation can occur by adsorption of CO_2 gas from the ambient atmosphere on cooling.

Therefore, the interpretation of FTIR spectra of KTO*ac* and KTO*acac* is not straightforward as it was in the case of $BaTiO_3$ and $SrTiO_3$ [372], where a disappearance of absorption band of carbonate ions destined in an elimination of CO_2 and complete formation of the perovskite phase. It is however not clear yet in sol-gel derived KTO why the intermediate (bi)carbonates lead directly to the perovskite phase formation (KTO*acac*), whereas their absence at the initial stage of the nucleation is replaced by the pyrochlore phase formation and then transformation at higher temperatures to the perovskite one (KTO*ac*); both scenarios in diol-based derived $KTaO_3$. Obviously, the growth of intermediate phases affect the crystallization of the perovskite phase.

4.3.3. Thin films deposition of $KTaO_3$

Besides studies on precursor solutions and powders reported in the previous sections, the most important from the technological point of view is to fabricate thin films. In this chapter, the deposition, crystallization and characterization of chemically deposited 2D structures are presented, using the precursor solutions described in previous sub-chapters: i) alkoxide KTO precursor solution, and ii) diol-based KTO precursor solutions (KTO*ac* and KTO*acac*). Some of the experimental details are also listed in Table 4-18. The films were crystallized according to the procedure *AP-I* (alkoxide KTO) and *AP-II* (using diol-based precursor solutions, KTO*ac*, KTO*acac*, LTO and NTO).

4.3.3.1. Alkoxide-based derived films

A series of KTO thin films were initially deposited onto platinized Si substrates by spin coating of alkoxide KTO precursor solution, and then heat treated (*AP-I*) in a wide range of temperatures from 700 to 950 °C, in order to crystallize the desired perovskite phase. Figure 4-59 presents the XRD diffraction patterns of KTO films crystallized at different temperatures, for 1 h. The as-deposited and dried films were annealed at 700, 800, 850, 900,

925 and 950 °C. KTO films heat treated at temperatures <900 °C are not monophasic with evidence of diffraction lines from pyrochlore $K_2Ta_2O_6$ and perovskite $KTaO_3$. When the annealing temperature reaches 900 °C, the intermediate pyrochlore is fully transformed into the perovskite phase. Thus, the minimum required conditions to obtain single $KTaO_3$ perovskite phase of thin films on platinized Si are 900 °C. These data are consistent with the ones conducted on the alkoxide derived KTO powders presented in Figure 4-43.

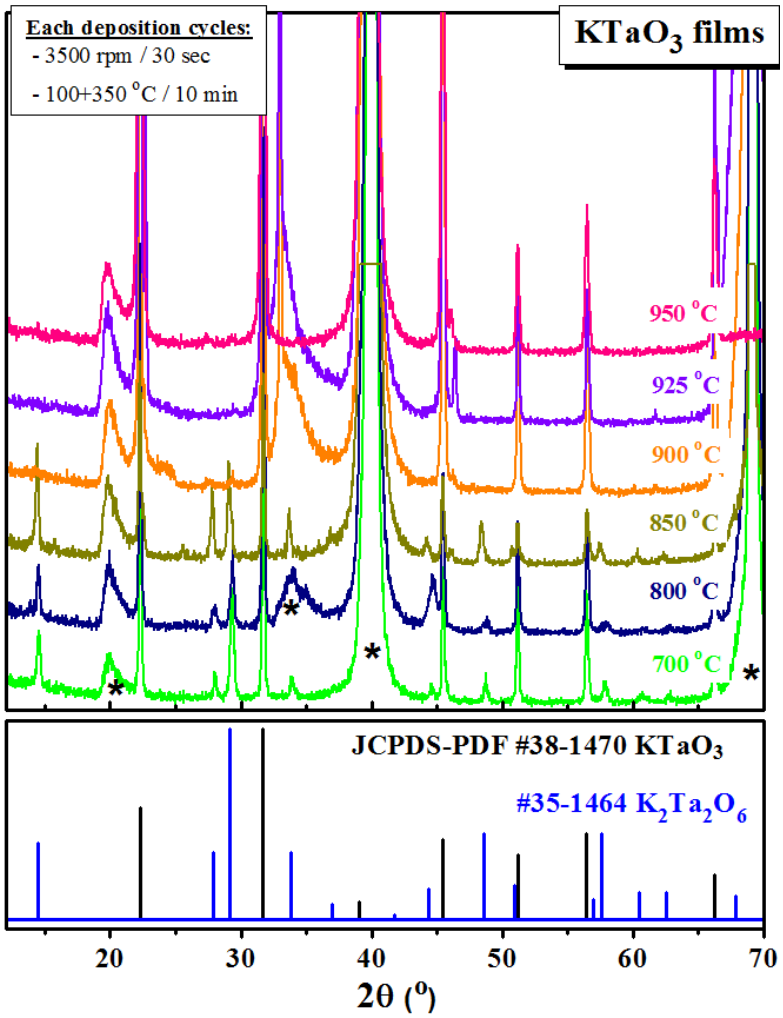

*Figure 4-59. XRD patterns of KTO thin films annealed at distinct temperatures: 700, 800, 850, 900, 925 and 950 °C, for 1 h using AP-I. Substrate reflections are marked by asterisk *. Monophasic perovskite $KTaO_3$ is achieved at temperatures ≥900 °C.*

Microstructural characterization of KTO films was performed by SEM and AFM. Figure 4-60 shows a set of microscopic images of KTO films derived from alkoxide precursor solution. The first two images, Figure 4-60 *(a)* and *(b)*, depict surface images of as-deposited

films from two separate precursor solutions: *(a)* KTO precursor solution without any modifiers in the initial chemistry (potassium and tantalum ethoxides dissolved only in ethanol), and *(b)* KTO precursor solution with addition of AcOH as a chelating agent. It is clearly seen that too fast hydrolysis in KTO precursor solution without any additive results in extremely porous films, while modifier, *i.e.* acetic acid, stabilizes this process and ultimately gives quite well defined microstructure.

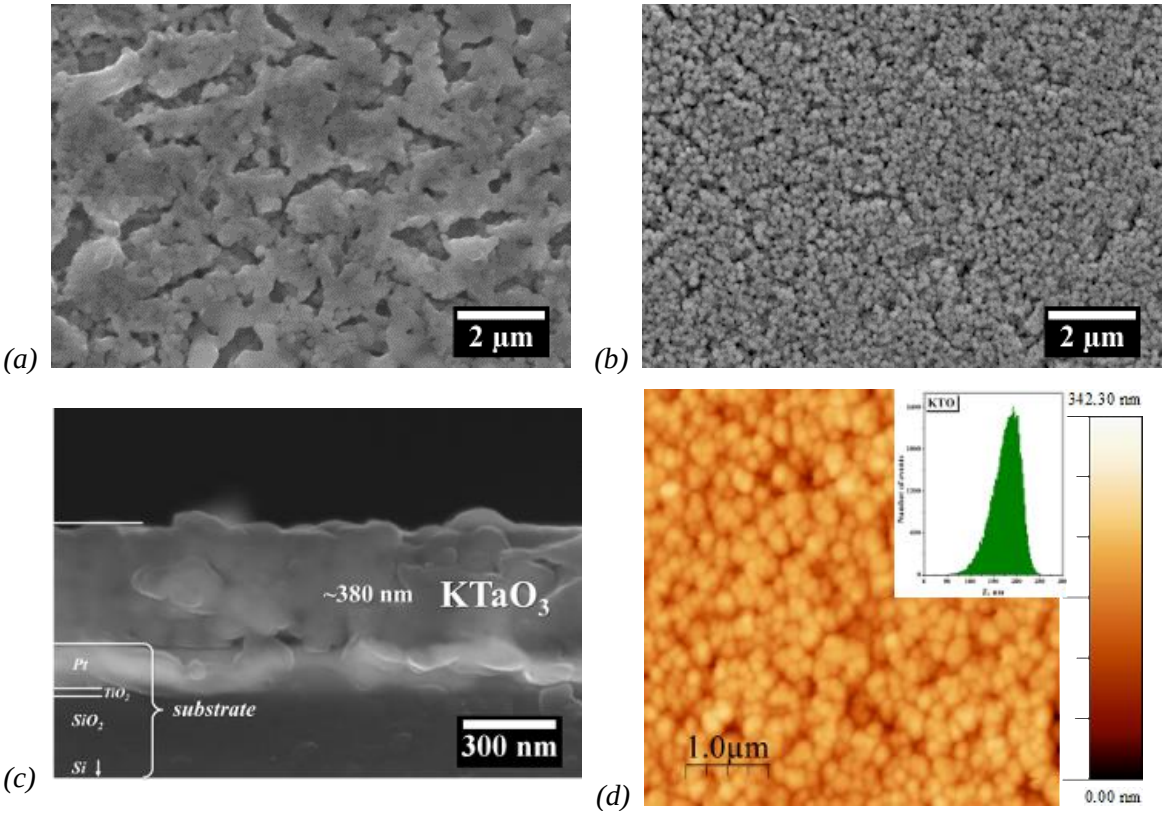

Figure 4-60. SEM micrographs of top views of KTO thin films deposited by using: (a) KTO precursor solution without any stabilizer, and (b) KTO precursor solution stabilized by AcOH. In addition, (c) SEM cross section of KTO film with thickness ~380 nm, together with constituent of substrate marks, and (d) AFM topography image, are presented (from AcOH stabilized KTO precursor solution).

Additionally, SEM micrographs of cross sections of KTO films were taken, and Figure 4-60 *(c)* depicts such microstructure, where film and constituent layers of substrate can be simply distinguished. The last image in this group (Figure 4-60 *(d)*) illustrates an AFM micrograph of KTO film topography, showing uniform grains distributions with rounded shapes. The roughness analysis was performed as well: R_{RMS} ~ 30 nm.

As it was described in previous sections, preparing thin films of $KTaO_3$ presents several difficulties, ranging from the reactivity of the reagents, the formation of intermediate phases, and volatility of potassium and sensitivity of the initial solution. Therefore, an additional approach was planned and the work was carried out, namely the template route using seed layers prior to the deposition of KTO on platinized Si. Therefore, the influence of the selected seed layers: KTOs, STOs and LNOs, on the crystallization and microstructural homogeneity of KTO thin films was investigated. The seed layers were prepared by chemical solution deposition and the details are described in Chapter 3 – Experimental Methods. The films were crystallized using *AP-I* procedure.

The main aim of this study was to assess the effect of seed layers on the crystallization temperature, perovskite phase formation, orientation and microstructure of the seeded KTO thin films. Thus, a constant crystallization temperature of 900 °C was firstly used for all seeded films, using KTOs, STOs and LNOs, in order to obtain comparable results. Figure 4-61 shows a set of XRD patterns of KTO seeded films, illustrating the phase development of the films. KTO films deposited on STOs and LNOs exhibit monophasic perovskite $KTaO_3$ phase, while the patterns of films prepared on KTOs display additional diffraction lines, mainly related to potassium deficient KTO ($K_2Ta_4O_{11}$ and $K_6Ta_{10.8}O_{30}$) or tantalum oxide phases. The formation of those structures in the films is related to the excessive loss of potassium during heat treatment, allowing the formation of tantalum rich phases. In the films in which STO and LNO were used as seed layers, there were no extra phases observed.

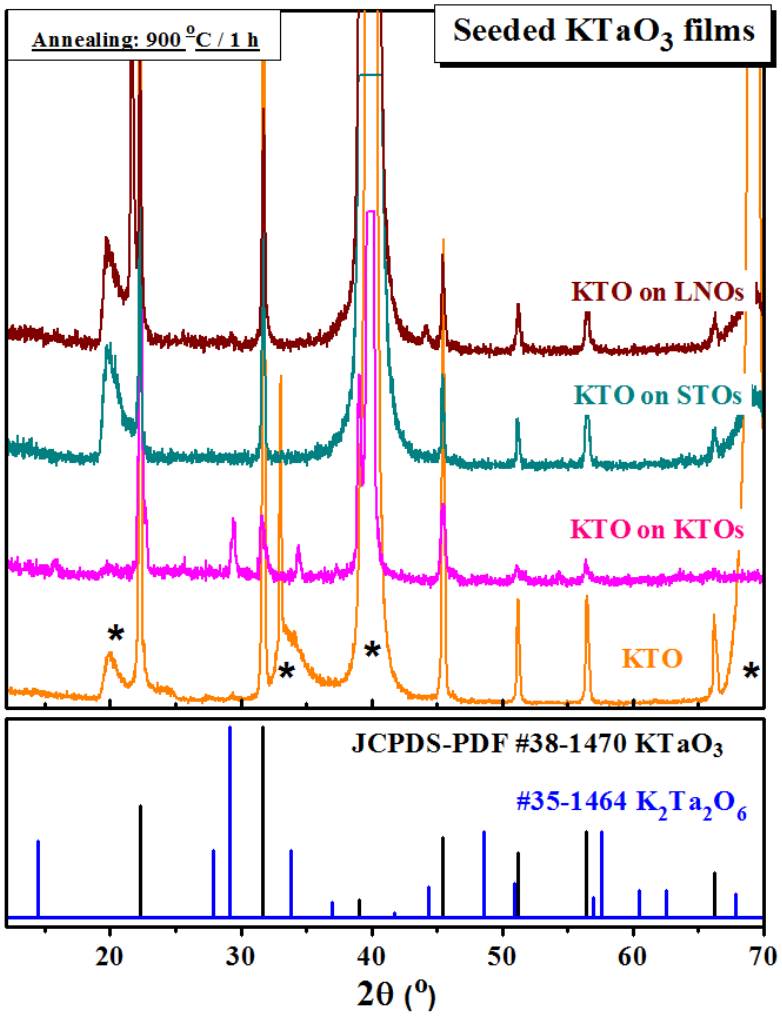

Figure 4-61. XRD patterns of KTO thin films seeded on KTOs, STOs and LNOs, and crystallized at 900 °C for 1 h. KTO seeded films on STOs and LNOs are monophasic, while the one on KTOs possesses secondary phases, such as $K_2Ta_4O_{11}$, $K_6Ta_{10.8}O_{30}$ or Ta_2O_5.

Figure 4-62 presents a set of XRD patterns of KTO films with LNOs and STOs seed layers crystallized at two distinct temperatures: 850 and 900 °C. For annealing temperature of 850 °C, diffraction peaks of intermediate phases were detected, besides the ones of perovskite $KTaO_3$ structure. It means that the crystallization temperature for perovskite phase formation in KTO films is not lowered by implementation of underlying films, and the use of 900 °C is still required.

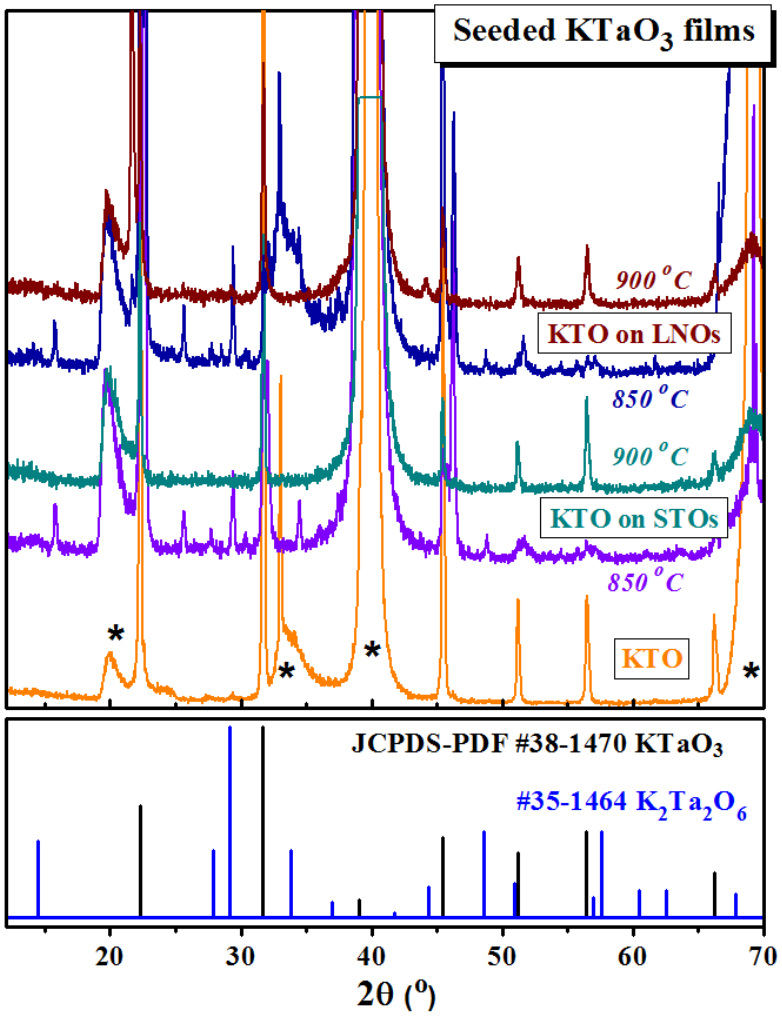

Figure 4-62. XRD pattern of $KTaO_3$ thin films, deposited onto LNOs and STOs, crystallized at two distinct temperatures: 850 and 900 °C for 1 h. The crystallization temperature of $KTaO_3$ is not reduced while using STOs and LNOs seed layers.

KTO films deposited directly onto platinized Si substrate showed a polycrystalline random pattern with (100) and (200) predominant peaks, in contrast to the seeded KTO films. Thus, texture analysis was conducted by XRD rocking curves, and the results are depicted in Figure 4-63. The rocking curves were constructed around the Bragg angle corresponding to the (100) plane ($2\theta = 22.27°$). The most intense curve is the one of unseeded KTO films, while a small and broad peak is observed in the curve of KTO seeded on KTOs, showing some degree of orientation. The rocking curves of KTO films seeded on STOs and LNOs are practically equivalent, showing a completely random character. The smaller the Full Width at Half Maximum (FWHM) of the rocking curve, the better the

orientation of the textured sample. Surprisingly, the use of seed layers diminishes the orientation of KTO thin films.

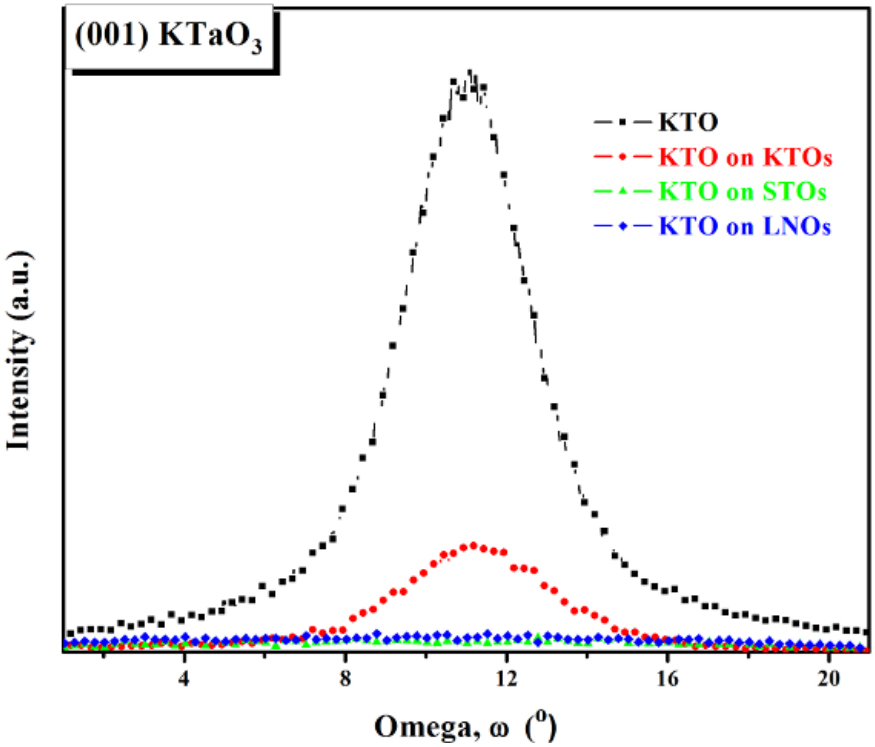

Figure 4-63. Rocking curves of (100) peak of $KTaO_3$ films deposited onto seed layers. A relatively intense and narrow peak is only displayed for unseeded KTO film when compared to others, much less intense and broadened peak of seeded with KTOs, or those without any peak, seeded with STOs and LNOs, meaning that these films are randomly oriented.

SEM microstructures of cross sections of seeded KTO thin films are shown in Figure 4-64. From the micrographs the thickness of KTO films is ~380 nm, whereas the seed layers thickness is between 35 and 40 nm; the slight variation of the seed layer thickness is related to chemical differences of initial solutions. Elemental analysis by EDS was performed on the cross sections of the seeded KTO films. The elemental distribution of potassium and tantalum is uniform across the films, with an absence of other elements, namely from the template layers compositions.

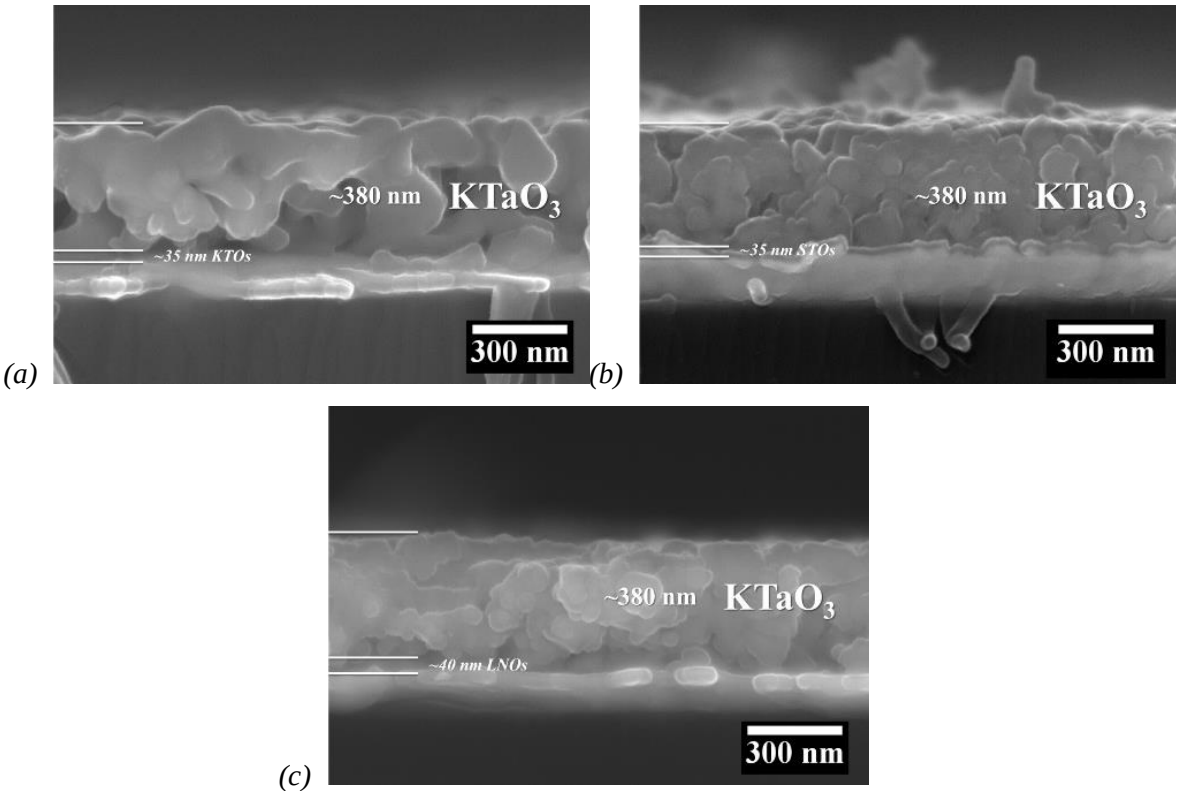

Figure 4-64. Cross sectional SEM images of seed KTO thin films onto KTOs (a), STOs (b) and LNOs (c), crystallized at 900 °C for 1 h. KTO films thickness was estimated to be ~380 nm.

Topography analysis were performed by AFM, using contact mode. Figure 4-65 illustrates a collection of AFM surface images of seeded KTO films. Grain size and their distribution presents homogeneous pattern, similar to unseeded films. Additionally, roughness analysis reveals minor differences in the R_{RMS} values, being ~14, ~16, and ~10 nm, for KTO onto KTOs *(a)*, STOs *(b)*, and LNOs *(c)*, respectively. While, the R_{RMS} of KTO deposited directly onto platinized Si substrate is ~30 nm (see Figure 4-60 *(d)*), being almost the double of that of seeded ones.

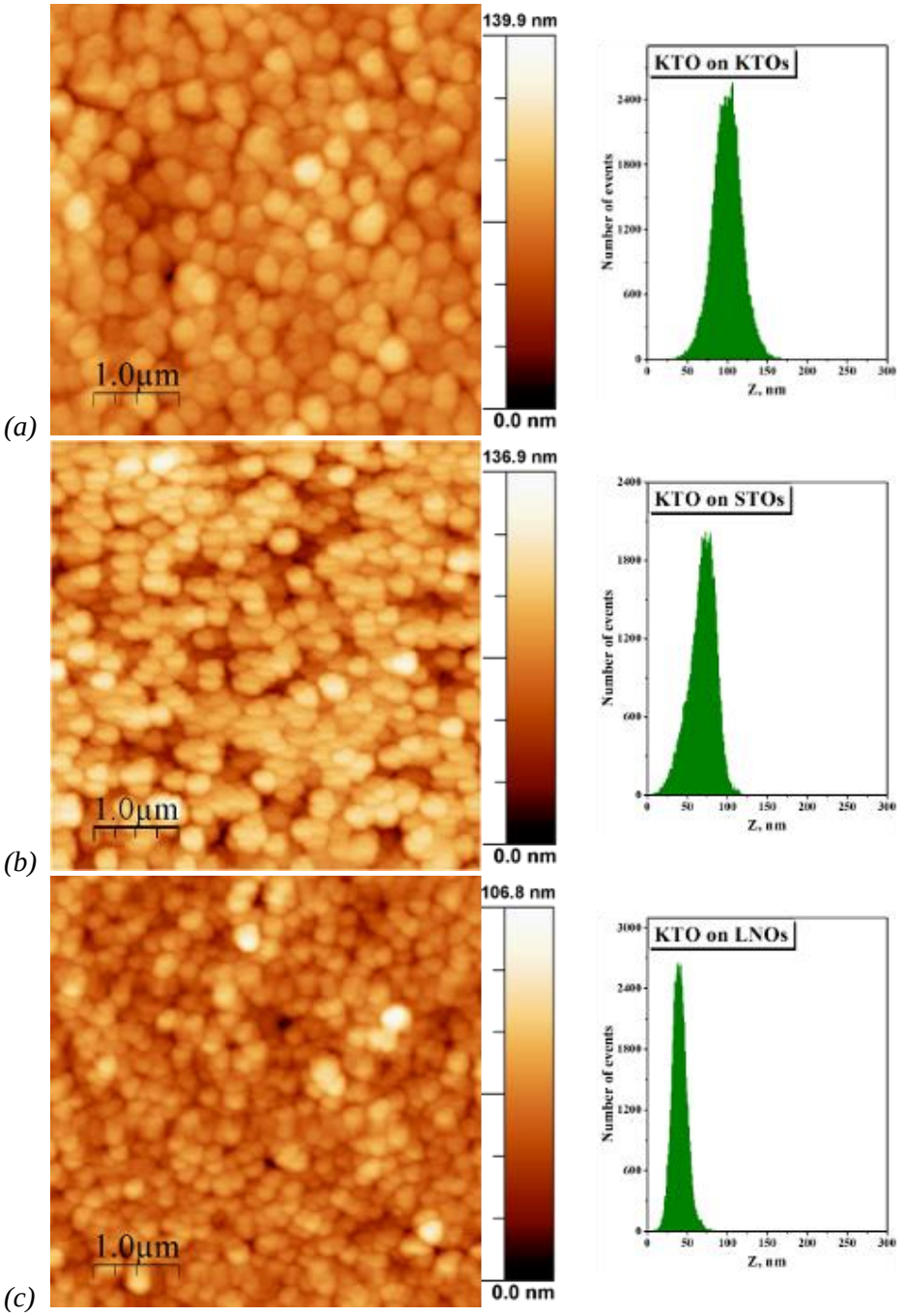

Figure 4-65. 2D AFM topography images of seed KTO thin films onto KTOs (a), STOs (b), and LNOs (c). The R_{RMS} values are ~14, ~16, and ~10 nm, for KTO onto KTOs, STOs, and LNOs, respectively. There is no difference in the grain size of the films.

Summing up this part of work it can be concluded that: i) the densification of seeded films was not improved, only the surface roughness reduced, ii) some of the under-layers, *i.e.* KTOs, caused the formation of secondary phases, namely potassium-deficient KTO and Ta_2O_5, iii) there was no evident influence on the crystallization temperature of perovskite

$KTaO_3$ phase, and iv) the preferred orientation of seeded KTO films was reduced by introducing the seed layers, resulting in randomly oriented films (KTO on STOs and LNOs).

In comparison with other systems the role of the seed layers in KTO is somehow masked by the high temperatures that are required for the processing of KTO films from alkoxide-based precursor solution. Thus, it is imperative to decrease the synthesis temperature of $KTaO_3$ films.

4.3.3.2. Diol-based derived films

Due to the unsuccessful attempts in processing of monophasic perovskite $KTaO_3$ films at relatively low temperatures, further research on KTO thin films fabrication was conducted. The goal is to decrease the heat treatment conditions for perovskite $KTaO_3$ formation, preferably ≤700 °C, using carefully designed solution processing and controlled heat-treatment. The aim includes combined three-folded strategy: i) the use of diol-based synthesis route that has been reported as successful route in processing of lead-based systems (increasing the stability and reducing the toxicity of the solutions [393-395]), ii) design of precursor chemistry through change of the metal precursor, using alkali carboxylate with short alkyl chain length (potassium acetate) versus alkali β-diketonate (potassium acetylacetonate), and iii) implementation of rapid thermal treatment in O_2 atmosphere. Rapid thermal processing facilitates the formation of desired phase at reduced thermal budget [96, 142].

The as-deposited set of KTO films onto platinized Si substrate were annealed at distinct temperatures, in order to follow the phase formation in respect to the used precursor solution, either KTO*ac* or KTO*acac*. Firstly, XRD analysis of thin films was conducted, and the patterns are shown in Figure 4-66. The chosen crystallization temperatures of the films were 650 and 700 °C for KTO*ac*, 550, 600, 650, 700 and 900 °C for KTO*acac*. The reference diffraction lines of perovskite $KTaO_3$ (JCPDS-PDF #38-1470) and pyrochlore $K_2Ta_2O_6$ (JCPDS-PDF #35-1464) are added at the bottom of the graph for comparative observation of the crystallized phase. KTO*ac* produces films with the perovskite phase as the major one, but traces of secondary pyrochlore peaks are detected, independent on the annealing temperature. In the case of KTO*acac*, perovskite $KTaO_3$ is the only phase in the films annealed at 650 and 700 °C, while the films heat-treated at temperatures <600 and 900 °C

reveal secondary phases of pyrochlore $K_2Ta_2O_6$ (at low temperatures) and K-deficient structure such as $K_6Ta_{10.8}O_{30}$ (at 900 °C). Therefore, the phase evolution depends strongly on the precursor solution used for films preparation, as it was demonstrated in studies on powders from the same solutions (Figure 4-55). The use of KTO*acac* facilitates the formation of the perovskite phase.

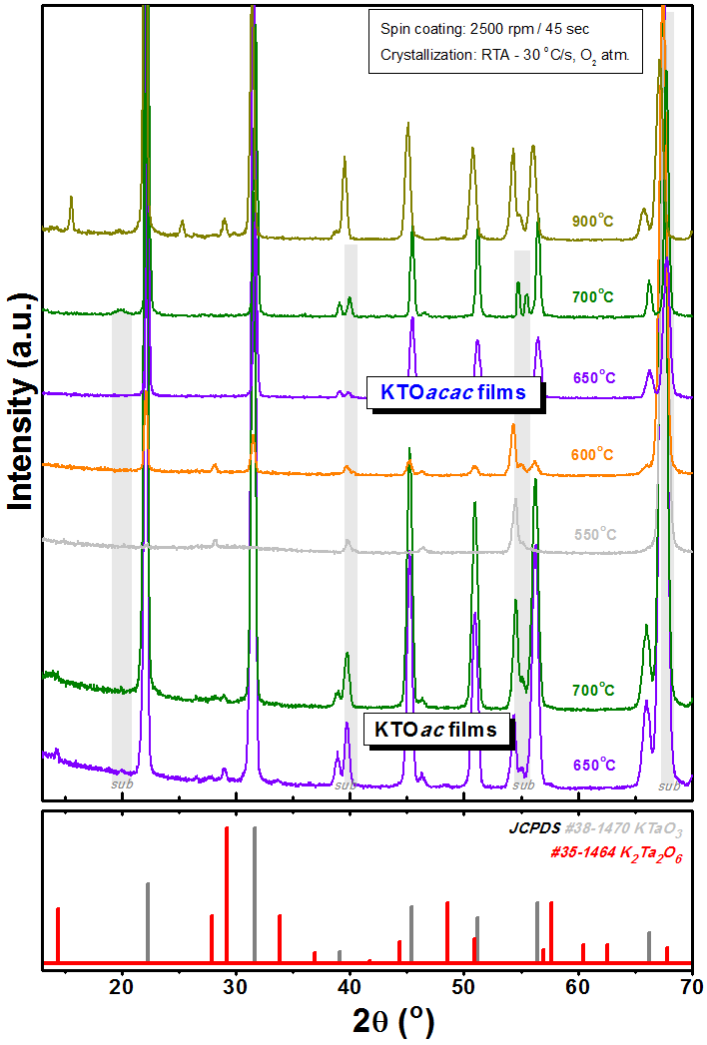

Figure 4-66. Set of X-ray diffraction (XRD) patterns of KTO thin films deposited onto platinized Si substrate at distinct temperatures: 550, 600, 650, 700 and 900 °C, for 5 min in static O_2 atmosphere. The films were deposited using KTOac and KTOacac precursor solutions. Bottom frame present XRD reference patterns of pyrochlore $K_2Ta_2O_6$ (JCPDS-PDF card #35-1464) and perovskite $KTaO_3$ (JCPDS-PDF card #38-1470) phases. The highly monophasic films with desired perovskite $KTaO_3$ were grown using KTOacac solution and crystallized at 650 and 700 °C.

Additionally, a potassium excess effect on the perovskite $KTaO_3$ phase was examined. Therefore, KTO*acac* precursor solutions with distinct K excess were prepared and then the films were processed at elevated temperature: 700 °C. Figure 4-67 shows the XRD patterns of KTO films derived from KTO*acac* precursor solutions with chosen K excess of 5, 15, 17.5, 20 and 25 %; the highest K content was commonly used in the previous studies. A minimum 20 % of K excess is needed to fabricate monophasic $KTaO_3$ films, while lower K contents produce diphasic films composed of the pyrochlore and perovskite phases. In the case of bulk ceramics processed via solid state reaction the used K excess is much lower, normally ~5 % [98, 101, 396, 397].

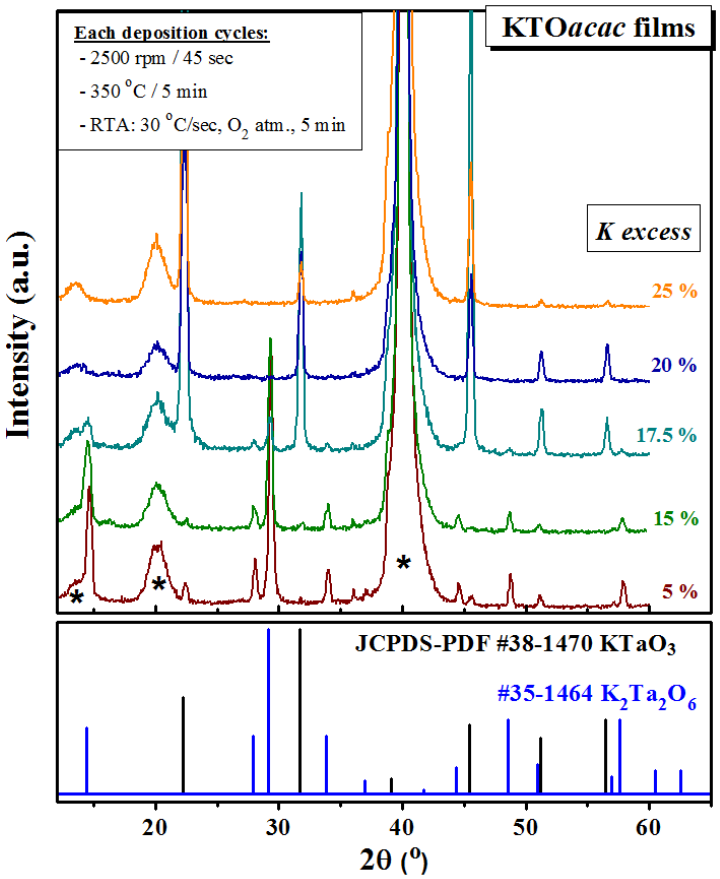

*Figure 4-67. XRD patterns of KTOacac thin films deposited onto platinized Si substrate at 700 °C for 5 min in static O_2 atmosphere. Distinct K excess was used in KTOacac precursor solutions: 5, 15, 17.5, 20 and 25 %. Bottom frame present XRD reference patterns of pyrochlore $K_2Ta_2O_6$ (JCPDS-PDF card #35-1464) and perovskite $KTaO_3$ (JCPDS-PDF card #38-1470) phases. Substrate reflections are also marked by *. A minimum 20 % of K excess is needed to fabricate monophasic KTO films.*

The microstructure of the films was analysed using AFM (topography) and SEM (cross-section) microscopy. The AFM and SEM micrographs of KTO*ac* and KTO*acac* films annealed at 650 °C (with 25 % K excess) are presented in Figure 4-68. AFM micrographs were collected in the 5 × 5 μm scan size, and a roughness analysis carried out in WSxM software. The histograms of the analyses are depicted as insets, displaying the height on the *x*-axis and number of events on the *y*-axis, and the output gives R_{RMS} for KTO*ac* film of 4.5 nm while for KTO*acac* of 6.9 nm. The electron micrographs of the films cross sections, show the film thickness ~370 nm for both, KTO*ac* and KTO*acac* films, qualitatively demonstrating the adhesion of the film to the substrate.

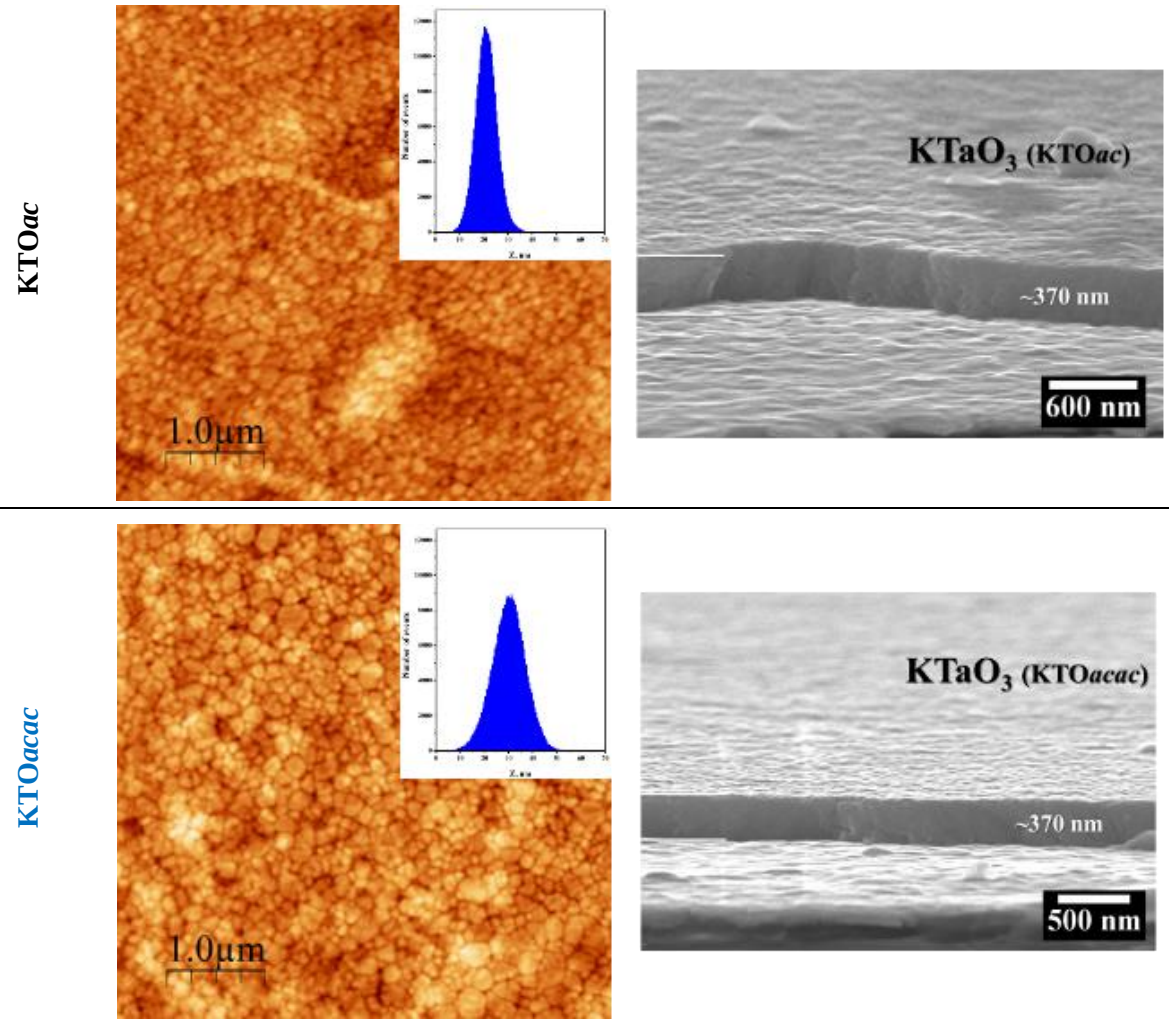

Figure 4-68. Atomic Force Microscopy (AFM) and Scanning Electron Microscopy (SEM) micrographs of KTOac and KTOacac thin films annealed at 650 °C. AFM micrographs depict the top views (morphology) of the films, while SEM the cross sections (interfaces).

The as-prepared KTO films with modified methodology, diol-based with distinct potassium precursors crystallized by RTA, are well-developed coatings with fine grain distribution and densification. The major difference between KTO*ac* and KTO*acac* lies in the phase formation, being related to the chemistry of the precursor solutions. This approach, combining three-folded strategy, is an effective route for preparation of perovskite $KTaO_3$ thin films. Monophasic KTO films with perovskite structure were successfully prepared at the temperatures ≤700 °C, being compatible with Si technology. Therefore, this approach is used to fabricate LTO and NTO films on platinized Si substrates.

4.3.4. Diol-based derived $LiTaO_3$ thin films

Ferroelectric $LiTaO_3$ thin films were synthesized using low-toxic diol-based precursor solution, described in details in experimental part, and crystallized in RTA furnace. Different annealing temperatures (600, 650 and 700 °C) were tested, within *AP-II* procedure, and the XRD results are presented in Figure 4-69. Here, 600 °C is already a sufficient temperature to synthesize monophasic $LiTaO_3$ films with rhombohedral crystal symmetry (space group: *R3c*), with a good matching of the characteristic diffraction lines to JCPDS-PDF #29-0836; peaks in the 2θ range of 20–70° corresponding to the following crystallographic planes: (012), (104), (110), (006), (113), (202), (024), (116), (211), (122), (018), (214), (300), (125) and (208), as illustrated in the bottom graph of the XRD results. The films crystallized at higher temperatures, 650 and 700 °C, present comparable patterns, thus, the tested temperatures do not influence the crystallization of desired phase.

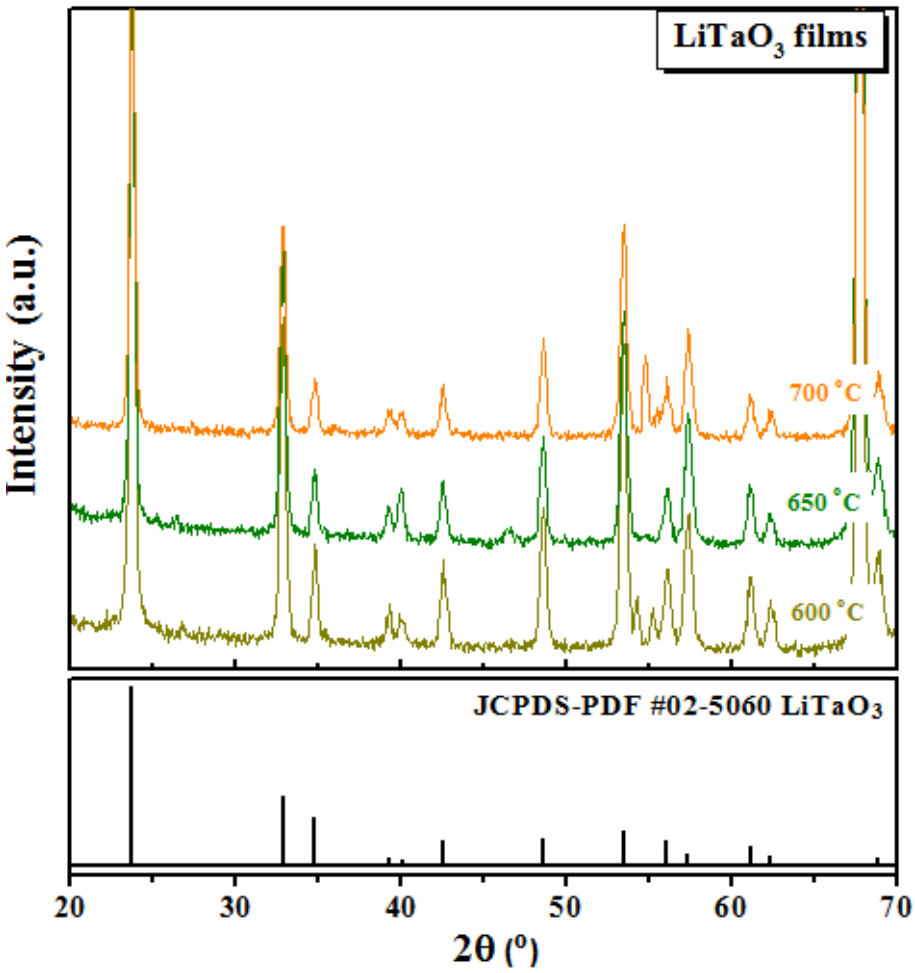

Figure 4-69. GI-XRD patterns of $LiTaO_3$ thin films annealed at distinct temperatures: 600, 650 and 700 °C for 5 min in O_2 atmosphere. All data, recorded in the 2θ range of 20–70°, show monophasic patterns consistent with rhombohedral crystal structure (space group: R3c) matching well with JCPDS-PDF card #02-5060.

The microstructure of as-prepared LTO films was analysed by AFM and SEM. Figure 4-70 shows the top view and cross section of $LiTaO_3$ film annealed at 650 °C. The roughness of the films, R_{RMS}, was calculated to be 2.7 nm, and the histogram of the analysis is enclosed as the inset of AFM micrograph, with the peak centre located at ~10 nm. The film thickness was estimated to be ~350 nm, and microstructure looks very well-developed, dense, with relatively small grain size.

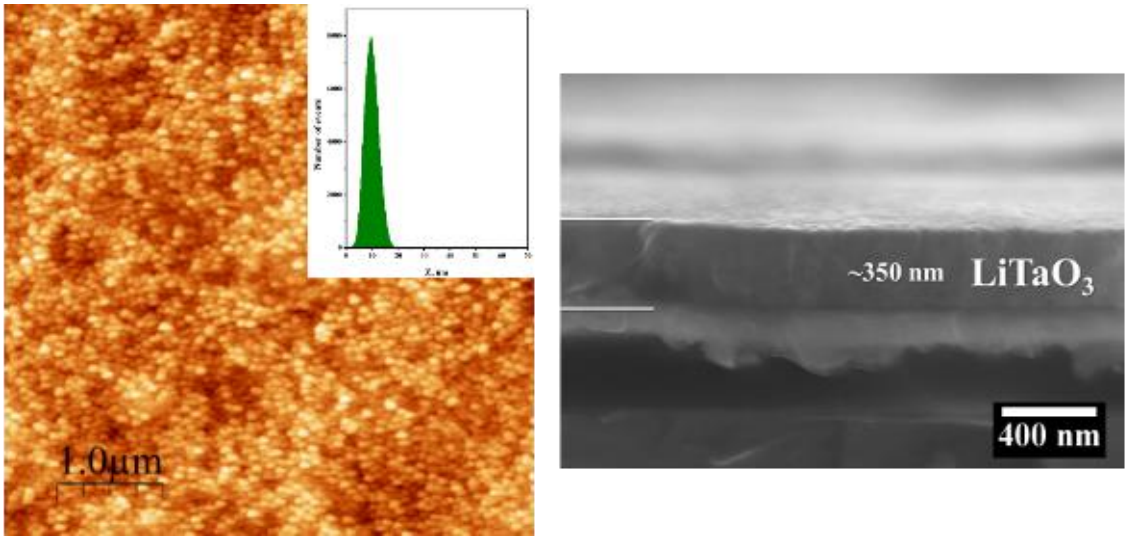

Figure 4-70. AFM and SEM micrographs of $LiTaO_3$ thin films annealed at 650 C, illustrating the top view (morphology) of the films by AFM and cross section (interfaces) by SEM. Inset in the AFM presents the histogram of roughness analysis, R_{RMS} = 2.7 nm.

Electrical properties of the $LiTaO_3$ film annealed at 650 °C were measured to evaluate the ferroelectric and piezoelectric character of the sample. Capacitance variations as function of DC voltage (C-V measurements) were used to study the electrical properties of the $LiTaO_3$ thin films. Figure 4-71 presents the C-V curves of LTO films annealed at 650 °C, measured at 10, 50 and 100 kHz for DC voltage from -16 to 16 V. The C-V characteristic curves of the produced films confirm their ferroelectric behaviour, representing the change of polarization in the film, and typical butterfly-shaped loops were observed. The initial rise in the capacitance with the applied voltage is due to the increased domain wall movement which is locked-in by defects at zero bias and partial switching of the domains [398]. The maximum capacitance is observed when most of the domains are in the process of switching and the domain wall movement contribution to the polarization is maximum; the peaks at voltages correspond to the coercive field strength of the film. At higher fields, the capacitance decreases due to two phenomena: i) a lowering of the number of domains (and their walls) because they align with the DC field, and ii) a preserving of the oscillation of remaining domain walls by a large DC bias. The asymmetry of the loops with respect to the capacitance axis in this case can be explained as a result of the difference between the bottom and top electrodes (gold and platinum in the present case), that is due to different work functions of the metals; the space charge at the two electrodes create an internal bias shifting

the curve. The reduced peak height in negative applied bias can be because of the depletion layer capacitance or possible self-polarization of the film [399, 400].

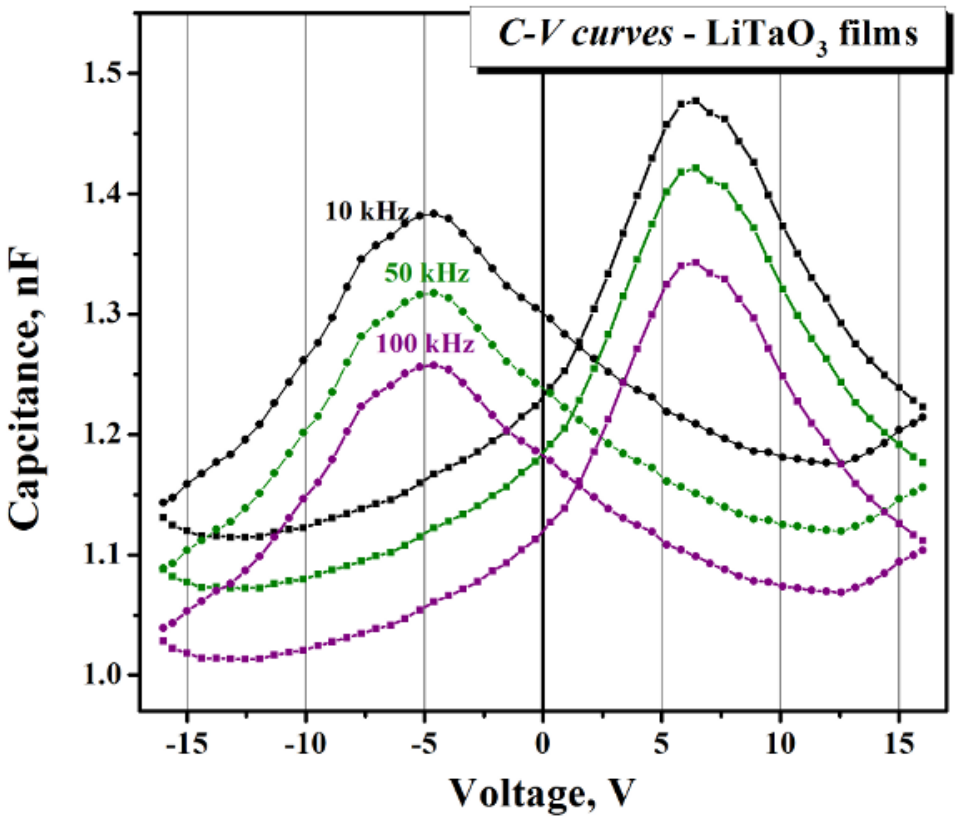

Figure 4-71. Macroscopic electrical measurements of $LiTaO_3$ thin films in parallel capacitor configuration. C-V measurements of the films were conducted using LCR Meter, showing a typical ferroelectric butterfly-shaped loops.

Piezoelectric character of LTO thin film was proved by local analysis of film by PFM. The feedback of the analysis is shown in Figure 4-72. Lateral piezoelectric contrast (LPFM, amplitude) provides information on the magnitude of the local electromechanical coupling. The local piezoresponse hysteresis loops show polarization switching in two distinct polarization directions (marked on the piezoresponse micrograph).

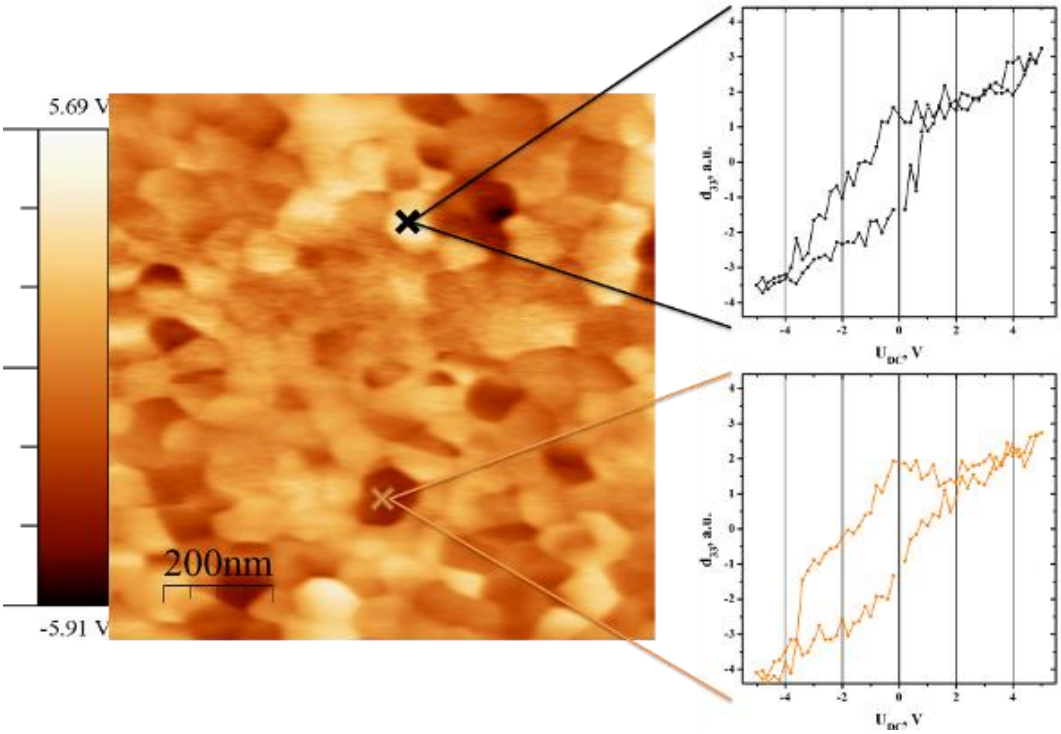

Figure 4-72. Lateral PFM signals (amplitude) of $LiTaO_3$ thin film, with local piezoresponse hysteresis loops showing polarization reversibility.

LTO thin films were successfully prepared on platinized Si substrates via low-toxic chemical solution processing with RTA assisted annealing. The use of diol-based route for LTO films processing proved that the low-toxic precursor solution is effective to process other than KTO alkali tantalate compounds. However, LTO films have already been prepared using diol-based approach over last years (see Table 4-19). Gou *et al.* [401] fabricated LTO films on platinized Si substrate, and the dielectric, ferroelectric and pyroelectric properties of those films were measured: the dielectric constant and loss were 45 and 0.006, respectively (at 10 kHz), the remanent polarization was 10.71 $\mu C \cdot cm^{-2}$, and the pyroelectric coefficient of 1.43×10^{-8} $C \cdot cm^{-2} \cdot K^{-1}$ (at 62 °C). Kao *et al.* [142, 144] also reported the preparation of LTO films derived from diol-based sol-gel process. The relative dielectric constant of ~45 and tanδ of 0.0035 were obtained.

Table 4-19. Review of the selected reports on chemical solution deposition of $LiTaO_3$-based thin films. Versatile routes were used and the experimental details of each of them are listed.

Group/ references	Compositions	Cryst. temp.	Experimental details	Remarks
Cheng *et al.* [135-138]	$Li(Ta_{1-x}Nb_x)O_3$, x = 0, 0.67, 0.5, 0.33 and 1	≥500 °C (depending on heating regime)	Precursors and solvents: Li-, Nb- and Ta-ethoxide, ethanol Precursor solution procedure: mixing in a dry nitrogen chamber, over a week Heat-treatment: pyrolysis at 300 - 400 °C for 15 min, crystallization by slow heating (0.2, 0.5, 2 and 5 °C/min) for 30 min at 400 - 700 °C or rapid thermal processing (8 - 13 °C/sec) for 120 sec at 500 - 800 °C Substrates: SiO_2/Si, p-type (111)Si	Li:Ta = 1
Kao *et al.* [141-145]	$LiTaO_3$	700 °C	Precursors and solvents: Li-acetylacetonate and Ta-isopropoxide, 1,3-propanediol Precursor solution procedure: reflux at 140 °C for 30 min (Li:diol = 1:5) and then at 120 °C for 1 h (with Ta), at the end stirring at 80 °C for 20 h Heat-treatment: pyrolysis at 400 °C for 2 or 30 min in air or at 300 °C for 2 min in O_2, crystallization by conventional heating (5 °C/min) at 700 °C for 1 h, or by rapid thermal processing (10 - 50 °C/sec) at 500 - 800 °C for 2 min in O_2 Substrates: (111)Pt/Ti/SiO_2/(100)Si	Diol route
González *et al.* [402]	$LiTaO_3$	≥500 °C	Polymeric precursor method (Pechini process) Precursors and solvents: Li carbonate and Ta-ethoxide, citric acid, ethylene glycol Heat-treatment: pyrolysis at 300 °C for 1 h in air (2 °C/min), crystallization by slow heating (5 °C/min) for 3 h at 350 - 600 °C Substrates: (100)Si	
Kimura *et al.* [403]	$LiTaO_3$	≥600 °C	Precursors and solvents: Li- and Ta-ethoxide, ethanol, aqueous H_2O_2 Precursor solution procedure: stirring in dry argon gas, reflux at 100 °C for several hours Heat-treatment: pyrolysis at ~ 300 °C for 1.5 h in O_2, crystallization at 500 - 750 °C Substrates: Si and Pt/Si	Li:Ta = 1

Table 4-19. Review of the selected reports on chemical solution deposition of $LiTaO_3$-based thin films. Versatile routes were used and the experimental details of each of them are listed. (Cont'd.)

Group/ references	Compositions	Cryst. temp.	Experimental details	Remarks
Satapathy *et al.* [139, 140]	$LiTaO_3$	≥650 °C	Precursors and solvents: Li- and Ta-ethoxide, ethanol, acetic acid Precursor solution procedure: mixing in a dry argon chamber Heat-treatment: drying at 200 °C for 15 min, crystallization at 350 - 1000 °C for 15 min in oxygen Substrates: (111)Pt/TiO_2/SiO_2/(100)Si, (111)Si and (006)sapphire	
Youssef *et al.* [146, 147]	$LiTaO_3$	≥550 °C	Precursors and solvents: Li-acetylacetonate and Ta-isopropoxide, 1,3-propanediol Precursor solution procedure: reflux at 140 °C for 30 min (Li:diol = 1:5) and then at 120 °C for 1 h (with Ta), at the end stirring at 80 °C for 15 h Heat-treatment: pyrolysis at 300 °C for 2 or 30 min in air, crystallization by rapid thermal processing (5 or 50 °C/sec) at 550 - 750 °C for 2 min in O_2 Substrates: (100)Si, (001)sapphire	Diol route
Gou *et al.* [401, 404-407]	$LiTaO_3$	≥650 °C	Precursors and solvents: Li-acetate and Ta-ethoxide, 1,2-propanediol or 2-methoxyethanol, acetic acid Precursor solution procedure: mixing at 120 °C and then reflux at 140 °C for 4 h + 110 °C for 12 h in air or N_2 Heat-treatment: drying at ~ 200 °C for 5 min, pyrolysis at 400 - 450 °C for 30 min in air, crystallization at 650 - 750 °C for 5 min in air Substrates: p-type (111)Si, (111)Pt/SiO_2/(100)Si, fluorine doped tin oxide (FTO) glass	Li:Ta = 1

LTO films prepared in this work present well-developed microstructure with small grains, flat surface, uniform and homogenous microstructure. Electrical characterizations demonstrated that the monophasic LTO films hold ferroelectric and piezoelectric characteristics.

4.3.5. Diol-based derived $NaTaO_3$ thin films

Similarly to LTO, other member of alkali tantalate family, NTO thin films on platinized Si substrates via diol-based chemical solution deposition were prepared. The precursor solution was synthesized by diol-based route, the films were spin coated and ultimately crystallized in the RTA furnace. Initially, various annealing temperatures were tested to optimize the conditions for achieving monophasic perovskite $NaTaO_3$. XRD patterns of NTO films crystallized at 600, 650 and 700 °C for 5 min are depicted in Figure 4-73; bottom frame shows diffraction lines corresponding to pyrochlore $Na_2Ta_2O_6$ (JCPDS-PDF #70-1155) and perovskite $NaTaO_3$ (JCPDS-PDF #10-2738).

Here, 600 °C is already a sufficient temperature to synthesize monophasic perovskite $NaTaO_3$ films with orthorhombic crystal symmetry (space group: *Pnma*), with well matching of characteristic diffraction lines. The films crystallized at higher temperatures, 650 and 700 °C, present comparable patterns. Thus, the tested temperatures do not influence the crystallization of the desired phase, and the pyrochlore structure formation is avoided.

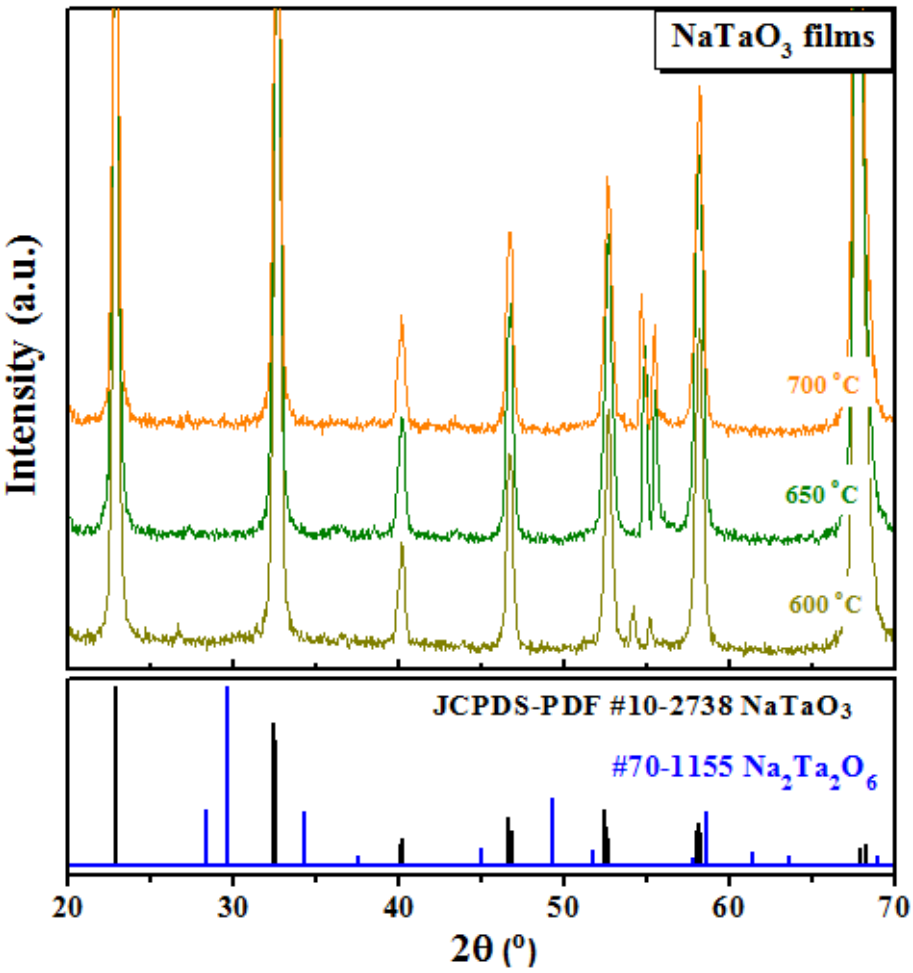

Figure 4-73. XRD patterns of $NaTaO_3$ thin films annealed at distinct temperatures: 600, 650 and 700 °C for 5 min in O_2 atmosphere. All curves are composed of monophasic $NaTaO_3$ patterns within recorded range of 2θ (20–70°), matching with JCPDS-PDF #10-2738.

The microstructure of the as-prepared films annealed at 650 °C were analysed and micrographs are depicted in Figure 4-74; top view AFM micrograph with histogram of the height as inset (left), and cross section SEM (right). The topological microstructure shows very distinctive characteristics with spherical grains (diameter ~150 nm) and interconnected microcracks. Despite this, the microstructure is well-compacted and dense, with relatively low roughness, R_{RMS} ~ 8.5 nm, and estimated thickness ~350 nm.

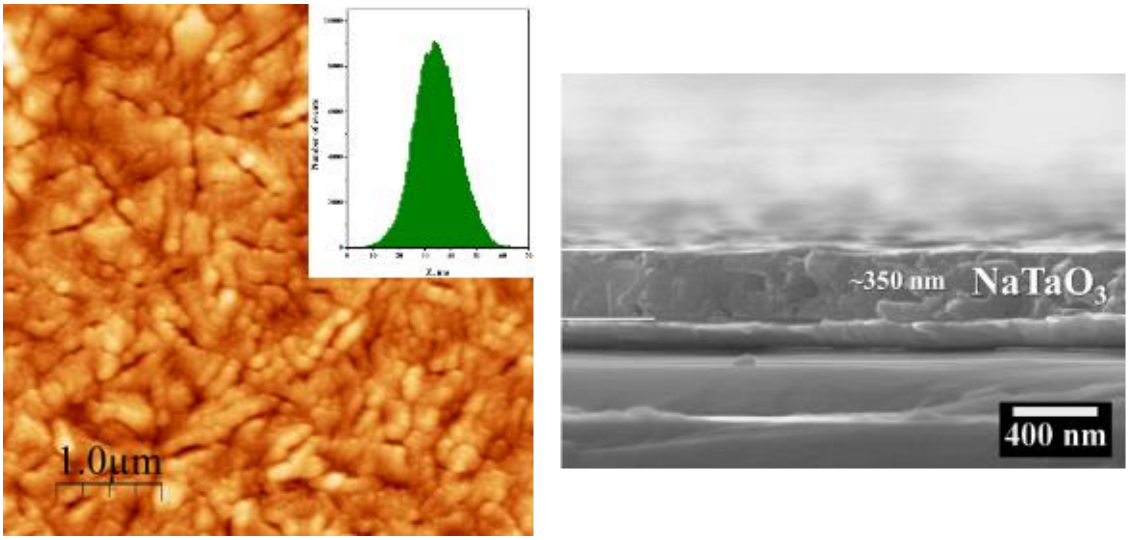

Figure 4-74. Atomic Force Microscopy (AFM) and Scanning Electron Microscopy (SEM) micrographs of $NaTaO_3$ thin films. AFM depicts the top views (morphology) of the films, while SEM the cross sections (interfaces). Roughness was estimated to be ~8.5 nm and thickness ~350 nm.

Electrical properties of NTO films were investigated, and C-V curves recorded at room temperature are shown in Figure 4-75. The measurements were carried out at frequency of 10 kHz (AC signal amplitude was set at 0.1 V) with applied DC bias from negative to positive 20 V. This behaviour is typical for materials with antiferroelectric order.

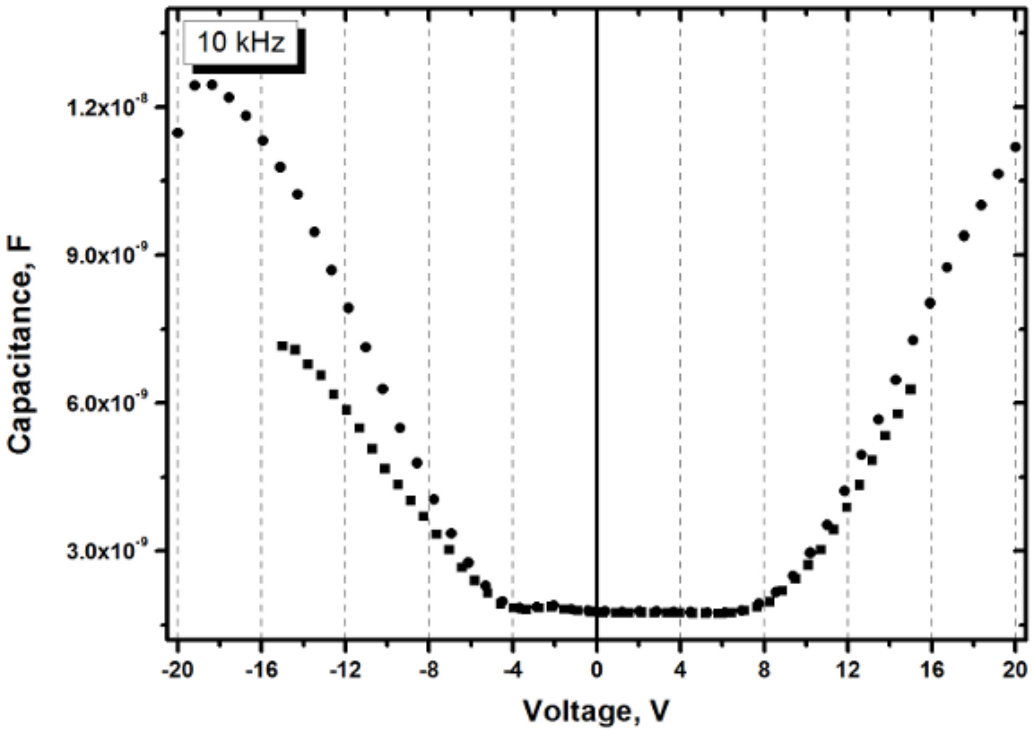

Figure 4-75. Macroscopic electrical measurements of $NaTaO_3$ thin films in parallel capacitor configuration. C-V measurements of the films were conducted using LCR Meter at frequency of 10 kHz.

The very recent works on bulk ceramics of NTO [42, 153] reported that dielectric properties traced down to liquid helium temperatures did not reveal any phase transitions, and dielectric permittivity was frequency independent with slight rise on cooling. Due to the absence of ferroelectric or antiferroelectric order, the microwave losses are very low, and it was detected that the microwave dielectric permittivity of $NaTaO_3$ ceramics exhibits increase on cooling and saturation at low temperatures, thus the system can be classified as incipient ferroelectric [153]. However, the only studies on $NaTaO_3$ films revealed, contrary to bulk ceramic, an anomaly at low temperatures, a dielectric relaxation below ~50 K assigned to polar hopping due to the charges induced by oxygen vacancies; any irreversible polarization mechanism was excluded [42]. Therefore, our results are in contradiction to the reported where it was claimed that a classic incipient ferroelectric behaviour (continuous increase of dielectric permittivity with temperature decrease) was observed while our data show room temperature antiferroelectric order. Further studies, especially at low

temperatures, need to be conducted to clarify these differences because the literature is rather poor in dielectric properties of $NaTaO_3$ films.

The dielectric permittivity of 350 nm thick $NaTaO_3$ thin films is $\varepsilon_r \sim 290$ while dielectric loss, $\tan\delta$, ~0.025, measured at room temperature and at frequency of 10 kHz. The ε_r values are comparable with bulk ceramics and much higher than 650 nm thick films deposited by RF magnetron sputtering, <100 [42]. In this case the interface-induced phenomena and/or grain size effect may play a crucial role, affecting the switching characteristics and dielectric properties of thin films. Tagantsev and Gerra identified three groups of such effects, examining PZT and BST [408]: i) passive layer type that can exist in the nearby-electrode regions, giving rise to certain characteristics in the measured films, ii) ferroelectric-electrode contact potential phenomena, *e.g.* depletion effect due to the electrochemical interaction between the conductive electrode and the electronic carriers of the dielectric, and iii) poling of the ferroelectric-electrode interface, such as the internal bias due to the mechanical coupling between the dielectric material and the electrodes. Thus, one of the presented scenario have to be taken into account while measuring thin films in capacitor configuration.

Summary

The chemical solution deposition methodology is shown to be versatile and adjustable method for processing of alkali tantalate thin films on rigid substrates. The two different routes were adopted to optimize the formation of the perovskite $KTaO_3$ films: i) alkoxide, and ii) diol-based for the synthesis of KTO precursor solutions. The former one is a classical approach used for decades in the processing of thin films of complex oxides. KTO precursor solution derived from this process results in the perovskite $KTaO_3$ phase formation at high temperatures, ≥900 °C. Nevertheless, such temperatures are too high for processing of the films on platinized Si substrates. On the other hand, a diol-based route combined with careful selection of the potassium precursor, specifically potassium acetylacetonate instead of potassium ethoxide or acetate, modifies the perovskite phase formation. The lack of intermediate pyrochlore phase led to lowering of crystallization temperature of the perovskite structure down to 650 °C. Within this procedure, the low moisture-sensitive tantalum compound was used, Ta(V)-glycol, allowing to handle the further preparations at ambient conditions. Therefore, it was demonstrated that the use of a diol-based sol-gel method can be very effectively optimized by the solution chemistry of the method, in order to fabricate the lead-free films. As a proof of concept, other alkali tantalates, LTO and NTO thin films, were successfully prepared using a diol-based approach to demonstrate the feasibility of the methodology.

4.4. Photocatalytic activity of alkali tantalates and niobates

Abstract

Alkali tantalates and niobates are listed as important photocatalysts for the development of renewable energy technologies and environmental remediation. In this work, the photocatalytic degradation of methylene blue dye in an aqueous solution using two groups of compounds: i) potassium tantalum oxides (K-Ta oxides) with distinct structures and stoichiometry: sol-gel derived perovskite $KTaO_3$, stoichiometric pyrochlore $K_2Ta_2O_6$, non-stoichiometric pyrochlore $KTa_{2.2}O_6$ and tetragonal tungsten bronze $K_6Ta_{10.8}O_{30}$, and ii) well-crystalline perovskite-like structures prepared by solid-state method, $LiTaO_3$, $LiNbO_3$, $NaTaO_3$, $NaNbO_3$, $KNbO_3$ and $KTaO_3$, was investigated.

It is demonstrated that ferroelectric $KNbO_3$ is the most efficient photocatalyst among the tested ones because it combines an electronic band structure, which can respond successfully to the UVA-light with a relatively high surface energy that enhances catalytic properties. This work provides an ideal platform for a rational design of more efficient ferroelectric based photocatalytic devices.

Nowadays, the dye pollutants have become a major source of environmental pollution because the conventional technologies are not capable of reducing them at the lowest levels demanded by the environmental laws [409]. Therefore, in the last decades, the development of new technologies such as the advanced oxidation processes (AOPs) for treating both gas and water pollutants, has been promoted [409, 410]. Among the AOPs, the heterogeneous photocatalyst has been reported as a promising tool to solve some environmental issues [410, 411]. Photocatalysis using semiconductor oxides is already well-established [410]: the photoradiation in a semiconductor material promotes the electron excitation from the valence band to the conduction band, leaving thus an electron deficiency or hole in the valence band,

which generates electron/hole pairs. Both the reduction and oxidation processes can occur at/or near the surface of the photoexcited semiconductor particle. The band gap energy is the property, which indicates the required energy for a semiconductor material to promote its electrons from valence level to the conduction level in order to convert photon energy into chemical energy for redox reactions [409].

In aerated aqueous suspensions, the reduction of molecular oxygen (O_2) produces superoxide ions ($O_2^{\bullet-}$), and its protonated form, the hydroperoxyl radical ($HO_2^{\bullet}$) [410]:

$$O_2 + e^- \rightarrow O_2^{\bullet-} \quad (18)$$

$$O_2^{\bullet-} + H^+ \rightarrow HO_2^{\bullet} \quad (19)$$

In this way, electron/hole recombination can be effectively prevented and lifetime of holes is prolonged. $HO_2^{\bullet}$ can lead to the formation of H_2O_2:

$$HO_2^{\bullet} + e^- \rightarrow HO_2^- \quad (20)$$

$$HO_2^- + H^+ \rightarrow H_2O_2 \quad (21)$$

Photogenerated holes can react with adsorbed water molecules (or hydroxide anions) to give hydroxyl radicals:

$$H_2O + h^+ \rightarrow HO^{\bullet} + H^+ \quad (22)$$

or they can also be filled by an adsorbed organic donor. In aqueous solutions oxidation of water to hydroxyl radical seems to be the predominant pathway. Superoxide anion can also act as an oxidant. The whole process can end in the complete mineralization of the organic compounds.

Among photoactive materials with good photo-physical properties are tantalates, that possess conduction bands consisting of Ta *5d* orbitals located at a more negative position than the dominant in this field titanates (Ti *3d*), or niobates (Nb *4d*). Thus, the high potential of the conduction band of tantalates might be beneficial in the photocatalytic reactions [191]. It has been reported that perovskite tantalates, as well as niobates, are a series of promising photocatalysts which can induce not only photocatalytic water splitting, but also promote oxidative decomposition of organic contaminants under suitable illumination. Other attractive aspects of these compounds are low toxicity and high stability [412, 413]. Ta-based oxides are known to be active photocatalysts for water splitting under UV irradiation;

under band gap (4.0 eV) irradiation, pure Ta_2O_5 can only produce a very small amount of H_2 and no O_2 from pure water [184, 185, 414], but NiO-loaded mesoporous Ta_2O_5 (and heat treated) displays great activity for overall water decomposition, >500 μmol/h of H_2 and >250 μmol/h of O_2 [187]. Alkali tantalates, $ATaO_3$ (*A* = Na, Li and K), and niobates, $ANbO_3$, have also attracted an interest showing high efficiency for splitting of water into hydrogen fuels [186, 189].

Removing non-biodegradable organic pollutants by their degradation is another important aspect that heterogeneous photocatalysis can assist in. The sol-gel synthesized alkali tantalates were reported to degrade an organic dye, azo type dying agent, methylene blue (MB), with the performance in the following order: $NaTaO_3 > LiTaO_3 > KTaO_3$ [415]. Later, the most extensively investigated has become NTO, mostly the doped one [409, 416-420]. The nanosized $NaTaO_3$ powders doped with Sm have also been found to be a highly active photocatalyst for the degradation of pollutants under UV irradiation [409]. The Bi-, Cr- and N-doped NTO catalysts were even highly active under visible-light irradiation [416-420]. It was also proven that the activity of N-doped NTO is significantly higher in Rhodamine B dye degradation under visible light than the TiO_2 type P25 [420].

In this case study, a series of alkali tantalates and niobates were synthesized and their photocatalytic activity, degradation of methylene blue (MB) chosen as model dye, was assessed. Methylene blue is a heterocyclic aromatic chemical compound with the molecular formula: $C_{16}H_{18}ClN_3S$, largely used in the industry for dyeing of paper, linen and silk textiles as well as in the painting of bamboo and wood [421, 422]. In the presence of air or oxygen, the irradiated semiconductor particles are capable of destroying many organic contaminants. The activation of particles by light ($h\upsilon$) produces electron-hole pairs, which are powerful oxidizing and reducing agents. In the degradation of organic compounds (MB), the hydroxyl radical that comes from the oxidation of adsorbed water or adsorbed OH^-, is the primary oxidant, and the presence of oxygen can prevent the re-combination of hole-electron pairs. The molecule of MB is known to be converted to small organic species, which are subsequently mineralized, thus, degradation leads to the conversion of: i) organic carbon into harmless gaseous CO_2, and ii) nitrogen and sulfur heteroatoms into inorganic ions, such as nitrate, NO_3^-, ammonium, NH_4^+, and sulfate, SO_4^{2-}, ions [423]. For a complete reaction, the final products of the reaction among others are CO_2 and H_2O [421, 422]:

$$MB + HO^{\bullet} \rightarrow products\ (CO_2 + H_2O + NH_4^+ + NO_3^- + SO_4^{2-} + Cl^-) \qquad (23)$$

The photocatalytic activity of the prepared powders was evaluated in liquid-solid phase, by monitoring the degradation of an organic dye, methylene blue (Aldrich, ≥82 %), using a UV-vis spectrometer. The tests were performed at RT, in a cylindrical photocatalytic reactor (100 mm in diameter) containing an aqueous solution of the dye (1 L), at an initial concentration of 5 mg L^{-1}. The concentration of the photocatalyst in the slurry was 0.25 g L^{-1}. In order to mix the solution thoroughly, the slurry was magnetically stirred throughout the reaction; the reactor was covered with a watch-glass, so as to avoid the evaporation of the solution. The reactor was designed following the guidelines of the international standard ISO 10678. A modification was applied concerning the lightning of the reacting system – this was assured by placing two lamps at each side of the reactor; the distance between the lamps and the reactor was 5 cm (Figure 4-76). The UVA-light source was a germicidal lamp (Philips PL-S 9W, NL), having an irradiance of approximately 13 W m^{-2} in the UVA range, measured via a radiometer (Delta OHM, HD2302.0, IT), and whose maximum emission was at ~365 nm.

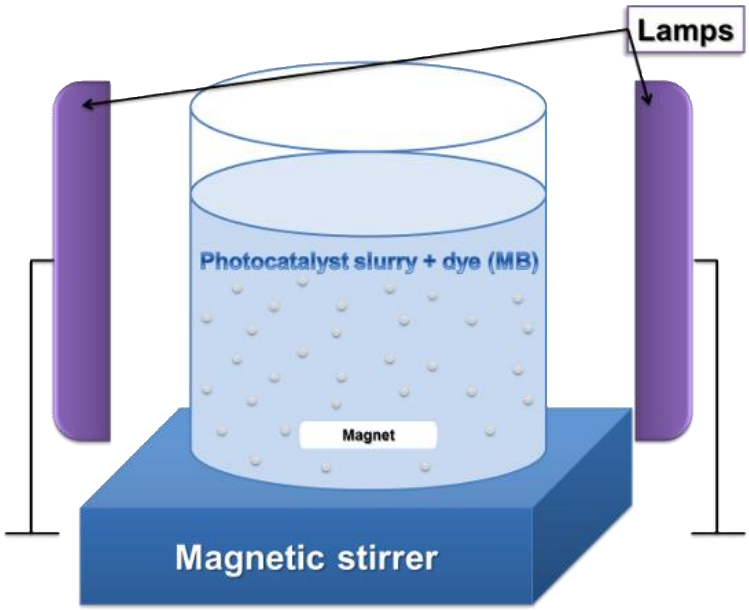

Figure 4-76. Schematic representation of the reactor used for the photocatalytic tests.

In the experiments, the photocatalytic degradation of MB was monitored by sampling about 4 mL of the slurry from the reactor, at regular time intervals. Before switching the lamps on, the suspension was stirred in the dark for 30 min, with the aim of allowing the

adsorption of MB onto the powders. The powders in the samples were firstly separated by centrifugation, and then the MB concentration in the liquid was determined. The Lambert-Beer law was implemented to determine the MB concentration, by measuring the absorbance in a spectrometer at a wavelength of 665 nm (characteristic peak that decreases in intensity with increasing irradiation time indicating degradation degree); distilled water was used as a reference. The extent of MB photodegradation efficiency, ξ, was evaluated as:

$$\xi, \% = \frac{C_0 - C_S}{C_0} \cdot 100 \tag{24}$$

where C_0 is the initial MB concentration and C_S is the concentration after a certain UVA/visible irradiation time (the total irradiation time was set at 7 h).

The photocatalytic decomposition of organic pollutants in water generally follows the Langmuir-Hinshelwood mechanism [424]:

$$r = \frac{kKC}{1 + KC} \tag{25}$$

where r is the photocatalytic reaction rate ($mol \cdot L^{-1} \cdot min^{-1}$), k is the photocatalysis rate constant ($mol \cdot L^{-1} \cdot min^{-1}$), K is the equilibrium adsorption coefficient ($L \cdot mol^{-1}$), and C is the reactant concentration ($mol \cdot L^{-1}$) at time t. At low concentrations, the term KC in the denominator can be neglected, and the reaction kinetics exhibit pseudo first-order behaviour, *i.e.*, $r = kKC$. This kinetic equation may be written in the integral form:

$$\ln \frac{C_0}{C} = kKt = k_{app}t \tag{26}$$

where C_0 is the initial reactant concentration ($mg \cdot L^{-1}$) and k_{app} is the apparent photocatalysis rate constant (h^{-1}) of the pseudo-first-order reaction. To make a more convenient comparison, the reaction kinetics of alkali tantalates and niobates were fitted according to a pseudo first-order model [425].

4.4.1. K-Ta compounds

The relatively high photocatalytic activity of tantalates was attributed to the suitable conduction band structures and proper distortion of TaO_6 octahedra. Therefore, many alkali tantalates, in principle K-Ta oxides, with distinct crystal structures and stoichiometry have

been studied over the last decade. Ishihara *et al.* [52] reported photocatalytic hydrogen evolution using perovskite $KTaO_3$ and pyrochlore $K_2Ta_2O_6$, and the latter exhibited higher activity in H_2O splitting. Then, pyrochlore $K_2Ta_2O_6$ have become a compound of interest in few studies related to photocatalysis [68, 426-428].

Particular compounds, like defect pyrochlore oxides, are also attractive as photocatalysts in wastewater treatment. These photocatalysts (defect pyrochlores) could be as effective as or even better than conventional photocatalysts [429]. Compounds of defect pyrochlores mainly containing transition metals, *e.g.* Ta, Nb, Sb, W and Mo have been studied over the years for the decomposition of organic dyes and splitting of water for hydrogen generation under UV and visible light irradiation. Therefore, the studies on K-Ta oxides with distinct structures and stoichiometry of K:Ta were carried out.

Firstly, potassium tantalum oxides were produced and tested. The samples varied in composition and structure: perovskite $KTaO_3$, stoichiometric $K_2Ta_2O_6$ and non-stoichiometric $KTa_{2.2}O_6$ pyrochlores, and TTB $K_6Ta_{10.8}O_{30}$. The compositions were synthesized by conventional solid state reaction – $K_6Ta_{10.8}O_{30}$, alkoxide route (sol-gel process) – $KTaO_3$ (assigned as $KTaO_3$ sg) and $K_2Ta_2O_6$ (assigned as $K_2Ta_2O_6$ sg), and hydrothermal process – $KTa_{2.2}O_6$ (assigned as $KTa_{2.2}O_6$ hyd); detailed procedures are described in the experimental part of the thesis. The crystallographic studies of as-prepared powders were firstly checked by XRD, and Figure 4-77 shows their patterns in the 2θ range of 20–50°. In all cases monophasic and well-crystalline samples were synthesized, and the patterns matched to the following JCPDS-PDF files: cubic perovskite $KTaO_3$ sg to #38-1470, cubic pyrochlores $K_2Ta_2O_6$ sg and $KT_{2.2}O_6$ hyd to #35-1464, and tetragonal $K_6Ta_{10.8}O_{30}$ to #70-1088. Additionally, lattice parameters were refined (in Jade 8.0), and the results are presented in Table 4-20.

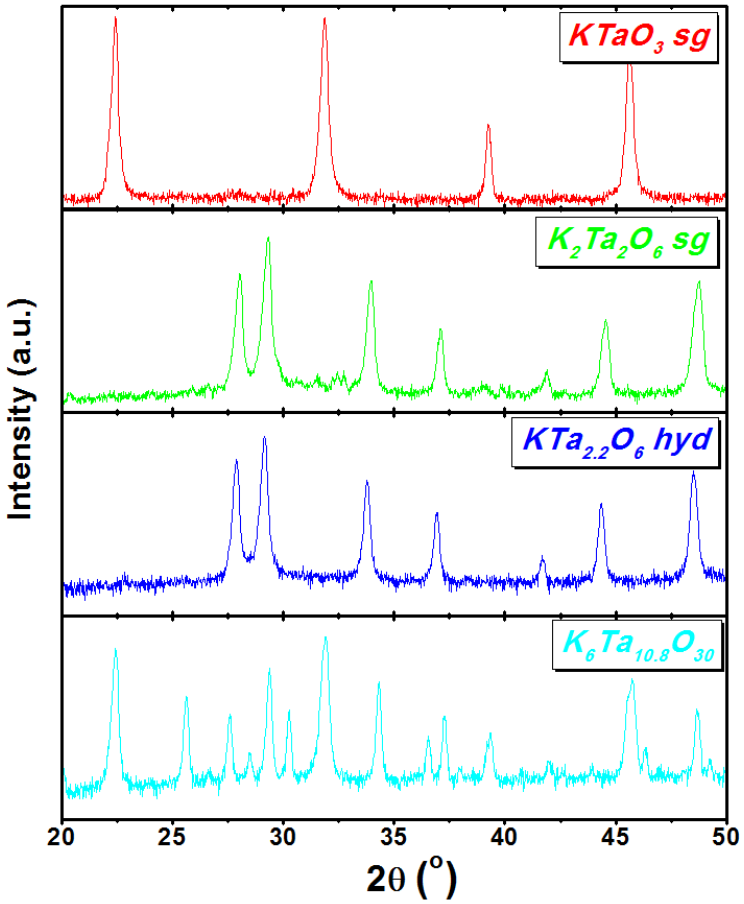

Figure 4-77. XRD patterns of K-Ta oxides with various stoichiometry and structures.

Furthermore, morphological studies of the particles were conducted. Particle size distribution plots of all compositions are shown in Figure 4-78. The particles demonstrate a bimodal distribution for $KTa_{2.2}O_6$ hyd and $K_6Ta_{10.8}O_{30}$, or a trimodal one for $KTaO_3$ sg and $K_2Ta_2O_6$ sg. The mean particle size, D_P, and BET (Brunauer–Emmett–Teller) specific surface area, SA_{BET}, of particles are shown in Table 4-20.

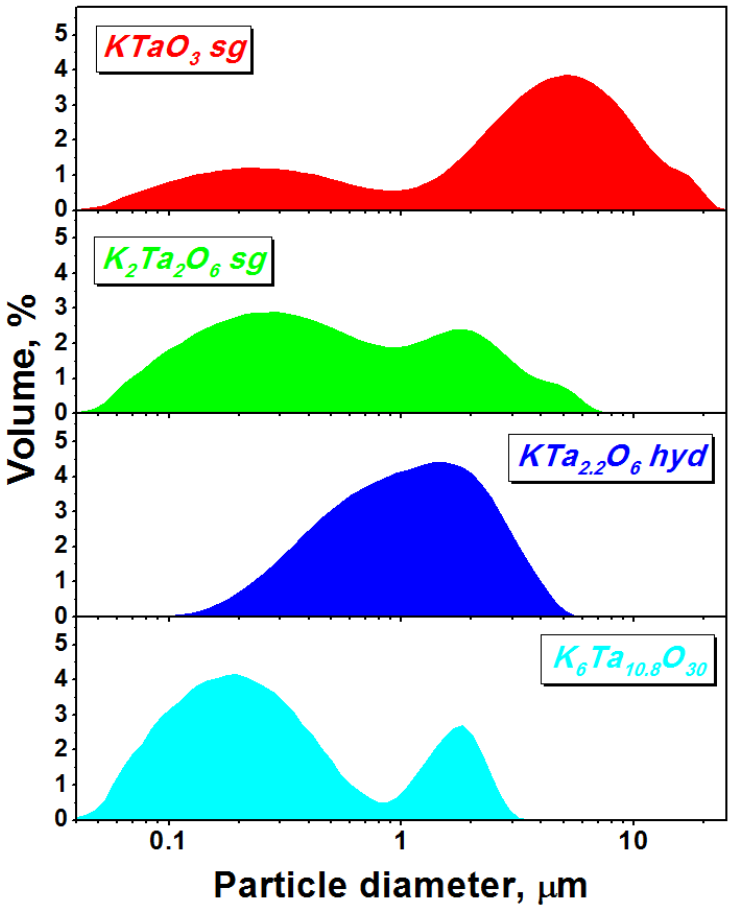

Figure 4-78. Particle size distribution of K-Ta oxides with various stoichiometry and structures.

UV-vis spectra of the analysed compositions were recorded and the diffuse reflectance spectra are depicted in Figure 4-79 *(a)*. Diffuse reflectance spectroscopy (DRS) was performed with a UV-vis spectrometer and spectra of the samples were acquired in the UV-vis range, 220–800 nm. The Kubelka–Munk function was applied with the aim to convert the diffuse reflectance into the absorption coefficient α:

$$\alpha \approx \frac{K}{S} = \frac{(1-R_\infty)^2}{2R_\infty} \equiv F(R_\infty) \qquad (27)$$

where K and S are the absorption and scattering coefficients; the reflectance R_∞ is equal to $R_{sample}/R_{standard}$ [430].

Table 4-20. Refined parameters, specific surface area and band gap of K-Ta oxides and other alkali tantalates and niobates.

	Unit cell parameters	SA_{BET}, m^2/g	D_P, µm	Band gap, eV
$KTaO_3$ sg	a = 3.9787 ± 0.0013 Å	2.570	4.638	3.60 ± 0.01 (3.4 - 3.8 eV [49, 194, 431, 432])
$K_2Ta_2O_6$ sg	a = 10.5528 ± 0.0021 Å	2.605	1.023	4.79 ± 0.08 (4.2 - 5.2 eV [52, 68, 426])
$KTa_{2.2}O_6$ hyd	a = 10.6097 ± 0.0011 Å	0.422	1.376	4.41 ± 0.17 (4.2 - 5.2 eV [52, 68, 426])
$K_6Ta_{10.8}O_{30}$ ssr	$a = b$ = 12.5451 ± 0.0036 Å, c = 3.9818 ± 0.0036 Å	1.147	0.568	3.74 ± 0.09 (3.6 - 4.1 eV [67, 68])

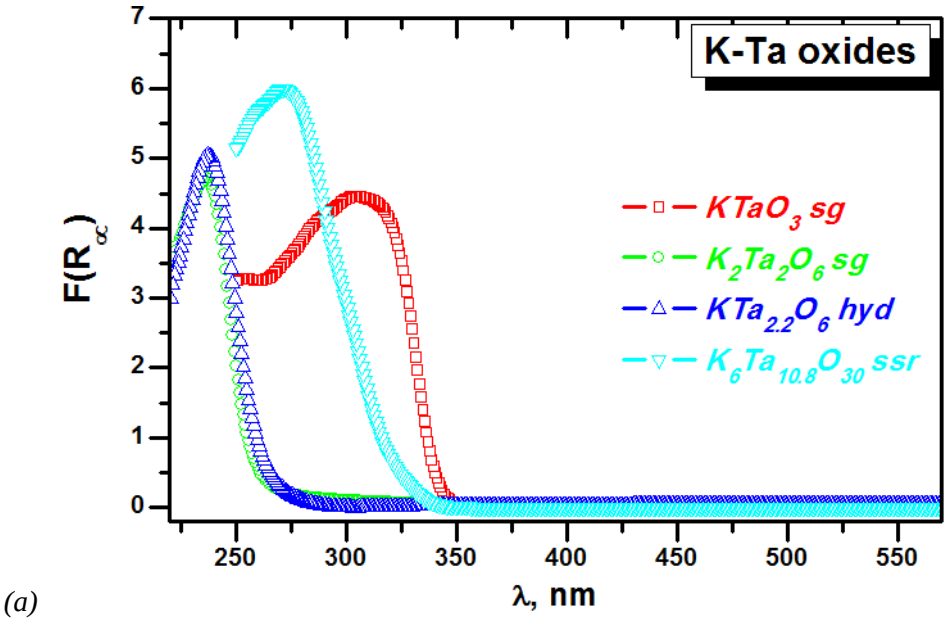

(a)

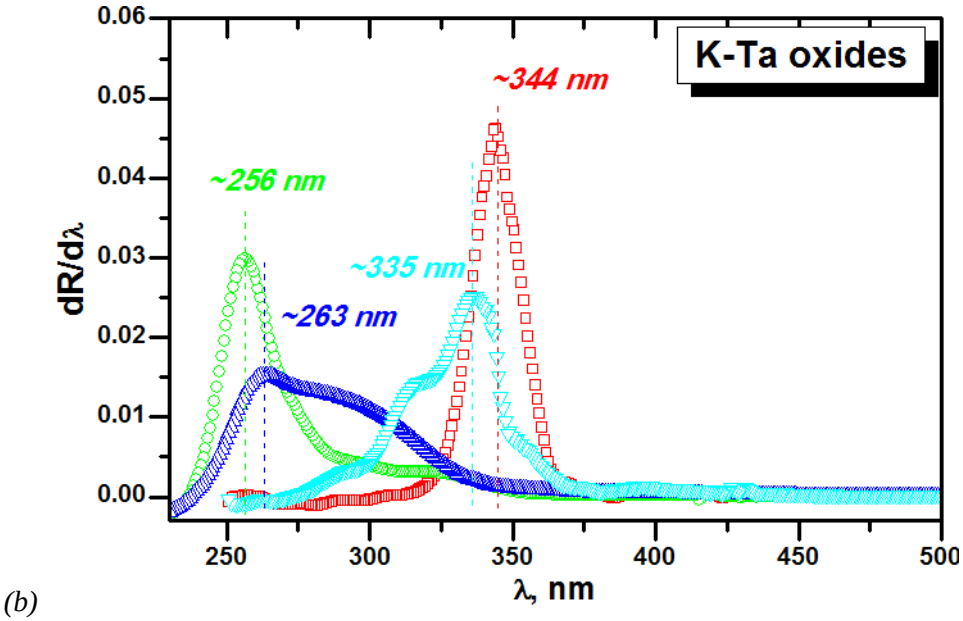

(b)

Figure 4-79. (a) Diffuse reflectance spectra of the K-Ta oxides and (b) first derivative of diffuse reflectance spectra versus wavelength of K-Ta oxides; the vertical dashed lines represent the band gaps of compounds.

It can be clearly seen that the onset of each compound (except two pyrochlores) differs significantly. Then, the energy band gap (E_g) of the compounds was calculated using the differential reflectance method (a method mainly applied for well-crystalline semiconductor materials). This method assumes that, plotting the first derivative of reflectance ($dR/d\lambda$)

versus the wavelength (λ), the maximum value of such a plot corresponds to the band gap of the semiconductor material [433]. Figure 4-79 *(b)* presents these relations for the K-Ta oxides; the absorption edge of the perovskite $KTaO_3$ sg is about 344 nm, the TTB $K_6Ta_{10.8}O_{30}$ is ~335 nm, the non-stoichiometric pyrochlore $KTa_{2.2}O_6$ hyd is ~263 nm, and the pyrochlore $K_2Ta_2O_6$ is ~256 nm. As expected, none of the powders show an absorption in the visible region, >400 nm, and the spectrum of two specimens: perovskite $KTaO_3$ sg and pyrochlore $K_2Ta_2O_6$ sg, consist of a single absorption band. The other two, TTB $K_6Ta_{10.8}O_{30}$ and pyrochlore $KTa_{2.2}O_6$ hyd, besides the main band possess also an absorption tail (shoulder) that can be attributed to mid-gap states due to impurities (second phases). The corresponding band gap energy of each sample, calculated by the differential reflectance method, is depicted in Table 4-20. The resulting curves were successfully fitted with a Gaussian function, and the maximum values were found from the fitting.

The wavelength of the main absorption edge of TTB $K_6Ta_{10.8}O_{30}$ is close to the reported by Zhang *et al.* [68], 342 nm that corresponds to the E_g = 3.63 eV, but the E_g evaluated in nanowires of the same composition by Lan *et al.* [67] was higher, 4.1 eV, that can be caused by quantum-size effect, as claimed by the authors. The adsorption edge of both pyrochlore powders is at about 260 nm, which is rather different than the reports [52, 68, 426], and it can be attributed to the strong stoichiometric deviation depending on the synthesis method and experimental conditions. The perovskite $KTaO_3$ sg has the narrowest band gap among the listed above K-Ta oxides, but its absorption edge is also located in the ultraviolet region, ~344 nm. Considering the same chemical composition of perovskite $KTaO_3$ and stoichiometric pyrochlore $K_2Ta_2O_6$, difference in the electronic configuration between these two is most likely assigned to the geometrical effects of cation and anion arrangements in the crystal lattice [52].

Photocatalytic activity results, reported as the relative MB concentration (C/C_0) during the reactions (under light exposure), are depicted in Figure 4-80 *(a)*; the negative time represents the time during which the adsorption of the dye occurs (reactor not irradiated). The K-Ta oxides exhibit a photocatalytic activity with the following order: $K_2Ta_2O_6$ sg (ξ = 11.1 %) > $KTa_{2.2}O_6$ hyd (ξ = 6.8 %) > $KTaO_3$ sg (ξ = 5.3 %) > $K_6Ta_{10.8}O_{30}$ ssr (ξ = 4.3 %). Stoichiometric pyrochlore $K_2Ta_2O_6$ was the best photocatalyst amongst the tested K-Ta oxides, being around twice more efficient than the other compounds. A reaction kinetics study was conducted as well, using a pseudo-first-order model. The apparent rate

constant, k_{app}, calculated from the slope of the linear plots of $\ln(C_0/C)$ versus irradiation time, for assessed powders is depicted in Figure 4-80 *(b)*. The MB decomposition rate also follows the order of $K_2Ta_2O_6$ sg [k_{app} = 0.028 (min^{-1}×100)] > $KTa_{2.2}O_6$ hyd [k_{app} = 0.017 (min^{-1}×100)] > $KTaO_3$ sg [k_{app} = 0.013 (min^{-1}×100)] > $K_6Ta_{10.8}O_{30}$ ssr [k_{app} = 0.011 (min^{-1}×100)].

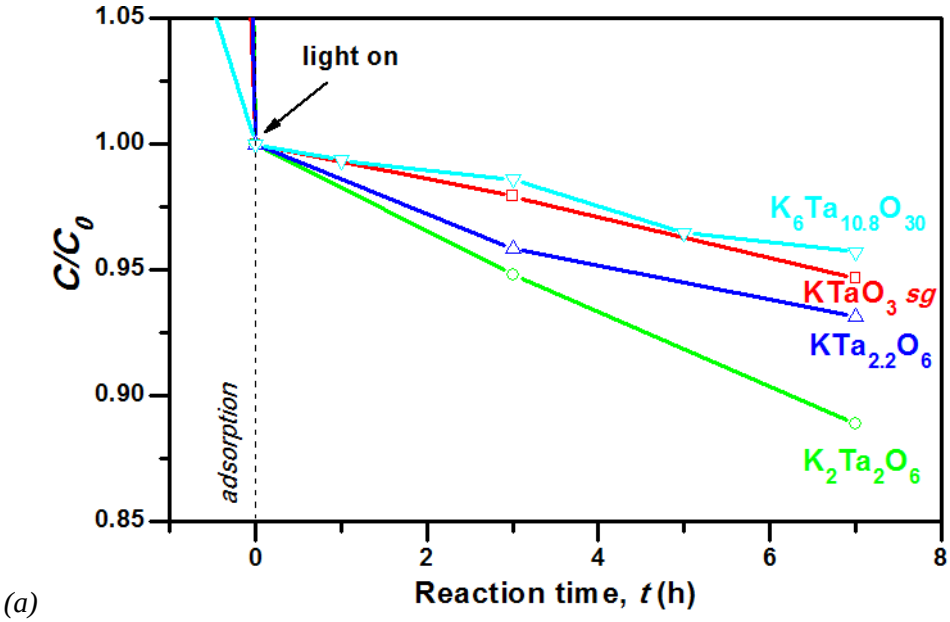

(a)

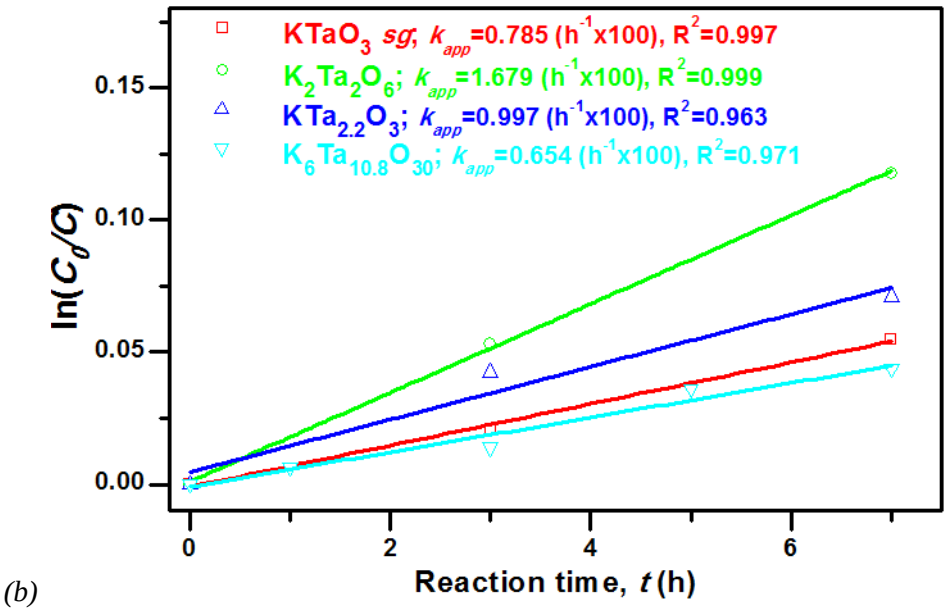

(b)

Figure 4-80. (a) Photocatalytic degradation of MB, C/C_0, and (b) first-order apparent constant, k_{app}, of the photocatalytic reaction of the assessed K-Ta oxides.

Only few studies were reported on K-Ta oxides used for photocatalytic degradation. For example, Zhang *et al.* [68] synthesized potassium tantalum oxides with defect pyrochlore, $K_2Ta_2O_6$, and tetragonal tungsten bronze type, $K_6Ta_{10.8}O_{30}$, structures. The defect pyrochlore exhibits higher photoactivity for the decomposition of acid red G and 4-nitrophenol than $K_6Ta_{10.8}O_{30}$. The crystal structure and size of the particle were the key factors of $K_2Ta_2O_6$ responding for its high photoactivity. Saiki *et al.* [434] fabricated $K_2Ta_2O_6$ films by a hydrothermal and sputtering technique using KOH and Ta/glass films. They found that the films of $K_2Ta_2O_6$ decomposed MB aqueous solution under UV light irradiation. Similarly, there have been studies on sodium tantalates ($Na_2Ta_2O_6$) as photocatalysts to treat dye wastewater [429].

4.4.2. Alkali tantalate and niobate perovskites

The as-synthesized set of alkali tantalate and niobate samples (second group) were firstly analysed by XRD as well, and in all cases monophasic patterns were detected within instrument limitation. XRD patterns are matched to the following JCPDS-PDF files: cubic $KTaO_3$ to #58-7249 (SG: $Pm\bar{3}m$), orthorhombic $KNbO_3$ to #07-9572 (SG: *Bmm2*), rhombohedral $LiTaO_3$ to #87-2461 (SG: *R3c*), rhombohedral $LiNbO_3$ to #09-3436 (SG: *R3c*), orthorhombic $NaTaO_3$ to #10-2738 (SG: *Pnma*) and orthorhombic $NaNbO_3$ to #14-2322 (SG: *Pbcm*). Structural and partially microstructural analysis was carried out using XRD patterns. The instrumental parameters were carefully selected to collect the reliable XRD data: a 20–125° 2θ range and with a step scan of 0.02° 2θ and time per step of 300 s; the incident beam pathway was as follows: 0.1251 divergence slit, 0.1251 anti-scattering slit, 0.04 rad soller slits, and a 15 mm copper mask; the pathway of the diffracted beam included a Ni filter, soller slits (0.04 rad), and an antiscatter blade (5 mm). The whole powder pattern modelling (WPPM) method was implemented to determine the average crystallite size (also referred as crystalline domain diameter), using PM2K software [255, 256, 435]. The instrumental contribution was obtained by modelling (using the same software) 14 hkl reflections from the NIST SRM 660b standard (LaB_6), according to the Caglioti relationship [436]. Crystalline domains were assumed to be spherical, and distributed according to a lognormal size distribution. Figure 4-81 *(a)* shows the graphical output of the WPPM modelling of the XRD patterns of $LiTaO_3$, $LiNbO_3$, $NaTaO_3$, $NaNbO_3$, $KTaO_3$ and

$KNbO_3$, recorded in the 2θ range of 20–125° (except $NaNbO_3$, limited 2θ to 105°). This modelling allows to refine the microstructural parameters in the same way as the structural parameters in Rietveld refinement. Additionally, structural and microstructural data of the samples were determined from a refinement of the XRD patterns by the WPPM method. The agreement factors of the refinements, unit cell parameters, crystallite size (diameter of the sphere) and mode of the size distributions are shown in Table 4-21, and size distribution is depicted in Figure 4-81 *(b)*. The quality of the refinements, represented by R-factors: R_{wp} and R_{exp}, and a goodness of fit: χ^2, is reasonable because the R-factors values are below 10 % and χ^2 is close to 1 in all cases [437]. The refined average crystallite size is 114.0, 82.1, 130.7, 201.0, 25.0 and 97.8 nm for $KTaO_3$, $KNbO_3$, $LiTaO_3$, $LiNbO_3$, $NaTaO_3$ and $NaNbO_3$, respectively. In the case of Li- and Na-containing samples, the alkali tantalates were found to be smaller in crystallite size than niobates with corresponding A-site ion. The narrowest size distribution was detected for $NaTaO_3$, while the widest for $LiNbO_3$. The stoichiometry of the samples was also confirmed by chemical analyses (ICP-MS and EPMA), being consistent with metal ratio of A:$B \approx 1$. BET surface areas, SA_{BET}, of the nanocrystalline alkali tantalates and niobates are shown in Table 4-4 as well.

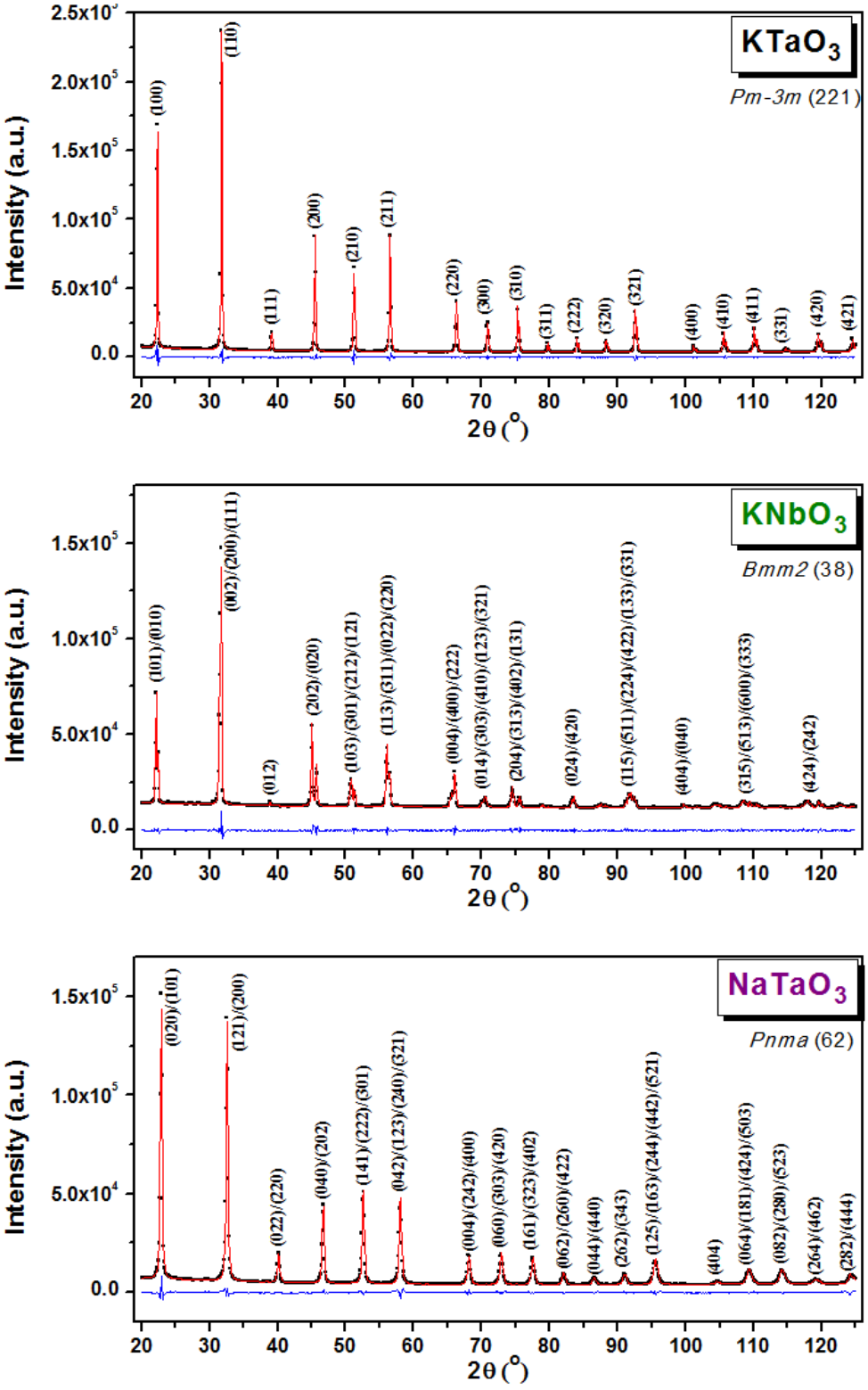

(a)

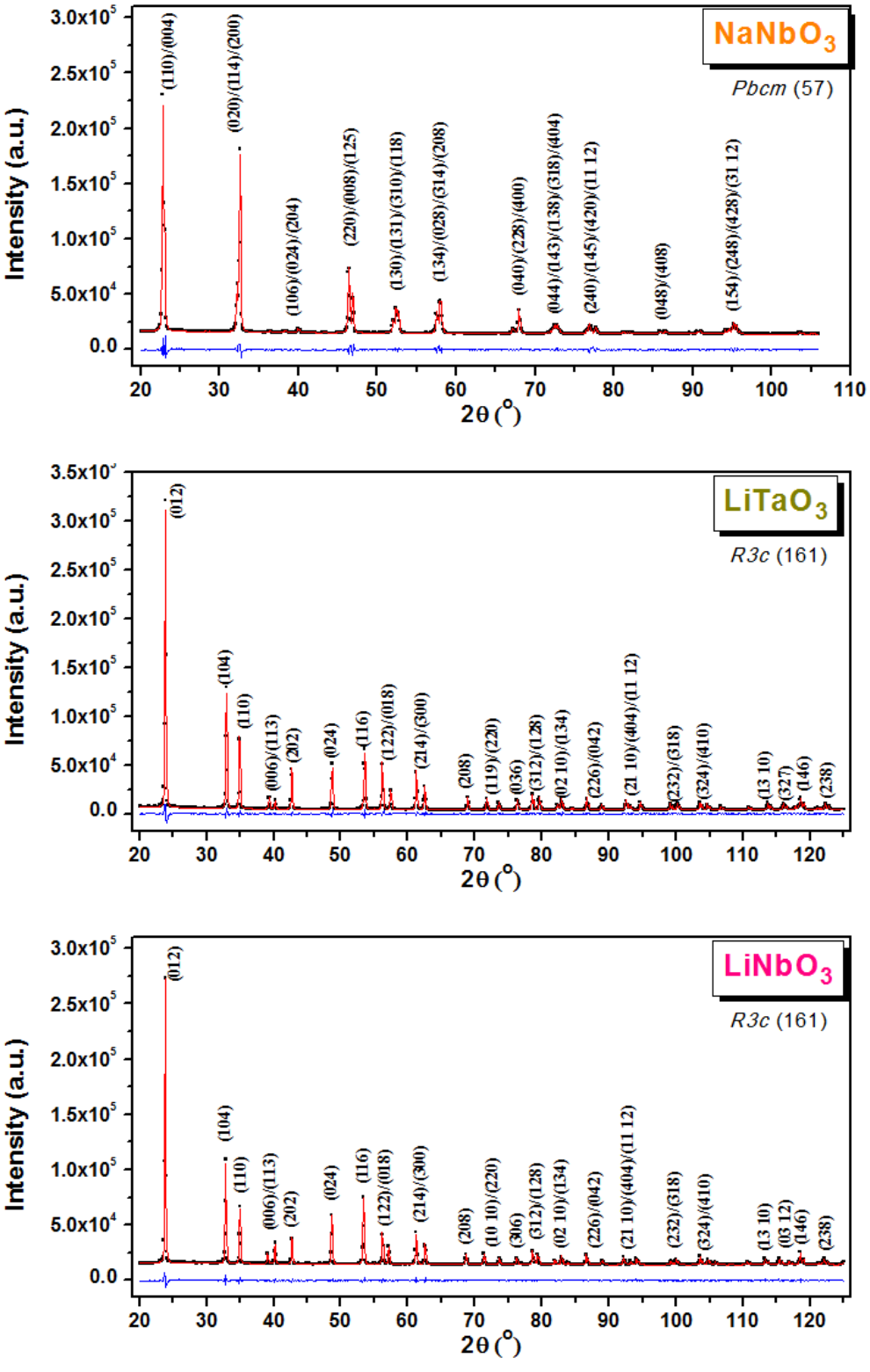
NaNbO3
Pbcm (57)
Intensity (a.u.)
2θ (°)
(110)/(004)
(020)/(114)/(200)
(106)/(024)/(204)
(220)/(008)/(125)
(130)/(131)/(310)/(118)
(134)/(028)/(314)/(208)
(040)/(228)/(400)
(044)/(143)/(138)/(318)/(404)
(240)/(145)/(420)/(11 12)
(048)/(408)
(154)/(248)/(428)/(31 12)
LiTaO3
R3c (161)
Intensity (a.u.)
2θ (°)
(012)
(104)
(110)
(006)/(113)
(202)
(024)
(116)
(122)/(018)
(214)/(300)
(208)
(119)/(220)
(036)
(312)/(128)
(02 10)/(134)
(226)/(042)
(21 10)/(404)/(11 12)
(232)/(318)
(324)/(410)
(13 10)
(327)
(146)
(238)
LiNbO3
R3c (161)
Intensity (a.u.)
2θ (°)
(012)
(104)
(110)
(006)/(113)
(202)
(024)
(116)
(122)/(018)
(214)/(300)
(208)
(10 10)/(220)
(306)
(312)/(128)
(02 10)/(134)
(226)/(042)
(21 10)/(404)/(11 12)
(232)/(318)
(324)/(410)
(13 10)
(03 12)
(146)
(238)

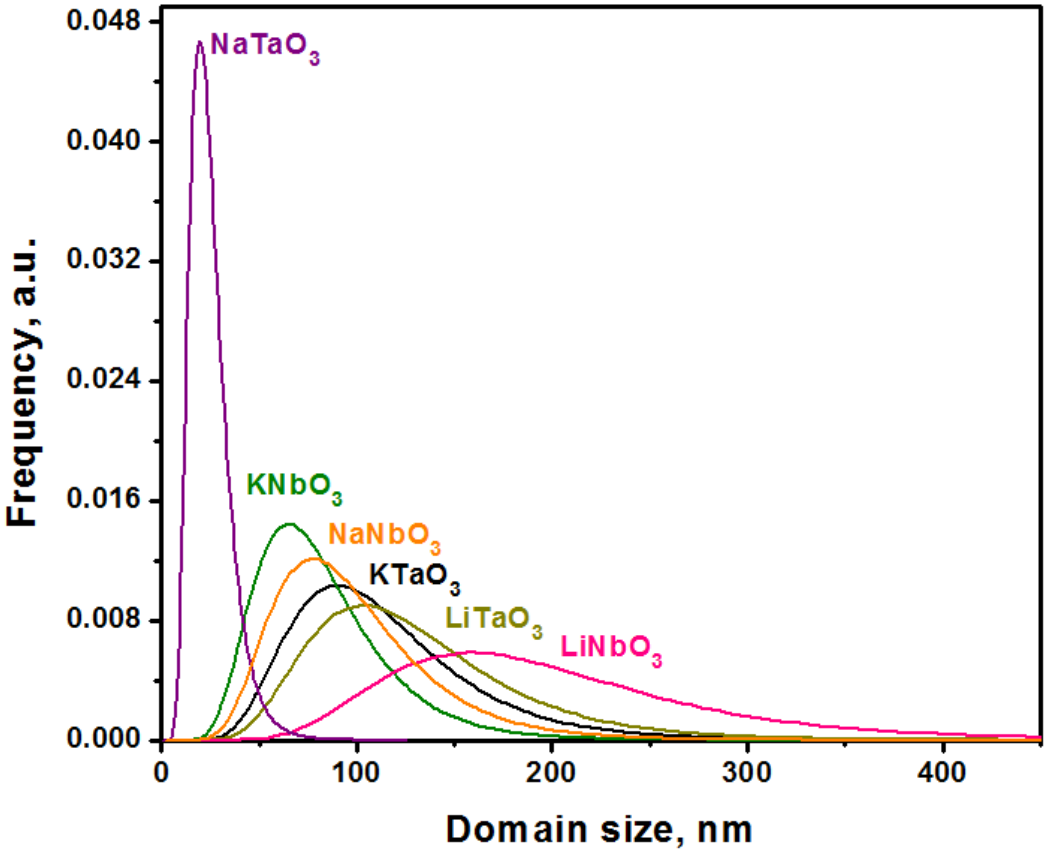

(b)

Figure 4-81. (a) The graphical output of the WPPM modelling of the XRD patterns. Black open squares are observed data, red continuous line the calculated data, and the lower blue continuous line is the difference curve between observed and calculated profiles. Additionally, Miller indices are included, belonging to the modelled space group. (b) Crystalline size distribution of the as-synthesized alkali tantalate and niobate samples, as obtained from the WPPM modelling.

Table 4-21. WPPM agreement factors, unit cell parameters, average crystalline domain diameter, and mode of the size distribution of the modelled XRD patterns of as-prepared alkali tantalate and niobate samples. SG: space group.

		Agreement factors			Unit cell parameters	Average crystallite diameter	Mode of the size distribution	Energy band gap
		R_{wp} (%)	R_{exp} (%)	χ^2	*a, b, c* (nm)	<*D*> (nm)	*M* (nm)	E_g (eV)
$KTaO_3$ ssr	Cubic SG: *Pm$\bar{3}$m*	4.87	1.23	3.96	0.3988799	114.0 ± 2.8	90.0 ± 2.2	3.65 ± 0.03 (3.4 - 3.8 eV [49, 194, 431, 432])
$KNbO_3$	Orthorhombic SG: *Bmm2*	2.57	0.81	3.17	0.5692902 0.3976589 0.5714716	82.1 ± 3.0	65.0 ± 2.3	3.27 ± 0.06 (3.1 - 3.3 eV [194, 438])
$LiTaO_3$	Trigonal SG: *R3c*	5.20	1.15	4.53	0.5152190 1.377177	130.7 ± 3.7	103.1 ± 2.9	4.84 ± 0.05 (3.9 - 4.7 eV [189, 439, 440])
$LiNbO_3$	Trigonal SG: *R3c*	2.35	0.75	3.12	0.5148214 1.385254	201.0 ± 13.7	158.3 ± 10.8	4.14 ± 0.10 (3.6 - 3.9 eV [439, 441])
$NaTaO_3$	Orthorhombic SG: *Pnma*	4.01	1.08	3.72	0.5503757 0.7813874 0.5519692	25.0 ± 1.1	19.7 ± 0.9	4.07 ± 0.03 (4.0 - 4.1 eV [159, 189, 194])
$NaNbO_3$	Orthorhombic SG: *Pbcm*	3.41	0.77	4.45	0.5526010 0.5581274 1.554486	97.8 ± 2.8	77.5 ± 2.2	3.49 ± 0.03 (3.1 - 3.5 eV [194, 442])

The diffuse reflectance spectra of the as-synthesized powders are depicted in Figure 4-82 *(a)*. As expected, all compounds showed no absorption in the visible region. Their spectra, consisting of a single absorption band below approximately 400 nm, are characteristic of this group of oxides. The energy band gaps, E_g, of the powders were calculated by the differential reflectance method (Table 4-21 and Figure 4-82 *(b)*). The resulting curves were successfully fitted with a Gaussian function, and the maximum values were found from the fitting. The subsequent band gap energies are 4.84, 4.14, 4.07, 3.49, 3.27 and 3.65 eV for $LiTaO_3$, $LiNbO_3$, $NaTaO_3$, $NaNbO_3$, $KNbO_3$ and $KTaO_3$, respectively; these band gap values are comparable to the ones of the literature.

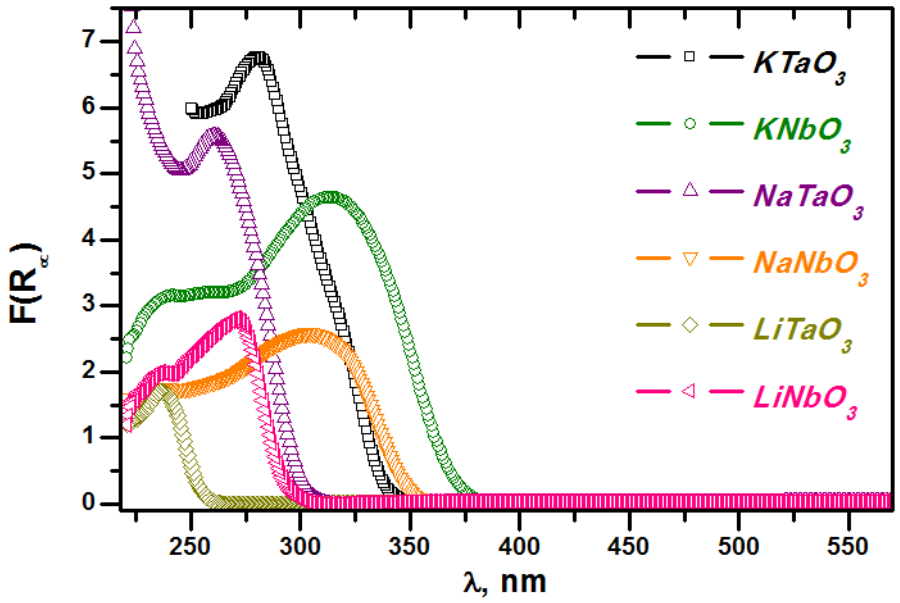

(a)

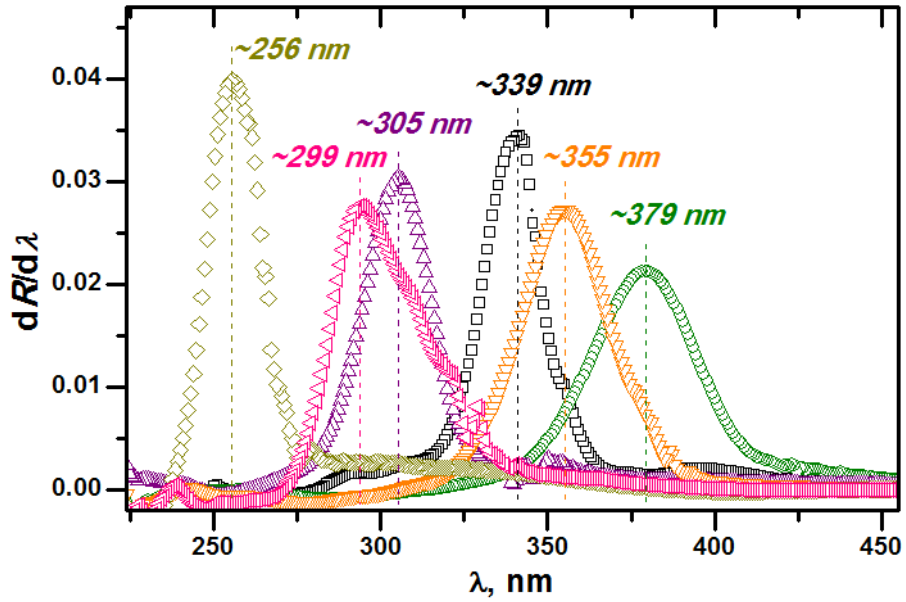

(b)

Figure 4-82. (a) Diffuse reflectance spectra and (b) first derivative of diffuse reflectance spectra versus wavelength (the vertical dashed lines represent the band gaps of compounds) of perovskite-like alkali tantalates and niobates.

Photocatalytic activities of the as-prepared alkali tantalate and niobate samples, C/C_0 versus reaction time, are listed in Figure 4-83 *(a)*; the photo-degradation results of commercial Aeroxide® TiO_2 P25 photocatalytic powder are also included for comparison (using the same protocol as in the present work) [433]. The negative time indicates the time during which the adsorption of the dye occurs (light is off), and the MB photolysis was considered to be negligible, being $\xi \leq 3$ % under UVA exposure (after 7 h). Alkali tantalates and niobates exhibit a photocatalytic activity with the following order: $KNbO_3$ (ξ = 56.3 %) > $NaTaO_3$ (ξ = 24.1 %) > $NaNbO_3$ (ξ = 18.5 %) > $KTaO_3$ (ξ = 5.8 %) > $LiNbO_3$ (ξ = 5.5 %) > $LiTaO_3$ (ξ = 5.4 %); a full degradation (ξ = 100 %) of the dye using P25 is achieved in ~4 h of irradiation time. $KNbO_3$ was the best photocatalyst amongst all tested tantalates and niobates, degrading the dye minimum twice better than the next one, $NaTaO_3$, and 10 times more efficiently than $LiTaO_3$ and $LiNbO_3$. A reaction kinetics study was conducted, in order to quantitatively evaluate the reaction of MB photo-degradation with assistance of various alkali tantalates and niobates using a pseudo-first-order model. The apparent rate constant, k_{app}, calculated from the slope of the linear plots of $\ln(C_0/C)$ versus irradiation time, for assessed powders is depicted in Figure 4-83 *(b)*. The MB decomposition rate also follows

the order of $KNbO_3$ [k_{app} = 0.181 (min^{-1}×100)] > $NaTaO_3$ [k_{app} = 0.064 (min^{-1}×100)] > $NaNbO_3$ [k_{app} = 0.050 (min^{-1}×100)] > $KTaO_3$ [k_{app} = 0.014 (min^{-1}×100)] > $LiNbO_3$ [k_{app} = 0.014 (min^{-1}×100)] > $LiTaO_3$ [k_{app} = 0.012 (min^{-1}×100)].

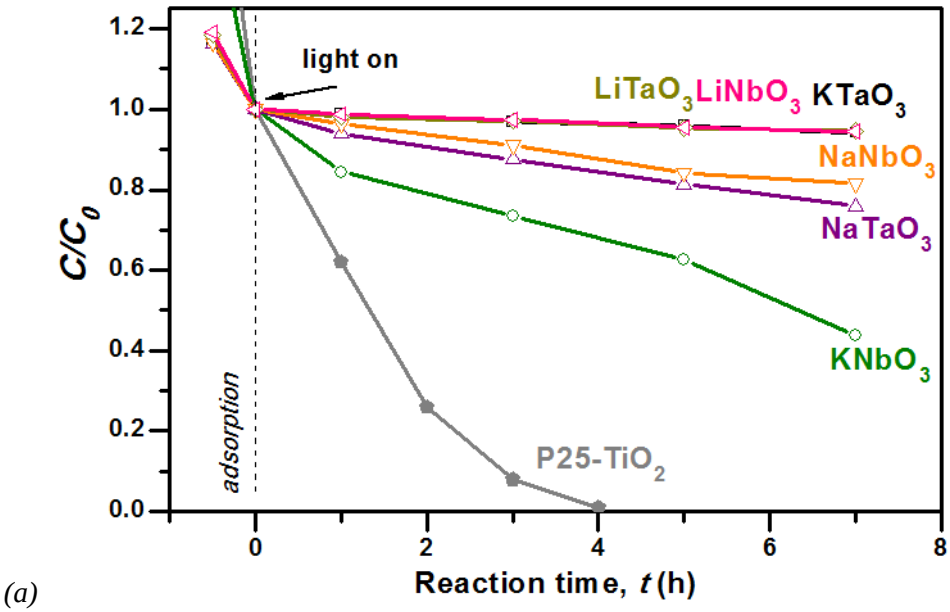

(a)

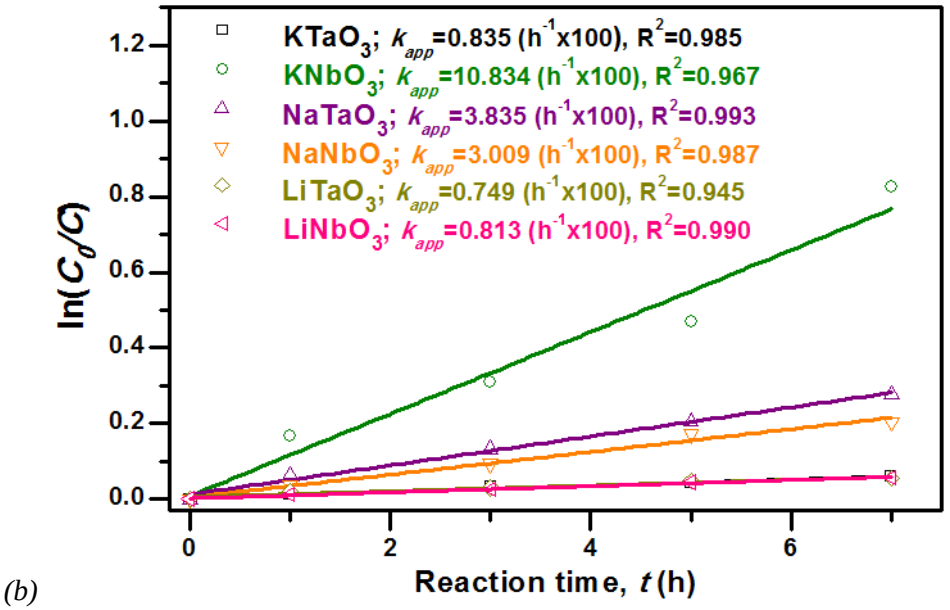

(b)

Figure 4-83. (a) Photocatalytic degradation of MB, C/C_0, and (b) first-order apparent constant, k_{app}, of the photocatalytic reaction of the assessed perovskites. The photo-degradation of MB using reference, commercial Aeroxide® TiO_2 P25 powder, is included for comparative observation.

In principle, the photocatalytic activity of a metal oxide semiconductor depends on a number of parameters, as surface area, particle size, crystallinity, particle shape anisotropy, local structure, light absorption and diffusion rates of charge carriers [67, 443]. The conduction bands of alkali tantalates, $KTaO_3$, $NaTaO_3$ and $LiTaO_3$, consist of Ta *5d* while alkali niobates, $KNbO_3$, $NaNbO_3$ and $LiNbO_3$, of Nb *4d*. The band gap of $KNbO_3$ is the narrowest among the analysed samples, following the order of $LiTaO_3$ > $LiNbO_3$ > $NaTaO_3$ > $KTaO_3$ > $NaNbO_3$ > $KNbO_3$ (the values are listed in Table 4-21), and the absorption edge of KNO (~370 nm) is the closest, among the analysed compounds, to the maximum wavelength of the used lamp. Because the valence bands of the semiconductor oxides consisting of d_0 transition metal ions are usually formed with O *2p* orbitals, the difference in the band gaps is mainly attributed to the potential difference in the conduction bands, and not affected by the flat band potential [194]. Thus, this parameter can be the most decisive, having the biggest influence on the photocatalytic activity of $KNbO_3$.

It is known that a slight modification of the structure may have a dramatic effect on the concentration and mobility of charge, which directly affect photocatalytic and photophysical properties of semiconductors [194].

The real perovskite ABO_3 lattice is distorted, having a crucial impact on the dipole and electronic band structures that results in the behaviours of photogenerated charge carriers [183, 442]. It was reported that the Ta–O–Ta bond angles is one of the key factors influencing photocatalytic activity in alkali tantalates [183, 191, 442]. For instance, in ilmenite-like $LiTaO_3$ the excited energy is localized due to the bond angle of Ta–O–Ta being much lower than 180°, while in $KTaO_3$ and $NaTaO_3$ the excited energy is delocalized (bond angle close to 180°) [183]. Therefore, the photogenerated charge carriers may be easier transferred in KTO and NTO. The effect of the crystal structure on the photocatalytic activity in NTO was investigated in details [157, 158]. It was found that monoclinic NTO has Ta–O–Ta bond angle close to 180°, thus favourable for delocalization of the excited energy. Besides, monoclinic NTO has an indirect band gap (a type of the optical transition is required for absorption or emission of a phonon), leading to the low recombination rate for the photogenerated charge carriers. In contrast, orthorhombic NTO has a direct band gap and the bond angle of Ta–O–Ta ~163°, thus a lower number of effective states is available for the photogenerated charge carrier. These aspects are the reason why monoclinic NTO has a higher photocatalytic activity than orthorhombic NTO.

The effect of catalyst dose is an important parameter for the removal efficiency of the dye (being 0.25 $g \cdot L^{-1}$ in the present studies). The catalyst concentration (amount of the powders in the aqueous dye solution) has a big impact on the availability of active sites on the surface and the penetration of light into the suspension. The higher is the number of active sites on the photocatalyst surface, the higher the amount of hydroxyl and superoxide radicals having influence on the degradation of the dye [416]. Therefore, a comparison with the reported photocatalytic performance is rather difficult. Additionally, references on photocatalytic activity of organic pollutant of alkali tantalates and niobates are not that many. Torres-Martínez *et al.* [415] reported a photocatalytic degradation of MB (30 $mg \cdot L^{-1}$) using a set of sol-gel prepared alkali tantalate (0.4 $g \cdot L^{-1}$), and well crystallized samples (at 800 °C) demonstrated a photocatalytic efficiency <20 % (at 3 h of irradiation time, UV light, λ = 254 nm). The rate constant, k_{app}, was calculated to be 0.00030, 0.00074 and 0.00035 min^{-1} for $KTaO_3$, $NaTaO_3$ and $LiTaO_3$, respectively. Though the catalyst concentration was ~2 times higher than in our study, the reaction rates were comparable. It was also demonstrated by the same group that in doped NTO with high surface area, >5 m^2/g, that even higher catalyst concentration (0.75 $g \cdot L^{-1}$) leads to a full MB degradation after 7 h UV irradiation with reaction rate ~0.007 min^{-1} [409].

The morphological aspects, surface area, particle/crystallite size, are important factors affecting the photocatalytic activity by providing more reaction sites [444-446]. The stability of the surface affects the efficiency of the photocatalytic reactions. Usually a higher surface energy yields a higher catalytic activity [447], due to the fact that thermodynamic properties of nanomaterials differ from those of bulk by a surface energy term; its contribution increases as the surface area grows with decreasing particle size, then the surface-to-volume ratio is considerably higher and the surface term accounts for a much larger fraction of the total free energy.

There have been many theoretical calculations of the energies of various oriented surfaces and interfaces of oxides, but their experimental determinations are rarely reported. However, solution calorimetry has been developed to successfully determine the surface energies, in particular oxide nanomaterials [297]. Within this context, the surface energies of the alkali tantalate and niobate perovskites were recently measured by us. The calculated surface energies are shown in Table 4-4, referring to “real” surfaces; the resulting surface energy is that of hydrated surface, being an average of the different crystal faces and of surface defects,

i.e. step edges, kinks, screw dislocation centers. Figure 4-84 presents the relationship between photocatalytic activity (reaction rate constant), surface energy and electronic structure (band gap energy) of the alkali tantalate and niobate perovskites; UVA lamp emission spectra is presented as well (white peak).

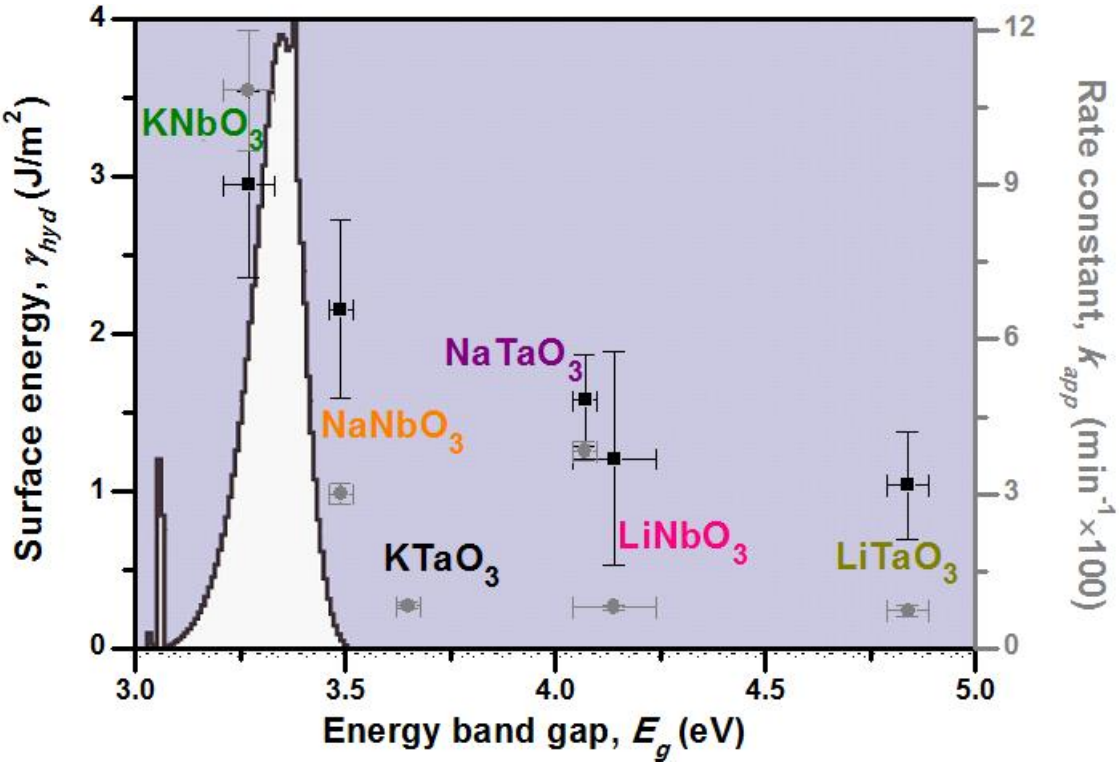

Figure 4-84. Surface energy, γ_{hyd}, and reaction rate constant, k_{app}, of the alkali tantalate and niobate perovskite versus energy band gap, E_g. The emission spectrum of the UVA-light source lamp is enclosed as background of the graph.

It can be seen that ferroelectric $KNbO_3$ gives the highest surface energy while the other compounds, $LiTaO_3$, $LiNbO_3$ and $NaTaO_3$, have the lowest values, $\gamma_{hyd} < 2$ J/m^2 and lower affinity to water. Within this group, $KNbO_3$ is the most hygroscopic material (more hydrophilic than the other particles). Thus, sensitivity to ambient conditions, *i.e.* humidity, needs to be strongly considered in order to control moisture content in these compounds. Additionally, $KNbO_3$ possesses the band gap energy matching well the UVA radiation spectrum. The spontaneous polarization in this ferroelectric may also have beneficial impact on a transport of photogenerated charge carriers and photochemical reactivity, as it was pointed by Li *et al.* [448].

Summary

A photocatalytic degradation study is presented for two groups of compounds: i) K-Ta complex oxides with different structures and stoichiometry, and ii) highly crystalline alkali tantalate and niobate perovskites. Within the same experimental conditions, $KNbO_3$ possesses the highest photocatalytic performance because of the good matching between the band gap energy, surface energy and UVA radiation range of the lamp. Thus, presumably the higher mobility of charge carriers promotes the photo-induced carriers transport in the photocatalysts inducing pollutant degradation. The perovskite oxides with internal electric field due to ferroelectric phenomena (such as $KNbO_3$) have been proposed as an effective photocatalysts, however, the present study demonstrate that there is still room for improvements, in particular related to the size and morphology of alkali tantalate and niobate particles. These results provide some useful information to design efficient photocatalytic materials, ideally to develop new visible light-responsive photocatalysts. There is a need to develop photocatalysts capable of utilizing more abundant visible light spectrum (~43 % of the solar energy range), since it is known that ultraviolet light only occupies around 4 % of the solar energy spectrum [397, 404].

4.5. Bioactive $LiTaO_3$ coatings on metallic substrate

Abstract

In the context of bone tissue engineering, it is crucial to have a platform with appropriate stimulus that can support the attachment and direct the growth, proliferation and differentiation of the cells. In the orthopedic field, metals and alloys are still the dominant materials used as implants, however their bioinert character leads to failure or to the need of multiple revision procedures. In lieu of this here we exploit an alternative strategy for bone implants or repairs, based on charged mediating signals for bone growth. This strategy includes coating metallic 316L-type stainless steel (316L-SST) substrates with charged, functionalized via electrical charging or UV-light irradiation, ferroelectric $LiTaO_3$ (LTO) layers. We show that the formation of calcium phosphates and protein adsorption is considerably enhanced for 316L-SST functionalized-ferroelectric-coatings. Our findings go beyond the current knowledge and demonstrate that the protein conformation is sensitive to the type of charge-functionalization of the ferroelectric coatings. Our approach can be viewed as a set of guidelines for the development of platforms electrically functionalized that can stimulate tissue growth promoting direct integration of the implant with the host tissue by bone ingrowth and, hence contributing ultimately to reduce implant failure.

The design of new biomaterials for hard tissue repair is highly required, and bone tissue engineering has been viewed as an important field in regenerative medicine. Bone is a quite diverse tissue with extraordinary properties, structure and functions, providing protection and locomotion to the host organs [197], and its replacement or regeneration is crucial in clinical treatments. The osseous tissue is known to have an ability of self-healing and remodeling, however large-scale bone defects cannot be completely healed, leading to the need of an external intervention, commonly called bone replacement [449]. The

development of implant artificial materials is generally based on mimicking the structure and function of the biological systems, in this case the bone. Main efforts have been dedicated to the development of scaffolds, namely 3D porous structures providing support for cells and new tissue formation, however dense bioceramics are considered as good alternative platforms due to their relatively good mechanical properties. A wide range of synthetic materials have been proposed as bone substitutes [450]: metals, polymers and ceramics. Among ceramic materials calcium phosphate based ones are some of the most attractive owing to their similarities to bone composition. Even though due to their superior mechanical strength and chemical/biological inertness metals and their alloys are important structural biomaterials in orthopedics [5]. Among approved metals and alloys and routinely used in clinical practice, one of the most common is austenitic stainless steel being applied as temporary devices (fracture plates, screws, hip nails) and total hip replacements [5]. Type 316L stainless steel and its variants are quite popular in implant technology because of their availability, low cost, very good fabrication properties, relatively good biocompatibility and toughness, as well as controlled mechanical properties. However their poor bioactivity leads to problematic successful osseointegration.

Indeed, currently implant strategies face numerous difficulties and some adverse effects arising from poor biological interaction at the implant interface what results in failures, as aseptic loosening and implant infection [199]. Success in the application of an orthopedic implant depends on a number of factors. For instance, infections of orthopedic fracture and reconstructive devices occur in up to ~10 % of cases, mainly due to mechanical aseptic loosening of the implant [451, 452]. Although most of these materials are biocompatible and/or biodegradable, there is a lack of stimulatory cues for guided bone tissue regeneration. However if the implant itself is able to deliver particular chemical and physical functions stimulating faster tissue regeneration and avoiding scarring some of these limiting issues will be overcome.

Previously, orthopedic implants were designed simply as mechanical devices, but recently this reality is changing and the approach towards the formation of a functional bioactive implant surface by coating with a functional material is gaining interest as an effective strategy to improve acceptance from the human body [452]. Besides exploring the numerous possibilities of local delivery of biologics to modulate local tissue reactions, it is

of interest if the implant coating itself would facilitate earlier and more robust osseointegration [452].

Electrically active compounds may be a choice since it has been reported that *in vivo* endogenous electric potentials can control cell functions such as growth, migration [453, 454] and mitosis rate, among others [455]. In addition *ex vivo* experiments have proven that under electrical stimulation synchronous contractions of cultured cardiac constructs are induced [456], cell proliferation and expression of bone morphogenetic proteins in osteoblastic cell lines increased [457], and directed cell migration in epithelial tissues during wound healing [458] took place. Moreover clinical electrical stimulation of living tissues demonstrated that growth, maintenance or regeneration of bones, tendons and ligaments were boosted. It is well established that electrical potentials are also generated in bone under mechanical loading due to the piezoelectric nature of collagen and by the movement of ionic fluids within the structure [209]. This phenomena also assists bone remodeling [14, 209, 459]. Hence electrically active materials may be potentially attractive for implants in hard tissue [209].

Among them piezoelectrics may have a prominent role. The uniqueness of piezoelectrics in creating electrical potentials under stress (and vice versa) is an advantage over other non-piezoelectric ceramics, since there will be no need for an external electric field source. It was proven that on negatively charged surfaces of electrically poled barium titanate ($BaTiO_3$), there is a preferential formation of calcium phosphate and cell growth and proliferation may be tailored by the pulsed electrical stimulus [12, 209]. Although not yet totally comprehensible how electrical activity influences biological responses, it is evident that polarized surfaces attract proteins and ions. Further research on the use of electrically active ceramics is indeed needed to unleash the full potential of these electroactive materials as functional implants [209].

Perovskite oxides are the dominant piezoelectrics because of their superior electromechanical and ferroelectric properties. Within this family there is a particular group of the so-called lead-free piezoelectrics that might be relevant for bone remodeling; among them alkali niobates and tantalates, *e.g.* potassium sodium niobate [$(K_{0.5}Na_{0.5})NbO_3$, KNN], lithium niobate ($LiNbO_3$) and lithium tantalate ($LiTaO_3$), have already been proposed as biomaterials with potential and their biological responses examined [11, 14, 15, 219-221].

Protein and cell behavior investigations carried out in periodically poled LTO single crystals, have evidenced an absence of morphological differences of fibroblast cells, independent on domain orientation, but with tendency to avoid the ferroelectric domain boundaries [11]. *In vitro* studies of the influence of the surface charge of LNO on the osteoblast cells proliferation revealed enhanced proliferation rates and osteoblast function through mineral formation on positively and negatively charge surfaces [14]. Accordingly, this group of materials has been presented as potential platforms for cell attachment and subsequently as tissue growth templates, as relevant for further integration with the host bone tissue and subsequently in the clinical trials. In addition, our recent studies on LNO and LTO powders classify them as bioactive ferroelectrics [13].

On this background here we propose an alternative strategy, the exploitation of piezoelectric lithium tantalate ($LiTaO_3$, LTO) as a coating of 316L stainless steel supports to stimulate biological responses; *i.e.* the combination of a functional piezoelectric layer with a metallic implant in which the piezoelectric might be a potential approach for successful osseointegration. *In vitro* bioactivity studies of LTO coated 316L-SST are conducted and the feasibility of apatite formation on the surface of LTO coatings is assessed. The effect of the functionalization of LTO coatings (electric charging and photofunctionalization) is tested via a protein adsorption process.

The study is focused on the design and development of implant devices composed of metal (316L-SST) and piezoelectric coating (ferroelectric $LiTaO_3$) to improve osseointegration and corrosion resistance of metallic component by applying non-toxic, biocompatible and piezoelectric layer on the top of it. The proposed concept is schematically presented in Figure 4-85. To induce the functionality of the polycrystalline LTO coating (mostly its surface), two physical treatments of the film surface have been utilized: i) electric charging, and ii) photofunctionalization. The details of the treatments are presented in the following paragraphs.

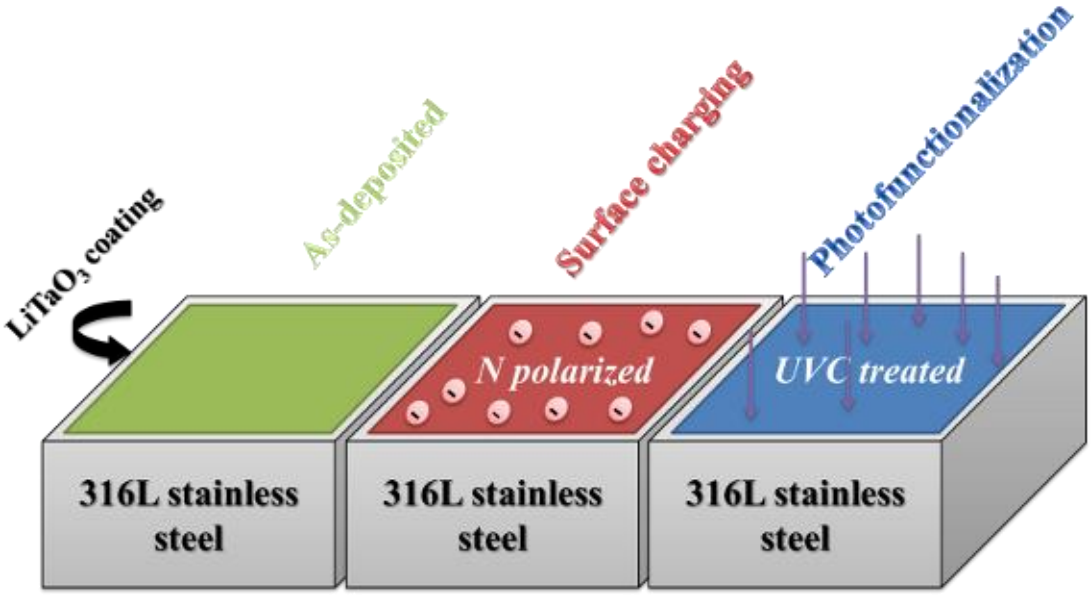

Figure 4-85. Schematic representation of piezoelectric $LiTaO_3$ (LTO) coatings onto metallic substrates (316L-SST). Three distinct heterostructures are analysed: i) as-deposited LTO (not treated), LTO/316L-SST, ii) polarized LTO, N-LTO/316L-SST, and iii) UV-irradiated (photofunctionalized) LTO coatings, UV-LTO/316L-SST. Piezoelectric coatings are stimulated by external forces (electric field or light) to promote osseointegration.

These two functionalization processes are widely employed in many scientific and industrial practices due to their relatively short treatment times, atmospheric pressure operations, and requirement of simple setups without vacuum facilities. Additionally, sterilization of biomedical devices usually requires reactive surface functionalization.

4.5.1. Functionalization methods

i) Electric charging via corona discharge system

For the functionalization with an electric filed, corona poling was the chosen method. It is a non-contact poling method in which the air becomes conductive by applying a high electrical field. The procedure was conducted in the vicinity of an electrode with small radius of curvature (corona tip) being located at a certain distance from the counter electrode (a grounded conductive plate) that acts as support (being in contact) for the piezoelectric LTO coatings on 316L-SST. The distance between the tip and the LTO coating was set at

~15 mm. The charge flowing from the sharp corona tip accumulates on the dielectric layer due to an ionization effect, and a static electric field over the coating orients the dipoles (within the ferroelectric domains) along the electric field direction [460]. The corona setup is described in detail elsewhere [461]. A negative high dc voltage of ~10 kV was applied for 30 min at ~80 °C and kept constant while cooling down to room temperature (for another 30 min). Indeed negatively charged surface of piezoelectric oxides generally increases the bioactivity in terms of the calcium phosphate formation, comparing to positively charged or uncharged [12].

ii) Photofunctionalization via UV-irradiation

Light illumination reactions in semiconductors are well established in heterogeneous photocatalysis: photogenerated charge carriers, electrons from the valence band of the semiconductors, are activated to the conduction band generating electron-hole pairs that migrate to the surface acting as oxidizers through redox processes [4]. In this process the main requirement to generate electron-hole pairs is that the energy of the incident light is larger than the band gap energy of the semiconductors. Thus, in the case of $LiTaO_3$ with a band gap of ~4.7 eV the wavelength of the UV-light should be lower than ~265 nm (UVC range). A lamp emitting light in the UVC range (Philips TUV PL-S 9W/2P UVC radiation 2.3 W), located at a distance of ~50 mm to the LTO coatings on 316L-SST and for the period of ~15 h was used.

4.5.2. Biological assays

For assessing the *in vitro* bioactivity of functionalized LTO/316L-SST platforms, an acellular simulated body fluid (SBF) was prepared, with ions concentration nearly equal to those of the human blood plasma. The SBF composition and preparation was according to the procedure described by Kokubo *et al.* [462]. A ~1 cm^2 $LiTaO_3$ films were dispersed in 10 ml of SBF solution previously filtered through a Millipore 0.22 micron. The samples were soaked in the SBF solution for 1, 3, 7, 14 and 21 days, labelled as 1D, 3D, 7D, 14D and 21D, respectively, and stored at ~37 °C. 0D designation corresponds in all cases to coatings prior to SBF immersion. After removing from the incubator, the samples were gently washed with distilled water, dried at 60 °C for 1 h and then kept in desiccator at least

one day before examination. The remnant liquid was kept in a refrigerator at ~5 °C for further tests.

The effects of surface functionalization on the adsorption of protein, in this case bovine serum albumin (Serva Electrophoresis GmbH, lyophilized powder, fraction V, pH 7.0, assay ≥98 %; BSA) were investigated. The choice of BSA is related to the fact that it is the most abundant plasma protein in the circulatory system with negative surface charge at pH 7.0 [463]. Protein solutions with 1 mg/ml concentration were prepared in Milli-Q water, by constant magnetic stirring for 3 h. Then, 3 ml of BSA solution was added to each well of a sterilized tissue culture plate with the samples (LTO/316L-SST, N-LTO/316L-SST and UV-LTO/316L-SST) placed in; three replicas of each sample were used. The assays were conducted at ~37 °C for 1 h. Then, the samples were washed prior to further analysis.

The BSA protein concentration was determined according to the Beer-Lambert Law calculation adapted for proteins of known absorption coefficient [464]:

$$[BSA] = \frac{A_{278} - A_{320}}{l \times \varepsilon_P} \tag{28}$$

where [BSA] is BSA concentration, *A* represents absorption at 278 nm and 320 nm, *l* is the optical path length (normally the absorption cell (cuvette) dimension), that is set at 1 cm in a standard spectrometer and ε_p is absorbance coefficient of the BSA solution of 0.667 ml/mg·cm^{-1} (valid at a concentration range of 0.3–1.8 ml/ml). The absorbance at 320 nm is related to aggregation and is normally low relative to the absorbance at 278 nm. UV-vis spectra of the BSA solutions were recorded with a Shimadzu UV 3100, JP, spectrometer; spectra were acquired with 0.2 nm in step-size.

Therefore, the LTO coatings subjected to protein adsorption assays were characterized by FTIR-ATR analysis in order to study the extent of conformational changes in the protein. The recorded FTIR spectra were corrected for water content, and smoothed by 10–12 points of adjacent averaging method using OriginPro software. Quantitative analysis of the amide I band contour in the wavenumber range of 1710–1590 cm^{-1} was conducted using curve fitting; a linear baseline was selected in the fitting procedure. Second derivative spectral analysis was applied to locate the position of the components of the amide I band, and component peaks were fitted with Gaussian band profile. The peaks obtained by

deconvolution of the amide I band were then assigned to specific types of secondary structures.

4.5.3. Characterization of $LiTaO_3$ deposited on 316L stainless steel

Firstly, as-deposited LTO coatings were analyzed in terms of phase purity, microstructure and chemical composition. XRD patterns of LTO coated 316L-SST are shown in Figure 4-86 *(a)*. LTO coatings are monophasic and correspond to the rhombohedral *R3c* $LiTaO_3$ phase (JCPDS-PDF card #29-0836). The microstructure of these LTO coatings is pictured in Figure 4-86 *(b)-(d)*. Cross-section SEM micrographs show a very uniform coverage of the substrate with an estimated thickness of around 550 nm. The LTO coatings are dense, with a good adhesion to the substrate and with no visible interfacial debonding or surface microcracks. The grain size of LTO is ~150 nm, although it is barely detectable in the presented micrographs. Clearly the coating microstructure reflects the shape of the outer surface of the underlying substrate microstructure; the microstructure of the bare metallic substrate was also examined (not shown here) and is characterized by an average grain size lower than 30 μm. Chemical analysis conducted by EDS and enclosed as inset in Figure 4-86 *(d)* confirms the presence of Ta from LTO (Li cannot be detected; X-rays are of too low energy) and Fe, Cr and Ni from 316L-SST. The surface topography of the LTO coatings was also assessed by AFM (Figure 4-86 *(b)*) and optical profilometry (Figure 4-87). The AFM surface micrographs are consistent with the SEM ones (Figure 4-86 *(d)*). The surface topography evolution of LTO coatings is illustrated in the height histogram reflecting the statistical distribution of *z*-values (inset in Figure 4-86 *(b)*). The roughness of the coatings deposited on 316L-SST is R_{RMS} ~ 62 nm (root mean square of the roughness) is reduced by ~40 % comparing to bare 316L-SST due to the multiple layering of LTO.

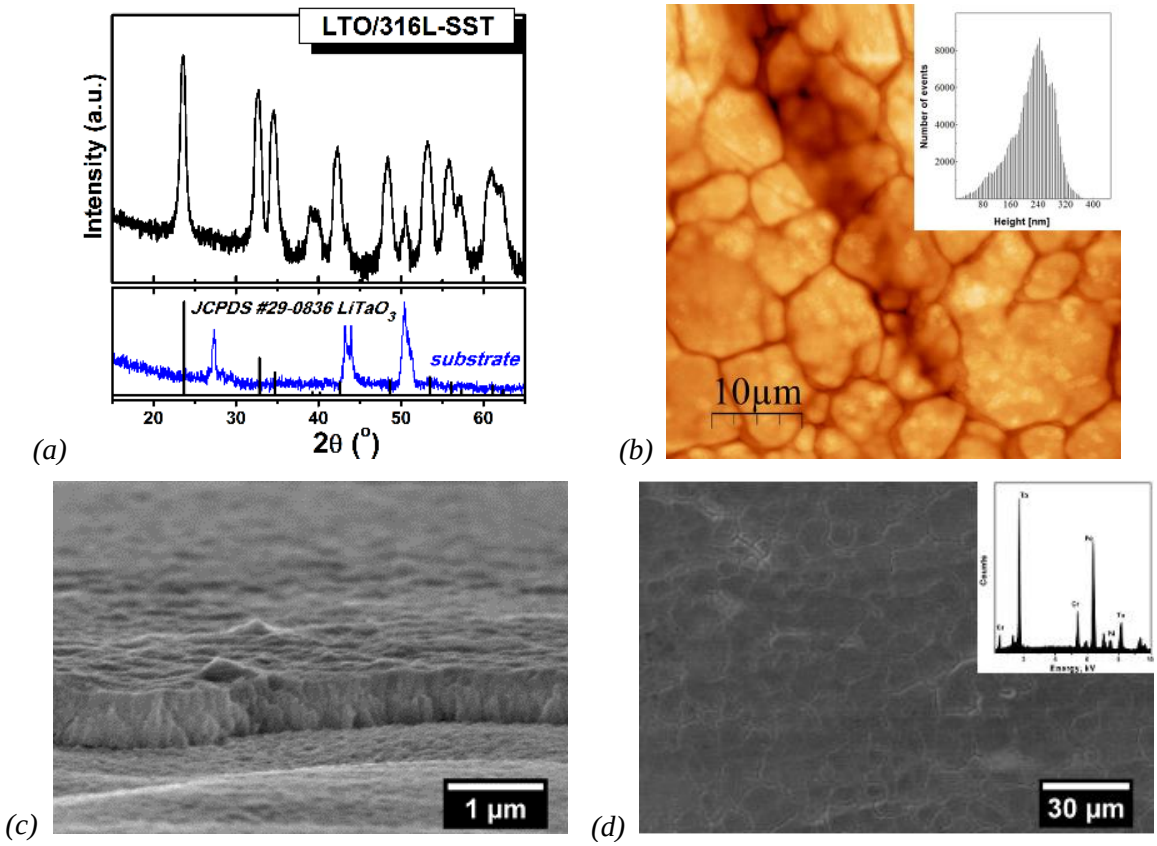

Figure 4-86. Structural, microstructural and chemical characteristics of as-deposited LTO films on 316L stainless steel: (a) XRD pattern presenting monophasic $LiTaO_3$ structure (JCPDS-PDF #29-0836), (b) AFM micrograph with inset of histogram of the height (roughness R_{RMS} ~ 62 nm), (c) cross-sectional SEM micrograph, LTO films have average thickness ~550 nm, and (d) plan view SEM micrograph with the chemical analysis by EDS. Monophasic, well-developed and chemically homogeneous piezoelectric LTO layers are coated on 316L-SST metallic substrates.

4.5.4. Effect of $LiTaO_3$ functionalization

After the surface functionalization by corona poling and UV irradiation the surface changes of LTO coatings were monitored by optical profilometry and static contact angle measurements (Figure 4-87). The surface roughness of LTO coatings only slightly changes (<15%) after functionalization, increasing in the order LTO/316L-SST (R_{RMS} = 62.57 ± 8.33 nm) < N-LTO/316L-SST (R_{RMS} = 65.69 ± 13.69 nm) < UV-LTO/316L-SST (R_{RMS} = 72.08 ± 8.87 nm). To note that the values change is within the standard deviation

range, supporting the statement that the surface topography is not drastically modified by the functionalization treatments.

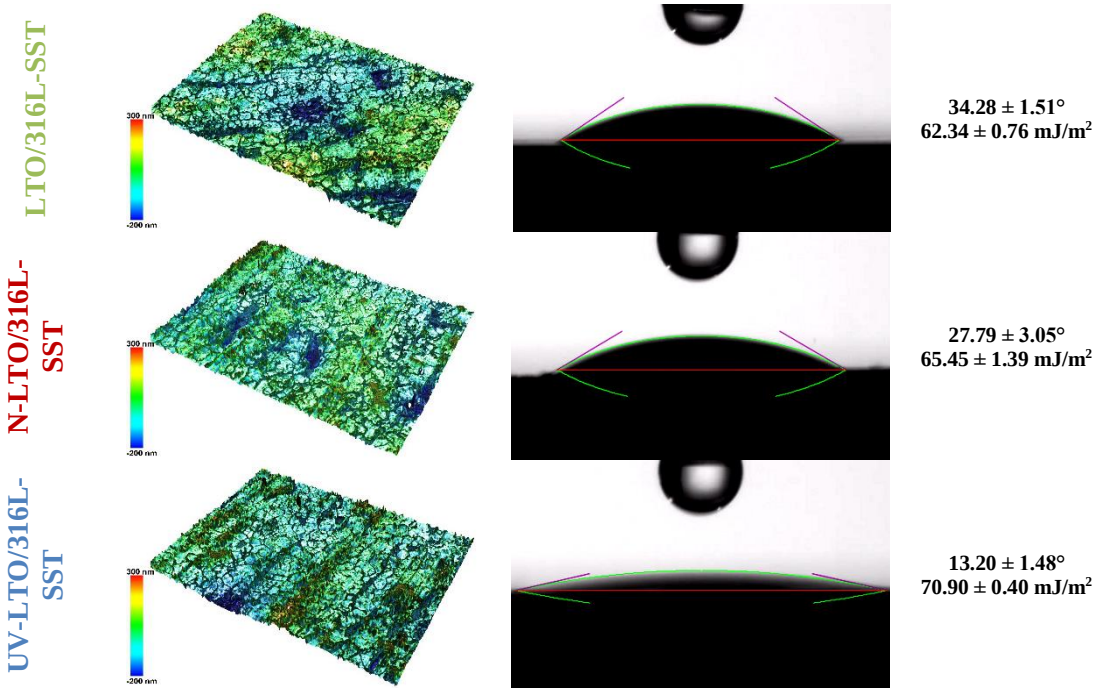

Figure 4-87. Results of surface topography analysis from optical profilometry are presented in the form of 3D images. R_{RMS} values are also included. Surface roughness marginally increases after functionalization, however the values are within experimental errors. Static contact angle, θ, measurements of sessile 2 µL water droplets on LTO coatings are shown. The contact angle values decrease for LTO surface treated coatings, indicating a more hydrophilic surface than the as-prepared one. Surface energy, γ^{SV}, calculations were carried out from the contact angle data proving that the functionalized films (N-LTO/316L-SST and UV-LTO/316L-SST) create on their surfaces new functional groups comparing to LTO/316L-SST.

The optical micrographs of the contact angle measurements present the shapes of sessile drops and the measured contact angle (θ), respectively on LTO/316L-SST with $\theta = 34.28 \pm 1.51°$, on N-LTO/316L-SST with $\theta = 27.79 \pm 3.05°$, and on UV-LTO/316L-SST with $\theta = 13.20 \pm 1.48°$. The contact angle is lower for the functionalized samples and decreases in the following order: LTO/316L-SST > N-LTO/316L-SST > UV-LTO/316L-SST. UV irradiation noticeably reduces the contact angle of water droplets on LTO coatings by ~60 % while electrical charging reduces only by ~20 %, when comparing to non-functionalized surfaces. The hydrophilicity of the surface of LTO coatings increased and it

is then expected that the wettability of these functionalized coatings increases as well. The surface tension, γ^{SV}, of LTO coatings was calculated utilizing the contact angle data and using the equation of state approach, and for LTO/316L-SST is 62.34 ± 0.76 mJ/m^2, and increases to 65.45 ± 1.39 mJ/m^2 for N-LTO/316L-SST and to 70.90 ± 0.40 mJ/m^2 for UV-LTO/316L-SST. These results are an indirect evidence of the presence of functional groups (either different types or different concentration) on functionalized LTO surfaces, and as a consequence surface tension (surface energy) increases improving the bonding abilities. Higher surface energy is associated with an improvement in the wettability of a surface, as well. In addition it has been reported that high surface energy favors cells attachment and proliferation [465].

For a deeper examination of the functionalized LTO surfaces XPS analysis was carried out. Figure 4-88 *(a)* shows the wide scan of the as-deposited and functionalized LTO coatings on 316L-SST. The presence of lithium, tantalum, oxygen and carbon is evident in the general spectra. The Ta 4f signal is composed of two peaks, Ta $4f_{7/2}$ and Ta $4f_{5/2}$ spin orbital splitting at ~26 eV and ~28 eV, respectively. The energy position of these peaks is characteristic of the binding energy of Ta^{5+}, thus it is a proof of the presence of tantalum pentoxide, Ta_2O_5 [466]. The Ta 4f spectrum shows also a tail with negligible intensity at ~22 eV that can be assigned to metallic Ta [466, 467]. Figure 4-88 *(b)* depicts the typical XPS of O 1s and C 1s core levels, respectively. The O 1s spectrum can be fitted with two components. The major peak of lower binding energy at 530.5 eV (1) is ascribed to the lattice oxygen in LTO coatings. Peak (2) located at 531.5 eV is ascribed to adsorbed organic species on the surface of LTO, possibly hydroxyl groups. The C 1s core level is crucial in the present studies because it is the most diverse between the LTO coatings (not functionalized and functionalized) and represents adsorbates due to air exposure. The spectrum can be fitted with four components (Figure 4-88 *(b)*), assigned to (1) C–C, (2) C–O, (3) O–C=O and (4) C–M (M stands for metals), with respective binding energies of 285 eV (1), 286.5 eV (2), 289 eV and 282 eV. The deconvolution revealed that in functionalized LTO either the carbonyl or carboxyl functional groups (component 2 and 3) are dominant comparing to as-prepared LTO on 316L-SST. There is a higher coverage with carbonyl groups (C=O) of UV-LTO (34 % to 13 % comparing to N-LTO), and with carboxyl groups (–COOH) in the case of N-LTO (28 % to 14 % comparing to UV-LTO).

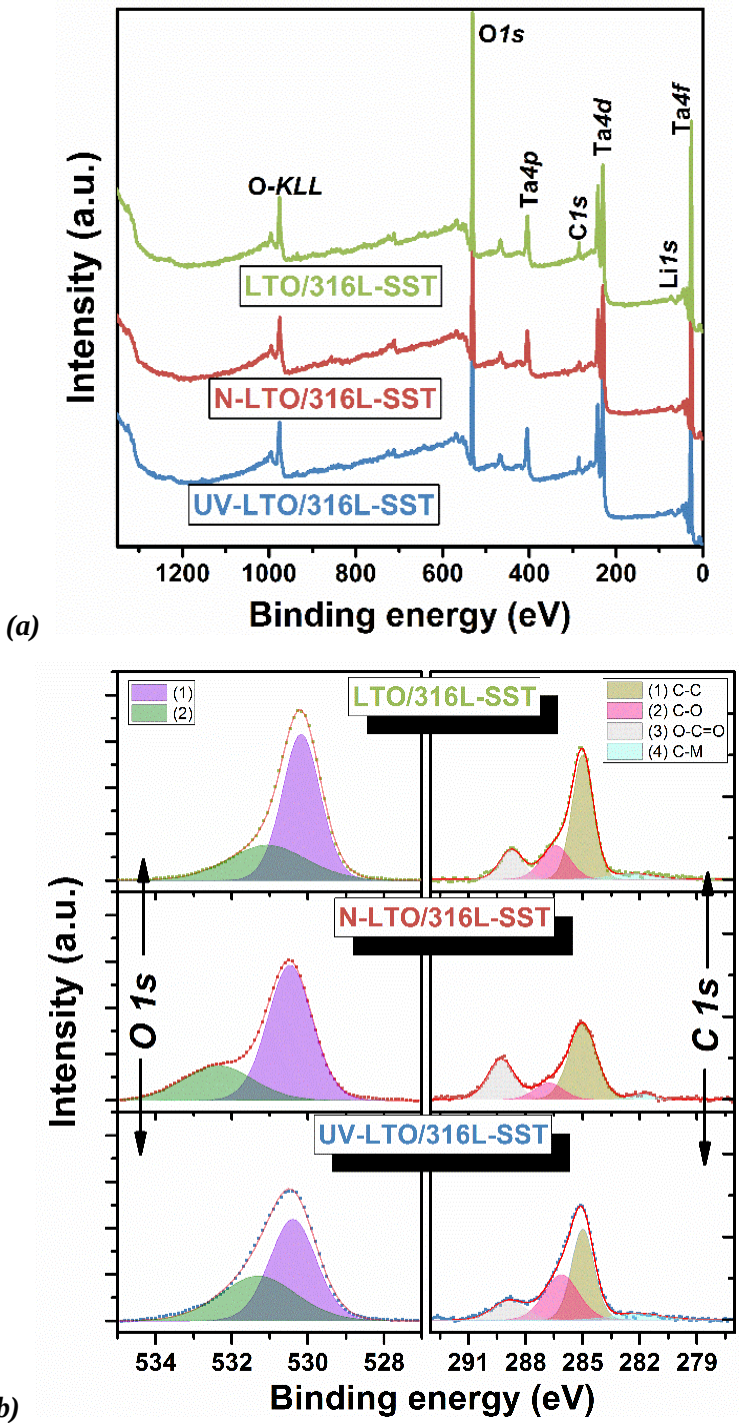

Figure 4-88. X-ray photoelectron spectroscopy (XPS) of as-coated LTO and functionalized LTO onto 316L-SST. (a) General scans of the LTO coatings. (b) High resolution XPS scan of O 1s the C 1s core level peak, with deconvolution into four components, assigned into C–C, C–O, O–C=O and carbon-metal. Carbonyl or carboxyl functional groups are higher in content in functionalized LTO than as-prepared LTO.

4.5.5. Biomineralization tests

A biomineralization of apatite (material's bioactivity) on a surface modified metallic implant is crucial to assess successful implantation of potential candidate. The chemical quality of the interface between the implant and the surrounding bone tissue is of prime importance, thus, a bone-bonding ability is initially tested in supersaturated solutions to evaluate the nucleation and growth of a bone-like apatite layer on a surface; the most common being the so-called SBF solution – Simulated Body Fluid [462]). Such tests (*in vitro* simulations) are usually conducted for several days or weeks at ~37 °C to mimic physicological conditions in human body, and can only be informative of implant capabilities but then additional cell behaviour assessments and *in vivo* tests need to be carried out for overall biological behaviour of the material/device.

After soaking in SBF a white deposit was observed on all the samples. Figure 4-89 presents the X-ray diffraction patterns of the three sets of examined coatings: i) LTO/316L-SST (Figure 4-89 *(a)*), ii) N-LTO/316L-SST (Figure 4-89 *(b)*), and iii) UV-LTO/316L-SST (Figure 4-89 *(c)*). For comparison additional reference patterns of the substrate, $LiTaO_3$ (JCPDS-PDF file #29-0836) and apatite (JCPDS-PDF file #09-0432) are included at the bottom of the figure. All the coatings exhibit monophasic patterns composed of crystalline LTO (matching JCPDS-PDF file #29-0836) and do not show evidences of crystalline or amorphous (identified as broad halos background near the main diffraction lines) calcium phosphate phases when compared to the standards (0D coatings). A certain uncertainty may be associated with these observations resulting from the equipment detection limit (>3 vol%), the low degree of crystallinity of the newly formed phases when compared with the underneath layers (LTO and 316L-SST) both with a high degree of crystallinity, and the possible overlapping of the diffraction lines of LTO and apatite phases, that may interfere with the phase identification.

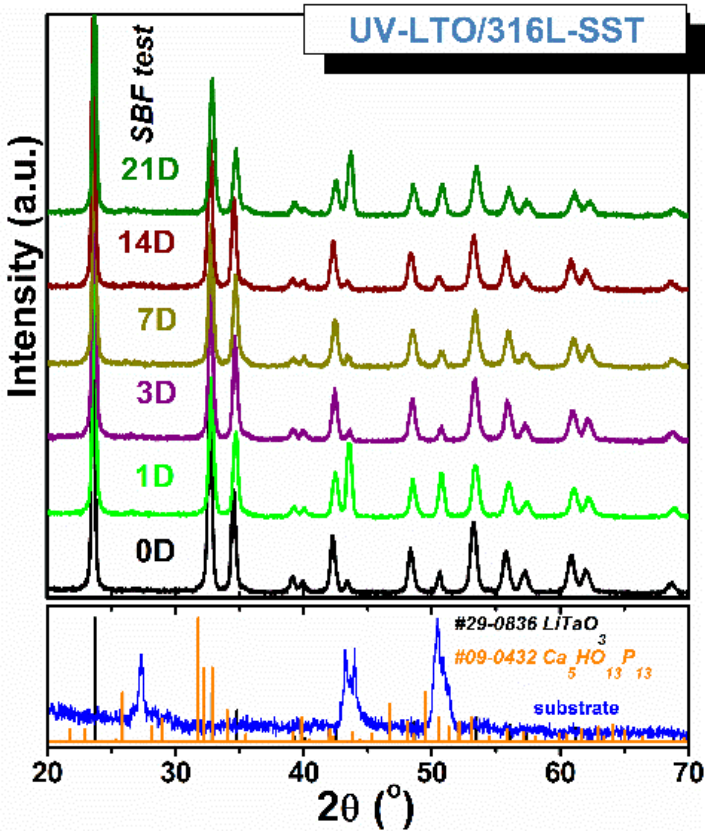
UV-LTO/316L-SST
SBF test
21D
14D
7D
3D
1D
0D
Intensity (a.u.)
#29-0836 LiTaO3
#09-0432 Ca5HO13P3
substrate
20
30
40
50
60
70
2θ (°)

(a)

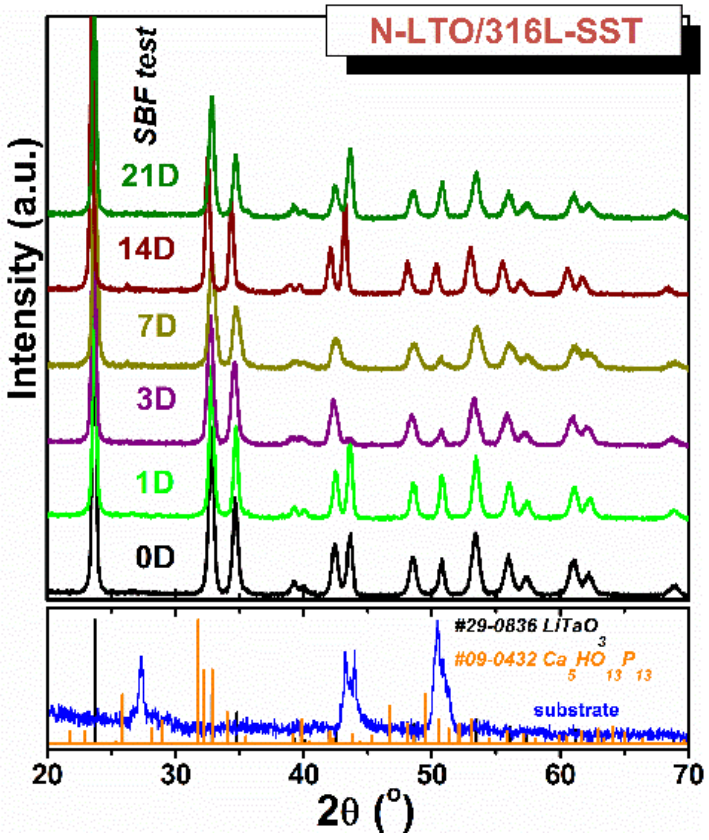
N-LTO/316L-SST
SBF test
21D
14D
7D
3D
1D
0D
Intensity (a.u.)
#29-0836 LiTaO3
#09-0432 Ca5HO13P3
substrate
20
30
40
50
60
70
2θ (°)

(b)

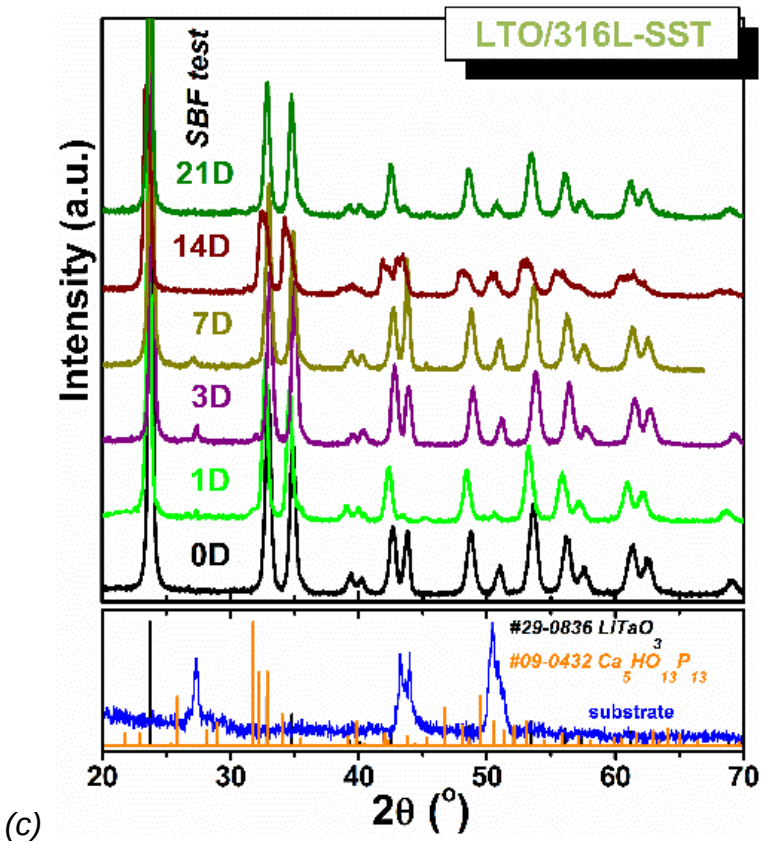

(c)

Figure 4-89. XRD patterns of LTO coatings: (a) as-prepared, (b) polarized and (c) UV-irradiated, soaked in SBF solution for 1, 3, 7, 14 and 21 days. Diffraction lines of $LiTaO_3$ (JCPDS-PDF #29-0836) hydroxyapatite (JCPDS-PDF #09-0432), and diffractogram of bare 316L-SST are enclosed as well in the bottom frame. There are no appreciable variations in the XRD patterns and no indication of hydroxyapatite (JCPDS-PDF #09-0432) formation.

To clarify this ambiguity we used complementary techniques. Figure 4-90 depicts a series of SEM micrographs of the surface of: i) LTO/316L-SST (Figure 4-90 *(a)-(d)*), ii) N-LTO/316L-SST (Figure 4-90 *(e)-(h)*), and iii) UV-LTO/316L-SST (Figure 4-90 *(i)-(l)*), after the incubation in SBF for 3, 7, 14 and 21 days (bottom arrow as indicator). In spite of the absence of new crystalline phases by XRD, the presence of bright particulates on the surface of the different coatings is very clear in all images. As the incubation time increases the concentration of these particulates increases as well, for all the platforms, being more visible for the coatings with functionalized surfaces. The particulate rate formation is distinct for the three sets of coatings, being higher for UV-irradiated LTO coatings. We also observed that for the functionalized coatings the presence of these particulates becomes maximized, covering almost the entire coating surface, as is the case of UV-irradiated LTO after being

soaked in SBF for 21 days. The size of the particulates depends on the initial treatment of the coatings as well, and it is visible that for the as-prepared LTO coatings the precipitates are bigger in size and randomly distributed while for polarized or irradiated coatings the precipitates are smaller, more homogeneous and forming agglomerates, as well seen from the SEM cross section of Figure 4-91 *(a)*.

Furthermore, EDS analysis identified these particulates as being mainly composed of Ca and P. Ca/P ratio is almost constant for all the analyzed precipitates independent on the surface properties of LTO and varies between 0.5–1.0 (Figure 4-91 *(b)*). The Ca/P ratio in calcium phosphates changes between 0.5–2.0, and some of them, as monocalcium phosphate ($Ca(H_2PO_4)_2$), calcium metaphosphate ($Ca(PO_3)_2$), or heptacalcium phosphate ($Ca_7(P_5O_{16})_2$) [468] have a low Ca/P ratio. The most useful for biomedical applications are those having a Ca/P ratio ≥1 due to their low solubility and acidity [469]. However it should be noted that bone-like apatites are frequently highly non-stoichiometric with non-apatitic surface layers (hosting anions, such as HPO_4^{2-} or CO_3^{2-}, or cations) [470].

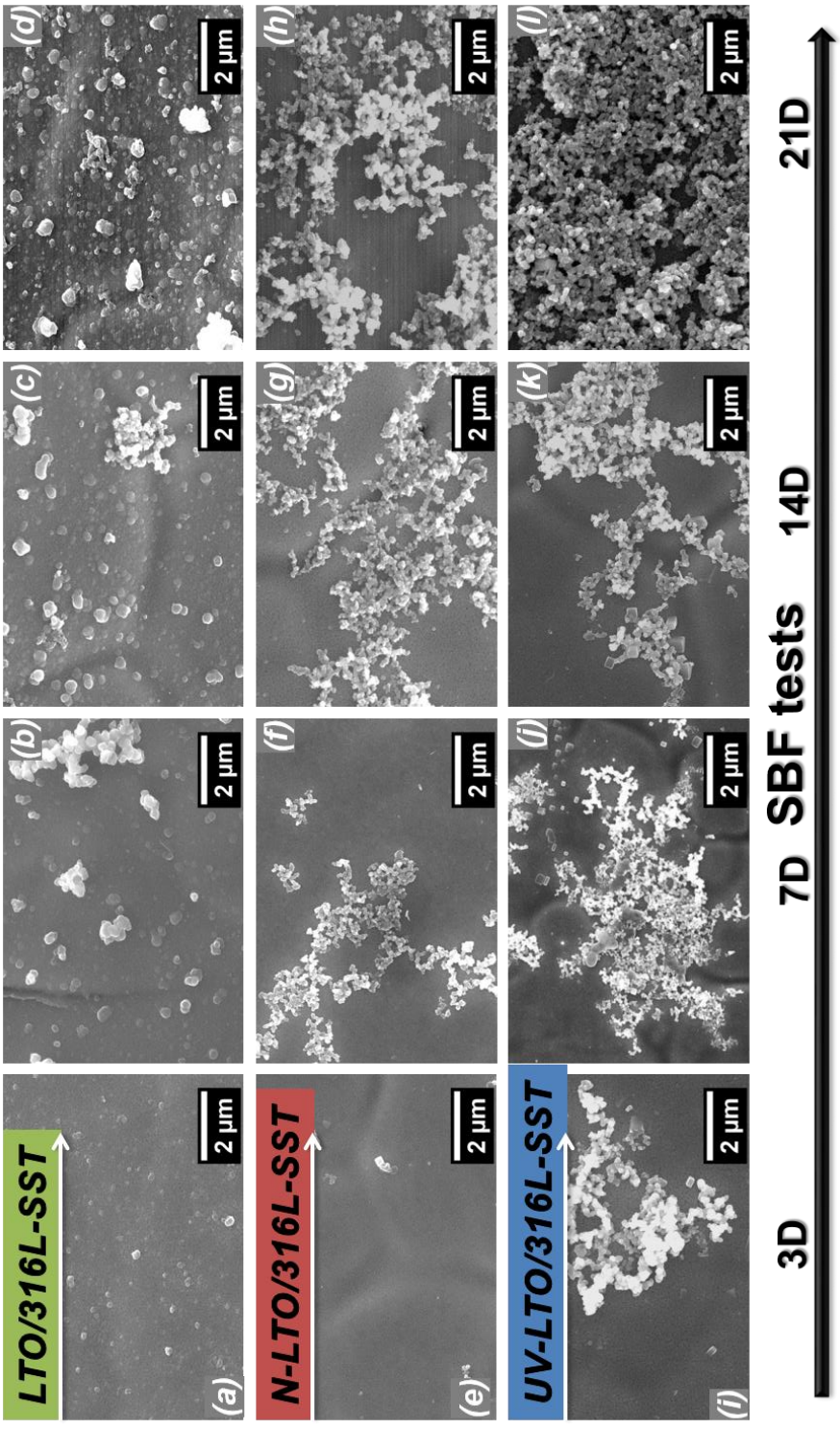

Figure 4-90. Top view SEM micrographs of non-treated and functionalized LTO coatings soaked in SBF solution for 3, 7, 14 and 21 days: as-deposited LTO soaked in SBF for 3 (a), 7 (b), 14 (c) and 21 (d) days (top row); negatively polarized LTO soaked in SBF for 3 (e), 7 (f), 14 (g) and 21 (h) days (middle row); and UV-irradiated LTO soaked in SBF for 3 (i), 7 (j), 14 (k) and 21 (l) days (bottom row). The microstructures clearly depict the formation of precipitates (bright contrast) and its evolution with soaking time and the type of surface. Functionalized LTO surfaces were able to promote the precipitates formation, being it more obvious for UV-irradiated surfaces and longer soaking times.

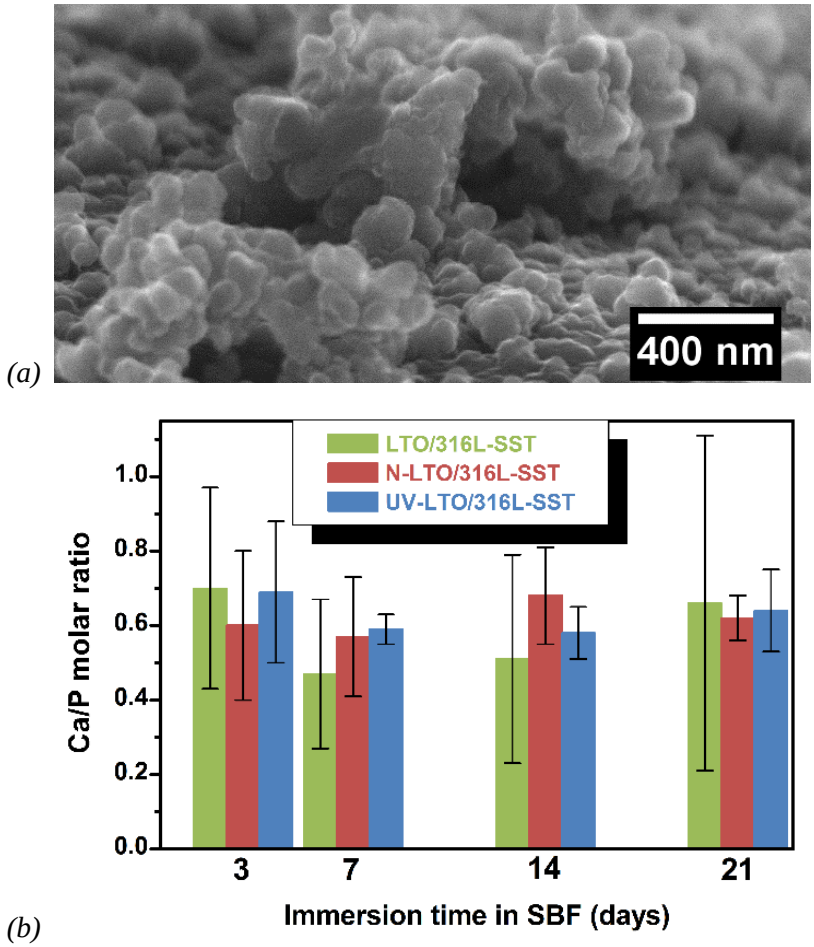

Figure 4-91. (a) Cross-sectional SEM micrograph of functionalized LTO coating soaked in SBF for 21 days. The formed precipitates are organized as agglomerates. (b) EDS analysis confirmed the calcium phosphate nature of these precipitates. The Ca/P molar ratio of the precipitates is independent on the surface functionalization of LTO and soaking time.

The nature of the formed particulates was further analyzed by vibrational spectroscopies, IR and Raman. FTIR spectra of the functionalized LTO/316L-SST incubated in SBF for various periods are depicted in Figure 4-92 *(a)* and *(b)*. The graphs contain the spectra arranged in two wavenumber ranges: 4000–2700 cm^{-1} (left narrower frame) and 1820–350 cm^{-1} (right broader frame), to facilitate interpretation. Additionally, the inset graph enlarges the data from 1720–860 cm^{-1} and illustrates the positions of the characteristic bands of PO_4^{3-}, CO_3^{2-} and OH^- groups in the films kept in SBF for 3, 7, 14 and 21 days. The following vibrational features were identified as: i) broad band at ~3400 cm^{-1} and smaller at ~1600 cm^{-1} (see insets) assigned to adsorbed water molecules, ii) noticeable band at 1150–900 cm^{-1} assigned to the triply degenerated asymmetric stretching mode of the P–O–P bonds

of the phosphate groups, and iii) minor band at ~1400 cm^{-1} assigned to the doubly degenerated stretching mode of CO_3 groups. The clear evidence of the broad v_3 (PO_4) bands is a confirmation of the apatitic nature of the precipitates and the confirmation of the previous SEM results.

Raman spectra of as-deposited as well as polarized and UV-treated LTO coatings incubated in SBF solution for 3, 7 and 14 days are shown in Figure 4-93. Once again the graph is separated in two regions: i) 200–750 cm^{-1} and ii) 900–1160 cm^{-1}. The spectra are composed of many peaks, some of them are sharp and clear and others broad mostly due to the superposition of more than one phonon mode. The spectrum of LTO/316L-SST (bottom plot, 0D) is composed of peaks for both A_1 and E modes (transverse and longitudinal) due to the polycrystalline character of these coatings. It has been reported that the fundamental phonon mode positions in Raman spectrum of $LiTaO_3$ are located at 74, 140, 206, 251, 316, 383, 462, 596, and 662 cm^{-1} for E(TO), at 80, 163, 248, 278, 318, 452, 474, 648, and 870 cm^{-1} for E(LO), at 201, 253, 356, and 600 cm^{-1} for A_1(TO), and at 245, 347, 401, and 864 cm^{-1} for A_1(LO) [471]. Many of the minor peaks that cannot be assigned to any of the listed modes might be attributed to the strain at the substrate/coating interface or to lattice defects, as oxygen vacancies and slight non-stoichiometry [472].

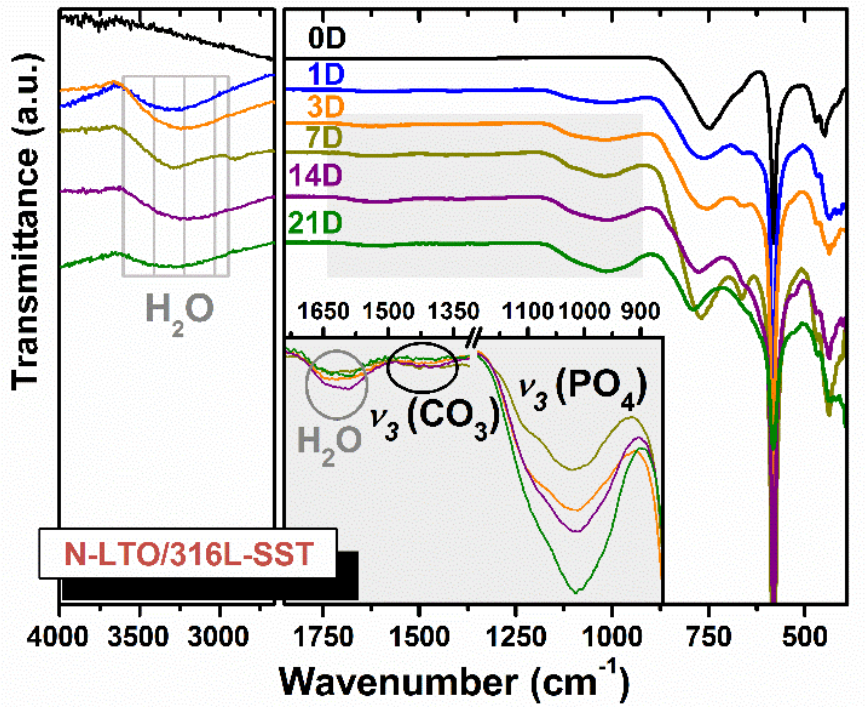

(a)

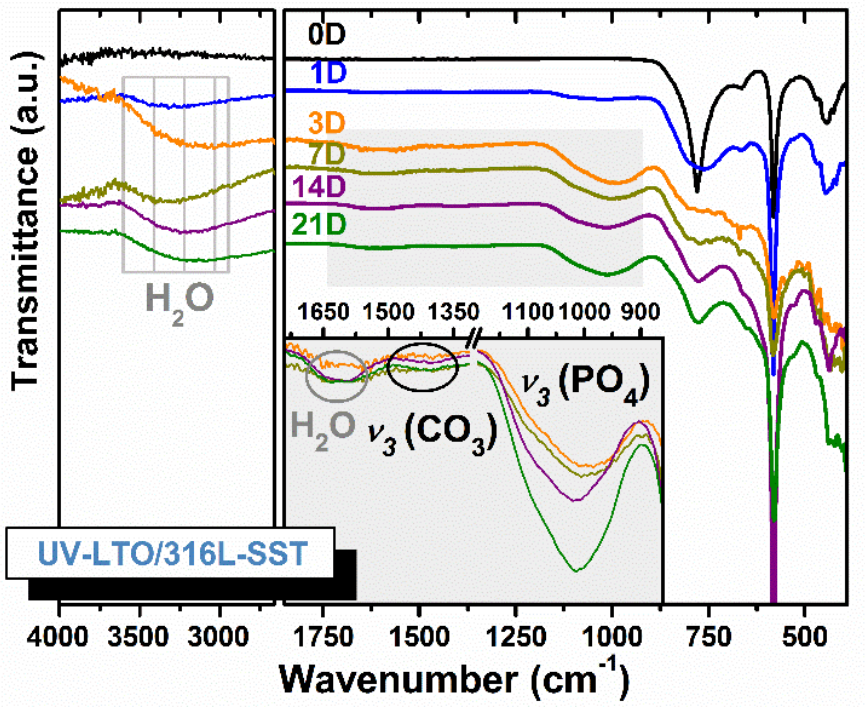

(b)

Figure 4-92. FTIR spectra of (a) negatively polarized and (b) UV-irradiated LTO coatings soaked for different periods (0, 1, 3, 7, 14 and 21 days) in SBF. Characteristic bonds of PO_4^{3-}, CO_3^{2-} and OH^- groups are marked, with gradual increase in intensity of band at 1150–900 cm^{-1} that is related to the phosphate groups.

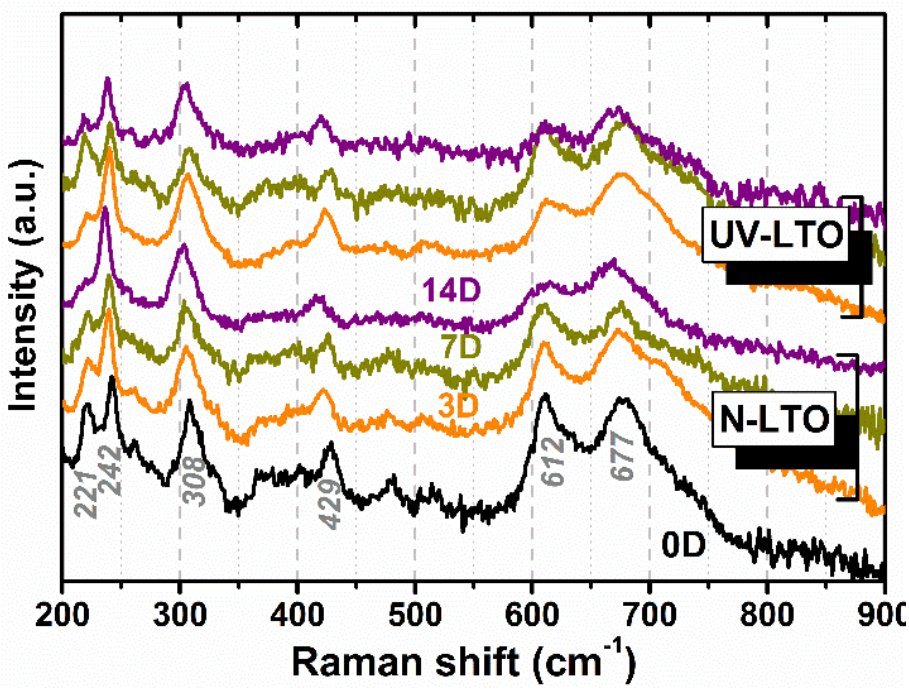

Figure 4-93. Raman spectra of polarized and UV-irradiated LTO films immersed in SBF solution for 3, 7 and 14 days. Multiple peaks for both A_1 and E modes because of the polycrystalline character of thin film are detected.

Besides the direct analysis of the LTO coatings after being incubated in the supersaturated fluids, an examination of the chemical composition of the fluid itself after the bioactivity tests may provide useful data on the ionic concentration changes that occurred in SBF solutions. The ICPS results regarding the Li changes versus soaking time for the LTO coatings under study are shown in Figure 4-94. Li ions concentration detected in SBF solutions reaches ~265 μg/L in the case of as-deposited LTO and being reduced to ~120 μg/L for functionalized LTO coatings (for samples soaked in SBF for 21 days).

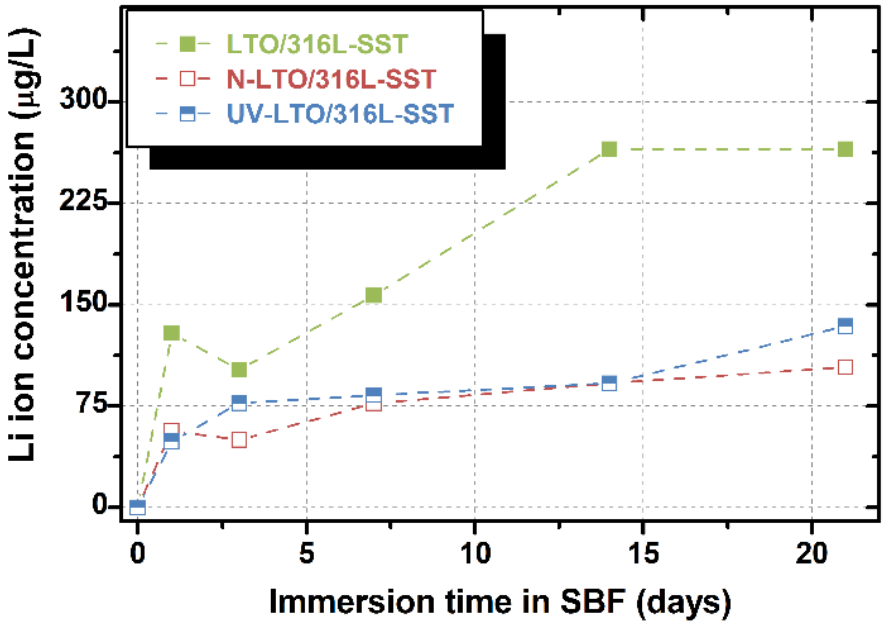

Figure 4-94. Li ion concentration determined by ICPS analysis versus soaking time. The results indicate that there is Li lixiviation from LTO films to SBF; the biggest Li release occurs within one day (129 µg/L for as-deposited LTO coating and ~50 µg/L for functionalized films), reaching ~260 µg/L for as-deposited LTO and ~100 µg/L for functionalized LTO coatings (for the 21 days test samples).

4.5.6. Protein adsorption

The adsorption of proteins is critical within the sequence of biological activities, thus interactions of biomaterials and proteins need to be examined [473]. The behavior of proteins at surfaces determines the nature of the tissue-implant interface, being essential during bone tissue regeneration, and furthermore the adsorbed proteins affect bacterial and cell adhesion, and even the degradation of the biomaterial [474]. Therefore, in the present studies the effect of LTO coatings and its functionalization on the adsorption of BSA was investigated. Serum albumin is a versatile carrier protein, and one of the most important blood proteins.

Quantification of BSA in the remaining solution (after incubation for 1 h), as an indirect measure of the amount of adsorbed protein, was conducted using absorbance measurements with UV-vis spectrometry. Figure 4-95 *(a)* shows the results of BSA adsorption on

LTO/316L-SST, N-LTO/316L-SST and UV-LTO/316L-SST. The highest BSA concentration in the remaining solution was detected for LTO/316L-SST assays, while the lowest one was found for N-LTO/316L-SST. Initial concentration of BSA solution was set at 1 mg/ml, thus any decrease from this concentration indicates a protein adsorption on the surface of the tested materials. Therefore, it can be estimated that the following amount of BSA proteins was adsorbed: 1.8 ± 4.9 % in the case of LTO/316L-SST, 7.6 ± 2.4 % for N-LTO/316L-SST, and 6.4 ± 0.9 % for UV-LTO/316L-SST. There is a clearly higher protein adsorption at the LTO functionalized surfaces. The differences between both types of functionalized surfaces is not statistically relevant.

FTIR-ATR was used to study the conformational changes in the protein structures after adsorption on LTO/316L-SST, N-LTO/316L-SST and UV-LTO/316L-SST. The results are shown in Figure 4-95 *(b)*. Characteristic bands found in the infrared spectra of BSA protein include the amide I and amide II related to the amide bonds from the amino acids. Curve fitting was performed in the amide I region (1710–1585 cm^{-1}) that mainly corresponds to C=O stretching vibrations (~80 %) with some contribution from the stretching of C–N groups [475]. The deconvolution of this band allows to evaluate the secondary structure changes and its content in the backbone structure, *i.e.* α-helix, β-sheet/turn and random coils. Generally, the α-helices absorb between 1660 and 1640 cm^{-1}, β-sheets between 1640 and 1620 cm^{-1}, as well as around 1675 cm^{-1}, and β-turns from 1700 to 1660 cm^{-1} [476]. The curve fitting analysis data are included in Table 4-22. The amide II region (1580–1475 cm^{-1}) is less sensitive and more complex than amide I, and it originates from N–H in-plane bending and C–N stretching vibrations [475]. However, the amide I/II intensity ratio is a good indicator of orientation changes of the relevant bonds.

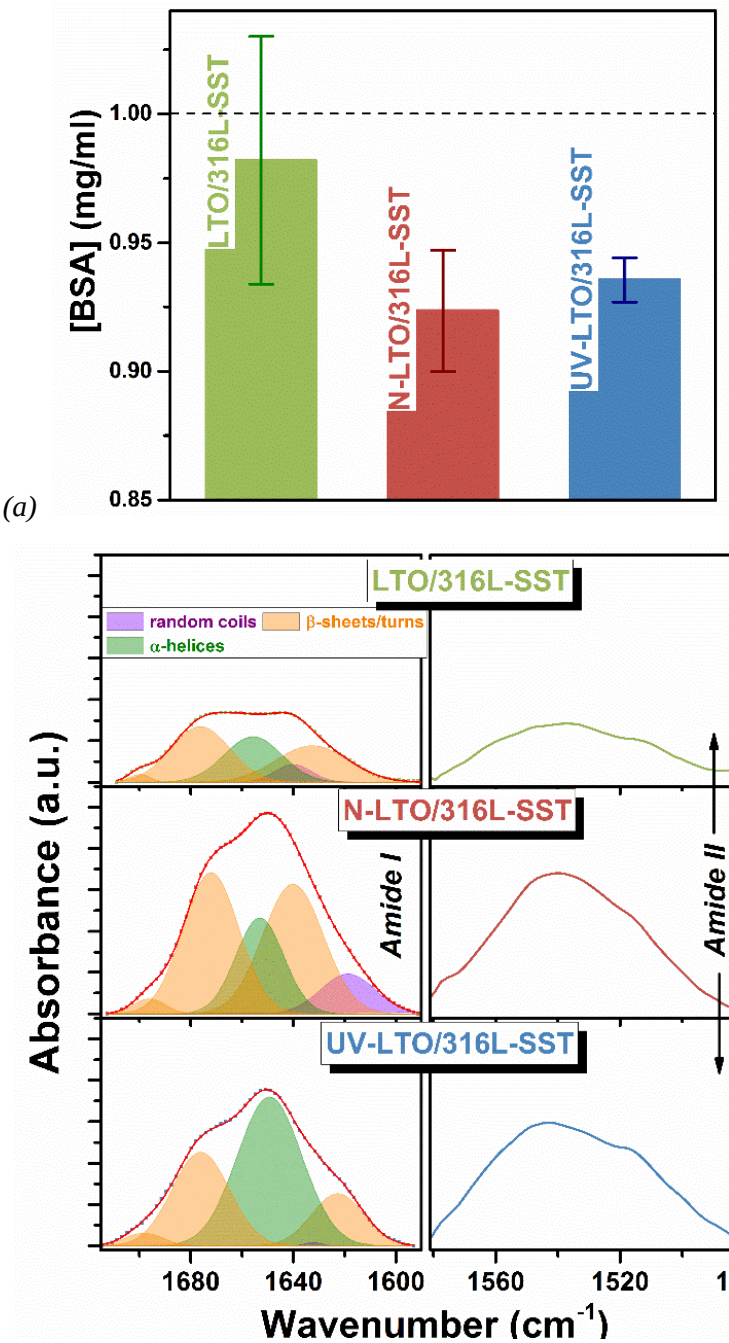

Figure 4-95. BSA protein adsorption results. (a) Quantified BSA solution concentration subjected to the assays determined by UV-vis spectrometry. The highest BSA adsorption is detected on N-LTO/316L-SST, while the lowest on LTO/316L-SST. (b) FTIR-ATR spectra of the curve-fitted amide I band (1710–1585 cm^{-1}) and not-treated amide II band (1580–1475 cm^{-1}) of BSA protein after adsorption on LTO surfaces. The amide I secondary structures (α-helices, β-sheets/turns and random coils) are marked.

Table 4-22. Conformational analysis of adsorbed BSA proteins on LTO surfaces. The amide I and II positions, the amide I/II ratio, and the content of secondary structures obtained from amide I deconvolution are listed for each platform.

	Amide I position (cm^{-1})	Amide I position (cm^{-1})	Amide I/II intensity ratio	Amide I		
				α-helices (%)	*β-sheets/ turns (%)*	*Random coils (%)*
LTO/316L-SST	1654	1537	1.1562	28.03	64.97	7.00
N-LTO/316L-SST	1649	1541	1.4221	19.95	70.59	9.46
UV-LTO/316L-SST	1650	1542	1.2679	52.67	47.01	0.32

The amide I and II positions are independent on the type of LTO surface, but the change in amide I/II ratios is obvious. The most substantial reduction of amide II bonds is detected in N-LTO, comparing to as-prepared LTO (considered as control). This is an indicator that BSA loses its predominant amide II structure upon the adsorption to functionalized LTO. Additionally, it can be observed that the conformation of the adsorbed BSA on various LTO surfaces is different. The BSA undergoes adsorption-induced conformational changes. In N-LTO/316L-SST there is a loss of the α-helix content and an increase of the β-turn/sheet amounts, while in UV-LTO/316L-SST the percentage of α-helical structure is significantly increased and β-structures is reduced.

4.5.7. Proposed mechanism of biomineralization and protein conformation

The results above described are summarized in Table 4-23. The results clearly demonstrate that functionalization of LTO coatings on 316L-SST by external stimuli, electric field or UV-light, favor the formation of polar groups (carboxyl and carbonyl ones) on the surface of LTO coatings what leads to the increase of: i) surface wettability and energy, ii) rate of calcium phosphate formation, and iii) adsorption of BSA proteins. This enhancement of the bioactivity is independent on the type of functionalization. However, and of particular interest, is the dependence of the protein conformation on the type of functionalization. UV-light functionalized LTO/316L-SST surfaces exhibit a significant

increase of the percentage of α-helical structures whereas β-ones are reduced, while for electrical functionalized LTO/316L-SST surfaces a loss of the α-helix content and an increase of the β-turn/sheet amounts is observed.

Table 4-23. Summary of the surface modification, biomineralization and protein adsorption on LTO/316L-SST, N-LTO/316L-SST and UV-LTO/316L-SST surfaces.

Variables	**LTO/316L-SST (non-functionalized)**	**N-LTO/316L-SST (functionalized)**	**UV-LTO/316L-SST (functionalized)**
Surface functional groups, O-containing (by XPS)	C = O: 21 % –COOH: 15 %	C = O: 13 % –COOH: 28 %	C = O: 34 % –COOH: 14 %
Surface hydrophilicity (by contact angle measurements)	Low	Medium	High
Surface energy (by contact angle measurements)	Low	Medium	High
Calcium phosphate formation (by SEM/EDS))	Residual	High	High
Li lixiviation, at 21 days (by ICPS)	High (265 µg/L)	Low (104 µg/L)	Low (134 µg/L)
Protein adsorption (by UV-vis spectrometry)	Low (1.8 %)	High (7.6 %)	High (6.4 %)
Protein conformation *Amide I/II ratio α-helices:β-sheets/turns:Random coils* ***(by FTIR-ATR)***	1.16 0.28:0.65:0.07	1.42 0.20:0.71:0.09	1.28 0.53:0.47:0.00(3)

The reasons for the observed behavior are related with the enhanced or reduced activity at the surface of LTO. Indeed XPS results show that the functionalization treatments by electrical discharge and UV-light both increments the presence polar groups on the surface and changes the ratio between carbonyl and carboxyl groups. Indeed the proportion of each of these groups depends on the nature of the functionalization. UV-light favors carbonyl groups (C=O), while corona discharge favors carboxyl ones (–COOH). Consequently, the functionalized surfaces become more hydrophilic and with higher surface energy when compared with the non-functionalized ones. The more hydrophilic surfaces may interact

easier with the charged and polar functional groups of proteins and cells; what indeed was observed in this study for BSA proteins.

In addition functionalized surfaces have also an effect at the level of Li lixiviation and mineralization. The highest Li release occurs for non-functionalized LTO coatings, ~130 μg/L and ~265 μg/L for 1 and 21 days in SBF, respectively, while functionalized ones exhibit much lower lixiviation levels, from ~50 μg/L up to ~120 μg/L, for 1 and 21 days of incubation, respectively. The functionalization of LTO surfaces with carbonyl and carboxyl groups acts as a screen limiting Li release. The amounts of Li lixiviation observed for the LTO coatings are three orders of magnitude lower than those observed in our previous studies on LTO powders (~45 mg/L just after 1 day of immersion [13]), and consequently well below the lethal doses. Li in doses ≤10 mg/L is used for treatment of bipolar disorders and other mental problems, but above 20 mg/L there is a risk of death [477]. Therefore, in the current thin film coatings, as opposed to the high surface area of LTO powders, there is no problem of Li lixiviation and can be even more reduced if surfaces are functionalized, limiting the lixiviation.

A mineralization kinetics change is also expected for the functionalized surfaces. For non-functionalized LTO/316L-SST, an immediate Li leaching to the SBF solution changes the surface charge being neutral prior to immersion to the SBF. Thus, and as proposed before, when Li lixiviates for the surrounding media the surface of the films become deficient in Li^+, consequently, negatively charged (Figure 4-96) [13]. To compensate these negative charges the film surface selectively absorbs first the positively charged Ca^{2+} ions. As the calcium ions accumulate the surface becomes positively charged and, as a result, the negatively charged phosphate ions (PO_4^{3-}) are adsorbed so as to produce a calcium phosphate rich phase that might even be amorphous and which is eventually transformed in hydroxyapatite. At the same time, as Li ions are lixiviated Ta ions become exposed and presumably negatively charged Ta–OH groups also form near the surface changing at the same time the pH of the surrounding fluid, as proved by Miyazaki *et al.* [478]; amorphous tantalum oxide-based hydrogels can be formed by exchange with H_3O^+ ions from SBF that might be responsible for the apatite formation, as well. When compared with our previous work on LTO powders [13], because here lixiviation is much limited (milligrams against micrograms), the amount of formed precipitates is also restricted, the ionic exchange is only partial and almost no precipitates are formed, and if formed the degree of crystallinity is

quite poor. However when the surfaces of LTO coatings are functionalized the amount of precipitates is prompted; being higher for the UV treated surface. Since in the functionalized platforms the Li release is lower, the observation of higher concentrations of CaP precipitates might be an inconsistency. This apparent contradiction is indeed an indication of a different mechanism for the CaP precipitates formation. In the first case lixiviation is required to induce the surface charges that trigger the CaP precipitation, while in the second case charges at the surface were intentionally imposed by the functionalization treatments; in this case because the surface is pre-charged the reaction with the surrounding media starts immediately and CaP precipitates start forming instantly and the coverage of the surface is prompted, what limits Li lixiviation as well.

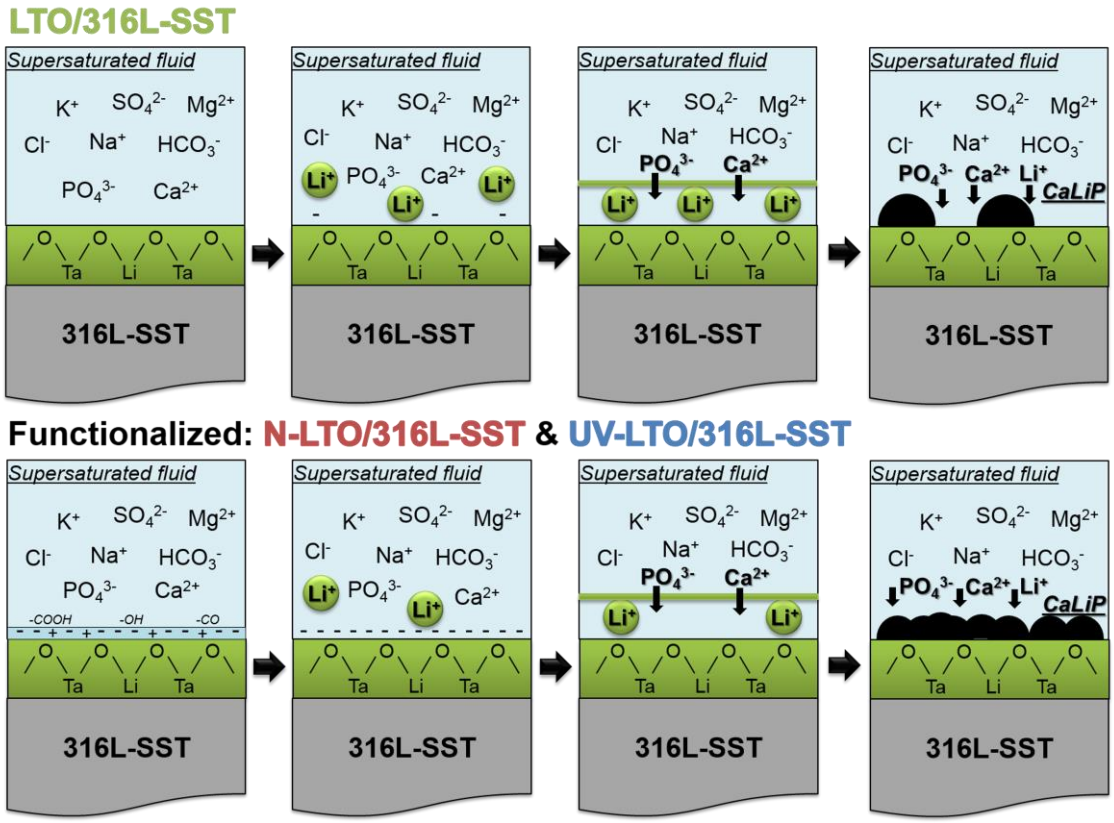

Figure 4-96. Schematic representation of the proposed mechanism for calcium phosphate formation (biomineralization) of metallic implant substrates coated with ferroelectric $LiTaO_3$ coatings. Two different paths were considered: i) as-deposited LTO, LTO/316L-SST (top), and ii) functionalized LTO, N-LTO/316L-SST and UV-LTO/316L-SST (bottom), leading to formation of amorphous and non-stoichiometric CaLiP.

Our results indicate that UV-light treated surfaces are more prone to CaP precipitates formation than electrical functionalization. Since in the first surfaces the concentration of carbonyl (C=O) groups is higher than carboxyl (–COOH) ones, it indicates a higher affinity of carbonyl groups to trigger calcium phosphate precipitation, what might be associated with the net charge of these functional groups. However we should not also discard the fact that the UV-light treated LTO surfaces are more hydrophilic (have a lower contact angle), *i.e*. they are more prone to be wet by the surrounding liquid, and as consequence, more prone to ionic exchanges. Thus, these both factors may respond for the observation that a higher amount of precipitates are here formed, when compared with the previous non-treated surfaces.

In our studies the calcium phosphate precipitates are non-crystalline and the stoichiometry of calcium phosphate precipitates is lower than Ca/P > 1 and over the tested period of time they do not develop chemically towards Ca/P > 1 apatite crystalline structures. Here we argue that this observation may be related with Li^+ ions that may have an effect on the direct precipitation of apatite in the supersaturated solution. It has been proved that a certain level of Li reduces significantly the rate of crystallization of apatite, becoming pronounced at Li levels of ~40 ppm [479]. Therefore it is believed that the lixiviated Li ions act as a kind of barrier (inhibitor) for the crystallization of stoichiometric apatite layer in the current platforms. However, this cannot be viewed as a negative indicator for these platforms performance. Recent *in vivo* studies have demonstrated that local application of lithium effectively facilitates recovery from bone injury by promoting osteoblastogenesis and inhibiting osteoclastogenesis [480]. Another aspect to have in consideration in the biomineralization of calcium phosphates in these studies is related with the role of the changing surrounding media. Li lixiviation may affect the local pH and ionic concentration in SBF may change, thus as a consequence the kinetics of the formation mechanism and expected apatite crystallization may vary. It is well known that additives (or impurities) may drastically change the nucleation and growth process of any crystalline or semi crystalline substance. They may act as inhibitors or accelerators in the regulation of biological mineralization. Normally biological apatites show strong stoichiometric variations with distinct Ca/P ratio, due to a prompt acceptance of inclusions, possibly Li in this case, in amorphous or low crystalline phases.

Lastly our results revealed that the functionalized LTO surfaces accelerate the BSA adsorption, when compared with as-deposited LTO. The protein adsorbed in these surfaces is not denatured. The ratio of amide I/II and α-helical structures / β-ones in Amide I indicates that the protein maintains its global organization. Although interactions of proteins with a material surface are not straightforward and may be very complex, it is known that carboxyl groups frequently ionize, releasing the hydrogen from the hydroxyl group as a free proton (H^+), with the remaining O carrying a negative charge. This charge ”flip-flops” back and forth between the two oxygen atoms, which makes this ionized state relatively stable [481]. On the other hand carbonyl groups do not ionize so easily however their polar nature may favor bondings with near neighbors. This might be the origin for the higher protein adsorption observed for the functionalized LTO surfaces. Interestingly our results demonstrate a dependence of the protein conformation on the type of functionalization. UV-light functionalized LTO/316L-SST surfaces exhibit a significant increase of the percentage of α-helical structures whereas β-ones are reduced. While for electrical functionalized LTO/316L-SST surfaces a loss of the α-helix content and an increase of the β-turn/sheet amounts is observed. The high % of the α-helical structures indicates a more compact shape of the protein verified in the UV treated surface and the low content of α-helical structures indicates a less compact shape of the protein for the case of corona charged surfaces. In addition a decrease of the α-helical structures is expected if some parts of the protein form H bonds within the surface. Indeed our results clearly show that the corona charged surfaces have a higher content of carboxyl groups and, consequently a high ability to protonate and to promote H bonds reactions.

Summary

The concept of a biological platform composed of ferroelectric $LiTaO_3$ and 316L stainless steel is proposed in this work, as an alternative to be used in the implant technology. Taking advantage of ferroelectric and semiconductor character of lithium tantalate, the surface functionalization of ferroelectric coatings is suggested as an effective method to induce functionality. Systematic in vitro studies (tested in supersaturated fluid) were conducted examining bone-like ability of the proposed platforms, and their protein adsorption behaviour. Functionalization of LTO coatings on 316L-SST by external stimuli, electric field or UV-light, favour the formation of polar groups (carboxyl and carbonyl ones) on the surface of LTO coatings what leads to the increase of: i) surface wettability and energy, ii) rate of calcium phosphate formation, and iii) adsorption of BSA proteins. The protein adsorbed in these surfaces is not denatured and the protein maintains its global organization. It is suggested that the non-stoichiometric calcium phosphate precipitates are formed on the surface of ferroelectric LTO coatings as a consequence of Li lixiviation (the key factor in the case of non-functionalized films) and functional groups attached to the surface due to UV-light and corona discharge (the key factor in the case of functionalized films). This enhancement of the bioactivity is independent on the type of functionalization. However, the type of functionalization affects the protein conformation. Our results are a direct proof of the concept to use platforms electrically functionalized that can stimulate tissue growth promoting direct integration of the implant with the host tissue by bone ingrowth and, hence contributing ultimately to reduce implant failure.

Chapter 5. Summary and output

The main conclusions obtained from the experimental results presented and discussed in this thesis are summarized.

At this stage we have learned that:

I. High-temperature oxide melt solution calorimetry was successfully demonstrated to measure the formation and surface enthalpies of an array of ternary oxides directly, alkali tantalate and niobate perovskites. The formation enthalpies of alkali tantalate and niobate perovskites become more exothermic with increase in the size of the alkali cations, however for a given alkali cation, the niobate and tantalate perovskite have comparable energetics. The variation of formation enthalpies of $LiTaO_3$, $LiNbO_3$, $NaTaO_3$, $NaNbO_3$, $KNbO_3$ and $KTaO_3$ with respect to their tolerance factors shows that with increase in the tolerance factor of the alkali tantalate and niobate perovskites formation enthalpies become more negative. This is an obvious indication of the stability of the structure, and for those perovskites with *t* close to 1, the enthalpies of formation are the most exothermic. Among alkali tantalates and niobates, K-containing perovskites are the most structurally stable because their tolerance factor is only +0.03 away from the ideal one. The surface energy increases with the increase of tolerance factor and ionic radius of the A-site cation (Li, Na and K).

II. Phase formation in potassium tantalum oxide system is rather complex and strongly depends on the processing method. It was confirmed by our results that for mixed oxide method (conventional solid state reaction), the perovskite phase is formed directly from constituent components at temperatures as low as 650 °C and is not dependent on the reaction atmosphere. However, while processing potassium tantalate via alkoxide-based sol-gel method, the very stable intermediate pyrochlore structure, $K_2Ta_2O_6$, is formed, to be then transformed into perovskite, $KTaO_3$, only at temperatures ≥900 °C.

III. Solid state kinetic studies (by the JMAK model for isothermal crystallization processes) of alkoxide-based sol-gel derived amorphous gels showed that the perovskite phase formation is dominated by a two-stage mechanism, as indicated by the Avrami exponents: at the early stage, the reaction is suggested to be phase-

boundary controlled, while in the second regime, the exponent values does not follow in any categories described in the JMAK model.

IV. Processing of potassium tantalate from wet chemical methods, sol-gel and hydrothermal, leads to formation of intermediate pyrochlore structures with various stoichiometry, $K_{2-x}Ta_{2+x/5}O_{6-\delta}$. This stoichiometry drives the decomposition paths as follows: a) stoichiometric or nearly-stoichiometric $K_2Ta_2O_6$ decomposes to perovskite $KTaO_3$ at >600 °C, and b) non-stoichiometric $KTa_{2.2}O_6$ breaks apart into TTB $K_6Ta_{10.8}O_{30}$ at >900 °C with absence of perovskite phase at any stage. Initial metal stoichiometry evidently determines the phase formation pathways and ultimately the crystallographic structure of the product.

V. Thermodynamic studies of thermodynamic stability of various potassium tantalum oxides were experimentally determined via calorimetric approach, revealing that the stability of pyrochlores increases with increase in K:Ta ratio thereby confirming that the stoichiometric pyrochlore is energetically more stable than to the non-stoichiometric ones. Additionally, the decomposition enthalpy of $K_2Ta_2O_6$ to $KTaO_3$ indicates that the stoichiometric pyrochlore is energetically more stable than the perovskite, and also confirms that the pyrochlore is the low temperature phase.

VI. Modification of the original phase diagram of Ta_2O_5–$KTaO_3$ system is proposed, to include the low temperature pyrochlores, $K_{2-x}Ta_{2+x/5}O_6$.

VII. Temperatures required to synthesised monophasic $KTaO_3$ thin films from chemical solution deposition are quite high, >750 °C and, as a direct consequence, the compatibility with Si-based substrates is very difficult. The low-toxic chemical solution deposition (with RTA-assisted annealing), a combination of diol-based route in sol-gel processing with careful selection of K-precursor (and its 25 % excess), allows to decrease the crystallization temperature of monophasic $KTaO_3$ thin films down to 650 °C. Other alkali tantalates, $LiTaO_3$ and $NaTaO_3$, were also successfully deposited via diol route and crystallized at the same conditions.

VIII. Photocatalytic activity assays in liquid medium (degradation of organic dye) of the alkali tantalate and niobate perovskites, and potassium tantalum oxides show that perovskite $KNbO_3$ is the most efficient photocatalyst among the tested because of

the good matching between the band gap energy, surface energy and UVA radiation range of the lamp.

IX. The concept of a biological platform composed of ferroelectric $LiTaO_3$ and type 316L stainless steel is proposed, as an alternative that can be used in the implant technology. The effect of surface functionalization of ferroelectric coating is suggested as an effective method to induce functionality, taking advantage of ferroelectric and semiconductive character of lithium tantalate. The *in vitro* tests revealed that strongly non-stoichiometric calcium phosphate precipitates are formed on the surface of $LiTaO_3$ coating being promising evidence of bone bonding ability of the platform. Functionalization of LTO coatings on 316L-SST by external stimuli, electric field or UV-light, favor the formation of polar groups (carboxyl and carbonyl ones) on the surface of LTO coatings what leads to the increase of: i) surface wettability and energy, ii) rate of calcium phosphate formation, and iii) adsorption of BSA proteins. The protein adsorbed in these surfaces is not denatured and the protein maintains its global organization.

Presentations & Publications

The list of ***presentations***:

1. ***Formation and Decomposition Energetics of Potassium Tantalate: Pyrochlores versus Perovskite***, Sebastian Zlotnik, Sulata K. Sahu, Alexandra Navrotsky, and Paula M. Vilarinho, in 13th European Meeting on Ferroelectricity, Porto, Portugal, June 28th-July 3rd 2015 – ***oral*** *presentation*.
2. ***Strategies for Surface Functionalization of Ferroelectric $LiTaO_3$ Coating Towards Biomineralization***, Sebastian Zlotnik, Nathalie Barroca, M. Helena V. Fernandes, and Paula M. Vilarinho, in 13th European Meeting on Ferroelectricity, Porto, Portugal, June 28th-July 3rd 2015 – ***oral*** *presentation*.
3. ***Thermochemistry of Lead-free Alkali Niobate and Tantalate Perovskites: A Comparison Study***, Sebastian Zlotnik, Sulata K. Sahu, Alexandra Navrotsky, and Paula M. Vilarinho, in X CICECO Meeting – *Nanotechnology…From the Lab to the Industry*, Aveiro, Portugal, April 14-15th 2015 – ***poster*** *presentation*.
4. ***Influence of the Chemistry of the Sol on the Lowering of the Crystallization of Solution Derived $KTaO_3$ Thin Films***, Sebastian Zlotnik, M. Lourdes Calzada, Iñigo Bretos, Ricardo Jiménez, and Paula M. Vilarinho, in Sol-Gel 2013 – XVII International Sol-Gel Conference, Madrid, Spain, August 25-30th 2013 – ***poster*** *presentation*.
5. ***Understanding the Sequence of the Phase Formation Process in Perovskite Alkaline Tantalates***, Sebastian Zlotnik, and Paula M. Vilarinho, in E-MRS 2012 Fall Meeting, University of Technology, Warsaw, Poland, September 17-21st 2012 – ***oral*** *presentation*.
6. ***A Comparative Raman Study of Lithium Doped Potassium Tantalate Single Crystals and Ceramics***, Sebastian Zlotnik, Alexander Tkach, Abilio Almeida, J. Agostinho Moreira, and Paula M. Vilarinho in ISAF ECAPD PFM 2012, University of Aveiro, Aveiro, Portugal, July 9-13th 2012 – ***poster*** *presentation*.
7. ***Seed Layer Effect on $KTaO_3$ Thin Films***, Sebastian Zlotnik, Rui Pinho, and Paula M. Vilarinho in IX CICECO Meeting, University of Aveiro, Aveiro, Portugal, May 2-3th 2012 – ***poster*** *presentation*.
8. ***Solution Processing of $KTaO_3$/$LiTaO_3$ Multilayers***, Paula M. Vilarinho, and Sebastian Zlotnik in the 2011 MRS Fall Meeting, Boston, U.S., November 28th-December 2nd 2011 – ***poster*** *presentation*.
9. ***Microscopy Investigations of Tantalate Based Thin Films***, Sebastian Zlotnik, Paula M. Vilarinho, and Ian M. Reaney in Microscopy at the Frontiers of Science, the 2nd Joint

Meeting of the Portuguese and Spanish Microscopy Societies, Aveiro, Portugal, October 18-21st 2011 – ***poster*** *presentation* (honourable prize in the field Microscopy in Materials Sciences).

10. ***Kinetics of Crystallization of $KTaO_3$***, Sebastian Zlotnik, Paula M. Vilarinho in Materiais 2011 – VI International Materials Symposium (XV Meeting of SPM – Sociedade Portuguesa de Materiais), Guimarães, Portugal, April 18-20th 2011 – ***oral*** *presentation*.
11. ***Structural and Electrical Characterization of As-Grown $KTaO_3$-based Single Crystals***, Sebastian Zlotnik, Paula M. Vilarinho, M. Elisabete V. Costa, and Abilio Almeida in ISAF-ECAPD 2010, Edinburg, United Kingdom, August 9-12th 2010 – ***poster*** *presentation.*
12. ***Growth and Characterization of $KTaO_3$-based Single Crystals by a Modified Flux Method***, Sebastian Zlotnik, Paula M. Vilarinho, M. Elisabete V. Costa, J. Agostinho Moreira, and Abilio Almeida in VII CICECO Meeting, University of Aveiro, Aveiro, Portugal, January 28-29th 2010 – ***poster*** *presentation.*

The list of ***publications***:

1. ***Thermodynamic Stability of Lead-free Alkali Niobate and Tantalate Perovskites***, Sulata K. Sahu, Sebastian Zlotnik, Alexandra Navrotsky and Paula M. Vilarinho, Journal of Materials Chemistry C, 2015 3(29), 7691, **DOI**: 10.1039/C5TC01308A.
2. ***Pyrochlore and Perovskite Potassium Tantalate: Enthalpies of Formation and Phase Transformation***, Sebastian Zlotnik, Sulata K. Sahu, Alexandra Navrotsky and Paula M. Vilarinho, Chemistry–A European Journal, 2015, 21(13), 5231, **DOI**: 10.1002/chem.201405666.
3. ***Are Lithium Niobate ($LiNbO_3$) and Lithium Tantalate ($LiTaO_3$) Ferroelectrics Bioactive?***, Paula M. Vilarinho, Nathalie Barroca, Sebastian Zlotnik, Pedro Félix, and Maria Helena Fernandes, Materials Science and Engineering: C, 2014, 39(1), 395-402, **DOI:** 10.1016/j.msec.2014.03.026.
4. ***Growth of Incipient Ferroelectric $KTaO_3$ Single Crystals by a Modified Self-Flux Solution Method***, Sebastian Zlotnik, Paula M. Vilarinho, M. Elisabete V. Costa, J. Agostinho Moreira, and Abilio Almeida, *Crystal Growth & Design*, 2010, 10(8), 3397-3404, **DOI**: 10.1021/cg100036v.
5. ***Photocatalytic Degradation of Pollutant by Alkali Niobate and Tantalate Perovskites***, Sebastian Zlotnik, David M. Tobaldi, M. Paula Seabra, João A. Labrincha and Paula M. Vilarinho (manuscript submitted to *Journal of Physical Chemistry C*).
6. ***Functional Tantalum Based Oxides: from the Structure to the Applications***, Sebastian Zlotnik, Alexander Tkach, and Paula M. Vilarinho (accepted as book chapter in

Advanced Materials Book Series – Advanced Ceramics Materials, Chapter ID: AMBS-1254, Wiley-Scrivener Publisher, USA).

7. ***Functionalized-ferroelectric-coatings-driven enhanced biomineralization and protein-conformation on metallic implants***, Sebastian Zlotnik, Marisa Maltez-da Costa, Nathalie Barroca, María J. Hortigüela, Manoj Kumar Singh, Maria Helena Fernandes and Paula M. Vilarinho (manuscript to be submitted to *ACS Applied Materials & Interfaces*).
8. ***Potassium Precursor Impact on the Phase Formation in Perovskite Potassium Tantalate***, Sebastian Zlotnik, Paula M. Vilarinho, Iñigo Bretos, Ricardo Jiménez and M. Lourdes Calzada (manuscript in preparation).
9. ***Understanding the Sequence of the Phase Formation Process of Perovskite Alkali Tantalate***, Sebastian Zlotnik, Masahiro Yoshimura and Paula M. Vilarinho (manuscript in preparation).

Doctoral Programme

List of disciplines, and obtained final marks, of Programa Doutoral em Ciência e Engenharia de Materiais (9206, Universidade de Aveiro):

	Course	Final mark (0-20)
1	***Técnicas Avançadas de Caracterização de Materiais***	17
2	***Cinética no Processamento Avançado de Sólidos***	17
3	***Nanoquímica***	16
4	***Dispositivos e Sensores***	17
5	***Materiais 2D e 3D Nanoestruturados***	19
6	***Laboratórios de Microscopia Electrónica de Transmissão***	17
7	***Sistemas de Gestão Ambiental***	14
8	***Português Língua Estrangeira***	18

Future plans

The following tasks might be continued, particularly with the proposed plans:

1. Comprehensive examination of interfaces in potassium tantalate thin films

The aim of this task is to investigate the interfaces in polycrystalline oxide thin films, their composition and electronic bonding, using high resolution techniques including high angle annular dark field scanning transmission electron microscopy (HAADF STEM), high resolution transmission electron microscopy (HRTEM), energy dispersive X-ray spectroscopy (EDS) and electron energy loss spectroscopy (EELS). The HAADF-STEM is a useful tool to analyse local structures at a spatial resolution of the atomic level in real space, which is impossible for XRD analysis. Particularly interesting could be to observe the transition layer at the interface of oxide film and bottom substrate (platinized Si and others), any irregularities around the interface near atomic steps of the substrate and irregular structures (second phases) in the bulk of thin film.

The main work to be done concerns: i) preparation of potassium tantalate thin films on rigid substrate (platinized Si wafer) via chemical solution deposition and sputtering techniques, ii) electron-transparent lamellae preparation and iii) structural, microstructural and chemical characterization of the as-prepared specimens at atomic resolution.

The following experimental work is proposed:

- ✓ Deposition of stoichiometric potassium tantalate thin films with perovskite structure with thickness up to ~100 nm and their annealing at temperatures compatible with Si substrates, <700 °C. Then, preparation of electron-transparent specimens by focused ion beam instrument. Careful structural, microstructural and chemical homogeneity analysis of the prepared samples to correlate the results with macroscopic properties.

2. Tailoring the macroscopic performance of multilayered structures composed of alkali tantalate and niobate perovskites

Multiferroic materials provide great opportunity to take advantage of multiple functionalities, e.g. ferroelectricity, ferromagnetism and ferroelasticity. Only very few multiferroic materials exist in the single phase, therefore a new generation systems are composed of two or more phases forming composite structures. One of the solution is the

use of multilayered structures composed of a number of oxide layers. A distinct configurations, bilayers and trilayers, based on alkali tantalates: $KaTaO_3$, $NaTaO_3$ and $LiTaO_3$, and niobates: $KNbO_3$, $NaNbO_3$ and $LiNbO_3$, can be designed to fulfil the requirements, and fabricated via chemical solution deposition.

Detailed chemical, structural and microstructural analyses need to be conducted on as-deposited coatings (but not limited): i) XRD analysis for characterization the phase content, lattice parameters, preferred orientation, and strain; ii) electron microscopy and AFM for microstructural and topographical studies, and iii) Rutherford backscattering spectrometry (RBS) for examination the interface phenomena and compositional depth profiles.

Functional performance of the nanolayered structures will be carried out by a systematic study of relaxation processes and polarization mechanisms in order to provide an understanding of the dielectric and electrical behaviour of the as-processed systems. Dielectric and ferroelectric properties measured at low and high temperatures in the range of 10–700 K will be examined.

3. Design of efficient photocatalyst based on perovskite potassium niobate

It is known that solar energy utilization, for water splitting (hydrogen production) and contaminants decomposition, is promising solution for a clean energy and purification. The present study showed that $KNbO_3$ is the most efficient perovskite among analysed alkali tantalates and niobates, however, there is still a room for improvements. The use of semiconductor in heterogeneous photocatalysis is widely implemented and there are numerous parameters that play a major role, e.g. surface area, energy band configuration, charge carriers transfer, etc. The engineering of photocatalysts involves a design of nanomaterials with large surface areas and diverse morphologies, thus, the synthesis of potassium niobate with high surface area and irregular morphology may have beneficial effect on photocatalytic efficiency. Additionally, the ferroelectric character of $KNbO_3$ might increase photochemical reactivity due to internal electric fields related to ferroelectric phenomena.

The main work to be done contains: i) controlled synthesis of nanoparticles with different shapes, ii) induction of internal electric field by external stimuli, and iii) systematic investigation of photocatalytic performance of the as-synthesized particles.

The following experiments are proposed:

- ✓ Synthesis of nanoparticles via solution-mediated processes, *i.e.* hydrothermal/solvothermal methods with sol-gel assisted solution preparation, co-precipitation and complexation, with an aim to produce nanoparticles with surface areas higher than 20 m^2/g. The electrical charging of the nanoparticles by non-contact method (corona discharge) can be carried out to improve spontaneous polarization (and depolarization field) and then transfer of photogenerated charge carriers.
- ✓ Other popular strategy to improve electron-hole separation and transportation is the modification of monophasic material with metal nanoparticles (forming metal/semiconductor heterostructured photocatalyst). Therefore, the use of Au to produce $Au/KNbO_3$ structures can be proposed in order to significantly separate the charge carriers and at the same time be active under visible light irradiation due to the surface plasmon resonance effect. The electric field near the $Au/KNbO_3$ interface can be generated due to Schottky junction.

4. Role of alkali ions on the biomineralization of calcium phosphate

Biomineralization as a process of the formation of solids by crystallization from aqueous solution is relevant in many disciplines, and biomineralization of calcium phosphate (Ca/P) in particular in bone bonding to implanted material. The crystallization mechanism is far from being well established and recently proposed pre-nucleation cluster pathway might be a solution. In the calcium phosphate system, amorphous calcium phosphate is firstly precipitated solid phase to transform later to crystalline apatite. However, this is valid when the process occurs in supersaturated fluid with respect to calcium and phosphate, and other factors may strongly affect this crystallization pathway, resulting in distinct stoichiometry of CaP. In order to fully understand the role of cations (like Li^+) in the CaP mineralization, there is a need to perform additional study.

Therefore, it is proposed to perform a quantitative CaP crystallization assay, which allows for the detection of all species present in saturated solution and during early crystal growth stage (based on Gebauer approach: Science 322 (2008) 1819 and Advanced Materials 21 (2009) 435). The following experimental work needs to be carried out:

- ✓ Dosing a calcium and lithium solution at a constant rate into phosphate buffer while recording the pH value. In parallel, the Ca^{2+} and Li^+ concentration is monitored, allowing the determination of ion activity, supersaturation and different dissolution equilibria.

- ✓ Additionally, XRD and cryo-TEM studies can be conducted to specifically determine *ex situ* the presence of small clusters (by using radial distribution functions), and *in situ* AFM to detect building blocks relevant for growth of CaP product.

It is stated based on a study of calcium carbonate crystallization that this assay facilitates the categorization of the action of additives during crystallization: i) binding of calcium ions, ii) influence on cluster formation equilibria, iii) inhibition of nucleation, iv) adsorption of nucleated particles and their stabilization, and v) influence on the local structure of nucleated particles, *i.e.* type of amorphous phase or crystalline polymorph.

References

1. Shaw, R., Goodenough, K.: *Niobium-Tantalum: April 2011*. 2011.
2. Manhart, A., Buchert, M., Bleher, D., *et al.*: *Recycling of Critical Metals from End-of-Life Electronics.* In *2012 Electronics Goes Green 2012+ (EGG)*; *9-12 Sept. 2012; Berlin*. Edited by Lang KD, Nissen NF, Middendorf A, Chancerel P. IEEE; 2012: 1-5.
3. Kikuchi, R., Yamamoto, T., Nakamoto, M.: *Preliminary Information of Laboratorial Tantalum Recovery and Considerations for a Potential Solution for Conflict Mineral and Wildlife Conservation.* Environment and Natural Resources Research, 2014, **4**, 31-38.
4. Zhang, P., Zhang, J., Gong, J.: *Tantalum-based Semiconductors for Solar Water Splitting.* Chemical Society Reviews, 2014, **43**, 4395-4422.
5. Chen, Q., Thouas, G.A.: *Metallic Implant Biomaterials.* Materials Science and Engineering: R: Reports, 2015, **87**, 1-57.
6. Volk, T., Wöhlecke, M.: *Introduction.* In *Lithium Niobate: Defects, Photorefraction and Ferroelectric Switching. Volume* 115. Edited by Volk T, Wöhlecke M. Berlin Heidelberg: Springer-Verlag; 2009: 1-7.
7. Zhang, L.Y., Laur, V., Pothier, A., *et al.*: *KTN Ferroelectrics-based Microwave Tunable Phase Shifter.* Microwave and Optical Technology Letters, 2010, **52**, 1148-1150.
8. Simon, Q., Bouquet, V., Peng, W., *et al.*: *Reduction of Microwave Dielectric Losses in $KTa_{1-x}Nb_xO_3$ Thin Films by MgO-doping.* Thin Solid Films, 2009, **517**, 5940-5942.
9. Kobayashi, K., Ryu, M., Doshida, Y., *et al.*: *Novel High-Temperature Antiferroelectric-Based Dielectric $NaNbO_3$–$NaTaO_3$ Solid Solutions Processed in Low Oxygen Partial Pressures.* Journal of the American Ceramic Society, 2013, **96**, 531-537.
10. Kong, L.B., Li, S., Zhang, T.S., *et al.*: *Electrically Tunable Dielectric Materials and Strategies to Improve Their Performances.* Progress in Materials Science, 2010, **55**, 840-893.
11. Christophis, C., Cavalcanti-Adam, E., Hanke, M., *et al.*: *Adherent Cells Avoid Polarization Gradients on Periodically Poled $LiTaO_3$ Ferroelectrics.* Biointerphases, 2013, **8**, 1-9.
12. Dubey, A.K., Basu, B.: *Pulsed Electrical Stimulation and Surface Charge Induced Cell Growth on Multistage Spark Plasma Sintered Hydroxyapatite-Barium Titanate Piezobiocomposite.* Journal of the American Ceramic Society, 2014, **97**, 481-489.
13. Vilarinho, P.M., Barroca, N., Zlotnik, S., *et al.*: *Are Lithium Niobate ($LiNbO_3$) and Lithium Tantalate ($LiTaO_3$) Ferroelectrics Bioactive?* Materials Science and Engineering: C, 2014, **39**, 395-402.
14. Carville, N.C., Collins, L., Manzo, M., *et al.*: *Biocompatibility of Ferroelectric Lithium Niobate and the Influence of Polarization Charge on Osteoblast Proliferation and Function.* Journal of Biomedical Materials Research Part A, 2015, **103**, 2540-2548.
15. Marchesano, V., Gennari, O., Mecozzi, L., *et al.*: *Effects of Lithium Niobate Polarization on Cell Adhesion and Morphology.* ACS Applied Materials & Interfaces, 2015, **7**, 18113-18119.
16. Cao, W.: *Multifunctional Materials: The Basis for Adaptronics.* In *Adaptronics and Smart Structures.* Edited by Janocha H. Berlin Heidelberg: Springer Publishing; 2007: 29-53.
17. *Hitachi's High Functional Materials*: www.hitachi.com/environment/showcase/solution/materials/high_functional.html.
18. Boch, P., Baumard, J.-F.: *Ceramic Compounds: Ceramic Materials.* In *Ceramic Materials: Processes, Properties and Applications.* Edited by Boch P, Nièpce JC. London: ISTE; 2007: 3-28.
19. Vilarinho, P.M.: *Functional Materials: Properties, Processing and Applications.* In *Scanning Probe Microscopy: Characterization, Nanofabrication and Device Application of Functional Materials. Volume* 186. Edited by Vilarinho PM, Rosenwaks Y, Kingon A. Netherlands: Springer; 2005: 3-33.
20. Setter, N., Damjanovic, D., Eng, L., *et al.*: *Ferroelectric Thin Films: Review of Materials, Properties, and Applications.* Journal of Applied Physics, 2006, **100**, 051606.
21. Gevorgian, S.: *Introduction: Overview of Agile Microwave Technologies.* In *Ferroelectrics in Microwave Devices, Circuits and Systems.* Edited by Gevorgian S. London: Springer Publishing; 2009: 1-19.
22. Gevorgian, S., Deleniv, A.: *Ferroelectric Devices.* In *Ferroelectrics in Microwave Devices, Circuits and Systems.* Edited by Gevorgian S. London: Springer; 2009: 175-223.
23. Gevorgian, S.S., Kollberg, E.L.: *Do We Really Need Ferroelectrics in Paraelectric Phase Only in Electrically Controlled Microwave Devices?* IEEE Transactions on Microwave Theory and Techniques, 2001, **49**, 2117-2124.

24. Nagarajan, V., Ganpule, C.S., Ramesh, R.: *Nanoscale Phenomena in Ferroelectric Thin Films.* In *Ferroelectric Random Access Memories Fundamentals and Applications. Volume* 93. Edited by Ishiwara H, Okuyama M, Arimoto Y. Berlin Heidelberg: Springer Publishing; 2004: 47-68.
25. Scott, J.F.: *Ferroelectric Nanostructures for Device Applications.* In *Handbook of Advanced Dielectric, Piezoelectric and Ferroelectric Materials: Synthesis, Properties and Applications.* Edited by Ye Z-G: Woodhead Publishing Limited; 2008: 541-569.
26. Carter, C.B., Norton, M.G.: *Some History - Ceramic Materials.* In *Ceramic Materials: Science and Engineering.* New York: Springer Publishing; 2007: 15-32.
27. Zubko, P.S., Vendik, G.O.: *Ferroelectrics as Constituents of Tunable Metamaterials.* In *Theory and Phenomena of Metamaterials.* Edited by Capolino F: CRC Press; 2009: 33-43.
28. Johnsson, M., Lemmens, P.: *Perovskites and Thin Films - Crystallography and Chemistry.* Journal of Physics: Condensed Matter, 2008, **20**, 264001.
29. Schlom, D.G., Chen, L.-Q., Pan, X., *et al.*: *A Thin Film Approach to Engineering Functionality into Oxides.* Journal of the American Ceramic Society, 2008, **91**, 2429-2454.
30. Fedorov, V.: *Perovskites.* In *Ceramics Science and Technology.* Wiley-VCH Verlag GmbH & Co. KGaA; 2010: 257-297.
31. Panda, P.K., Sahoo, B.: *PZT to Lead Free Piezo Ceramics: A Review.* Ferroelectrics, 2015, **474**, 128-143.
32. Rödel, J., Webber, K.G., Dittmer, R., *et al.*: *Transferring Lead-free Piezoelectric Ceramics Into Application.* Journal of the European Ceramic Society, 2015, **35**, 1659-1681.
33. Rödel, J., Jo, W., Seifert, K.T.P., *et al.*: *Perspective on the Development of Lead-free Piezoceramics.* Journal of the American Ceramic Society, 2009, **92**, 1153-1177.
34. Kalil, T., Wadia, C.: *Materials Genome Initiative for Global Competitiveness.* (Council NSaT ed. Washington, D.C.; 2011.
35. Valant, M., Axelsson, A.-K., Alford, N.: *Review of Ag(Nb, Ta)O_3 as a Functional Material.* Journal of the European Ceramic Society, 2007, **27**, 2549-2560.
36. Wang, G., Lee, J.-H., Yang, Y., *et al.*: *Three-Dimensional Networked Nanoporous Ta_2O_{5-x} Memory System for Ultrahigh Density Storage.* Nano Letters, 2015, **15**, 6009-6014.
37. Larsen, E.M.: *Tantalum.* (Education M-H ed. AccessScience; 2014.
38. Greve, N.: *Tungsten, tantalum, rare earths emerging as 'critical' global metals.* In *Cramer Media*; 2013.
39. *Tantalum - Raw Materials and Processing*: http://tanb.org/tantalum.
40. Geyer, R.G., Riddle, B., Krupka, J., *et al.*: *Microwave Dielectric Properties of Single-Crystal Quantum Paraelectrics $KTaO_3$ and $SrTiO_3$ at Cryogenic Temperatures.* Journal of Applied Physics, 2005, **97**, 104111-104116.
41. Samara, G.A.: *The Relaxational Properties of Compositionally Disordered ABO_3 Perovskites.* Journal of Physics: Condensed Matter, 2003, **15**, R367-R411.
42. Tkach, A., Almeida, A., Moreira, J.A., *et al.*: *Low-temperature Dielectric Response of $NaTaO_3$ Ceramics and Films.* Applied Physics Letters, 2012, **100**, 192909.
43. Hu, C.C., Tsai, C.C., Teng, H.: *Structure Characterization and Tuning of Perovskite-like $NaTaO_3$ for Applications in Photoluminescence and Photocatalysis.* Journal of the American Ceramic Society, 2009, **92**, 460-466.
44. Inbar, I., Cohen, R.E.: *Comparison of the Electronic Structures and Energetics of Ferroelectric $LiNbO_3$ and $LiTaO_3$.* Physical Review B, 1996, **53**, 1193-1204.
45. Adachi, M., Akishige, Y., Asahi, T., *et al.*: *$NaTaO_3$, 1A-4.* In *Oxides. Volume* 36A1. Edited by Shiozaki Y, Nakamura E, Mitsui T: Springer Berlin Heidelberg; 2001: 1-14.
46. Adachi, M., Akishige, Y., Asahi, T., *et al.*: *$LiTaO_3$ [F], 2A-2.* In *Springer Materials - The Landolt-Börnstein Database* (Shiozaki Y, Nakamura E, Mitsui T eds.), vol. 36A1-Oxides: Springer-Verlag; 2002.
47. Adachi, M., Akishige, Y., Asahi, T., *et al.*: *$KTaO_3$ Survey, 1A-5.* In *Springer Materials - The Landolt-Börnstein Database* (Shiozaki Y, Nakamura E, Mitsui T eds.), vol. 36A1-Oxides: Springer-Verlag; 2002.
48. Matthias, B.T.: *New Ferroelectric Crystals.* Physical Review, 1949, **75**, 1771-1771.
49. Wemple, S.H.: *Some Transport Properties of Oxygen-Deficient Single-Crystal Potassium Tantalate ($KTaO_3$).* Physical Review, 1965, **137**, A1575-A1582.
50. Weaver, H.E.: *Dielectric properties of single crystals of SrTiO3 at low temperatures.* Journal of Physics and Chemistry of Solids, 1959, **11**, 274-277.
51. Zhurova, E.A., Zavodnik, V.E., Tsirelson, V.G.: *Precision X-Ray-Diffraction Study of $KTaO_3$-Li Crystals.* Kristallografiya, 1995, **40**, 816-823.
52. Ishihara, T., Baik, N.S., Ono, N., *et al.*: *Effects of Crystal Structure on Photolysis of H_2O on K-Ta Mixed Oxide.* Journal of Photochemistry and Photobiology A, 2004, **167**, 149-157.

53. Zhurova, E.A., Ivanov, Y., Zavodnik, V., *et al.*: *Electron density and atomic displacements in KTaO3.* Acta Crystallographica Section B: Structural Science, 2000, **56**, 594-600.
54. Usui, H., Shibata, S., Kuroki, K.: *Origin of Coexisting Large Seebeck Coefficient and Metallic Conductivity in the Electron Doped $SrTiO_3$ and $KTaO_3$.* Physical Review B, 2010, **81**, 205121.
55. Neumann, T., Borstel, G., Scharfschwerdt, C., *et al.*: *Electronic Structure of $KNbO_3$ and $KTaO_3$.* Physical Review B, 1992, **46**, 10623-10628.
56. Jellison, G.E., Paulauskas, I., Boatner, L.A., *et al.*: *Optical Functions of $KTaO_3$ as Determined by Spectroscopic Ellipsometry and Comparison with Band Structure Calculations.* Physical Review B, 2006, **74**.
57. Reisman, A., Holtzberg, F., Berkenblit, M., *et al.*: *Reactions of the Group-VB Pentoxides with Alkali Oxides and Carbonates. 3. Thermal and X-Ray Phase Diagrams of the System K_2O or K_2CO_3 with Ta_2O_5.* Journal of the American Chemical Society, 1956, **78**, 4514-4520.
58. Roth, R.S., Parker, H.S., Brower, W.S., *et al.*: *Alkali Oxide-Tantalum Oxide and Alkali Oxide-Niobium Oxide Ionic Conductors.* pp. 1-54: National Bureau of Standards of United States; 1974, 1-54.
59. Nazeri, A., Kahn, M.: *Preparation of $KTaO_3$ and $KNbO_3$ Solid-Solutions Through Sol-Gel Processing.* Journal of the American Ceramic Society, 1992, **75**, 2125-2133.
60. Buršík, J., Vaněk, P., Mika, F.: *Role of Reaction Atmosphere in Preparation of Potassium Tantalate through Sol-Gel Method.* Journal of Sol-Gel Science and Technology, 2013, **68**, 219-233.
61. Weber, I.T., Audebrand, N., Bouquet, V., *et al.*: *$KTaO_3$ Powders and Thin Films Prepared by Polymeric Precursor Method.* Solid State Sciences, 2006, **8**, 606-612.
62. Vandenborre, M.T., Husson, E.: *Comparison of the Force Field in Various Pyrochlore Families. I. The $A_2B_2O_7$ Oxides.* Journal of Solid State Chemistry, 1983, **50**, 362-371.
63. Duan, N.G., Tian, Z.R., Willis, W.S., *et al.*: *Hydrothermal Synthesis and Structure of a Potassium Tantalum Defect Pyrochlore.* Inorganic Chemistry, 1998, **37**, 4697-4701.
64. Goh, G.K.L., Haile, S.M., Levi, C.G., *et al.*: *Hydrothermal Synthesis of Perovskite and Pyrochlore Powders of Potassium Tantalate.* Journal of Materials Research, 2002, **17**, 3168-3176.
65. He, Y., Zhu, Y.F., Wu, N.Z.: *Mixed Solvents: A Key in Solvothermal Synthesis of $KTaO_3$.* Journal of Solid State Chemistry, 2004, **177**, 2985-2990.
66. Awadalla, A.A., Gatehouse, B.M.: *Crystal Structures of Some Niobium and Tantalum Oxides. III $K_6Ta_{10.8}O_{30}$ - A Partially "Filled" Tetragonal Tungsten Bronze-like Structure.* Journal of Solid State Chemistry, 1978, **23**, 349-355.
67. Lan, C., Gong, J., Wang, Z., *et al.*: *Synthesis of $K_6Ta_{10.8}O_{30}$ Nanowires by Molten Salt Technique.* Materials Science and Engineering: B, 2011, **176**, 679-683.
68. Zhang, G., Jiang, W., Yu, S.: *Preparation, Characterization and Photocatalytic Property of Nanosized K-Ta Mixed Oxides via a Sol–Gel Method.* Materials Research Bulletin, 2010, **45**, 1741-1747.
69. Salce, B., Gravil, J.L., Boatner, L.A.: *Disorder and Thermal Transport in Undoped $KTaO_3$.* Journal of Physics: Condensed Matter, 1994, **6**, 4077-4092.
70. Nowick, A.S., Fu, S.Q., Lee, W.K., *et al.*: *Dielectric Relaxation of Paired Defects in Perovskite-type Oxides.* Materials Science and Engineering B, 1994, **23**, 19-24.
71. Laguta, V.V., Glinchuk, M.D., Bykov, I.P., *et al.*: *Paramagnetic Dipole Centers in $KTaO_3$: Electron-Spin-Resonance and Dielectric Spectroscopy Study.* Physical Review B, 2000, **61**, 3897-3904.
72. Kvyatkovskii, O.E.: *Quantum Effects in Incipient and Low-Temperature Ferroelectrics (A Review).* Physics of the Solid State, 2001, **43**, 1401-1419.
73. Pashkin, A., Zelezny, V., Petzelt, J.: *Infrared Spectroscopy of $KTa_{1-x}Nb_xO_3$ Crystals.* Journal of Physics: Condensed Matter, 2005, **17**, L265-L270.
74. Venkatesh, J., Sherman, V., Setter, N.: *Synthesis and Dielectric Characterization of Potassium Niobate Tantalate Ceramics.* Journal of the American Ceramic Society, 2005, **88**, 3397-3404.
75. Tyunina, M., Narkilahti, J., Plekh, M., *et al.*: *Evidence for Strain-Induced Ferroelectric Order in Epitaxial Thin-Film $KTaO_3$.* Physical Review Letters, 2010, **104**, 227601.
76. van der Klink, J.J., Rytz, D., Borsa, F., *et al.*: *Collective Effects in a Random-Site Electric-Dipole System: $KTaO_3$:Li.* Physical Review B, 1983, **27**, 89-101.
77. Uesu, Y., Yokota, H., Kiat, J.M., *et al.*: *Is $K_{1-x}Li_xTaO_3$ a Real Relaxor?* Ferroelectrics, 2007, **347**, 37-43.
78. Yokota, H., Uesu, Y.: *Critical Point of Relaxor $K_{1-x}Li_xTaO_3$ Under an Electric Field.* Ferroelectrics, 2008, **369**, 69-75.
79. Dec, J., Miga, S., Trybula, Z., *et al.*: *Dynamics of Li^+ Dipoles at Very Low Concentration in Quantum Paraelectric Potassium Tantalate.* Journal of Applied Physics, 2010, **107**, 094102.
80. Toulouse, J., Pattnaik, R.: *Collective Behaviors in the Disordered Ferroelectrics KLT and KTN.* Journal of the Korean Physical Society, 1998, **32**, S942-S946.

81. Tkach, A., Almeida, A., Moreira, J.A., *et al.*: *Lithium-Induced Dielectric Relaxations in Potassium Tantalate Ceramics.* Journal of Physics D: Applied Physics, 2011, **44**, 315406.
82. Shannon, R.: *Revised Effective Ionic Radii and Systematic Studies of Interatomic Distances in Halides and Chalcogenides.* Acta Crystallographica Section A, 1976, **32**, 751-767.
83. Smolenskii, G.A., Sotnikov, A.V., Syrnikov, P.P., *et al.*: *Investigation of the Phase-Transition Nature in $KTaO_3$-Li Crystals.* Izvestiya Akademii Nauk Sssr Seriya Fizicheskaya, 1985, **49**, 247-250.
84. Reisman, A., Triebwasser, S., Holtzberg, F.: *Phase Diagram of the System $KNbO_3$-$KTaO_3$ by the Methods of Differential Thermal and Resistance Analysis.* Journal of the American Chemical Society, 1955, **77**, 4228-4230.
85. Triebwasser, S.: *Study of Ferroelectric Transitions of Solid-Solution Single Crystal of $KNbO_3$-$KTaO_3$.* Physical Review, 1959, **114**, 63-70.
86. Baller, F., Gather, B., Hellermann, B., *et al.*: *The Influence of Stress on the Dielectric Properties of KTN Crystals.* Physica Status Solidi A, 1989, **116**, K195-K198.
87. Toulouse, J., Wang, X.M., Knauss, L.A., *et al.*: *Dielectric Nonlinearity and Spontaneous Polarization of $KTa_{1-x}Nb_xO_3$ in the Diffuse Transition Range.* Physical Review B, 1991, **43**, 8297-8302.
88. Ling-Yan, Z., Simon, Q., Laurent, P., *et al.*: *Performance Improvements of KTN Ferroelectric Thin Films for Microwave Tunable Devices.* In *Microwave Conference (EuMC), 2010 European*; *28-30 Sept. 2010; Paris*. IEEE; 2010: 1202-1205.
89. Trepakov, V., Smutny, F., Vikhnin, V., *et al.*: *The Effects of Defect System Ordering in a Weakly Doped Incipient Ferroelectric ($KTaO_3$).* Journal of Physics: Condensed Matter, 1995, **7**, 3765-3777.
90. Samara, G.A., Morosin, B.: *Anharmonic Effects in $KTaO_3$-Ferroelectric Mode, Thermal-Expansion, and Compressibility.* Physical Review B, 1973, **8**, 1256-1264.
91. Lemanov, V.V., Sotnikov, A.V., Smirnova, E.P., *et al.*: *Giant dielectric relaxation in SrTiO3-SrMg1/3Nb2/3O3 and SrTiO3-SrSc1/2Ta1/2O3 solid solutions.* Physics of the Solid State, 2002, **44**, 2039-2049.
92. Tagantsev, A.K., Sherman, V.O., Astafiev, K.F., *et al.*: *Ferroelectric Materials for Microwave Tunable Applications.* Journal of Electroceramics, 2003, **11**, 5-66.
93. Hirano, S., Yogo, T., Kikuta, K., *et al.*: *Preparation of Potassium Tantalate Niobate by Sol-Gel Method.* Journal of the American Ceramic Society, 1992, **75**, 1701-1704.
94. Kuang, A.X., Lu, C.J., Huang, G.Y., *et al.*: *Preparation of $KTa_{0.65}Nb_{0.35}O_3$ Thin-Films by a Sol-Gel Process.* Journal of Crystal Growth, 1995, **149**, 80-86.
95. Lu, C.J., Kuang, A.X.: *Preparation of Potassium Tantalate Niobate Through Sol-Gel Processing.* Journal of Materials Science, 1997, **32**, 4421-4427.
96. Bursik, J., Drbohlav, I., Vanek, P., *et al.*: *Preparation of Potassium Tantalate Thin Films Through Chemical Solution Deposition.* Journal of the European Ceramic Society, 2004, **24**, 455-462.
97. Bursik, J., Zelezny, V., Vanek, P.: *Preparation of Potassium Tantalate Niobate Thin Films by Chemical Solution Deposition and Their Characterization.* Journal of the European Ceramic Society, 2005, **25**, 2151-2154.
98. Axelsson, A.K., Pan, Y.Y., Valant, M., *et al.*: *Synthesis, Sintering, and Microwave Dielectric Properties of $KTaO_3$ Ceramics.* Journal of the American Ceramic Society, 2009, **92**, 1773-1778.
99. Hashizume, T., Saiki, A., Terayama, K.: *Preparation of Pyrochlore Potassium Tantalate Thin Films on Ta/ITO Glass via Mild Hydrothermal Growth.* Materials Transactions, 2010, **51**, 261-264.
100. Axelsson, A.K., Pan, Y.Y., Valant, M., *et al.*: *Chemistry, Processing, and Microwave Dielectric Properties of Mn-Substituted $KTaO_3$ Ceramics.* Journal of the American Ceramic Society, 2010, **93**, 800-805.
101. Tkach, A., Vilarinho, P.M., Almeida, A.: *Role of Initial Potassium Excess on the Properties of Potassium Tantalate Ceramics.* Journal of the European Ceramic Society, 2011, **31**, 2303-2308.
102. Chen, Z.X., Zhang, X.L., Cross, L.E.: *Low-Temperature Dielectric-Properties of Ceramic Potassium Tantalate ($KTaO_3$).* Journal of the American Ceramic Society, 1983, **66**, 511-515.
103. Glinšek, S., Malič, B., Rojac, T., *et al.*: *$KTaO_3$ Ceramics Prepared by the Mechanochemically Activated Solid-State Synthesis.* Journal of the American Ceramic Society, 2011, **94**, 1368-1373.
104. Nazeri, A.: *Crystallization of Sol-Gel Deposited Potassium-Tantalate-Niobate Thin-Films on Platinum.* Applied Physics Letters, 1994, **65**, 295-297.
105. Nazeri, A., Kahn, H., Bender, B., *et al.*: *Microstructure of $KTa_xNb_{1-x}O_3$ Thin-Films on MgO(100) Single-Crystals.* Journal of the American Ceramic Society, 1994, **77**, 2450-2454.
106. Yogo, T., Kikuta, K., Ito, Y., *et al.*: *Synthesis of Highly Oriented K(Ta,Nb)O_3 (Ta/Nb=65/35) Film Using Metal Alkoxides.* Journal of the American Ceramic Society, 1995, **78**, 2175-2179.

107. Suzuki, K., Sakamoto, W., Yogo, T., *et al.*: *Processing of Oriented K(Ta,Nb)O_3 Films Using Chemical Solution Deposition.* Journal of the American Ceramic Society, 1999, **82**, 1463-1466.
108. Bao, D.H., Kuang, A.X., Gu, H.S.: *Effects of Sol-Gel Processing Parameters and Substrates on Crystallization of Potassium Tantalate-Niobate Thin Films.* Physica Status Solidi A, 1997, **163**, 67-72.
109. Wang, S.M., Zhon, T.S., Wang, L.H., *et al.*: *Preparation of Highly Oriented KTN/$SrTiO_3$(111), KTN/$SrTiO_3$(100) Thin Films by Sol-Gel Method.* Ferroelectrics, 1997, **195**, 259-263.
110. Zelezny, V., Bursik, J., Vanek, P.: *Preparation and Infrared Characterization of Potassium Tantalate Thin Films.* Journal of the European Ceramic Society, 2005, **25**, 2155-2159.
111. Wood, I.G., Daniels, P., Brown, R.H., *et al.*: *Optical Birefringence Study of the Ferroelectric Phase Transition in Lithium Niobate Tantalate Mixed Crystals: $LiNb_{1-x}Ta_xO_3$.* Journal of Physics: Condensed Matter, 2008, **20**, 235237.
112. Sokoll, T., Norkus, V., Gerlach, G.: *Ion Beam Etching of Lithium Tantalate and Its Application for Pyroelectric Linear Arrays.* Surface and Coatings Technology, 1997, **97**, 469-474.
113. Chao-Chin, C., Ming-Cheng, K., Ying-Chung, C.: *Effects of Membrane Thickness on the Pyroelectric Properties of $LiTaO_3$ Thin Film IR Detectors.* Japanese Journal of Applied Physics, 2005, **44**, 951.
114. Roundy, C.B., Byer, R.L.: *Sensitive $LiTaO_3$ Pyroelectric Detector.* Journal of Applied Physics, 1973, **44**, 929-931.
115. Marques, J.G., Lorenz, K.: *Lattice location of Hf and its interaction with other impurities in $LiNbO_3$: a review.* Optical Engineering, 2014, **53**, 060901.
116. Yang, J., Long, J., Yang, L.: *First-Principles Investigations of the Physical Properties of Lithium Niobate and Lithium Tantalate.* Physica B: Condensed Matter, 2013, **425**, 12-16.
117. Navrotsky, A.: *Energetics and Crystal Chemical Systematics among Ilmenite, Lithium Niobate, and Perovskite Structures.* Chemistry of Materials, 1998, **10**, 2787-2793.
118. Wang, H., Wu, F., Jiang, H.: *Electronic Band Structures of $ATaO_3$ (A = Li, Na, and K) from First-Principles Many-Body Perturbation Theory.* The Journal of Physical Chemistry C, 2011, **115**, 16180-16186.
119. Hsu, R., Maslen, E.N., du Boulay, D., *et al.*: *Synchrotron X-ray Studies of $LiNbO_3$ and $LiTaO_3$.* Acta Crystallographica Section B, 1997, **53**, 420-428.
120. Ohgaki, M., Tanaka, K., Marumo, F.: *Anharmonic Thermal Vibration in a Crystal of Lithium(I) Tantalum(V) Trioxide, $LiTaO_3$.* Mineralogical Journal, 1989, **14**, 373-382.
121. Abrahams, S.C., Bernstein, J.L.: *Ferroelectric Lithium Tantalate - 1. Single Crystal X-Ray Diffraction Study at 24°C.* Journal of Physics and Chemistry of Solids, 1967, **28**, 1685-1692.
122. Abrahams, S.C., Hamilton, W.C., Sequeira, A.: *Ferroelectric Lithium Tantalate - 2. Single Crystal Neutron Diffraction Study at 24°C.* Journal of Physics and Chemistry of Solids, 1967, **28**, 1693-1698.
123. Huanosta, A., West, A.R.: *The Electrical Properties of Ferroelectric $LiTaO_3$ and Its Solid Solutions.* Journal of Applied Physics, 1987, **61**, 5386-5391.
124. Tomeno, I., Matsumura, S.: *Dielectric properties of $LiTaO_3$.* Physical Review B, 1988, **38**, 606-614.
125. *Undoped and Doped Lithium Niobate ($LiNbO_3$ or LNB) and Lithium Tantalate ($LiTaO_3$ or LTA)*: www.mt-berlin.com/frames_cryst/descriptions/lnb_lta.htm.
126. Hatano, H., Kitamura, K., Liu, Y.: *Growth and Photorefractive Properties of Stoichiometric $LiNbO_3$ and $LiTaO_3$.* In *Photorefractive Materials and Their Applications 2. Volume* 114. Edited by Günter P, Huignard J-P: Springer New York; 2007: 127-164.
127. Chen, C.-F., Llobet, A., Brennecka, G.L., *et al.*: *Powder Synthesis and Hot-Pressing of a $LiTaO_3$ Ceramic.* Journal of the American Ceramic Society, 2012, **95**, 2820-2826.
128. Yang, T., Liu, Y.-g., Zhang, L., *et al.*: *Powder Synthesis and Properties of $LiTaO_3$ Ceramics.* Advanced Powder Technology, 2014, **25**, 933-936.
129. Masaru, S., Yuji, F., Takashi, N., *et al.*: *Preparation and Optical Waveguide Properties of $LiNbO_3$ Thin Films by RF Magnetron Sputtering.* Japanese Journal of Applied Physics, 1993, **32**, 4111.
130. Véronique, B., Isabelle, H., Philippe, P., *et al.*: *$LiNbO_3$ and $LiTaO_3$ thin films deposited by chemical and/or physical processes.* Annales de Chimie Science des Matériaux, 2001, **26**, 49-54.
131. Bornand, V., Papet, P.: *Growth Technologies and Studies of Ferroelectric Thin Films--Application to $LiTaO_3$ and $LiNbO_3$ Materials.* Ferroelectrics, 2003, **288**, 187-197.
132. Combette, P., Nougaret, L., Giani, A., *et al.*: *RF magnetron-sputtering deposition of pyroelectric lithium tantalate thin films on ruthenium dioxide.* Journal of Crystal Growth, 2007, **304**, 90-96.
133. Nougaret, L., Combette, P., Pascal-Delannoy, F.: *Pyroelectric $LiTaO_3$ Thin Films Elaborated by RF Magnetron Sputtering with Li Enriched Target.* Integrated Ferroelectrics, 2007, **95**, 44-53.
134. Garraud, A., Nadar, S., Giani, A., *et al.*: *Self-polarized pyroelectric $LiTaO_3$ thin films.* In *Design, Test, Integration and Packaging of MEMS/MOEMS (DTIP), 2014 Symposium on*; *1-4 April 2014*. 2014: 1-4.

135. Cheng, S.D., Kam, C.H., Zhou, Y., *et al.*: *Sol-Gel Derived Ferroelectric Thin Films of $LiTaO_3$ on SiO_2/Si Substrate.* Ferroelectrics, 1999, **232**, 99-104.
136. Cheng, S.D., Kam, C.H., Zhou, Y., *et al.*: *C-axis Oriented Sol-Gel Derived $LiNb_{1-x}Ta_xO_3$ Thin Films on Si(111) Substrates.* Thin Solid Films, 2000, **365**, 77-81.
137. Cheng, S.D., Zhou, Y., Kam, C.H., *et al.*: *$LiTaO_3$ Films with C-axis Preferred Orientation Prepared on Si(111) Substrate by Sol-Gel Method.* Materials Letters, 2000, **44**, 125-129.
138. Cheng, S.D., Zhou, Y., Kam, C.H., *et al.*: *Sol-Gel Derived Thin Films of $LiTaO_3$ on SiO_2/Si Substrates for Optical Waveguide Applications.* Fiber and Integrated Optics, 2001, **20**, 45-52.
139. Satapathy, S., Varma, K.B.R.: *Orientated Nano Grain Growth and Effect of Annealing on Grain Size in $LiTaO_3$ Thin Films Deposited by Sol-Gel Technique.* Journal of Crystal Growth, 2006, **291**, 232-238.
140. Satapathy, S., Verma, P., Gupta, P.K., *et al.*: *Structural, Dielectric and Ferroelectric Properties of Multilayer Lithium Tantalate Thin Films Prepared by Sol-Gel Technique.* Thin Solid Films, 2011, **519**, 1803-1808.
141. Kao, M.C., Chen, H.Z., Wang, C.M., *et al.*: *Pyroelectric Properties of Sol-Gel Derived Lithium Tantalite Thin Films.* Physica B: Condensed Matter, 2003, **329-333**, 1527-1528.
142. Kao, M.C., Chen, H.Z., Wang, C.M., *et al.*: *Rapid Thermal Processing of Lithium Tantalite Thin Films Prepared by a Diol-Based Sol-Gel Process.* Applied Physics A, 2004, **79**, 103-108.
143. Kao, M.C., Chen, Y.C., Chen, H.Z., *et al.*: *Leakage Current Mechanisms in Rapid Thermal Annealed $LiTaO_3$ Thin Films Prepared by a Diol-Based Sol-Gel Method.* Ferroelectrics, 2004, **304**, 151-154.
144. Kao, M.C., Chen, Y.C., Wang, C.M., *et al.*: *$LiTaO_3$ Thin Films Prepared by a Diol-Based Sol-Gel Process and Crystallized by Conventional and RTA Processes.* Ferroelectrics, 2004, **304**, 147-150.
145. Young, S.L., Kao, M.C., Chen, H.Z.: *Optical Properties of $LiTaO_3$ Thin Films Crystallized by RTA Processes.* Journal of Electroceramics, 2006, **17**, 799-803.
146. Youssef, S., Al Asmar, R., Podlecki, J., *et al.*: *Characterization of $LiTaO_3$ Thin Films Fabricated by Sol-Gel Technique.* Microelectronics Journal, 2007, **38**, 63-66.
147. Youssef, S., Al Asmar, R., Podlecki, J., *et al.*: *Structural and Optical Characterization of Oriented $LiTaO_3$ Thin Films Deposited by Sol-Gel Technique.* EPJ Applied Physics, 2008, **43**, 65-71.
148. Kennedy, B.J., Prodjosantoso, A.K., Howard, C.J.: *Powder Neutron Diffraction Study of the High Temperature Phase Transitions in $NaTaO_3$.* Journal of Physics: Condensed Matter, 1999, **11**, 6319-6327.
149. Iwasaki, H., Ikeda, T.: *Studies on the System $Na(Nb_{1-x}Ta_x)O_3$.* Journal of the Physical Society of Japan, 1963, **18**, 157-163.
150. Aleksandrowicz, A., Wójcik, K.: *Electrical Properties of Single Crystals and Ceramic Samples of $NaTaO_3$.* Ferroelectrics, 1989, **99**, 105-113.
151. Ahtee, M., Unonius, L.: *The Structure of $NaTaO_3$ by X-Ray Powder Diffraction.* Acta Crystallographica Section A, 1977, **33**, 150-154.
152. Ahtee, M., Darlington, C.N.W.: *Structures of $NaTaO_3$ by Neutron Powder Diffraction.* Acta Crystallographica Section B, 1980, **36**, 1007-1014.
153. Kamba, S., Goian, V., Bovtun, V., *et al.*: *Incipient Ferroelectric Properties of $NaTaO_3$.* Ferroelectrics, 2012, **426**, 206-214.
154. König, J., Jančar, B., Suvorov, D.: *New $Na_{0.5}Bi_{0.5}TiO_3$–$NaTaO_3$-Based Perovskite Ceramics.* Journal of the American Ceramic Society, 2007, **90**, 3621-3627.
155. Kudo, A., Miseki, Y.: *Heterogeneous Photocatalyst Materials for Water Splitting.* Chemical Society Reviews, 2009, **38**, 253-278.
156. Kato, H., Asakura, K., Kudo, A.: *Highly Efficient Water Splitting into H_2 and O_2 over Lanthanum-Doped $NaTaO_3$ Photocatalysts with High Crystallinity and Surface Nanostructure.* Journal of the American Chemical Society, 2003, **125**, 3082-3089.
157. Lin, W.-H., Cheng, C., Hu, C.-C., *et al.*: *$NaTaO_3$ Photocatalysts of Different Crystalline Structures for Water Splitting into H_2 and O_2.* Applied Physics Letters, 2006, **89**, 211904.
158. Hu, C.-C., Teng, H.: *Influence of Structural Features on the Photocatalytic Activity of $NaTaO_3$ Powders from Different Synthesis Methods.* Applied Catalysis A: General, 2007, **331**, 44-50.
159. Modak, B., Srinivasu, K., Ghosh, S.K.: *Band Gap Engineering of $NaTaO_3$ Using Density Functional Theory: A Charge Compensated Codoping Strategy.* Physical Chemistry Chemical Physics, 2014, **16**, 17116-17124.
160. Ece Eyi, E., Cabuk, S.: *Ab initio study of the structural, electronic and optical properties of NaTaO3.* Philosophical Magazine, 2010, **90**, 2965-2976.
161. Wunderlich, W., Baufeld, B.: *Development of Thermoelectric Materials Based on $NaTaO_3$ - Composite Ceramics.* In *Ceramic Materials.* Edited by Wunderlich W: InTech; 2010: 1-28.

162. Darlington, C.N.W., Knight, K.S.: *High-Temperature Phases of $NaNbO_3$ and $NaTaO_3$.* Acta Crystallographica Section B: Structural Science, 1999, **55**, 24-30.
163. Lanfredi, S., Lente, M.H., Eiras, J.A.: *Phase Transition at Low Temperature in $NaNbO_3$ Ceramic.* Applied Physics Letters, 2002, **80**, 2731-2733.
164. Shanker, V., Samal, S.L., Pradhan, G.K., *et al.*: *Nanocrystalline $NaNbO_3$ and $NaTaO_3$: Rietveld Studies, Raman Spectroscopy and Dielectric Properties.* Solid State Sciences, 2009, **11**, 562-569.
165. Geguzina, G.A., Reznitchenko, L.A., Dergunova, N.V.: *Atomic Substitution Effects in Binary Solid Solution Systems based Upon $NaNbO_3$.* Ferroelectrics, 1998, **214**, 261-271.
166. Tong, X.C.: *Electro-Optic Waveguides.* In *Advanced Materials for Integrated Optical Waveguides. Volume* 46. Edited by Tong XC: Springer International Publishing; 2014: 335-376.
167. Comes, R., Lambert, M., Guinier, A.: *The Chain Structure of $BaTiO_3$ and $KNbO_3$.* Solid State Communications, 1968, **6**, 715-719.
168. Nakamura, K., Tokiwa, T., Kawamura, Y.: *Domain Structures in $KNbO_3$ Crystals and Their Piezoelectric Properties.* Journal of Applied Physics, 2002, **91**, 9272-9276.
169. Nakayama, Y., Pauzauskie, P.J., Radenovic, A., *et al.*: *Tunable Nanowire Nonlinear Optical Probe.* Nature, 2007, **447**, 1098-1101.
170. Jaeger, R.E., Egerton, L.: *Hot Pressing of Potassium-Sodium Niobates.* Journal of the American Ceramic Society, 1962, **45**, 209-213.
171. Rubio-Marcos, F., Romero, J.J., Martín-Gonzalez, M.S., *et al.*: *Effect of Stoichiometry and Milling Processes in the Synthesis and the Piezoelectric Properties of Modified KNN Nanoparticles by Solid State Reaction.* Journal of the European Ceramic Society, 2010, **30**, 2763-2771.
172. Li, J.F., Wang, K., Zhu, F.Y., *et al.*: *(K, Na)NbO_3-based Lead-free Piezoceramics: Fundamental Aspects, Processing Technologies, and Remaining Challenges.* Journal of the American Ceramic Society, 2013, **96**, 3677-3696.
173. Li, Y., Li, J., Zhou, Z., *et al.*: *Frequency Dependent Electro-Optic Properties of Potassium Lithium Tantalate Niobate Single Crystal.* Ferroelectrics, 2011, **425**, 82-89.
174. Chen, X., Shen, S., Guo, L., *et al.*: *Semiconductor-Based Photocatalytic Hydrogen Generation.* Chemical Reviews, 2010, **110**, 6503-6570.
175. Malato, S., Fernández-Ibáñez, P., Maldonado, M.I., *et al.*: *Decontamination and Disinfection of Water by Solar Photocatalysis: Recent Overview and Trends.* Catalysis Today, 2009, **147**, 1-59.
176. Richardson, S.D.: *Environmental Mass Spectrometry: Emerging Contaminants and Current Issues.* Analytical Chemistry, 2008, **80**, 4373-4402.
177. Suárez, S., Carballa, M., Omil, F., *et al.*: *How are Pharmaceutical and Personal Care Products (PPCPs) Removed from Urban Wastewaters?* Reviews in Environmental Science and Bio/Technology, 2008, **7**, 125-138.
178. Ribeiro, A.R., Nunes, O.C., Pereira, M.F.R., *et al.*: *An overview on the advanced oxidation processes applied for the treatment of water pollutants defined in the recently launched Directive 2013/39/EU.* Environment International, 2015, **75**, 33-51.
179. Fujishima, A., Honda, K.: *Electrochemical Photolysis of Water at a Semiconductor Electrode.* Nature, 1972, **238**, 37-38.
180. Castellote, M., Bengtsson, N.: *Principles of TiO_2 Photocatalysis.* In *Applications of Titanium Dioxide Photocatalysis to Construction Materials. Volume* 5. Edited by Ohama Y, Van Gemert D: Springer Netherlands; 2011: 5-10.
181. Dong, H., Zeng, G., Tang, L., *et al.*: *An overview on limitations of TiO_2-based particles for photocatalytic degradation of organic pollutants and the corresponding countermeasures.* Water Research, 2015, **79**, 128-146.
182. Royer, S., Duprez, D., Can, F., *et al.*: *Perovskites as Substitutes of Noble Metals for Heterogeneous Catalysis: Dream or Reality.* Chemical Reviews, 2014, **114**, 10292-10368.
183. Shi, J., Guo, L.: *ABO_3-based Photocatalysts for Water Splitting.* Progress in Natural Science: Materials International, 2012, **22**, 592-615.
184. Sayama, K., Arakawa, H., Domen, K.: *Photocatalytic Water Splitting on Nickel Intercalated $A_4Ta_xNb_{6-x}O_{17}$ (A = K, Rb).* Catalysis Today, 1996, **28**, 175-182.
185. Huang, Y., Xie, Y., Fan, L., *et al.*: *Synthesis and Photochemical Properties of La-doped $HCa_2Nb_3O_{10}$.* International Journal of Hydrogen Energy, 2008, **33**, 6432-6438.
186. Kato, H., Kudo, A.: *New Tantalate Photocatalysts for Water Decomposition into H_2 and O_2.* Chemical Physics Letters, 1998, **295**, 487-492.
187. Takahara, Y., Kondo, J.N., Takata, T., *et al.*: *Mesoporous Tantalum Oxide. 1. Characterization and Photocatalytic Activity for the Overall Water Decomposition.* Chemistry of Materials, 2001, **13**, 1194-1199.

188. Stodolny, M., Laniecki, M.: *Synthesis and Characterization of Mesoporous Ta_2O_5-TiO_2 Photocatalysts for Water Splitting.* Catalysis Today, 2009, **142**, 314-319.
189. Kato, H., Kudo, A.: *Water Splitting into H_2 and O_2 on Alkali Tantalate Photocatalysts $ATaO_3$ (A = Li, Na, and K).* Journal of Physical Chemistry B, 2001, **105**, 4285-4292.
190. Kato, H., Kudo, A.: *Photocatalytic Decomposition of Pure Water into H_2 and O_2 Over $SrTa_2O_6$ Prepared by a Flux Method.* Chemistry Letters, 1999, **28**, 1207-1208.
191. Kato, H., Kudo, A.: *Photocatalytic Water Splitting into H_2 and O_2 Over Various Tantalate Photocatalysts.* Catalysis Today, 2003, **78**, 561-569.
192. Iwase, A., Kato, H., Kudo, A.: *Nanosized Au Particles as an Efficient Cocatalyst for Photocatalytic Overall Water Splitting.* Catalysis Letters, 2006, **108**, 7-10.
193. Lee, Y., Watanabe, T., Takata, T., *et al.*: *Hydrothermal Synthesis of Fine $NaTaO_3$ Powder as a Highly Efficient Photocatalyst for Overall Water Splitting.* Bulletin of the Chemical Society of Japan, 2007, **80**, 423-428.
194. Liu, J.W., Chen, G., Li, Z.H., *et al.*: *Hydrothermal Synthesis and Photocatalytic Properties of $ATaO_3$ and $ANbO_3$ (A = Na and K).* International Journal of Hydrogen Energy, 2007, **32**, 2269-2272.
195. Ishihara, T., Nishiguchi, H., Fukamachi, K., *et al.*: *Effects of Acceptor Doping to $KTaO_3$ on Photocatalytic Decomposition of Pure H_2O.* Journal of Physical Chemistry B, 1999, **103**, 1-3.
196. Mitsui, C., Nishiguchi, H., Fukamachi, K., *et al.*: *Photocatalytic Decomposition of Pure Water over NiO Supported on $KTa(M)O_3$ ($M = Ti^{4+}, Hf^{4+}, Zr^{4+}$) Perovskite Oxide.* Chemistry Letters, 1999, **28**, 1327-1328.
197. Amini, A.R., Laurencin, C.T., Nukavarapu, S.P.: *Bone Tissue Engineering: Recent Advances and Challenges.* Critical Reviews in Biomedical Engineering, 2012, **40**, 363-408.
198. Navarro, M., Michiardi, A., Castaño, O., *et al.*: *Biomaterials in Orthopaedics.* Journal of The Royal Society Interface, 2008, **5**, 1137-1158.
199. Wang, W., Ouyang, Y., Poh, C.K.: *Orthopaedic Implant Technology: Biomaterials from Past to Future.* Annals of the Academy of Medicine Singapore, 2011, **40**, 237-243.
200. Salinas, A.J., Esbrit, P., Vallet-Regi, M.: *A Tissue Engineering Approach Based on the Use of Bioceramics for Bone Repair.* Biomaterials Science, 2013, **1**, 40-51.
201. Vallet-Regí, M., Ruiz-Hernández, E.: *Bioceramics: From Bone Regeneration to Cancer Nanomedicine.* Advanced Materials, 2011, **23**, 5177-5218.
202. Vallet-Regí, M., Salinas, A.J.: *Ceramics as Bone Repair Materials.* In *Bone Repair Biomaterials.* Edited by Planell JA, Best SM, Lacroix D, Merolli A: Woodhead Publishing; 2009: 194-230.
203. Hench, L.L.: *Bioceramics.* Journal of the American Ceramic Society, 1998, **81**, 1705-1728.
204. Gremillard, L., Meille, S., Chevalier, J., *et al.*: *Degradation of Bioceramics.* In *Degradation of Implant Materials.* Edited by Eliaz N. New York: Springer; 2012: 195-252.
205. Best, S.M., Porter, A.E., Thian, E.S., *et al.*: *Bioceramics: Past, Present and for the Future.* Journal of the European Ceramic Society, 2008, **28**, 1319-1327.
206. Fukada, E., Yasuda, I.: *On the Piezoelectric Effect of Bone.* Journal of the Physical Society of Japan, 1957, **12**, 1158-1162.
207. Hastings, G.W., Mahmud, F.A.: *Electrical Effects in Bone.* Journal of Biomedical Engineering, 1988, **10**, 515-521.
208. Teng, N.C., Nakamura, S., Takagi, Y., *et al.*: *A New Approach to Enhancement of Bone Formation by Electrically Polarized Hydroxyapatite.* Journal of Dental Research, 2001, **80**, 1925-1929.
209. Baxter, F.R., Bowen, C.R., Turner, I.G., *et al.*: *Electrically Active Bioceramics: A Review of Interfacial Responses.* Annals of Biomedical Engineering, 2010, **38**, 2079-2092.
210. Jianqing, F., Huipin, Y., Xingdong, Z.: *Promotion of Osteogenesis by a Piezoelectric Biological Ceramic.* Biomaterials, 1997, **18**, 1531-1534.
211. Hwang, K.S., Song, J.E., Jo, J.W., *et al.*: *Effect of Poling Conditions on Growth of Calcium Phosphate Crystal in Ferroelectric $BaTiO_3$ Ceramics.* Journal of Materials Science: Materials in Medicine, 2002, **13**, 133-138.
212. Park, Y.-J., Hwang, K.-S., Song, J.-E., *et al.*: *Growth of Calcium Phosphate on Poling Treated Ferroelectric $BaTiO_3$ Ceramics.* Biomaterials, 2002, **23**, 3859-3864.
213. Park, Y.J., Jeong, Y.H., Lee, Y.R., *et al.*: *Effect of Negatively Polarized Barium Titanate Thin Film, Formed on Ti, on Osteoblast Cell Activity.* Journal of Dental Research, 2003, **82**, B212-B212.
214. Dubey, A.K., Basu, B., Balani, K., *et al.*: *Dielectric and Pyroelectric Properties of HAp-$BaTiO_3$ Composites.* Ferroelectrics, 2011, **423**, 63-76.

215. Dubey, A.K., Basu, B., Balani, K., *et al.*: *Multifunctionality of Perovskites $BaTiO_3$ and $CaTiO_3$ in a Composite with Hydroxyapatite as Orthopedic Implant Materials.* Integrated Ferroelectrics, 2011, **131**, 119-126.
216. Chen, X.M., Yang, B.: *A New Approach for Toughening of Ceramics.* Materials Letters, 1997, **33**, 237-240.
217. Dubey, A.K., Gupta, S.D., Basu, B.: *Optimization of Electrical Stimulation Parameters for Enhanced Cell Proliferation on Biomaterial Surfaces.* Journal of Biomedical Materials Research Part B: Applied Biomaterials, 2011, **98B**, 18-29.
218. Beloti, M.M., de Oliveira, P.T., Gimenes, R., *et al.*: *In Vitro Biocompatibility of a Novel Membrane of the Composite Poly(vinylidene-trifluoroethylene)/Barium Titanate.* Journal of Biomedical Materials Research Part A, 2006, **79A**, 282-288.
219. Nilsson, K., Lidman, J., Ljungstrom, K., *et al.*: *Biocompatible Material for Implants.* St. Jude Medical AB (Jarfalla, SE) 2003.
220. Dubey, A.K., Yamada, H., Kakimoto, K.-i.: *Space Charge Polarization Induced Augmented In Vitro Bioactivity of Piezoelectric $(Na,K)NbO_3$.* Journal of Applied Physics, 2013, **114**, 124701.
221. Wang, Q., Yang, J., Zhang, W., *et al.*: *Manufacture and Cytotoxicity of a Lead-free Piezoelectric Ceramic as a Bone Substitute - Consolidation of Porous Lithium Sodium Potassium Niobate by Cold Isostatic Pressing.* International Journal of Oral Science, 2009, **1**, 99-104.
222. Ballarre, J., Manjubala, I., Schreiner, W.H., *et al.*: *Improving the Osteointegration and Bone-Implant Interface by Incorporation of Bioactive Particles in Sol-Gel Coatings of Stainless Steel Implants.* Acta Biomaterialia, 2010, **6**, 1601-1609.
223. Kokubo, T., Kim, H.M., Kawashita, M., *et al.*: *Bioactive Metals: Preparation and Properties.* Journal of Materials Science: Materials in Medicine, 2004, **15**, 99-107.
224. Gallardo, J., Galliano, P., Durán, A.: *Bioactive and Protective Sol-Gel Coatings on Metals for Orthopaedic Prostheses.* Journal of Sol-Gel Science and Technology, 2001, **21**, 65-74.
225. Kokubo, T., Kim, H.-M., Kawashita, M.: *Novel Bioactive Materials with Different Mechanical Properties.* Biomaterials, 2003, **24**, 2161-2175.
226. Zhang, Q., Leng, Y., Lu, X., *et al.*: *Bioactive Films on Metallic Surfaces for Osteoconduction.* Journal of Biomedical Materials Research Part A, 2009, **88A**, 481-490.
227. Wiff, J.P., Fuenzalida, V.M., Arias, J.L., *et al.*: *Hydrothermal-Electrochemical $CaTiO_3$ Coatings as Precursor of a Biomimetic Calcium Phosphate Layer.* Materials Letters, 2007, **61**, 2739-2743.
228. Rose, F.R.A.J., Hou, Q., Oreffo, R.O.C.: *Delivery Systems for Bone Growth Factors - The New Players in Skeletal Regeneration.* Journal of Pharmacy and Pharmacology, 2004, **56**, 415-427.
229. Yamashita, K., Oikawa, N., Umegaki, T.: *Acceleration and Deceleration of Bone-Like Crystal Growth on Ceramic Hydroxyapatite by Electric Poling.* Chemistry of Materials, 1996, **8**, 2697-2700.
230. Ercan, B., Webster, T.J.: *Greater Osteoblast Proliferation on Anodized Nanotubular Titanium upon Electrical Stimulation.* International Journal of Nanomedicine, 2008, **3**, 477-485.
231. Yang, J., Bei, J., Wang, S.: *Enhanced Cell Affinity of Poly(d,l-lactide) by Combining Plasma Treatment with Collagen Anchorage.* Biomaterials, 2002, **23**, 2607-2614.
232. Schwartz, R.W., Schneller, T., Waser, R.: *Chemical Solution Deposition of Electronic Oxide Films.* Comptes Rendus Chimie, 2004, **7**, 433-461.
233. Calzada, M.M.: *Ferroelectrics onto Substrates Prepared by Chemical Solution Deposition: From the Thin Film to the Self-Assembled Nano-sized Structures.* In *Multifunctional Polycrystalline Ferroelectric Materials. Volume* 140. Edited by Pardo L, Ricote J. Netherlands: Springer Netherlands; 2011: 93-144.
234. Fukushima, J.: *Preparation of $BaTiO_3$ Films by Hydrolysis of Organometallic Compounds.* American Ceramic Society Bulletin, 1976, **55**, 1064-1065.
235. Schwartz, R.W., Narayanan, M.: *Chemical Solution Deposition - Basic Principles.* In *Solution Processing of Inorganic Materials.* Edited by Mitzi DB: John Wiley & Sons, Inc.; 2008: 33-76.
236. Schneller, T., Majumder, S.B., Waser, R.: *Ceramic Thin Films.* In *Ceramics Science and Technology. Volume* 1. Edited by Riedel R, Chen i-W. Germany: Wiley-VCH Verlag GmbH & Co. KGaA; 2011: 443-509.
237. Glinsek, S., Malic, B., Vukadinovic, M., *et al.*: *Processing and Electric Field Dependent Dielectric Properties of $KTa_{0.6}Nb_{0.4}O_3$ Thin Films on Alumina.* Ferroelectrics, 2009, **387**, 112-117.
238. Bretos, I., Calzada, M.L.: *Approaches Towards the Minimisation of Toxicity in Chemical Solution Deposition Processes of Lead-Based Ferroelectric Thin Films.* In *Multifunctional Polycrystalline Ferroelectric Materials. Volume* 140. Edited by Pardo L, Ricote J. Netherlands: Springer Netherlands; 2011: 145-216.

239. Calzada, M.L., González, A.: *Tantalum Penta-Glycolate Sol as a Precursor of Strontium Bismuth Tantalate Ferroelectric Thin Films.* Journal of the American Ceramic Society, 2005, **88**, 2702-2708.
240. Byrappa, K., Yoshimura, M.: *Hydrothermal Technology - Principles and Applications.* In *Handbook of Hydrothermal Technology*. Edited by Yoshimura KB. Norwich, NY: William Andrew Publishing; 2001: 1-52.
241. Byrappa, K., Adschiri, T.: *Hydrothermal Technology for Nanotechnology.* Progress in Crystal Growth and Characterization of Materials, 2007, **53**, 117-166.
242. Stuart, B.H.: *Introduction.* In *Infrared Spectroscopy: Fundamentals and Applications.* John Wiley & Sons, Ltd; 2005: 1-13.
243. Davydov, A.: *Theoretical Fundamentals and Experimental Considerations of the Spectroscopic Methods Used in Surface Chemistry.* In *Molecular Spectroscopy of Oxide Catalyst Surfaces.* Edited by Davydov A. Chichester, UK: John Wiley & Sons, Ltd; 2003: 1-25.
244. Stuart, B.H.: *Experimental Methods.* In *Infrared Spectroscopy: Fundamentals and Applications.* John Wiley & Sons, Ltd; 2005: 15-44.
245. Corporation, T.N.: *Introduction to Fourier Transform Infrared Spectrometry.* 2001.
246. Coates, J.: *Interpretation of Infrared Spectra, A Practical Approach.* In *Encyclopedia of Analytical Chemistry.* John Wiley & Sons, Ltd; 2006.
247. Gabbott, P.: *A Practical Introduction to Differential Scanning Calorimetry.* In *Principles and Applications of Thermal Analysis.* Edited by Gabbott P. Oxford, UK: Blackwell Publishing Ltd; 2008: 1-50.
248. Gabbott, P., Bottom, R.: *Thermogravimetric Analysis.* In *Principles and Applications of Thermal Analysis.* Edited by Gabbott P. Oxford, UK: Blackwell Publishing Ltd; 2008: 87-118.
249. Brown, M.E.: *Differential Thermal Analysis (DTA) and Differential Scanning Calorimetry (DSC).* In *Introduction to Thermal Analysis. Volume* 1. Edited by Brown ME: Springer Netherlands; 2001: 55-90.
250. Laboratories, T.A.R.: *Basics of X-ray Diffraction.* 1999.
251. Dinnebier, R.E., Billinge, S.J.L.: *Principles of Powder Diffraction.* In *Powder Diffraction: Theory and Practice.* Edited by Dinnebier RE, Billinge SJL: The Royal Society of Chemistry; 2008: 1-19.
252. Leng, Y.: *X-Ray Diffraction Methods.* In *Materials Characterization: Introduction to Microscopic and Spectroscopic Methods.* Second edition. Edited by Leng Y: Wiley-VCH Verlag GmbH & Co. KGaA; 2013: 47-82.
253. Dutta, P.: *Grazing incidence X-ray diffraction.* Current Science, 2000, **78**, 1478-1483.
254. Birkholz, M.: *Texture and Preferred Orientation.* In *Thin Film Analysis by X-Ray Scattering.* Edited by Birkholz M: Wiley-VCH Verlag GmbH & Co. KGaA; 2006: 183-237.
255. Scardi, P., Leoni, M.: *Whole Powder Pattern Modelling: Theory and Applications.* In *Diffraction Analysis of the Microstructure of Materials. Volume* 68. Edited by Mittemeijer E, Scardi P: Springer Berlin Heidelberg; 2004: 51-91.
256. Leoni, M., Confente, T., Scardi, P.: *PM2K: A Flexible Program Implementing Whole Powder Pattern Modelling.* Zeitschrift Fur Kristallographie, v suppl, 2006, **23**, 249-254.
257. Egerton, R.F.: *An Introduction to Microscopy.* In *Physical Principles of Electron Microscopy.* Edited by Egerton RF: Springer US; 2005: 1-25.
258. Fultz, B., Howe, J.M.: *The TEM and its Optics.* In *Transmission Electron Microscopy and Diffractometry of Materials.* Edited by Fultz B, Howe JM: Springer Berlin Heidelberg; 2008: 61-118.
259. Williams, D.B., Carter, C.B.: *The Transmission Electron Microscope.* In *Transmission Electron Microscopy.* Edited by Williams DB, Carter CB: Springer US; 2009: 3-22.
260. Egerton, R.F.: *The Scanning Electron Microscope.* In *Physical Principles of Electron Microscopy.* Edited by Egerton RF: Springer US; 2005: 125-153.
261. Leng, Y.: *Scanning Electron Microscopy.* In *Materials Characterization: Introduction to Microscopic and Spectroscopic Methods.* Second edition. Edited by Leng Y. Germany: Wiley-VCH Verlag GmbH & Co. KGaA; 2013: 127-161.
262. Technologies, K.: *AFM/SPM Principles.* 2012.
263. (BBML), B.B.a.M.L.: *General Introduction to Atomic Force Microscopy.* 2014.
264. Johnson, D., Hilal, N., Bowen, W.R.: *Basic Principles of Atomic Force Microscopy.* In *Atomic Force Microscopy in Process Engineering.* Edited by Bowen WR, Hilal N. Oxford: Butterworth-Heinemann; 2009: 1-30.
265. Proksch, R., Kalinin, S.: *Piezoresponse Force Microscopy with Asylum Research AFMs.* Asylum Research; 2009.
266. Horcas, I., Fernández, R., Gómez-Rodríguez, J.M., *et al.*: *WSXM: A Software for Scanning Probe Microscopy and a Tool for Nanotechnology.* Review of Scientific Instruments, 2007, **78**, -.

267. Agilent Technologies, I.: *Basics of Measuring the Dielectric Properties of Materials.* Agilent Technologies, Inc.; 2006.
268. Carter, C.B., Norton, M.G.: *Locally Redistributing Charge.* In *Ceramic Materials Science and Engineering.* Edited by Carter CB, Norton MG: Springer New York; 2013: 573-592.
269. Waser, R., Lohse, O.: *Electrical Characterization of Ferroelectric, Paraelectric, and Superparaelectric Thin Films.* Integrated Ferroelectrics, 1998, **21**, 27-40.
270. Hao, X., Zhai, J., Kong, L.B., *et al.*: *A Comprehensive Review on the Progress of Lead Zirconate-based Antiferroelectric Materials.* Progress in Materials Science, 2014, **63**, 1-57.
271. Xu, R.: *Laser Diffraction.* In *Particle Characterization: Light Scattering Methods. Volume* 13. Edited by Scarlett B: Springer Netherlands; 2002: 111-181.
272. Condon, J.B.: *Interpreting the Physisorption Isotherm.* In *Surface Area and Porosity Determinations by Physisorption.* Edited by Condon JB. Amsterdam: Elsevier Science; 2006: 55-90.
273. Perkampus, H.-H.: *UV-VIS Spectroscopy and Its Applications.* Springer; 1992.
274. Leach, R.: *Optical Measurement of Surface Topography.* Berlin Heidelberg: Springer-Verlag; 2011.
275. Kino: *Drop Shape Analysis System CAST®3.0 - User Manual.*
276. Knop-Gericke, A.: *X-ray Photoelectron Spectroscopy. An Introduction to Principles and Practices. By Paul van der Heide.* Angewandte Chemie International Edition, 2012, **51**, 9218-9218.
277. Mittemeijer, E.J.: *Analysis of the Microstructure; Analysis of Lattice Imperfections: Light and Electron Microscopical and X-Ray Diffraction Methods.* In *Fundamentals of Materials Science.* Edited by Mittemeijer EJ: Springer Berlin Heidelberg; 2011: 245-302.
278. Ferraro, J.R., Nakamoto, K., Brown, C.W.: *Basic Theory.* In *Introductory Raman Spectroscopy (Second Edition).* Edited by Ferraro JR, Nakamoto K, Brown CW. San Diego: Academic Press; 2003: 1-94.
279. Mermet, J.-M.: *Fundamental Principles of Inductively Coupled Plasmas.* In *Inductively Coupled Plasma Spectrometry and its Applications.* Edited by Hill SJ: Blackwell Publishing Ltd; 2007: 27-60.
280. Ringgaard, E., Wurlitzer, T.: *Lead-free Piezoceramics based on Alkali Niobates.* Journal of the European Ceramic Society, 2005, **25**, 2701-2706.
281. Kakimoto, K.-i., Masuda, I., Ohsato, H.: *Lead-free $KNbO_3$ Piezoceramics Synthesized by Pressure-less Sintering.* Journal of the European Ceramic Society, 2005, **25**, 2719-2722.
282. Damjanovic, D., Klein, N., Li, J., *et al.*: *What Can Be Expected from Lead-free Piezoelectric Materials?* Functional Materials Letters, 2010, **3**, 5-13.
283. Sahu, S.K., Alexandra, N.: *High-Temperature Materials Chemistry and Thermodynamics.* In *High Temperature Materials and Mechanisms.* Edited by Bar-Cohen Y: CRC Press; 2014: 17-38.
284. Sahu, K.S., Ganesan, R., Gnanasekaran, T.: *Studies on Phase Diagram of Pb–Cr–O System.* Journal of Nuclear Materials, 2008, **376**, 366-370.
285. Sahu, S.K., Ganesan, R., Gnanasekaran, T.: *Standard Molar Gibbs Free Energy of Formation of Pb_5CrO_8(s), Pb_2CrO_5(s), and $PbCrO_4$(s).* The Journal of Chemical Thermodynamics, 2010, **42**, 1-7.
286. Sahu, S.K., Ganesan, R., Gnanasekaran, T.: *Studies on the Phase Diagram of Pb–Fe–O System and Standard Molar Gibbs Energy of Formation of '$PbFe_5O_{8.5}$' and $Pb_2Fe_2O_5$.* Journal of Nuclear Materials, 2012, **426**, 214-222.
287. Zeng, Z.H., Calle-Vallejo, F., Mogensen, M.B., *et al.*: *Generalized Trends in the Formation Energies of Perovskite Oxides.* Physical Chemistry Chemical Physics, 2013, **15**, 7526-7533.
288. Pozdnyakova, I., Navrotsky, A., Shilkina, L., *et al.*: *Thermodynamic and Structural Properties of Sodium Lithium Niobate Solid Solutions.* Journal of the American Ceramic Society, 2002, **85**, 379-384.
289. Xu, H., Navrotsky, A., Su, Y., *et al.*: *Perovskite Solid Solutions along the $NaNbO_3$-$SrTiO_3$ Join: Phase Transitions, Formation Enthalpies, and Implications for General Perovskite Energetics.* Chemistry of Materials, 2005, **17**, 1880-1886.
290. Popovič, A., Bencze, L., Koruza, J., *et al.*: *Knudsen Effusion Mass Spectrometric Approach to the Thermodynamics of Na_2O–Nb_2O_5 System.* International Journal of Mass Spectrometry, 2012, **309**, 70-78.
291. Kobertz, D., Müller, M., Molak, A.: *Vaporization and Caloric Studies on Sodium Niobate.* Calphad, 2015, **48**, 55-71.
292. Frey, M.H., Payne, D.A.: *Nanocrystalline Barium Titanate: Evidence for the Absence of Ferroelectricity in Sol-Gel Derived Thin-Layer Capacitors.* Applied Physics Letters, 1993, **63**, 2753-2755.
293. Sahu, S.K., Ganesan, R., Srinivasan, T.G., *et al.*: *The Standard Molar Enthalpies of Formation of Pb_2CrO_5(s) and Pb_5CrO_8(s) by Acid Solution Calorimetry.* The Journal of Chemical Thermodynamics, 2011, **43**, 750-753.

294. Sahu, S.K., Ganesan, R., Gnanasekaran, T.: *The Standard Molar Enthalpies of Formation of $Pb_2Fe_2O_5$(s) and $PbFe_5O_{8.5}$(s) by Acid Solution Calorimetry.* The Journal of Chemical Thermodynamics, 2013, **56**, 57-59.
295. Sahu, S.K., Unruh, D.K., Forbes, T.Z., *et al.*: *Energetics of Formation and Hydration of a Porous Metal Organic Nanotube.* Chemistry of Materials, 2014, **26**, 5105-5112.
296. Navrotsky, A., Ma, C., Lilova, K., *et al.*: *Nanophase Transition Metal Oxides Show Large Thermodynamically Driven Shifts in Oxidation-Reduction Equilibria.* Science, 2010, **330**, 199-201.
297. Navrotsky, A.: *Nanoscale Effects on Thermodynamics and Phase Equilibria in Oxide Systems.* ChemPhysChem, 2011, **12**, 2207-2215.
298. Sahu, S.K., Maram, P.S., Navrotsky, A.: *Thermodynamics of Nanoscale Calcium and Strontium Titanate Perovskites.* Journal of the American Ceramic Society, 2013, **96**, 3670-3676.
299. Navrotsky, A.: *Progress and New Directions in High Temperature Calorimetry Revisited.* Physics and Chemistry of Minerals, 1997, **24**, 222-241.
300. Navrotsky, A.: *Thermochemical Insights into Refractory Ceramic Materials Based on Oxides with Large Tetravalent Cations.* Journal of Materials Chemistry, 2005, **15**, 1883-1890.
301. Ushakov, S.V., Navrotsky, A.: *Experimental Approaches to the Thermodynamics of Ceramics Above 1500°C.* Journal of the American Ceramic Society, 2012, **95**, 1463-1482.
302. Forbes, T.Z., Nyman, M., Rodriguez, M.A., *et al.*: *The Energetics of Lanthanum Tantalate Materials.* Journal of Solid State Chemistry, 2010, **183**, 2516-2521.
303. Costa, G.C.C., Ushakov, S.V., Castro, R.H.R., *et al.*: *Calorimetric Measurement of Surface and Interface Enthalpies of Yttria-Stabilized Zirconia (YSZ).* Chemistry of Materials, 2010, **22**, 2937-2945.
304. Zhang, P., Xu, F., Navrotsky, A., *et al.*: *Surface Enthalpies of Nanophase ZnO with Different Morphologies.* Chemistry of Materials, 2007, **19**, 5687-5693.
305. Robie, R.A., Hemingway, B.S., Fisher, J.R.: *Thermodynamic Properties of Minerals and Related Substances at 298.15K and 1 Bar (105 Pascals) Pressure and at Higher Temperatures.* U.S. Government Printing Office; 1978.
306. Kubatko, K.A., Helean, K.B., Navrotsky, A., *et al.*: *Thermodynamics of Uranyl Minerals: Enthalpies of Formation of Rutherfordine, UO_2CO_3, Andersonite, $Na_2CaUO_2(CO_3)_3$ $(H_2O)_5$, and Grimselite, $K_3NaUO_2(CO_3)_3H_2O$.* American Mineralogist, 2005, **90**, 1284-1290.
307. Shigemi, A., Wada, T.: *Enthalpy of Formation of Various Phases and Formation Energy of Point Defects in Perovskite-Type $NaNbO_3$ by First-Principles Calculation.* Japanese Journal of Applied Physics, 2004, **43**, 6793.
308. Shigemi, A., Wada, T.: *Evaluations of Phases and Vacancy Formation Energies in $KNbO_3$ by First-Principles Calculation.* Japanese Journal of Applied Physics, 2005, **44**, 8048.
309. Shigemi, A., Wada, T.: *First-principles Studies of Phase Stability and the Neutral Atomic Vacancies in $LiNbO_3$, $NaNbO_3$ and $KNbO_3$.* MRS Online Proceedings Library, 2005, **902**.
310. Körbel, S., Marton, P., Elsässer, C.: *Formation of Vacancies and Copper Substitutionals in Potassium Sodium Niobate under Various Processing Conditions.* Physical Review B, 2010, **81**, 174115.
311. Reznitskii, L.A.: *Formation Enthalpies of Nb(IV,V) Oxide Compounds.* Inorganic Materials, 2001, **37**, 491-495.
312. Goldschmidt, V.M.: *Die Gesetze der Krystallochemie.* Naturwissenschaften, 1926, **14**, 477-485.
313. Navrotsky, A.: *Chemical Bonding.* In *Physics and Chemistry of Earth Materials.* Sixth edition. Edited by Navrotsky A: Cambridge University Press; 1994: 172-272.
314. Navrotsky, A.: *Repeating Patterns in Mineral Energetics.* American Mineralogist, 1994, **79**, 589-605.
315. Stølen, S., Grande, T.: *Trends in Enthalpy of Formation.* In *Chemical Thermodynamics of Materials: Macroscopic and Microscopic Aspects.* Edited by Stølen S, Grande T, Allan NL: John Wiley & Sons, Ltd; 2004: 197-227.
316. Lux, H.: *"Säuren" und "Basen" im Schmelzfluss: Die Bestimmung der Sauerstoffionen-Konzentration.* Zeitschrift für Elektrochemie und angewandte physikalische Chemie, 1939, **45**, 303-309.
317. Flood, H., Förland, T.: *The Acidic and Basic Properties of Oxides.* Acta Chemica Scandinavica, 1947, **1**, 592-604.
318. Flood, H., Förland, T., Roald, B.: *The Acidic and Basic Properties of Oxides. III. Relative Acid-Base Strengths of some Polyacids.* Acta Chemica Scandinavica, 1947, **1**, 790-798.
319. Kimizuka, N., Yamamoto, A., Ohashi, H., *et al.*: *The Stability of the Phases in the Ln_2O_3-FeO-Fe_2O_3 Systems which are Stable at Elevated Temperatures (Ln: Lanthanide Elements and Y).* Journal of Solid State Chemistry, 1983, **49**, 65-76.

320. Kanke, Y., Navrotsky, A.: *A Calorimetric Study of the Lanthanide Aluminum Oxides and the Lanthanide Gallium Oxides: Stability of the Perovskites and the Garnets.* Journal of Solid State Chemistry, 1998, **141**, 424-436.
321. Takayama-Muromachi, E., Navrotsky, A.: *Energetics of Compounds ($A^{2+}B^{4+}O_3$) with the Perovskite Structure.* Journal of Solid State Chemistry, 1988, **72**, 244-256.
322. Navrotsky, A.: *Energetics of Oxide Nanoparticles.* International Journal of Quantum Chemistry, 2009, **109**, 2647-2657.
323. Castro, R.H.R., Quach, D.V.: *Analysis of Anhydrous and Hydrated Surface Energies of gamma-Al_2O_3 by Water Adsorption Microcalorimetry.* The Journal of Physical Chemistry C, 2012, **116**, 24726-24733.
324. McHale, J.M., Auroux, A., Perrotta, A.J., *et al.*: *Surface Energies and Thermodynamic Phase Stability in Nanocrystalline Aluminas.* Science, 1997, **277**, 788-791.
325. Levchenko, A.A., Li, G., Boerio-Goates, J., *et al.*: *TiO_2 Stability Landscape: Polymorphism, Surface Energy, and Bound Water Energetics.* Chemistry of Materials, 2006, **18**, 6324-6332.
326. Radha, A.V., Bomati-Miguel, O., Ushakov, S.V., *et al.*: *Surface Enthalpy, Enthalpy of Water Adsorption, and Phase Stability in Nanocrystalline Monoclinic Zirconia.* Journal of the American Ceramic Society, 2009, **92**, 133-140.
327. Costa, G.C.C., Saradhi Maram, P., Navrotsky, A.: *Thermodynamics of Nanoscale Lead Titanate and Barium Titanate Perovskites.* Journal of the American Ceramic Society, 2012, **95**, 3254-3262.
328. Swartz, S.L., Shrout, T.R.: *Fabrication of Perovskite Lead Magnesium Niobate.* Materials Research Bulletin, 1982, **17**, 1245-1250.
329. Lejeune, M., Boilot, J.P.: *Ceramics of Perovskite Lead Magnesium Niobate.* Ferroelectrics, 1984, **54**, 191-194.
330. Cardoso da Costa, G.C., Wu, L., Navrotsky, A.: *Synthesis and Thermochemistry of Relaxor Ferroelectrics in the Lead Magnesium Niobate-Lead Titanate (PMN-PT) Solid Solutions Series.* Journal of Materials Chemistry, 2011, **21**, 1837-1845.
331. Kameda, H., Li, J.W., Chi, D.H., *et al.*: *Crystallization of Lead Zirconate Titanate without Passing Through Pyrochlore by New Solution Process.* Journal of the European Ceramic Society, 2012, **32**, 1667-1680.
332. Tiwari, V.S., Kumar, A., Wadhawan, V.K., *et al.*: *Kinetics of Formation of the Pyrochlore and Perovskite Phases in Sol-Gel Derived Lead Zirconate Titanate Powder.* Journal of Materials Research, 1998, **13**, 2170-2173.
333. Jang-Sik, L.: *Control of Nucleation and Grain Growth Processes in Lead Zirconate Titanate Thin Films.* Electronic Materials Letters, 2007, **3**, 97-102.
334. Malic, B., Jenko, D., Holc, J., *et al.*: *Synthesis of Sodium Potassium Niobate: A Diffusion Couples Study.* Journal of the American Ceramic Society, 2008, **91**, 1916-1922.
335. Lente, M.H.: *Influence of Niobium Pentoxide Phase and Calcination Route on the Formation of Potassium Sodium Niobate Powders.* Ferroelectrics, 2015, **479**, 15-21.
336. Hashizume, T., Yokota, A., Saiki, A., *et al.*: *Fabrication of Potassium Tantalate Films by Hydrothermal Electrochemical Method at Low Temperature.* Journal of Thermal Analysis and Calorimetry, 2008, **92**, 431-434.
337. Kushima, A., Yildiz, B.: *Role of Lattice Strain and Defect Chemistry on the Oxygen Vacancy Migration at the (8.3%Y_2O_3-ZrO_2)/$SrTiO_3$ Hetero-Interface: A First Principles Study.* ECS Transactions, 2009, **25**, 1599-1609.
338. Reaney, I.M., Taylor, D.V., Brooks, K.G.: *Ferroelectric PZT Thin Films by Sol-Gel Deposition.* Journal of Sol-Gel Science and Technology, 1998, **13**, 813-820.
339. Camargo, E.R., Longo, E., Leite, E.R., *et al.*: *Phase Evolution of Lead Titanate from Its Amorphous Precursor Synthesized by the OPM Wet-Chemical Route.* Journal of Solid State Chemistry, 2004, **177**, 1994-2001.
340. Amini, M.M., Sacks, M.D.: *Synthesis of Potassium Niobate from Metal Alkoxides.* Journal of the American Ceramic Society, 1991, **74**, 53-59.
341. Jung, S.-Y., Hwang, S.-J., Sung, Y.-M.: *Enhanced Aurivillius Phase Formation Kinetics in Seeded SBT Thin Films.* Journal of Crystal Growth, 2003, **254**, 92-99.
342. Sung, Y.-M.: *Enhanced Crystal Growth Kinetics in Cation-Doped $Sr_{0.7}Bi_{2.3}Ta_2O_9$ Ferroelectric Thin Films.* Crystal Growth and Design, 2004, **4**, 325-329.
343. Avrami, M.: *Kinetics of Phase Change I - General Theory.* Journal of Chemical Physics, 1939, **7**, 1103-1112.
344. Avrami, M.: *Kinetics of Phase Change II - Transformation-Time Relations for Random Distribution of Nuclei.* Journal of Chemical Physics, 1940, **8**, 212-224.

345. Avrami, M.: *Granulation, Phase Change, and Microstructure - Kinetics of Phase Change. III.* Journal of Chemical Physics, 1941, **9**, 177-184.
346. Anilkumar, G.M., Sung, Y.-M.: *Phase formation kinetics of nanoparticle-seeded strontium bismuth tantalate powder.* Journal of Materials Science, 2003, **38**, 1391-1396.
347. Shigemi, A., Koyama, T., Wada, T.: *First-Principles Studies of Various Crystallographic Phases and Neutral Atomic Vacancies in $KNbO_3$ and $KTaO_3$.* Physica Status Solidi C, 2006, **3**, 2862-2866.
348. Stølen, S., Grande, T.: *Phase Stability.* In *Chemical Thermodynamics of Materials: Macroscopic and Microscopic Aspects.* Edited by Stølen S, Grande T, Allan NL: John Wiley & Sons, Ltd; 2004: 127-155.
349. Verma, A.R., Krishna, P.: *Polymorphism and Polytypism in Crystals.* In *Crystal Research & Technology. Volume* 1. Edited by Kleber W. New York-London-Sydney: WILEY-VCH Verlag; 1966.
350. Roy, R.: *Gel Route to Homogeneous Glass Preparation.* Journal of the American Ceramic Society, 1969, **52**, 344-344.
351. Schwartz, R.W.: *Chemical Solution Deposition of Perovskite Thin Films.* Chemistry of Materials, 1997, **9**, 2325-2340.
352. Nagarajan, V., Ganpule, C.S., Roytburd, A., *et al.*: *Nanoscale Phenomena in Ferroelectric Thin Films.* Integrated Ferroelectrics, 2002, **42**, 173-189.
353. Rabe, K., Dawber, M., Lichtensteiger, C., *et al.*: *Modern Physics of Ferroelectrics: Essential Background.* In *Physics of Ferroelectrics A Modern Perspective. Volume* 105. Edited by Rabe K, Ahn C, Triscone J-M. Berlin/Heidelberg: Springer; 2007: 1-30.
354. Van Bael, M.K., Nelis, D., Hardy, A., *et al.*: *Aqueous Chemical Solution Deposition of Ferroelectric Thin Films.* Integrated Ferroelectrics, 2002, **45**, 113-122.
355. Ganguli, D.: *Sol-Gel Derived Powders and Bulk Ceramics.* In *Sol-Gel Processing. Volume* 1. Edited by Kozuka H. New York: Kluwer; 2005: 149-167.
356. Skoromets, V., Glinsek, S., Bovtun, V., *et al.*: *Ferroelectric Phase Transition in Polycrystalline $KTaO_3$ Thin Film Revealed by Terahertz Spectroscopy.* Applied Physics Letters, 2011, **99**, 052908.
357. Glinšek, S., Arčon, I., Malič, B., *et al.*: *Structural Evolution of the $KTa_{0.6}Nb_{0.4}O_3$ Alkoxide-based Solutions: Probing the Transition Metals Local Environment by X-ray Absorption Spectroscopy.* Journal of Sol-Gel Science and Technology, 2012, **62**, 1-6.
358. Schneller, T.: *Simple Alkoxide Based Precursor Systems.* In *Chemical Solution Deposition of Functional Oxide Thin Films.* Edited by Schneller T, Waser R, Kosec M, Payne D: Springer Vienna; 2013: 3-28.
359. Turova, N.Y., Turevskaya, E.P., Kessler, V.G., *et al.*: *The Chemistry of Metal Alkoxides.* Springer US; 2006.
360. Kessler, V., Spijksma, G., Seisenbaeva, G., *et al.*: *New insight in the role of modifying ligands in the sol-gel processing of metal alkoxide precursors: A possibility to approach new classes of materials.* Journal of Sol-Gel Science and Technology, 2006, **40**, 163-179.
361. Ribot, F., Toledano, P., Sanchez, C.: *Hydrolysis-condensation process of .beta.-diketonates-modified cerium(IV) isopropoxide.* Chemistry of Materials, 1991, **3**, 759-764.
362. Schneller, T., Griesche, D.: *Carboxylate Based Precursor Systems.* In *Chemical Solution Deposition of Functional Oxide Thin Films.* Edited by Schneller T, Waser R, Kosec M, Payne D: Springer Vienna; 2013: 29-49.
363. Xiao, J., Wu, A., Vilarinho, P.M.: *Sol-gel Derived Morphotropic Phase Boundary $0.37BiScO_3$-$0.63PbTiO_3$ Thin Films.* Applied Physics Letters, 2008, **92**, 032902-032903.
364. Wu, A., Gonzalez-Aguilar, G., Vilarinho, P., *et al.*: *Comparing Macroscopic and Microscopic Properties of Seeded Ferroelectric Thin Films.* Journal of Electroceramics, 2008, **21**, 193-197.
365. Kwok, C.K., Desu, S.B.: *Low Temperature Perovskite Formation of Lead Zirconate Titanate Thin Films by a Seeding Process.* Journal of Materials Research, 1993, **8**, 339-344.
366. Xin, H., Ren, W., Wu, X.Q., *et al.*: *Effect of $SrTiO_3$ Buffer Layers on Crystallization and Properties of Sol-Gel Derived $Pb(Zr_{0.52}Ti_{0.48})O_3$ Thin Films.* Ferroelectrics, 2010, **406**, 206-212.
367. Hao, X., Zhai, J.: *Low-temperature Growth of (110)-Preferred $Pb_{0.97}La_{0.02}(Zr_{0.88}Sn_{0.10}Ti_{0.02})O_3$ Antiferroelectric Thin Films on $LaNiO_3$/Si Substrate.* Journal of Crystal Growth, 2008, **310**, 1137-1141.
368. Birnie III, D.P., Jilavi, M.H., Krajewski, T., *et al.*: *The Effect of Barrier Layer Composition and Structure on the Crystallization of PZT Coatings on Silicon.* Journal of Sol-Gel Science and Technology, 1998, **13**, 855-859.
369. Narkilahti, J., Tyunina, M.: *The structure of strained perovskite $KTaO_3$ thin films prepared by pulsed laser deposition.* Journal of Physics: Condensed Matter, 2012, **24**, 325901.

370. Meng, X.-J., Sun, J.-L., Yu, J., *et al.*: *Preparation of Highly (100)-Oriented Metallic $LaNiO_3$ Films on Si Substrates by a Modified Metalorganic Decomposition Technique.* Applied Surface Science, 2001, **171**, 68-70.
371. Yang, X., Cheng, J., Yu, S., *et al.*: *Effect of $LaNiO_3$ Sol Concentration on the Structure and Dielectric Properties of $Pb(Zr_{0.53}Ti_{0.47})O_3$ Thin Films Grown on $LaNiO_3$-Coated Si Substrates.* Journal of Crystal Growth, 2008, **310**, 3466-3469.
372. Hasenkox, U., Hoffmann, S., Waser, R.: *Influence of Precursor Chemistry on the Formation of $MTiO_3$ (M = Ba, Sr) Ceramic Thin Films.* Journal of Sol-Gel Science and Technology, 1998, **12**, 67-79.
373. Hoffmann, S., Waser, R.: *Control of the Morphology of CSD-Prepared $(Ba,Sr)TiO_3$ Thin Films.* Journal of the European Ceramic Society, 1999, **19**, 1339-1343.
374. Bretos, I., Jiménez, R., Sirera, R., *et al.*: *Improvement of the Properties of CSD-Processed $(Pb_{0.76}Ca_{0.24})TiO_3$ Thin Films by Control of the Solution Chemistry.* Applied Physics A, 2010, **99**, 297-304.
375. Hoffmann-Eifert, S., Schneller, T.: *Orientation and Microstructure Design.* In *Chemical Solution Deposition of Functional Oxide Thin Films.* Edited by Schneller T, Waser R, Kosec M, Payne D: Springer Vienna; 2013: 407-429.
376. Okhay, O.: *Strontium Titanate Based Films for Tunable Device Applications.* University of Aveiro, Department of Ceramics and Glass Engineering; 2009.
377. Wu, A., Vilarinho, P.M., Salvado, I.M.M., *et al.*: *Sol-Gel Preparation of Lead Zirconate Titanate Powders and Ceramics: Effect of Alkoxide Stabilizers and Lead Precursors.* Journal of the American Ceramic Society, 2000, **83**, 1379-1385.
378. Hoene, J.V., Charles, R.G., Hickam, W.M.: *Thermal Decomposition of Metal Acetylacetonates: Mass Spectrometer Studies.* The Journal of Physical Chemistry, 1958, **62**, 1098-1101.
379. Patil, K.C., Chandrashekhar, G.V., George, M.V., *et al.*: *Infrared Spectra and Thermal Decompositions of Metal Acetates and Dicarboxylates.* Canadian Journal of Chemistry, 1968, **46**, 257-265.
380. Afzal, M., Butt, P.K., Ahmad, H.: *Kinetics of Thermal Decomposition of Metal Acetates.* Journal of thermal analysis, 1991, **37**, 1015-1023.
381. Zhao, C., Guo, Y., Li, C., *et al.*: *Carbonation Behavior of K_2CO_3/AC in Low Reaction Temperature and CO_2 Concentration.* Chemical Engineering Journal, 2014, **254**, 524-530.
382. Sokrates, G.: *Infrared and Raman Characteristic Group Frequencies: Tables and Charts.* Colloid and Polymer Science, 2004, **283**, 235-235.
383. Bradley, D.C., Mehrotra, R.C., Rothwell, I.P., *et al.*: *Homometallic Alkoxides.* In *Alkoxo and Aryloxo Derivatives of Metals.* Edited by Bradley DC, Mehrotra RC, Rothwell IP, Singh A. London: Academic Press; 2001: 3-181.
384. Deacon, G.B., Phillips, R.J.: *Relationships Between the Carbon-Oxygen Stretching Frequencies of Carboxylato Complexes and the Type of Carboxylate Coordination.* Coordination Chemistry Reviews, 1980, **33**, 227-250.
385. George, W.O., Robinson, F.V.: *The Vibrational Spectra of Sodium Acetylacetonate and Sodium $[^2H_1]$acetylacetonate.* Journal of the Chemical Society A: Inorganic, Physical, Theoretical, 1968, 1950-1954.
386. Ernstbrunner, E.E.: *Vibrational Spectra of Acetylacetone and Its Anion.* Journal of the Chemical Society A: Inorganic, Physical, and Theoretical Chemistry, 1970, 1558-1561.
387. Miller, F.A., Wilkins, C.H.: *Infrared Spectra and Characteristic Frequencies of Inorganic Ions.* Analytical Chemistry, 1952, **24**, 1253-1294.
388. Gatehouse, B.M., Livingstone, S.E., Nyholm, R.S.: *The Infrared Spectra of Some Simple and Complex Carbonates.* Journal of the Chemical Society, 1958, 3137-3142.
389. Fujita, J., Martell, A.E., Nakamoto, K.: *Infrared Spectra of Metal Chelate Compounds. VIII. Infrared Spectra of Co(III) Carbonato Complexes.* The Journal of Chemical Physics, 1962, **36**, 339-345.
390. Nakamoto, K.: *Theory of Normal Vibrations.* In *Infrared and Raman Spectra of Inorganic and Coordination Compounds.* Edited by Nakamoto K: John Wiley & Sons, Inc.; 2008: 1-147.
391. Rojac, T., Segedin, P., Kosec, M.: *Using Infrared Spectroscopy to Identify New Amorphous Phases - A Case Study of Carbonato Complex Formed by Mechanochemical Processing.* In *Infrared Spectroscopy - Materials Science, Engineering and Technology.* Edited by Theophile T: InTech; 2012: 13-42.
392. Schutte, C.J.H., Buijs, K.: *The Infra-Red Spectra of K_2CO_3 and Its Hydrates.* Spectrochimica Acta, 1961, **17**, 921-926.
393. Phillips, N.J., Calzada, M.L., Milne, S.J.: *Sol-gel-derived Lead Titanate Films.* Journal of Non-Crystalline Solids, 1992, **147-148**, 285-290.

394. Calzada, M.L., Bretos, I., Jiménez, R., *et al.*: *Chemical Solution Deposition of ($Pb_{1-x}Ca_x$)TiO_3 Thin Films with x=0.5 as New Dielectrics for Tunable Components and Dynamic Random Access Memories.* Journal of the American Ceramic Society, 2005, **88**, 3388-3396.
395. Calzada, M.L., Algueró, M., Ricote, J., *et al.*: *Preliminary Results on Sol-Gel Processing of <100> Oriented $Pb(Mg_{1/3}Nb_{2/3})O_3$-$PbTiO_3$ Thin Films Using Diol-based Solutions.* Journal of Sol-Gel Science and Technology, 2007, **42**, 331-336.
396. Tchernychova, E., Glinšek, S., Malič, B., *et al.*: *Combined Analytical Transmission Electron Microscopy Approach to Reliable Composition Evaluation of $KTaO_3$.* Journal of the American Ceramic Society, 2011, **94**, 1611-1618.
397. Wiegand, S., Flege, S., Baake, O., *et al.*: *Synthesis and Characterization of ($Na_{0.5}K_{0.5}$)NbO_3 (NKN) Thin Films Formed by a Diol-based Sol-gel Process.* Journal of Materials Science & Technology, 2012, **28**, 500-505.
398. Herbert, J.M.: *Ferroelectric Transducers and Sensors.* Gordon and Breach Science Publishers; 1982.
399. Bell, J.M., Knight, P.C.: *Ferroelectric Electrode Interactions in $BaTiO_3$ and PZT Thin Films.* Integrated Ferroelectrics, 1994, **4**, 325-332.
400. Bell, J.M., Knight, P.C., Johnson, G.R.: *Ferroelectric-Electrode Interactions.* In *Ferroelectric Thin Films: Synthesis and Basic Properties.* Edited by Paz de Araujo C, Scott JF, Taylor GW: Taylor & Francis; 1996: 93-134.
401. Yang, M., Wang, J., Yan, M., *et al.*: *A Novel Sol-Gel Method of Preparation of the $LiTaO_3$ Thin Film and Its Property Research.* Integrated Ferroelectrics, 2014, **154**, 43-49.
402. González, A.H.M., Simões, A.Z., Zaghete, M.A., *et al.*: *Effect of Thermal Treatment Temperature on the Crystallinity and Morphology of $LiTaO_3$ Thin Films Prepared from Polymeric Precursor Method.* Journal of Electroceramics, 2004, **13**, 353-359.
403. Cheng, Z.X., Kimura, H., Ozawa, K., *et al.*: *Ferroelectric Lithium Tantalate Thin Film Derived from Peroxide.* Journal of Alloys and Compounds, 2005, **402**, 208-212.
404. Gou, J., Wang, J., Huang, Z.H., *et al.*: *Preparation of $LiTaO_3$ Nano-Crystalline Films by Sol-Gel Process.* In *Key Engineering Materials* (Zhang C, Zhang L eds.), vol. 531-532. pp. 446-449; 2013, 446-449.
405. Gou, J., Wang, J., Yang, M., *et al.*: *Preparation and Characterization of $LiTaO_3$ Films Derived by an Improved Sol-Gel Process.* Acta Metallurgica Sinica (English Letters), 2013, **26**, 299-302.
406. Wang, J., Yang, M., Gou, J., *et al.*: *Preparation and Characterization of Lithium Tantalate Thin Films Using a High-Concentration Precursor Solution.* Journal of Pure and Applied Microbiology, 2013, **7**, 759-764.
407. Wang, J., Gou, J., Li, W.: *Preparation of Room Temperature Terahertz Detector with Lithium Tantalate Crystal and Thin Film.* AIP Advances, 2014, **4**, 027106.
408. Tagantsev, A.K., Gerra, G.: *Interface-induced Phenomena in Polarization Response of Ferroelectric Thin Films.* Journal of Applied Physics, 2006, **100**, 051607.
409. Torres-Martínez, L.M., Cruz-López, A., Juárez-Ramírez, I., *et al.*: *Methylene Blue Degradation by $NaTaO_3$ Sol-Gel Doped with Sm and La.* Journal of Hazardous Materials, 2009, **165**, 774-779.
410. Augugliaro, V., Litter, M., Palmisano, L., *et al.*: *The Combination of Heterogeneous Photocatalysis with Chemical and Physical Operations: A Tool for Improving the Photoprocess Performance.* Journal of Photochemistry and Photobiology C: Photochemistry Reviews, 2006, **7**, 127-144.
411. Gogate, P.R., Pandit, A.B.: *A Review of Imperative Technologies for Wastewater Treatment I: Oxidation Technologies at Ambient Conditions.* Advances in Environmental Research, 2004, **8**, 501-551.
412. Shi, H., Zou, Z.: *Photophysical and Photocatalytic Properties of $ANbO_3$ (A=Na, K) Photocatalysts.* Journal of Physics and Chemistry of Solids, 2012, **73**, 788-792.
413. Jiang, L., Qiu, Y., Yi, Z.: *Potassium Niobate Nanostructures: Controllable Morphology, Growth Mechanism, and Photocatalytic Activity.* Journal of Materials Chemistry A, 2013, **1**, 2878-2885.
414. Xing, J., Fang, W.Q., Zhao, H.J., *et al.*: *Inorganic Photocatalysts for Overall Water Splitting.* Chemistry - An Asian Journal, 2012, **7**, 642-657.
415. Torres-Martínez, L.M., Garza-Tovar, L.L., López R, E.M.: *Photocatalytic Degradation of Methylene Blue in Water by UV-irradiated $ATaO_3$ (A = Li, Na, K) Sol-Gel.* In *Ceramic Transactions*, vol. 193. pp. 197-211; 2006, 197-211.
416. Liu, D.-R., Jiang, Y.-S., Gao, G.-M.: *Photocatalytic Degradation of an Azo Dye using N-doped $NaTaO_3$ Synthesized by One-step Hydrothermal Process.* Chemosphere, 2011, **83**, 1546-1552.
417. Kanhere, P.D., Zheng, J., Chen, Z.: *Site Specific Optical and Photocatalytic Properties of Bi-Doped $NaTaO_3$.* The Journal of Physical Chemistry C, 2011, **115**, 11846-11853.

418. Zhao, Y.-X., Liu, D.-R., Li, F.-F., *et al.*: *Preparation, characterization and photocatalytic activity of N-doped $NaTaO_3$ nanocubes.* Powder Technology, 2011, **214**, 155-160.
419. Su, Y., Wang, S., Meng, Y., *et al.*: *Dual substitutions of single dopant Cr^{3+} in perovskite $NaTaO_3$: synthesis, structure, and photocatalytic performance.* RSC Advances, 2012, **2**, 12932-12939.
420. Qi, L., Li, X.: *N-doped $NaTaO_3$: novel visible-light-driven photocatalysts synthesised by a sol–gel method.* Journal of Sol-Gel Science and Technology, 2014, **69**, 625-629.
421. Zhao, J., Yang, X.: *Photocatalytic Oxidation for Indoor Air Purification: A Literature Review.* Building and Environment, 2003, **38**, 645-654.
422. Das, D.P., Biswal, N., Martha, S., *et al.*: *Solar-Light Induced Photodegradation of Organic Pollutants Over CdS-Pillared Zirconium–Titanium Phosphate (ZTP).* Journal of Molecular Catalysis A: Chemical, 2011, **349**, 36-41.
423. Houas, A., Lachheb, H., Ksibi, M., *et al.*: *Photocatalytic Degradation Pathway of Methylene Blue in Water.* Applied Catalysis B: Environmental, 2001, **31**, 145-157.
424. Fu, H., Pan, C., Yao, W., *et al.*: *Visible-Light-Induced Degradation of Rhodamine B by Nanosized Bi_2WO_6.* The Journal of Physical Chemistry B, 2005, **109**, 22432-22439.
425. Kumar, S., Khanchandani, S., Thirumal, M., *et al.*: *Achieving Enhanced Visible-Light-Driven Photocatalysis Using Type-II $NaNbO_3$/CdS Core/Shell Heterostructures.* ACS Applied Materials & Interfaces, 2014, **6**, 13221-13233.
426. Ikeda, S., Fubuki, M., Takahara, Y.K., *et al.*: *Photocatalytic Activity of Hydrothermally Synthesized Tantalate Pyrochlores for Overall Water Splitting.* Applied Catalysis A: General, 2006, **300**, 186-190.
427. Zielinska, B., Mijowska, E., Kalenczuk, R.J.: *Synthesis and Characterization of K-Ta Mixed Oxides for Hydrogen Generation in Photocatalysis.* International Journal of Photoenergy, 2012, **2012**, 7.
428. Hu, C.-C., Yeh, T.-F., Teng, H.: *Pyrochlore-like $K_2Ta_2O_6$ synthesized from different methods as efficient photocatalysts for water splitting.* Catalysis Science & Technology, 2013, **3**, 1798-1804.
429. Jitta, R.R., Gundeboina, R., Veldurthi, N.K., *et al.*: *Defect pyrochlore oxides: as photocatalyst materials for environmental and energy applications - a review.* Journal of Chemical Technology & Biotechnology, 2015, **90**, 1937-1948.
430. Marfunin, A.S.: *Physics of Minerals and Inorganic Materials: An Introduction.* Berlin–Heidelberg–New York: Springer-Verlag; 1979.
431. Fleury, P.A., Worlock, J.M.: *Electric-Field-Induced Raman Effect in Paraelectric Crystals.* Physical Review Letters, 1967, **18**, 665-667.
432. Frova, A., Boddy, P.J.: *Optical Field Effects and Band Structure of Some Perovskite-Type Ferroelectrics.* Physical Review, 1967, **153**, 606-616.
433. Tobaldi, D.M., Pullar, R.C., Gualtieri, A.F., *et al.*: *Sol-Gel Synthesis, Characterisation and Photocatalytic Activity of Pure, W-, Ag- and W/Ag Co-Doped TiO_2 Nanopowders.* Chemical Engineering Journal, 2013, **214**, 364-375.
434. Saiki, A., Hashizume, T.: *Fabrication of $K_2Ta_2O_6$ Films by Hydrothermal Method and Their Optical Property.* In *Design, Development, and Applications of Structural Ceramics, Composites, and Nanomaterials. Volume* 244. Edited by Singh D, Zhu D, Kriven WM, Mathur S, Lin H-T: John Wiley & Sons, Inc.; 2014: 119-125.
435. Scardi, P., Leoni, M.: *Whole Powder Pattern Modelling.* Acta Crystallographica Section A, 2002, **58**, 190-200.
436. Caglioti, G., Paoletti, A., Ricci, F.P.: *On Resolution and Luminosity of a Neutron Diffraction Spectrometer for Single Crystal Analysis.* Nuclear Instruments and Methods, 1960, **9**, 195-198.
437. Toby, B.H.: *R Factors in Rietveld Analysis: How Good is Good Enough?* Powder Diffraction, 2006, **21**, 67-70.
438. Michel-calendini, F.M., Castet, L.: *Band Structure, Optical and Transport Properties of $KTaO_3$, $KNbO_3$ and $BaTiO_3$ in the Paraelectric Phase.* Ferroelectrics, 1976, **13**, 367-370.
439. Çabuk, S., Mamedov, A.: *A Study of the $LiNbO_3$ and $LiTaO_3$ Absorption Edge.* Turkish Journal of Physics, 1998, **22**, 41-45.
440. Çabuk, S., Mamedov, A.: *Urbach Rule and Optical Properties of the $LiNbO_3$ and $LiTaO_3$.* Journal of Optics A: Pure and Applied Optics, 1999, **1**, 424.
441. Yang, W.-C., Rodriguez, B.J., Gruverman, A., *et al.*: *Polarization-dependent Electron Affinity of $LiNbO_3$ Surfaces.* Applied Physics Letters, 2004, **85**, 2316-2318.
442. Li, P., Ouyang, S., Xi, G., *et al.*: *The Effects of Crystal Structure and Electronic Structure on Photocatalytic H_2 Evolution and CO_2 Reduction over Two Phases of Perovskite-Structured $NaNbO_3$.* The Journal of Physical Chemistry C, 2012, **116**, 7621-7628.

443. Wang, R., Zhu, Y., Qiu, Y., *et al.*: *Synthesis of Nitrogen-doped $KNbO_3$ Nanocubes with High Photocatalytic Activity for Water Splitting and Degradation of Organic Pollutants Under Visible Light.* Chemical Engineering Journal, 2013, **226**, 123-130.
444. Osgood, R.: *Photoreaction Dynamics of Molecular Adsorbates on Semiconductor and Oxide Surfaces.* Chemical Reviews, 2006, **106**, 4379-4401.
445. Thompson, T.L., Yates, J.T.: *Surface Science Studies of the Photoactivation of TiO2New Photochemical Processes.* Chemical Reviews, 2006, **106**, 4428-4453.
446. Luttrell, T., Halpegamage, S., Tao, J., *et al.*: *Why Is Anatase a Better Photocatalyst Than Rutile? - Model Studies on Epitaxial TiO_2 Films.* Scientific Reports, 2014, **4**, 4043.
447. Tong, H., Ouyang, S., Bi, Y., *et al.*: *Nano-photocatalytic Materials: Possibilities and Challenges.* Advanced Materials, 2012, **24**, 229-251.
448. Li, L., Salvador, P.A., Rohrer, G.S.: *Photocatalysts with Internal Electric Fields.* Nanoscale, 2014, **6**, 24-42.
449. Mouriño, V., Boccaccini, A.R.: *Bone tissue engineering therapeutics: controlled drug delivery in three-dimensional scaffolds.* Journal of The Royal Society Interface, 2010, **7**, 209-227.
450. Bohner, M.: *Resorbable Biomaterials as Bone Graft Substitutes.* Materials Today, 2010, **13**, 24-30.
451. Shah, N.J., Hong, J., Hyder, M.N., *et al.*: *Osteophilic multilayer coatings for accelerated bone tissue growth.* Advanced Materials, 2012, **24**, 1445-1450.
452. Goodman, S.B., Yao, Z., Keeney, M., *et al.*: *The Future of Biologic Coatings for Orthopaedic Implants.* Biomaterials, 2013, **34**, 3174-3183.
453. Yao, L., McCaig, C.D., Zhao, M.: *Electrical Signals Polarize Neuronal Organelles, Direct Neuron Migration, and Orient Cell Division.* Hippocampus, 2009, **19**, 855-868.
454. Zhao, M.: *Electrical Fields in Wound Healing - An Overriding Signal that Directs Cell Migration.* Seminars in Cell & Developmental Biology, 2009, **20**, 674-682.
455. Levin, M.: *Bioelectric mechanisms in regeneration: Unique aspects and future perspectives.* Seminars in Cell & Developmental Biology, 2009, **20**, 543-556.
456. Radisic, M., Park, H., Shing, H., *et al.*: *Functional assembly of engineered myocardium by electrical stimulation of cardiac myocytes cultured on scaffolds.* Proceedings of the National Academy of Sciences, 2004, **101**, 18129-18134.
457. Aaron, R.K., Boyan, B.D., Ciombor, D.M., *et al.*: *Stimulation of growth factor synthesis by electric and electromagnetic fields.* In *Clinical Orthopaedics and Related Research*. pp. 30-37; 2004, 30-37.
458. Zhao, M., Song, B., Pu, J., *et al.*: *Electrical signals control wound healing through phosphatidylinositol-3-OH Kinase-γ and PTEN.* Nature, 2006, **442**, 457-460.
459. Barroca, N., Vilarinho, P.M., Fernandes, M.H.V., *et al.*: *Stability of Electrically Induced-Polarization in Poly (L-Lactic) Acid for Bone Regeneration.* Applied Physics Letters, 2012, **101**, 023701.
460. Wang, J.-C., Zhang, D., Leoni, N., *et al.*: *Charging of Moving Surfaces by Corona Discharges Sustained in Air.* Journal of Applied Physics, 2014, **116**, 043301.
461. Barroca, N.: *Electromechanically active Poly (L-actic) acid based structures for regenerative medicine. Doctoral dissertation.* University of Aveiro, Department of Materials and Ceramic Engineering; 2015.
462. Kokubo, T., Takadama, H.: *How Useful is SBF in Predicting In Vivo Bone Bioactivity?* Biomaterials, 2006, **27**, 2907-2915.
463. Peters Jr, T.: *The Albumin Molecule: Its Structure and Chemical Properties.* In *All About Albumin.* Edited by Peters T. San Diego: Academic Press; 1995: 9-75.
464. Aitken, A., Learmonth, M.: *Protein Determination by UV Absorption.* In *The Protein Protocols Handbook.* Edited by Walker J: Humana Press; 2009: 3-6.
465. Bodhak, S., Bose, S., Bandyopadhyay, A.: *Role of Surface Charge and Wettability on Early Stage Mineralization and Bone Cell–materials Interactions of Polarized Hydroxyapatite.* Acta Biomaterialia, 2009, **5**, 2178-2188.
466. Atanassova, E., Tyuliev, G., Paskaleva, A., *et al.*: *XPS study of N_2 annealing effect on thermal Ta_2O_5 layers on Si.* Applied Surface Science, 2004, **225**, 86-99.
467. Liu, J., Liu, J., Li, Z.: *Preparation and photocatalytic activity for water splitting of Pt–$Na_2Ta_2O_6$ nanotube arrays.* Journal of Solid State Chemistry, 2013, **198**, 192-196.
468. Dorozhkin, S.V.: *Bioceramics of Calcium Orthophosphates.* Biomaterials, 2010, **31**, 1465-1485.
469. Dorozhkin, S.: *Calcium Orthophosphates.* Journal of Materials Science, 2007, **42**, 1061-1095.
470. Drouet, C.: *Apatite Formation: Why It May Not Work as Planned, and How to Conclusively Identify Apatite Compounds.* BioMed Research International, 2013, **2013**, 12.

471. Barker, A.S., Ballman, A.A., Ditzenberger, J.A.: *Infrared Study of the Lattice Vibrations in $LiTaO_3$.* Physical Review B, 1970, **2**, 4233-4239.
472. Satapathy, S., Kumar, S., Raja Sekhar, B.N., *et al.*: *Resonant Raman of O–H/O–D Vibrations and Photoluminescence Studies in $LiTaO_3$ Thin Film.* Journal of Applied Physics, 2008, **104**, 033542.
473. Wang, K., Zhou, C., Hong, Y., *et al.*: *A review of protein adsorption on bioceramics.* Interface Focus, 2012, **2**, 259-277.
474. Dee, K.C., Puleo, D.A., Bizios, R.: *Protein-Surface Interactions.* In *An Introduction To Tissue-Biomaterial Interactions.* John Wiley & Sons, Inc.; 2003: 37-52.
475. Militello, V., Casarino, C., Emanuele, A., *et al.*: *Aggregation kinetics of bovine serum albumin studied by FTIR spectroscopy and light scattering.* Biophysical Chemistry, 2004, **107**, 175-187.
476. Lu, R., Li, W.-W., Katzir, A., *et al.*: *Probing the secondary structure of bovine serum albumin during heat-induced denaturation using mid-infrared fiberoptic sensors.* Analyst, 2015, **140**, 765-770.
477. Aral, H., Vecchio-Sadus, A.: *Toxicity of Lithium to Humans and the Environment - A Literature Review.* Ecotoxicology and Environmental Safety, 2008, **70**, 349-356.
478. Miyazaki, T., Kim, H.-M., Kokubo, T., *et al.*: *Mechanism of Bonelike Apatite Formation on Bioactive Tantalum Metal in a Simulated Body Fluid.* Biomaterials, 2002, **23**, 827-832.
479. Koutsoukos, P.G., Nancollas, G.H.: *The Effect of Lithium on the Precipitation of Hydroxyapatite from Aqueous Solutions.* Colloids and Surfaces, 1986, **17**, 361-370.
480. Arioka, M., Takahashi-Yanaga, F., Sasaki, M., *et al.*: *Acceleration of Bone Regeneration by Local Application of Lithium: Wnt Signal-mediated Osteoblastogenesis and Wnt Signal-independent Suppression of Osteoclastogenesis.* Biochemical Pharmacology, 2014, **90**, 397-405.
481. Sanpo, N.: *Influence of the Different Organic Chelating Agents on the Topography, Physical Properties and Phase of SPPS-Deposited Spinel Ferrite Splats.* In *Solution Precursor Plasma Spray System.* Edited by Sanpo N: Springer International Publishing; 2014: 61-74.